Mineral Formation and Sorption Mechanisms In Marine Ferromanganese-rich Sediments

Amy Leanne Atkins

Submitted in accordance with the requirements for the degree of

Doctor of Philosophy

The University of Leeds

School of Earth and Environment

October 2014

The candidate confirms that the work submitted is her own, except where work, which has formed part of jointly authored publications has been included. The contributions of the candidate and the other authors to this work have been indicated overleaf. The candidate confirms that appropriate credit has been given where reference has been made to the work of others.

Declaration

Chapter 4 is a reproduction of a peer-reviewed publication in the journal *Geochimica et Cosmochimica Acta* as:

Atkins A. L., Shaw S., Peacock C. L. (2014) Nucleation and growth of todorokite: Implications for trace-metal cycling in marine sediments. *Geochim. Cosmochim*. Acta. **144**, 109-125.

TEM images presented in chapter 4 were collected by Michael Ward at the Leeds Electron Microscopy and Spectroscopy centre with the guidance of the candidate. All other experimental work has been conducted by the candidate. The interpretation of the experimental data, and preparation of the manuscript has been undertaken by the candidate with the help and guidance of her supervisors: Caroline L. Peacock and Sam Shaw.

Chapter 5 is a reproduction of a manuscript currently in the final stages of preparation for submission to the journal *Geochimica et Cosmochimica Acta* as:

Atkins A. L., Shaw S., Peacock C. L. (2014) Transformation of Ni-rich birnessite: Implications for the fate of bioessential Ni.

TEM-EDS data presented in chapter 5 was collected by Michael Ward at the Leeds Electron Microscopy and Spectroscopy centre with the guidance of the candidate. ICP-OES analysis described in the methods section (chapter 3) was conducted by Bob Knight at the Department of Chemistry, University of Hull, UK. Micro thin-sections were prepared by Bob Jones and John Ford at the National Oceanography Centre, Southampton. Caroline Peacock was extensively involved in the collection and processing of the XAS and μ-XAS data presented in chapter 5. All other experimental work has been conducted by the candidate. The interpretation of the experimental data was undertaken by, and the manuscript was prepared by the candidate with the help and guidance of her supervisor: Caroline L. Peacock.

Chapter 6: All mineral synthesis procedures and Ni sorption experiments described in chapter 6 were conducted by the candidate. All of the Ni isotope analysis procedures outlined in the methods chapter (chapter 3) were conducted by Louise Gall at the Department of Earth Sciences, University of Oxford UK, and at the Institute for Research in Environmental Science, University of Colorado, USA. Interpretation of the

data presented in chapter 6 was undertaken by the candidate with guidance from Louise Gall and her supervisor, Caroline L. Peacock.

Acknowledgements

Thanks are due to my supervisors Caroline Peacock and Sam Shaw for their invaluable support and guidance throughout the project. Liane Benning for being part of my research support group and for the useful discussions on crystallization. The Natural Environmental Research Council and the School of Earth and Environment for funding my PhD and various trips to national and international conferences. Sam Allshorn for his assistance during lab work. Michael Ward for collecting countless TEM images, Lesley Neve for training me on the XRD and Bob Knight at the University of Hull for ICP-OES analysis. Everyone from the Cohen Geochemistry group, especially the people in office 8.154. Finally, I would like to thank my friends and family for their continued support.

Abstract

The phyllomanganate birnessite is the dominant Mn-bearing phase in oxic marine sediments and through coupled sorption and redox reactions exerts a strong control on the oceanic concentrations of micronutrient trace metals. However, during oxic diagenesis and under mild hydrothermal conditions, birnessite undergoes transformation to the tectomanganate todorokite. The mechanistic details of the transformation are important for the speciation and mobility of metals sequestered by birnessite, and are necessary in order to quantify the role of marine sediments in global trace element cycles.

This study provides new insight into the crystallization pathway and mechanism of todorokite formation from birnessite under conditions analogous to those found in marine diagenetic and hydrothermal settings. Using a combined approach employing X-ray diffraction, electron microscopy, infrared spectroscopy, X-ray absorption spectroscopy and wet chemical methods, I propose a new four-stage process for the transformation of birnessite to todorokite, beginning with todorokite nucleation, then crystal growth from solution to form todorokite primary particles, followed by their self-assembly and oriented growth via oriented attachment to form crystalline todorokite laths, culminating in traditional crystal ripening. Furthermore, the results of this study indicate that contrary to current understanding, the bioessential trace metal Ni impedes the transformation of birnessite to todorokite, and is eventually released into sediment porewaters. This mineralogical transformation may therefore provide a benthic flux of Ni and possibly other micronutrient trace metals to seawater.

Finally, I find that the uptake of Ni to the phyllomanganate birnessite under varying physiochemical conditions is accompanied by Ni stable isotope fractionation. During fractionation, the light Ni isotope is preferentially sorbed to birnessite, leaving the remaining solution heavy with respect to its Ni isotopic composition. These findings raise important questions about the mechanisms and processes responsible for the heavy δ^{60}Ni isotopic compositions recently measured in marine ferromanganese-rich sediments.

Contents

Figures

Tables

Chapter 1

Introduction

1.1 Background information

The phyllomanganate birnessite is ubiquitous in marine ferromanganese-rich sediments (Post, 1999). This highly reactive nanophase is one of the strongest naturally occurring sorbents and oxidants in the environment (e.g. Tebo et al., 2005; Bargar et al., 2005), where it participates in a variety of coupled sorption and redox processes, to mediate the mobility, speciation and the bioavailability of trace elements in seawater and the associated sedimentary system (Goldberg 1954; Sparks et al., 1999; Post, 1999; Spiro et al., 2010). Specifically in marine ferromanganese precipitates nickel (Ni) is found almost entirely incorporated into the birnessite structure (e.g. Peacock and Sherman, 2007a) where it is concentrated by around 10^6 over its average concentration in seawater (Arrhenius, 1969). As birnessite scavenges key micronutrient trace elements including Ni from seawater over time, it not only plays an important role in regulating the trace metal chemistry of the oceans, but marine ferromanganese-rich sediments also provide a ready geochemical reservoir for trace metal chemical information over the entire history of their formation.

As a mineral phase, however, birnessite is highly transient and its reductive dissolution during of burial below the sediment-water interface, results in the release and remobilization of both highly soluble Mn(II) and scavenged trace metals to marine sediment pore waters. (e.g. Burdige, 1993; Calvert and Pedersen, 1996; Morford et al., 2005). In addition, during oxic sediment diagenesis and under low temperature hydrothermal conditions birnessite transforms into the tectomanganate todorokite (Bodei et al., 2007). The exact mechanistic details of this transformation process have remained largely unclear, but will ultimately determine the fate and mobility of trace metals sorbed to the authigenic birnessite phase. With regards to Ni, work so far has suggested that Ni may become structurally incorporated into the neo-formed todorokite phase either during or after birnessite transformation (e.g. Post and Bish,

1988; Bodei et al., 2007), providing a permanent sink for Ni, and potentially other trace metals, in oxic marine sediments. Provided we understand the crystal nucleation and growth mechanisms involved in the formation of todorokite from birnessite, and the molecular-level mechanisms sequestering trace metals to both the birnessite and todorokite phases, then trace metal signatures recorded in ferromanganese-rich marine sediments could be used to reconstruct aspects of the chemical composition of seawater throughout the Earth's history.

Accordingly, in recent years, transition metal stable isotope compositions recorded in marine sediments have become increasingly popular as a means of investigating marine biogeochemical processes and trace metal cycling, in both modern and ancient seawater (e.g. Anbar and Rouxel, 2007). However, one isotope system that has been significantly slower to develop is that of Ni stable isotopes (Cameron and Vance, 2014). Ni is now recognized as a key bioessential trace metal, which is required as a key nutrient for primary productivity in photosynthetic algae (Frausto de Silva and Williams, 2001; Dupont et al., 2010), and as a unique enzyme cofactor in the metabolism of methanogenic archea (Thauer et al., 1998; Cameron et al., 2009). As such, measurements of the concentration and isotopic compositions of Ni recorded in marine sediment archives offer significant potential as a tracer for investigating both modern and ancient biogeochemical processes (e.g. Cameron et al., 2009; Konhauser et al., 2009).

Although these transition metal isotope systems, including the Ni system, show promise as biogeochemical tracers, often little is known about the fundamental controls that give rise to the isotopic fractionations measured in marine sediments. For example, recent measurements of the δ^{60}Ni isotopic composition of marine ferromanganese-rich crusts have revealed that these sediments are significantly heavier in their δ^{60}Ni isotopic composition (0.7‰ - 2.5‰ per mil) than any other geological samples measured to date for their Ni isotopic composition (0.00‰ - 0.5‰) (Gall et al., 2013). Currently there is a lack of understanding of the processes that give rise to the heavy Ni isotopic compositions measured in ferromanganese crusts. Theoretically, the large positive fractionations measured in these sediments could be accounted for by the sorption and subsequent incorporation of Ni into the birnessite structure. However, Ni isotope fractionation associated with the sorption of Ni to birnessite has never been measured experimentally and quantified in the laboratory. Knowledge of the full controls on isotopic fractionations that occur during the adsorption of trace species to minerals in the environment is vital in order to

accurately predict isotope effects in new isotope systems, and interpret variations in isotopic signatures in natural samples.

1.2 Research aims and objectives

In light of the above overview, the overarching aim of the current study is to further develop our understanding of manganese (Mn) oxide behaviour and the role of ferromanganese-rich marine sediments in the short- and long-term biogeochemical cycling of the bio-limiting trace metal Ni.

As such, the specific research objectives of this thesis can be divided into 4 main areas:

(1) Determine the mechanism of formation and growth of todorokite from birnessite under conditions analogous to those found in natural marine settings.
(2) Determine the effect of Ni on the mechanism of formation and growth of todorokite from Ni-enriched birnessite under conditions analogous to those found in natural marine settings.
(3) Determine the fate and mobility of Ni during the transformation of todorokite into birnessite under conditions analogous to those found in natural marine settings.
(4) Determine the extent of Ni isotope fractionation during the experimental sorption of aqueous Ni to Mn oxides under varying physiochemical conditions.

1.3 Thesis outline

This thesis consists of seven chapters. This introductory chapter (chapter 1) is followed by chapter 2, which provides a detailed overview of the literature relevant to the current project. Chapter 3 contains a detailed description of the experimental and analytical methods used throughout this work. Chapter 3 is followed by 3 individual results chapters. Firstly, chapter 4 provides new insight into the mechanism of todorokite formation from birnessite, and the potential implications of the transformation mechanism for trace-metal cycling in ferromanganese-rich marine sediments. Chapter 5 determines the affects of Ni, sorbed to the precursor birnessite phase, on the transformation of birnessite to todorokite, and determines the fate and mobility of Ni during the birnessite to todorokite transformation in oxic marine sediments. Chapter 6 provides new information on Ni stable isotope fractionation during the experimental sorption of Ni to synthetic hexagonal birnessite, the precursor phase to todorokite in the marine environment. Finally, the results from chapters 4-6 are summarized and discussed in chapter 7. This final chapter also discusses possible future work resulting from this PhD thesis.

Chapter 2

Literature review

The following chapter summarizes the background literature relevant to this work. The chapter is divided into 6 major sections as follows:

(1) The role of manganese minerals in trace-metal cycling

(2) Manganese oxides in the marine environment

(3) Manganese oxide precipitates in the marine environment

(4) Birnessite and todorokite mineralogy

(5) Sorption processes at the mineral-water interface

(6) Oceanic biogeochemistry of Ni

2.1 The role of manganese minerals in trace-metal cycling

Manganese oxides are widely abundant in both oxic marine and freshwater sediments, and in terrestrial soils (Burns 1976; Burns and Burns 1979; McKenzie 1989; Post 1999). These highly reactive nanoparticulate phases are amongst the strongest naturally occurring oxidants, capable of oxidizing a whole host of redox sensitive elements and organic matter, including the oxidation of As (III) to As (IV) and As (V), and Cr (III) to Cr (VI) (e.g. Fendorf and Zasoski, 1992; Manceau and Charlet 1992; Murray and Tebo, 2007). In addition to their strong oxidizing capacity, these phases have a strong affinity for the sorption of a wide variety of aqueous trace metal species including Ni (II), Cu (II), Co (II) Pb (II) and Zn (II) (e.g. Manceau et al., 1992; O′Reilly and Hochella 2003; Toner et al., 2006; Manceau et al., 2003; Peacock and Sherman; 2007a,b; Peacock, 2009; Sherman and Peacock 2010; Zhu et al., 2010). It is through this combination of coupled sorption and redox processes, that Mn oxides exert a primary control on the speciation, fate and mobility of trace-metal species and primary contaminants in both aqueous and terrestrial environments (e.g. Goldberg, 1954; Cronan, 1976; Burns and Burns, 1979; Post, 1999; Toner et al., 2006; Peacock and Sherman, 2007a; Sherman and Peacock, 2010; Spiro et al., 2010).

2.2 Manganese oxides in the marine environment

Currently there are over 30 known natural and synthetic Mn oxide minerals, which display a diverse array of structural variations (Post et al., 1999). At present, the most extensive deposition of natural manganese oxide minerals occurs in oxic marine sediments (Crerar and Barnes 1974; Post 1999). The fundamental building block of these phases is the MnO_6 octahedron, which in most cases assembles to form crystal structures of two principle types: (1) layer-type Mn oxides or 'phyllomanganates' and (2) tunnel-type Mn oxides or 'tectomanganates' (Post et al., 1992; Post 1999). Typically, Mn oxides are present in marine ferromanganese-rich sediments as extremely complex mixtures, in which they are intergrown and intermixed with a wide variety of other poorly crystalline oxy (hydr)oxide minerals (Post et al., 1992). As such, the identification and characterization of the manganese oxide phases has often proved challenging. The two most abundant Mn oxides in marine sediments, and therefore the primary concern in the context of the current study, are the phyllomanganate birnessite and the tectomanganate todorokite.

2.3 Manganese oxide precipitates in the marine environment

Marine ferromanganese precipitates precipitate form oxic seawater and marine porewaters, and they are also found as dispersed phases throughout oxic sediments. In addition, marine ferromanganese precipitates form three discrete types of deposits throughout the world's oceans, where they are generally classified as hydrogenetic, early diagenetic and hydrothermal deposits in order to reflect their formation environment and respective modes of accretion (e.g. Cronan, 1976; Hein et al., 1997; Usui and Glasby, 1998). Moreover, they exhibit distinct differences both in terms of mineralogy and trace element composition. A summary of the mineralogy, formation environment and Mn/Fe ratios of these three distinct types of ferromanganese precipitates is presented in Table 2.1.

2.3.1 Hydrogenetic ferromanganese crusts

Hydrogenetic ferromanganese crusts are amongst the slowest growing geological precipitates on Earth with growth rates estimated to be in the region of 1 mm/10^6 yr (Koschinsky and Hein, 2003). Crusts of hydrogenetic origin primarily form

in areas where sedimentation rates are extremely low, such as exposed rocks, plateaus, seamounts and other topographic highs. Their formation is attributed to the direct precipitation and aggregation of colloidal material from ambient seawater (Dymond et al., 1984; Joshima and Usui, 1998; Usui and Terashima, 1997). As hydrogenetic deposits accumulate on exposed surfaces, there is little or no direct input of trace metals from seafloor sediments hence, the chemistry of these precipitates closely reflects interactions with the surrounding water column (Peacock and Sherman, 2007b). Low Mn/Fe ratios, lower than average Ni and Cu concentrations, and particularly high Co and Pt concentrations are characteristic of crusts and nodules formed via hydrogenetic processes (Usui and Terashima, 1997). In terms of mineralogy, these deposits are rich in the poorly ordered phyllomanganate δMnO_2 (Calvert and Price, 1970; Jauhari, 1987).

2.3.2 Diagenetic ferromanganese nodules

Ferromanganese nodules of a diagenetic origin are typically formed at the sediment-water interface of pelagic sediments (Calvert and Price, 1977; Dymond et al., 1984). Bioturbation and continuous movement along the seabed gives rise to their spherical morphology (Somayajulu, 2000; Wang and Muller, 2009). In contrast to hydrogenetic deposits, the mineralogy of diagenetic nodules tends to consist of a mix of δMnO_2, 10 Å phyllomanganate phase (occasionally referred to as buserite in the literature) and the tectomanganate todorokite (Hein et al., 1997). In addition, chemical analysis usually shows particularly high Mn/Fe ratios (Bonatti et al., 1972; Dymond et al., 1984). As the name suggests, the growth and trace-metal composition of diagenetic-type precipitates is largely controlled by early diagenetic processes within the sediments (Calvert and Price, 1977; Dymond et al., 1984). For example, the burial and subsequent decay of organic matter within the seafloor sediments gives rise to a predominantly reducing environment in the underlying sediment column. This redox gradient drives the release and movement of trace-metals through the sediment porewaters towards the higher redox potential zone at the sediment-water interface. Therefore, under suitable Eh-pH conditions, trace metals mobilized during sediment diagenesis may eventually become incorporated into the growing nodules. Like hydrogenetic type deposits, ferromanganese nodules formed through diagenetic processes have extremely slow growth rates, on the order of 10-50 mm/10^6yr (Dymond et al., 1984).

2.3.3 Hydrothermal ferromanganese-rich deposits

Hydrothermal precipitates are the most distinct type of ferromanganese deposit, as they are found strictly in volcanically active areas, such as submarine volcanoes, divergent plate margins and fracture zones (Usui and Glasby, 1998). They are typically characterised by high Mn/Fe ratios and typically lower than average transition element concentrations (Koschinsky and Hein, 2003). The mineralogy of hydrothermal FeMn-rich precipitates is usually dominated by the tectomanganate todorokite (Usui and Glasby, 1998; Hein et al., 1997). In addition, the growth rate of hydrothermal FeMn-rich manganese deposits is believed to be up to three orders of magnitude greater than deposits of hydrogenetic origin (Usui et al., 1989).

Classification	Formation environment	Mineralogy	Mn/Fe ratio
Hydrogenetic	Topographic highs	δMnO_2	Low
Diagenetic	Deep-sea abyssal plain	δMnO_2 & Todorokite	Medium-High
Hydrothermal	Hydrothermal settings	Todorokite	High

Table 2.1 Summary of the 3 major types of marine ferromanganese precipitates.

2.4 Birnessite and todorokite mineralogy

Birnessite was first discovered and reported by Jones and Milne (1956) and has since been found to occur in a wide range of geological settings. In addition to being the major Mn bearing phase in oxic marine sediments and discrete hydrogenetic nodules and crusts (Calvert and Price, 1970; Chukrov, 1985; Jahuri, 1987), birnessite is also ubiquitous in terrestrial soils (Manceau et al., 2002b). The basic birnessite crystal structure consists of stacks of infinitely wide phyllomanganate sheets, formed by edge sharing MnO_6 octahedra (Post et al., 1992). Each sheet contains varying amounts of Mn(III)/Mn(IV) (Post, 1992; Drits et al., 1997). These phyllomanganate layers are separated by a hydrated interlayer region (~7 Å) which typically hosts a variety of hydrated cation species including, Na, K and Mg (Post 1999; Drits et al., 1997). Birnessites often show slight structural variations and are generally distinguished in terms of their crystallinity and long-range periodicity (Table 2.2). For example, crystalline birnessites (Hx-birnessite -hexagonal crystalline

birnessite), yield characteristic X-ray diffraction (XRD) peaks at ~7 Å [001], 3.6 Å [002], 2.4 Å and 1.4 Å (Drits et al, 1997). Whereas birnessites of poorer crystallinity, including 'c-disordered' birnessite and δMnO_2 (also termed vernadite within the literature), exhibit fewer stacks of phyllomanganate sheets and therefore lack any long range ordering (Spiro et al., 2010; Peacock and Sherman, 2007a; Jones and Milne, 1956). As a result, in these phases, the 7 Å and 3.6 Å peaks ([001] and [002] basal reflections, respectively) are often weak or absent altogether. In general, the long range ordering and crystallinity of synthetic birnessite varieties increases in the following order, δMnO_2 → 'c-disordered' birnessite → Hx-birnessite (Villalobos et al., 2003). Studies have shown that naturally occurring birnessites are analogous to δMnO_2 (Calvert and Price, 1970; Jauhari, 1987). However, as discussed above, the low crystallinity of δMnO_2 and lack of long-range order gives rise to poor diffraction patterns. As such, varieties of higher crystalline birnessite such as Hx-birnessite are often favored for use in fundamental experimental studies. The determination of the exact crystal chemical formula of these different structural birnessite varieties has often proved difficult, primarily due to the fact that mixed valence Mn cations are typically present in the birnessite structure in varying proportions (Drits et al., 1997). However, a generic formula for birnessite was proposed by Drits et al., 1997 as [(Na Ca Mn^{2+}) ($Mn^{3+}Mn^{4+}$) O_{14} $2H_2O$].

Synthetic birnessites prepared in the laboratory may have either hexagonal or triclinic layer symmetry. Hexagonal birnessites (e.g. Figure 2.1), including crystalline Hx-birnessite, 'c-disordered' birnessite and naturally occurring δMnO_2, possess octahedral vacancies in the phyllomanganate sheets, which generate significant negative structural charge. Permenant structural charge may also be generated due to the substation of Mn^{4+} for lower valence cations (e.g. Mn^{3+}, Ni^{2+},Cu^{2+} or Co^{3+}) (e.g. Manceau et al., 1997; Silvester et al., 1997; Webb et al., 2005; Villalobos et al., 2006; Peacock and Sherman, 2007; Sherman and Peacock, 2010. This charge deficit is compensated by the intercalation of hydrated and exchangeble metal cations (e.g. Na and Ca) into the birnessite interlayer region (e.g. Drits et al., 1997; Lanson et al., 2008). Studies have suggested that highly crystalline Hx-birnessite may contain approximately 0.833 Mn cations plus 0.167 vacancies per layer octahedron (e.g. Silvester et al., 1997; Lanson et al., 2000). Furthermore, these layer vacancies are also thought to display long range ordering, appearing roughly in every third row of Mn cations across the birnessite [100] surface (Drits et al., 1997). More specifically according to Pauling bond strength predicted charges, an oxygen atom surrounding a birnessite vacancy site is typically coordinated directly to 2 Mn^{4+} atoms which gives a

bond valance of 2 x 4 / 6 = 1 1/3, and an excess charge of 2/3 (Pauling 1960; Appelo and Postma, 1999). In total, the 3 oxygen atoms that surround each vacancy site therefore carry an excess charge of 3 x 2 / 3 = 2. In the case where structural charge arises as a result of the presence of Mn^{3+} in the birnessite layer, oxygen atoms surrounding the Mn^{3+} atom will be coordinated directly to 2 Mn^{3+} atoms and a single Mn^{4+} atom. As such, the 3 oxygen atoms carry an excess charge of 3 x 1/3 = 1. Ultimately it is the presence of these layer vacancies that leads to the hexagonal layer symmetry displayed by Hx-birnessite, 'c-disordered' birnessite and δMnO_2. Birnessites that express hexagonal layer symmetry and thus contain ordered cation vacancies display characteristic lattice parameters, where the ratio of the [100]/[110] reflections (i.e. the a/b ratio) is approximately equal to √3 (Drits et al., 1997; Lanson et al., 2000; Villalobos et al., 2003). The overall structure of hexagonal birnessite is dominated by the basal plane of the phyllomanganate sheets ([001] surface), on which there are three doubly coordinated O atoms in association with each Mn_2O vacancy site. In turn, the edges of the phyllomanganate sheets ([100] surface) are dominated by singly coordinated O atoms of the MnOH functional group (Peacock and Sherman, 2007b).

In triclinic birnessites (often termed Tc-birnessite), triclinic symmetry arises due to the fact that all octahedral layer positions are filled with either Mn^{4+} or Mn^{3+} cations, which gives rise to steric strain within the phyllomanganate layer (Drits et al., 1997). As such, triclinic birnessites are free of layer vacancies and structural layer charge is generated by the substitution of Mn^{4+} for Mn^{3+} cations (Drits et al., 1997; Appelo and Postma, 1999). Reactive surface sites on Tc-birnessite are limited to the MnOH sites that are located along the edges of the phyllomanganate sheets. Birnessites that possess triclinic symmetry are rarely found in the natural environment, and in particular, birnessites found in marine sediments and deep-sea ferromanganese precipitates are almost always of the hexagonal variety. Birnessites with a 10 Å interlayer spacing are also common in marine ferromanganese-rich sediments and are frequently referred to as buserite within the literature (Giovanoli, 1971). In these samples the 10 Å layer spacing arises due to an additional layer of water within the interlayer.

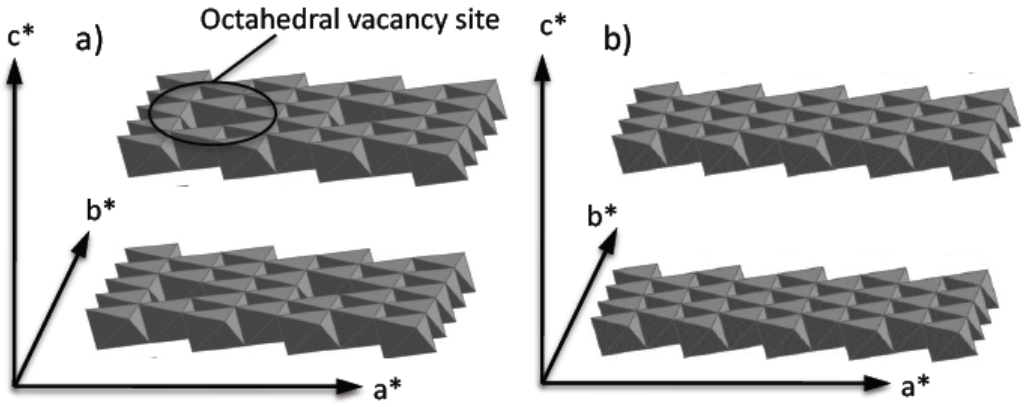

Figure 2.1 Structural representations of (a) Hexagonal birnessite and (b) Triclinic birnessite.

Tunnel-type manganese oxides include the mineral todorokite (occasionally referred to as 10 Å manganite within the literature) (Figure 2.2). The mineral was first discovered at the todoroki mine in Japan (Yoshimura, 1934; Giovanoli, 1985) and has since been identified as one of the primary Mn bearing phases in marine ferromanganese-rich precipitates of both diagenetic and hydrothermal origin (e.g. Usui and Terashima, 1997). The overall todorokite structure is comprised of triple chains of edge-sharing MnO_6 octahedra. These are linked by shared corners into a 3D framework, which in ideal todorokite samples is permeated by 3x3 octahedra-wide rectangular tunnels of infinite length in the b* direction (i.e. along the direction of tunnel growth) (Post 1999). The tunnel structure of todorokite was initially proposed by Turner and Buseck (1981) and eventually confirmed by Post and Bish (1988) after a detailed structural refinement study. Its important to note that the proposed (3x3) tunnel dimensions are highly idealized and various high resolution transmission electron microscopy studies (HRTEM) on natural and synthetic todorokite samples have shown that tunnels are often defective in the a* direction and frequently display tunnel width disorders (Burns et al., 1985; Post and Bish, 1988; Bodeï et al., 2007; Xu et al., 2010). Tunnel dimensions more commonly range from (3x2) up to (3x8) octahedra. It is therefore more appropriate to express the tunnel dimensions of todorokite as (3xn). Various hydrated species are believed to occupy the tunnel apertures of natural todorokite. However, the exact nature of the species varies depending on the formation environment. For example, marine todorokites are typically Mg-rich, where as freshwater todorokites are Ca-rich and terrestrial todorokite samples tend to be Ba and Ca-rich (Appelo and Postma, 1996; Rezaei et al., 2005).

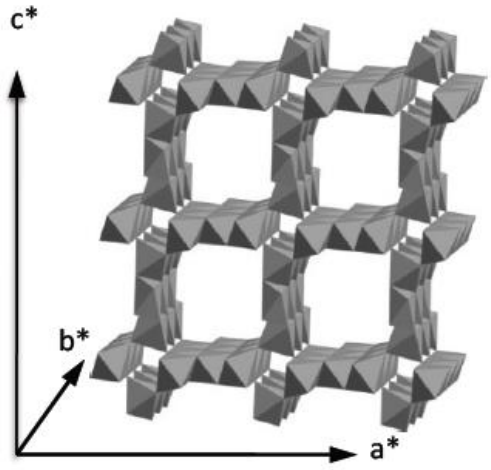

Figure 2.2 Polyhedral representation of the tectomanganate todorokite.

Todorokite exhibits characteristic X-ray diffraction peaks at ~10 Å and ~4.8 Å which correspond to the [100] and [002] reflections respectively (Bodei et al., 2007; Peacock and Sherman, 2007a; Spiro et al., 2010). Similarities in the diffraction features of todorokite and 10 Å birnessite has often resulted in ambiguities in the interpretation of XRD data (Mellin and Lei, 1993). As such, other complementary techniques are usually required to distinguish between 10 Å birnessite and todorokite. For example, todorokite displays a distinctive fibrous morphology that is easily identifiable under the TEM or scanning electron microscope (SEM). Reactive sites on the surface of the todorokite structure consist of singly coordinated oxygen atoms of the MnOH sites, which are located at the edges of the MnO_6 triple chains.

Mineral	Occurrence	Layer Vacancies	Crystal system
δMnO_2/Vernadite	Natural & Synthetic	Yes	Hexagonal
c-disordered birnessite	Synthetic	Yes	Hexagonal
Hexagonal birnessite	Synthetic	Yes	Hexagonal
Sodium birnessite	Synthetic	No	Triclinic
10 Å birnessite/buserite	Natural & synthetic	Yes	Unknown

Table 2.2. Table summarizing the natural and synthetic varieties of birnessite.

2.4.1 Birnessite formation

Naturally occurring birnessites are precipitated as a direct result of the microbially-mediated oxidation of aqueous Mn (II) (e.g. Francis and Tebo, 1999; Brouwers, 2000; Francis et al., 2001; Bargar et al., 2005; Tebo et al., 2005; Webb et al., 2005a; Webb et al., 2005b; Saratovsky et al., 2006; Spiro et al., 2010). Morgan (1964) has studied the oxidation of manganese (II) extensively, and although the process is both thermodynamically favourable and autocatalytic, the reaction is kinetically slow at circumneutral pH. Manganese (II) oxidising microorganisms, primarily bacteria and fungi, are believed to enhance the rate of Mn (II) oxidation by up to 5 orders of magnitude relative to abiotic oxidation (Hastings and Emerson, 1986; Tebo et al., 2005). To date, various strains of Mn(II) oxidizing bacteria and fungi have been isolated from a wide variety of geological settings (Krumbein and Jens, 1981; Adams and Ghiorse, 1987; Tebo et al., 2005; Templeton et al., 2005; Dick et al., 2006; Hansel and Francis, 2006; Miyata et al., 2006; Cahyani et al., 2009). In particular, these species appear to be prevalent in areas where Mn cycling is rapid and there is an abundance of reduced Mn (II) such as, deep-sea hydrothermal vent systems and oxic/anoxic transition zones in pelagic sediments (Villalobos et al., 2003; Tebo et al., 2005; Spiro et al., 2010). In addition, Mn (II) oxidising bacteria are also phyllogentically diverse and recent studies have shown that the marine bacterium *Bacillus* sp. strain SG-1, *Roseobacter* sp. AzwK-3b, and the freshwater bacteria *Pseudomonas putida* strain MnB1 and *Leptothrix discophora* SP-6 all readily oxidise Mn (II) (Bargar et al., 2000; Villalobos et al., 2003; Webb et al., 2005; Saratovsky et al., 2006; Learman et al., 2011). One of the most extensively studied and well-characterised bacteria are the spore forming marine *Bacillus* sp. strain SG-1 (Tebo and He, 1999). First isolated from near-shore marine sediments off the coast of California (Nealson and Ford, 1980), it has since been demonstrated that the SG-1 strain is capable of oxidising Mn (II) under a wide range of physiochemical conditions including temperatures ranging from 3-70°C, ionic strengths analogous to seawater and in the presence of nanomolar concentrations of metals (Francis and Tebo, 2002). Experimental studies have demonstrated that birnessites produced by Mn oxidising bacteria, including the marine *Bacillus* sp. SG-1, are initially extremely poorly ordered and highly defective, consisting of single randomly orientated phyllomanganate sheets with octahedral vacancies and limited stacking. As such, they are structurally very similar to δMnO_2 (Bargar et al., 2005; Webb et al., 2005). This initial phase is then believed to further crystallize abioticaly to form a more stable and ordered structure (Bargar et al., 2005; Webb et al., 2005).

2.4.2 Todorokite formation

At present, there is little direct experimental evidence indicating that todorokite is formed in the natural marine environment as a direct product of biotic Mn (II) oxidation. Instead, it is widely believed that todorokite forms *in situ*, via the topotactic transformation of a layer-type Mn oxide precursor such as δMnO_2 during the early stages of sediment diagenesis (Burns and Burns, 1978a; Halbach et al., 1981; Bodeï et al., 2007). This assertion is thought to explain the intimate association of todorokite and birnessite in ferromanganese-rich marine sediments and has been widely supported by numerous lab-based studies (e.g. Bodeï et al., 2007). Furthermore, the only known route to synthesizing todorokite involves the use of a birnessite precursor (e.g. Golden et al., 1987; Shen et al., 1992; Ching et al., 1999; Luo et al., 1999; Feng et al., 2004; Cui et al., 2006; Feng et al., 2010). In marine diagenetic and hydrothermal settings, todorokite is typically found intimately intermixed with the 10 Å variety of birnessite (buserite) (Bodeï et al., 2007). Thus suggesting that 10 Å birnessite may be an important intermediate in the transformation of birnessite to todorokite. Indeed, laboratory based studies continue to support this idea. As discussed in section 2.4, both natural and synthetic todorokites are often defective in the a* direction. However, along the c* axis, tunnel widths remain consistent (3 octahedra wide) as they are restricted by the layer dimensions of the 10 Å birnessite intermediate phase. This feature provides additional evidence for the formation of todorokite via a 10 Å birnessite intermediate phase.

Traditionally, synthesis of todorokite in the lab proceeds via the suspension of 7 Å triclinic Na-birnessite in a concentrated $MgCl_2$ solution (~1 M) (e.g. Feng et al., 2004). This ion exchange process expands the birnessite interlayer from ~7 Å to ~10 Å. In this case hydrated Mg acts as an ideal templating ion. With a diameter of ~8.6 Å, it closely matches the required dimensions of the todorokite tunnels (i.e. 10 Å in the diagonal direction) (Bodeï et al., 2007). Further to this, the apparent structure-directing role of Mg and its relatively high concentration in seawater are thought to partly explain why todorokite is abundant in marine ferromanganese-rich sediments, but rarely present in terrestrial soils (Chukhrov and Gorshkov, 1981; Dixon and Skinner, 1992) or in freshwater sediments (Manceau et al., 2007a,b). Birnessite samples collected from terrestrial and freshwater environments typically contain relatively high concentrations of Ca as opposed to Mg (Taylor et al., 1964; Glover, 1977; Chukhrov et al., 1980a, 1985; McKenzie, 1989; Bilinski et al., 2002; Manceau et al., 2007b) thus reflecting their respective concentrations in these settings (Appelo

and Postma, 1996; Andersen et al., 2005; Rezaei et al., 2005; Bodeï et al., 2007). Indeed, attempts to transform a Ca-rich birnessite phase to todorokite have failed (Golden et al., 1987). In the laboratory the 10 Å birnessite intermediate phase is subsequently heated to high temperatures and pressures to form todorokite (Golden et al., 1986; Shen et al., 1993; Tian et al., 1997; Vileno et al., 1998; Feng et al., 1998; Malinger et al., 2004). However, a major flaw with this traditional synthesis route is that triclinic Na-birnessite and the high temperature conditions traditionally applied during the synthesis procedure, have limited relevance to the marine environment. To date, there have been relatively few studies to address these crucial facts (Feng et al., 2010).

2.4.2.1 Physiochemical conditions influencing todorokite formation

The importance of Mn (III) present in the birnessite precursor for todorokite formation has become particularly apparent from recent laboratory based studies. For example, Cui et al. (2008) and Cui et al. (2009) attempted to synthesize todorokite from triclinic Na-birnessite with varying degrees of structural Mn (III). The Mn (III) content in the reaction was carefully controlled via the addition of the strong Mn (III) chelating agent sodium pyrophosphate to suspensions of Na-birnessite. Under pH conditions relevant to the marine environment (7-8), it was found that birnessites with an average Mn oxidation state of >3.8 could not be transformed to todorokite. This dependence on the presence of layer Mn (III) has also been alluded to in several other studies (Cui et al., 2006; Bodeï et al., 2007; Feng et al., 2010). These findings raise interesting questions surrounding the transformation of birnessite to todorokite in marine diagenetic and hydrothermal settings, as most natural birnessites have an average Mn oxidation state ~4.0 (e.g. Burns and Burns, 1977; Peacock and Sherman, 2007; Peacock and Moon, 2012).

The significance of the Mn (III) content in the birnessite precursor is primarily linked to the Jahn-Teller distortion displayed by Mn (III) octahedra. As the electronic configuration of Mn (III) is orbitally degenerate (i.e. electrons are unequally distributed amongst orbitals of the same energy) the complex distorts in order to achieve a lower energy state (Figure 2.3). Consequently, the two Mn^{3+}-O bonds along the z-axis are elongated and thus weaker than the other four Mn^{3+}-O bonds. This weak bond along the z-axis is believed by several authors to aid the kinking of the phyllomanganate layers and the subsequent pillaring of the Mn triple chains that form the todorokite

tunnel-walls (Cui et al., 2006; Bodeï et al., 2007; Cui et al., 2008; Cui et al., 2009; Feng et al., 2010). Recently, Feng et al. (2004) successfully synthesised todorokite in 24 hours at atmospheric pressure from a triclinic Na-birnessite precursor via a mild reflux procedure (100^{o}C). In the marine environment, todorokite is most commonly associated with diagenetic and hydrothermal manganese deposits (Mellin & and Lei, 1993; Usui and Someya, 1997). As such, this relatively new method is considered to better mimic the conditions under which natural marine todorokite forms.

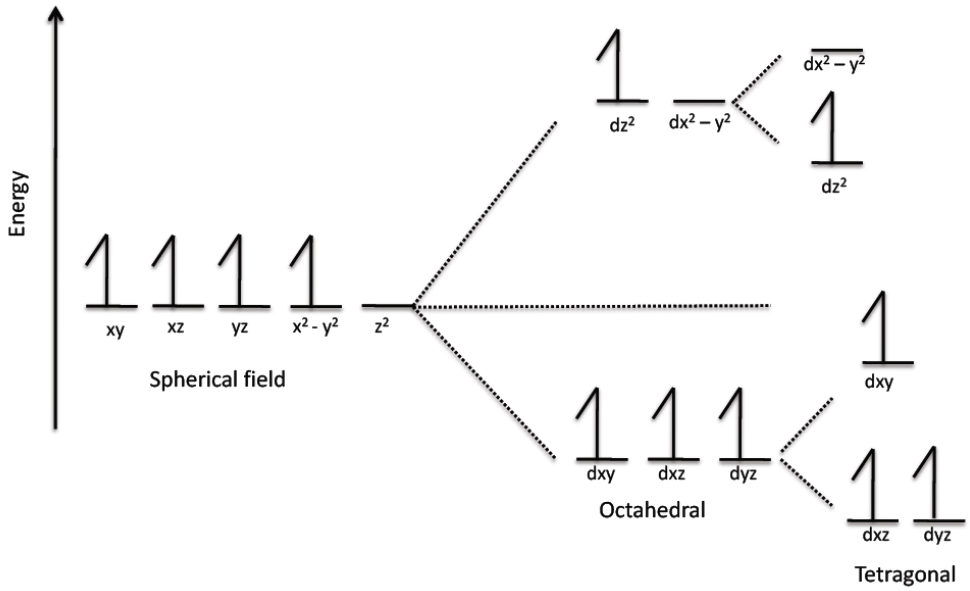

Figure 2.3 Crystal field splitting diagram for Mn(III). The unequal distribution of electrons amongst orbitals of similar energy gives rise to Jahn-Teller distortion of the Mn(III) octahedra.

More recently, Feng et al. (2010) synthesized todorokite from a layered biogenic manganese oxide, precipitated by the freshwater bacteria *Pseudomonas putida* strain MnB1. This hexagonal layered precursor was reportedly similar to poorly crystalline δMnO_2. To date, this single study perhaps best represents natural marine todorokite formation. However, although extensive mineral characterization was undertaken on the birnessite precursor, the 10 Å birnessite intermediate and all of the refluxed products, the study has several weaknesses and appears to be largely inconclusive. Firstly, the published XRD patterns lack clarity due to the highly disordered nature of the birnessite precursor. It is therefore difficult to interpret and evaluate any structural changes taking place over the course of the reflux process. For example, the XRD patterns of the reflux products do not show the characteristic 10 Å peak of todorokite. Secondly, the study does not use Fourier transform infrared

(FT-IR) analysis to distinguish the birnessite precursor and intermediate phases from the subsequent reflux products. Tunnel-type Mn oxides display a characteristic broad peak at 761 cm^{-1} and are clearly distinguishable from layer-type birnessites (Kang et al., 2007). Considering the poor resolution of the XRD patterns presented in the work, FT-IR data would have been invaluable to the study and conclusively shown whether the refluxed products had indeed undergone transformation to todorokite. Lastly, HR-TEM images of the final refluxed product suggest that the transformation of biogenic birnessite to todorokite is incomplete. On comparison of the TEM images, with those presented in other studies, the morphology of the final refluxed product appears to more closely resemble a layer-type birnessite as opposed to tunnel-type todorokite. The TEM images presented in the study also show that the refluxed product has a layer separation approximately equal to 5 Å. Birnessites often displays a layer spacing of 5 Å when viewed under the TEM, as the high vacuum conditions under the microscope can cause the phyllomanganate layer to collapse (Post and Veblen, 1990). In contrast, the tunnel-structure of todorokite has a higher degree of structural stability in comparison to its phyllomanganate precursor. As such, the 10 Å basal spacing is usually preserved and is not as susceptible to collapse. It is therefore plausible that the refluxed product presented in the study of Feng et al. (2010) is in fact predominantly birnessite. In light of the above study, it is crucial to obtain more resolved data to better constrain this environmentally important transformation mechanism.

2.5 Sorption processes at the mineral-water interface

Sorption reactions at the mineral-water interface are fundamental in governing the speciation and mobility of trace-metals and contaminants in both aquatic and terrestrial environments (Sparks et al., 1999). Due to their ubiquity in soils and sediments, the interactions between oxide and oxyhydroxide mineral surfaces and dissolved aqueous species are perhaps the most environmentally significant. When in contact with aqueous solution the surface of metal oxy (hydr)oxides develop a net electrical charge due to the ionization of surface functional groups, with the exact sign and magnitude of the charge dependent on solution pH (Parks, 1990). The pH at which an oxide mineral surface possesses equal concentrations of positively and negatively charged surface sites (i.e. no surface net charge) is termed the point of zero charge (pH_{pzc}). Above the PZC the oxide surface will typically posses a net negative charge and thus the sorption of cation species via electrostatic attraction is

favourable. Conversely, below the PZC the mineral surface will typically posses a net positive charge and thus the sorption of anion species via electrostatic attraction is favourable. The pH_{pzc} is thus a fundamental parameter and can be determined experimentally via potentiometric titration. In the case of birnessite, measured values for the pH_{PZC} range between pH 2.3 and pH 3.0 (Westall and Hohl, 1980; McKenzie, 1981; Peacock, 2009). Unfortunately, the pH_{PZC} for todorokite is less well constrained, but figures reported in the literature include pH 2.8 (Misaelides et al., 2002), pH 3.5 (Feng et al., 2007) and pH 3.98 (Wen-Feng et al., 2008).

Sorption however, is a relatively general term used to describe a variety of different mechanisms by which a chemical species (the sorbate) may partition from aqueous solution to the solid phase (the sorbent) (Brown et al., 1995; Sparks et al., 1999). In general, sorption complexes are classified as either outer-sphere complexes or inner-sphere complexes. The sorption of trace-metal species to a mineral surface may also lead to the eventual incorporation of the trace-species into the mineral structure. A schematic polyhedral representation of these surface complexes is presented in Figure 2.4.

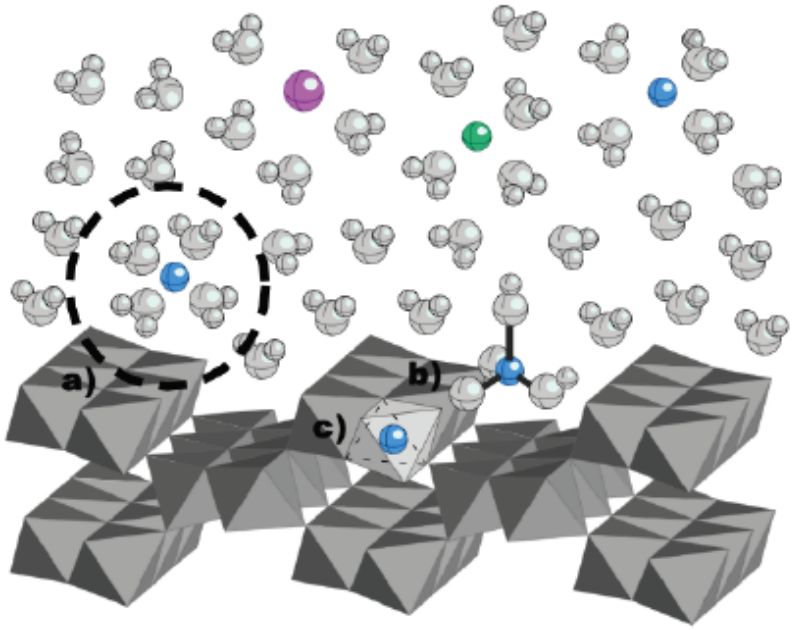

Figure 2.4 Potential molecular-level sorption mechanisms at the oxy (hydr)oxide-water interface. a) Outer-sphere sorption, b) Inner-sphere surface complexation and c) Structural incorporation.

2.5.1 Outer-sphere complexation

The formation of an outer-sphere complex occurs due to long-range coulombic forces between the hydrated ion and the mineral surface. In this case the sorbate ion is not bonded directly to the mineral surface and retains its full hydration sphere. Proximity to the mineral surface is maintained through purely electrostatic interactions. In general, sorption of the sorbate ion to the mineral surface is rapid but often transient. In addition, sorption is usually affected by the ionic strength of the background electrolyte solution.

2.5.2 Inner-sphere complexation

The formation of an inner-sphere complex occurs through short-range electrostatic forces, during which the sorbate ion undergoes the loss of one or more of its waters of hydration to form a direct bond to the mineral surface. In this case bonding may occur in multiple configurations, for example, if the sorbate ion forms a single bond to the mineral surface it is said to form a monodentate complex, two bonds is described as bidentate and three bonds is a tridentate surface complex (Sparks et al., 1999). Ultimately inner-sphere complexes are much more stable than outer-sphere complexes and usually a change in either temperature or pH is required for the process to be reversed.

2.5.3 Structural incorporation

Structural incorporation occurs when a chemical species becomes incorporated into the host crystal lattice of the sorbent phase without altering the bulk mineral structure. Generally, the sorbate ion is similar in size and exhibits the same valency as a structural ion. Incorporation of the sorbate species into the crystal structure may occur via the formation of a solid-solution either by co-precipitation or via solid-state diffusion (Brown et al., 1995).

2.5.4 Sorption of trace metals to birnessite and todorokite

As discussed previously, the uptake of trace-metals to birnessite and todorokite is a key mechanism in controlling the concentration of these species in seawater and the marine sedimentary system (Goldberg, 1954). The extent of trace-metal scavenging by these phases is substantial enough that the mining of marine ferromanganese-rich precipitates for both transition metals and rare earth elements is now considered economically viable (Glasby, 2006; Wang and Muller, 2009).

Traditionally, macroscopic methods (e.g. batch sorption experiments and sorption isotherms) have been used to investigate and measure the uptake of trace-metals and metalloids to Mn oxide surfaces, as a function of both solution pH and ionic strength (e.g. McKenzie, 1980; Green-Pederson et al., 1997; Peacock and Sherman 2007a; Meng et al., 2009). In general, the association of cation species with an oxide surface is negligible at low pH regimes, but increases with an increase in solution pH. A reversal of this behaviour is usually observed for anion species. Unfortunately, these macroscopic methods do not allow a precise description of the surface complexes that may be forming at the mineral surface (i.e. those presented in Figure 2.4). However, in recent years there has been a substantial amount of research directed towards understanding the molecular-level mechanisms of trace-metal uptake to Mn oxides, and in particular to the phyllomanganate birnessite (e.g. Burns 1976; Manceau et al., 1992; Manceau et al., 2002; O'Reilly and Hochella 2003; Toner et al., 2006; Peacock and Sherman, 2007 a,b; Peacock, 2009; Peña et al., 2010; Zhu et al., 2010; Peña et al., 2011; Peacock and Moon, 2012; Yin et al., 2012). These studies have been significantly aided by advances in synchrotron based X-ray absorption spectroscopy (XAS). The technique has been applied extensively to study the speciation and probe the local coordination environment of trace-metals (e.g. Ni^{2+}, Cu^{2+}, Pb^{2+}, Zn^{2+} and Tl) sorbed to natural birnessite in ferromanganese-rich sediments (e.g. Manceau et al., 2007b; Peacock and Sherman, 2007b; Peacock and Moon, 2012), synthetic abiotic birnessite varieties (e.g. Peacock and Sherman 2007a; Peacock et al., 2009; Sherman and Peacock, 2010; Yin et al., 2012) and biogenic birnessite (e.g. Toner et al., 2006; Peña et al., 2010; Zhu et al., 2010; Peña et al., 2011), under different physiochemical conditions. The unusually high affinity for trace-metal sorption displayed by birnessite is largely attributed to the presence of manganese octahedral vacancies present on the birnessite [001] surface which act as extremely strong sites for cation sorption (Appelo and Postma, 1999; Manceau et al.,

2002). This, coupled with a very high reactive surface area (typically > 100m^2/g), means that birnessite is an extremely efficient sorbent of trace-metal species.

As the literature on this subject area is vast, the following discussion will give a brief overview of the literature on trace-metal uptake to Mn oxides, with a primary focus on the uptake of Ni to birnessite and todorokite. A schematic polyhedral diagram showing all of the potential sorption environments for Ni on birnessite and todorokite is presented in Figure 2.5.

Detailed molecular-level studies investigating the association of Ni^{2+}, Cu^{2+} and Zn^{2+} with birnessite have shown that sorption to the birnessite surface occurs via the formation of strong inner-sphere triple corner-sharing (TCS) surface complexes, above and below manganese octahedral vacancy sites on the birnessite [001] surface (e.g. Manceau et al., 2002, 2007b; Toner et al., 2006; Kwon et al., 2009; Peña et al., 2010; Sherman and Peacock, 2010). In addition to surface adsorption, Ni^{2+} and Cu^{2+} species may also become incorporated into the phyllomanganate layer to form edge-sharing complexes (e.g. Peacock and Sherman 2007a; Peacock, 2009; Peña et al., 2010; Sherman and Peacock, 2010). Analogously, studies on the uptake of Pb^{2+} to birnessite have also shown that Pb^{2+} forms strong inner-sphere complexes above and below octahedral vacancy sites, where it is sorbed predominantly as a TCS complex, particularly at low surface loadings. However, at higher surface loadings, it has been shown that Pb^{2+} may also sorb above/below vacancy sites as a triple edge-sharing (TES) complex. In distinct contrast to what has been reported for other trace-metal species, Pb^{2+} may also form a strong inner-sphere complex via sorption to birnessite particle edge sites, as either a double edge-sharing (DES) or a double corner-sharing (DCS) complex (Villalobos et al., 2005; Takahashi et al., 2007; Kwon et al., 2010). The sorption of Pb^{2+} to both octahedral vacancy sites and to lateral edge sites is believed to occur simultaneously, although sorption to the birnessite particle edges is thought to be the more prevalent sorption mechanism (Villalobos et al., 2005).

Specifically in the case of Ni, recent EXAFS based studies performed on synthetic birnessite varieties, including δMnO_2, highly crystalline birnessite (Hx-birnessite) and triclinic birnessite have shown that the uptake of Ni to birnessite is a complex function of both structural (i.e. presence of vacancy sites and reactive surface area) and physiochemical (i.e. pH) factors (Manceau et al., 2007b; Peacock and Sherman 2007a; Peacock, 2009; Zhu et al., 2010; Yin et al., 2012). For example, in triclinic birnessite all of the phyllomanganate layer positions are filled with either Mn (III) or Mn (IV) cation species (Drits et al., 1997). As such, Ni is found to sorb

predominantly to synthetic Tc-birnessite as a TCS complex at the birnessite particle edge sites. Where as, in hexagonal birnessite varieties (i.e. Hx-birnessite and δMnO_2), Ni is sorbed predominantly above/below the octahedral vacancy sites as a strongly bound TCS complex (Peacock and Sherman 2007; Peña et al., 2009). Surface sorbed Ni^{2+} may also become progressively incorporated into the octahedral vacancy sites with increasing contact time, particularly under circumneutral pH conditions (Peacock et al., 2007; Peacock et al., 2009). For example, Peacock (2009) showed that the equilibration of birnessite with a Ni solution for 24 hrs resulted in approximately 90 % of the total Ni being complexed above/below vacancy sites, with the remaining 10 % structurally incorporated into the birnessite lattice. While equilibration for a further 16 days results in an increase in the amount of Ni incorporated into the birnessite structure, up to 30 %. These findings help explain recent EXAFS data obtained from natural ferromanganese crusts samples, which show that Ni is almost entirely incorporated into the birnessite structure in these precipitates (Manceau et al., 2007b; Peacock and Sherman, 2007b). The exact mechanism of Ni incorporation into birnessite is thought to be primarily a function of the rearrangement of surface adsorbed Ni (i.e. the formation of a solid-solution), as opposed to the direct incorporation of Ni into the birnessite crystal structure (Manceau et al., 2007b; Peacock and Sherman, 2007a; Peacock, 2009). In addition to the progressive incorporation of Ni into the birnessite structure, lowering the pH from circumneutral to pH ~4.0, also results in a substantial decrease in the amount of Ni incorporated into the birnessite vacancy sites (Peacock et al., 2009). This reversible structural incorporation of Ni into birnessite raises questions over traditional theories that treat the structural incorporation of trace-metals into oxy (hydr)oxide minerals as a relatively permanent and stable sequestration within the Eh-pH field of the host mineral phase. These findings have potential environmental implications and consequences in terms of palaeoclimatic studies (Peacock, 2009). For example, studies are increasingly using trace-metal compositions in marine ferromanganese precipitates to reconstruct aspects of past seawater chemistry. These palaeo-proxies rely on the idea that trace-metals sorbed to precipitates and their resulting crystal chemistries remain stable after sorption. Clearly a detailed molecular-level understanding of physiochemical affects on trace-metal sequestration is needed if such proxies are to be used with confidence.

Currently there is substantially less information available within the literature regarding trace-metal uptake to todorokite, both in terms of macroscopic and molecular-level information. Although, it is known that tectomanganates offer

significantly fewer possibilities for trace-metal uptake than phyllomanganates. Phyllomanganates have a much higher concentration of both chemical and structural defects such as layer vacancies and stacking faults, thus phyllomanganate phases can sorb more trace-metals per unit weight than tectomanganate phases (Bodeï et al., 2007). An early study by Post and Bish (1988), examining the todorokite structure suggested that large low valence cations such as Ni^{2+} could potentially be substituted for Mn within the octahedral sites at the edges of the todorokite triple chains. This hypothesis was postulated due to the fact that the Mn-O bond distances of the MnO_6 octahedra at the edge of the MnO_6 triple chains are suspected to be longer than those in the middle of the structure. However, there has since been no direct evidence to support this assertion. Furthermore, detailed bulk analyses of diagenetic-type ferromanganese precipitates, containing intermixed birnessite and todorokite, typically show that the todorokite phase contains significantly less Ni than the intermixed birnessite from which it supposedly crystallized. For example, TEM-EDX analysis of a diagenetic-type ferromanganese precipitate by Siegel and Turner (1983) reports a 10 Å birnessite phase containing ~3.8 % NiO, yet the associated neo-formed todorokite contains only ~0.2% NiO. Similarly, TEM-EDS analysis of a ferromanganese concretion collected from the South Pacific Ocean identified a 7 Å birnessite (δMnO_2) phase, which contained approximately ~1 wt % Ni, while in comparison the 10 Å birnessite phase contained ~ 2.8 wt % Ni and the neo-formed todorokite only ~0.16 wt% Ni (Bodei et al., 2007). Since birnessite is considered to transform to todorokite via a solid-phase topotactic transformation pathway, it is unclear why the 10 Å birnessite intermediate phase appears to concentrate significantly more Ni than the neo-formed todorokite. Furthermore, there is currently a lack of information on the exact molecular-level association of Ni, and indeed other trace-metal species, with both these phases during the transformation to todorokite.

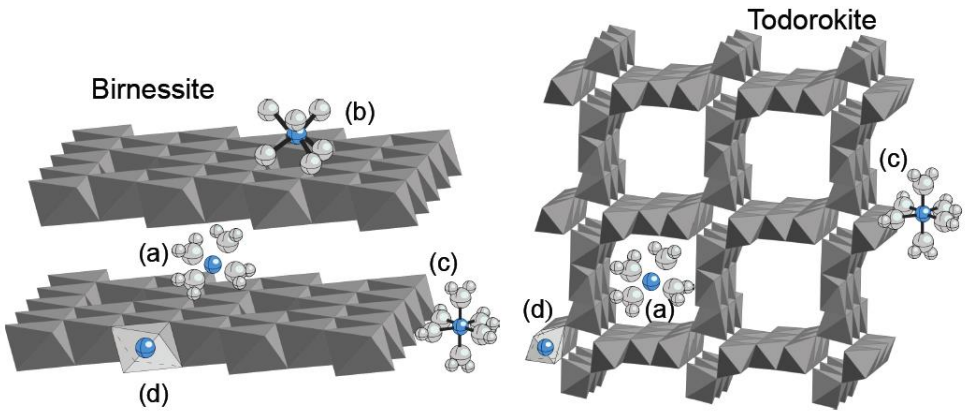

Figure 2.5 Potential sorption mechanisms for Ni^{2+} on birnessite and todorokite. (a) Electrostatic outer-sphere sorption in the birnessite interlayer region and todorokite tunnel apertures. (b) Tridentate inner-sphere complexation above manganese vacancy sites on hexagonal birnessite. (c) Bidentate inner-sphere complexation to MnOH edge sites on hexagonal birnessite, triclinic birnessite and todorokite. (d) Structural incorporation.

2.6 Oceanic biogeochemistry of Ni

In recent years trace-metal concentrations and isotopic compositions in seawater and in ferromanganese-rich ocean sediments have become increasingly used as tracers for biogeochemical processes in both the modern and ancient ocean (e.g. Anbar and Rouxel, 2007). Many of the first row transition metals are classed as biologically active elements, due to their unique biological roles as essential metal cofactors in metalloenzymes or as structural elements in proteins (Morel et al., 2003). Specifically with regards to Ni, the Ni-containing enzyme urease is utilized by marine phytoplankton in the hydrolysis of urea ($CO(NH_2)_2$) to produce NH_4^+ and CO_2 (Dupont et al., 2010). In short, marine phytoplankton are highly dependent on urease and thus in turn on Ni in order to successfully fix nitrogen (Frausto de Silva and Williams, 2001; Dupont et al., 2010). For example, culture studies have shown that when urease-utilizing phytoplankton are grown using urea as a nitrogen source are deprived of Ni, the growth of theses organisms slow and eventually ceases (Price and Morel, 1991; Dupont et al., 2008; Dupont et al., 2010). In addition, Ni is also required as a key enzyme cofactor in the metabolism of methanogenic *Archea,* (Thauer et al., 1998;

Cameron et al., 2009; Fujii et al., 2011) with 3 out of the 7 known Ni containing enzymes found in methanogens (Watt and Ludden 1999). Although with regards to the modern day ocean, methanogenic processes are largely confined to anoxic basins and sediments, it has been recently suggested that changes in Ni concentrations in the ancient oceans may have played a pivotal role in the oxygenation of the early Earth (Konhauser et al., 2009). Through the study of banded iron formations Konhauser and co-workers observed a significant decline in molar Ni/Fe ratios ~2.7 Gyr ago. During this time period, average oceanic Ni concentrations are thought to have fallen from around 400 nm during the Archaean to concentrations similar to those found in the world's oceans today (~8-9 nm). It is believed that cooling of the upper-mantle during the late Archean led to a substantial decrease in seafloor volcanism, and thus ultimately a reduced flux of Ni into the Archean oceans (Konhauser et al., 2009). Such a catastrophic collapse in oceanic Ni concentrations is believed to have significantly disrupted methanogenic activity and thus in turn the production of methane, ultimately paving the way for a progressive rise in atmospheric oxygen levels (Konhauser et al., 2009). This study highlights the potential of Ni signatures recorded in marine sediments to offer insight into the co-evolution of ocean chemistry and life, and thus record key biogeochemical events.

In the modern ocean, Ni displays similar biogeochemical behaviour to many other trace-metal species (Bruland and Lohan, 2003; Cameron and Vance, 2014). Measurements of Ni distributions throughout the world's oceans have shown that Ni displays a typical "nutrient-type" profile, with depleted concentrations in the surface waters (~3 nm/kg) reflecting its biological uptake (Dupont et al., 2010; Cameron and Vance 2014). In a similar manner to the major nutrients silica and phosphorus, Ni concentrations show a general increase with depth, up to ~ 5-12 nm/kg (Sclater et al., 1977; Bruland 1980; Bruland and Lohan 2003). In terms of speciation, Ni is predominantly distributed between several inorganic species including, Ni^{2+}, $NiCl^{+}$, $NiCl_2$, $NiCO_3$, $NiHCO_3^{+}$ and $NiSO_4$, but it is likely that complexation to organic ligands also has a role in controlling the distribution of Ni in seawater (Turner et al., 1981; Byrne et al., 1988; Saito 2004; Turner and Martino, 2006; Vraspir and Butler, 2009). It has been calculated that, in the absence of organic ligands, dissolved Ni in seawater is present in approximately the following proportions, Ni^{2+} (47 %), $NiCl^{+}$ and $NiCl_2$ (34 %), $NiCO_3$ and $NiHCO_3^{+}$ (14 %) (Turner et al., 1981).

Major inputs of Ni to the world's oceans originate from two major sources. Firstly, Ni is associated with the products of continental weathering that subsequently enter the ocean via transport in groundwater and via the dissolved riverine load (e.g.

see Figure 2.6). Atmospheric inputs such as mineral dust and volcanic ash also provide a significant influx of Ni to seawater (Li and Schoonmaker, 2003). In fact it is thought that continental weathering and atmospheric inputs combined contribute to around 80 % of the annual Ni budget (Gailardet et al., 2003). In comparison, hydrothermal vent fluids are considered to provide a relatively minor source of Ni to the modern ocean, contributing to around 20 % of the annual Ni budget (Gailardet et al., 2003).

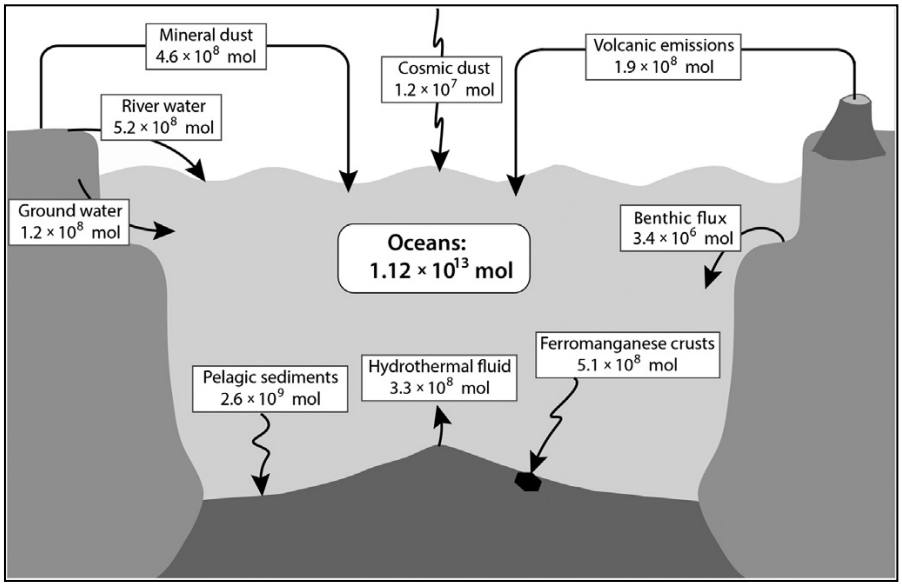

Figure 2.6 Schematic representation of the sources and sinks of dissolved Ni including Ni fluxes calculated by Gall et al., 2013 (from Gall et al, 2013).

As discussed previously, a major sink for Ni in the world's oceans is uptake to ferromanganese-rich crusts, specifically via sorption to the poorly crystalline Mn oxide birnessite (Koschinsky and Hein, 2003; Peacock and Sherman, 2007a). A recent investigation by Gall et al. (2013) into the global variability of Ni isotopic compositions in these precipitates shows that marine ferromanganese crusts display a significantly heavier δ^{60}Ni isotopic composition than any other geological samples reported in the literature to date. As illustrated in Figure 2.7, the measured crust samples display δ^{60}Ni isotopic compositions that vary between +0.7 ‰ and +2.5 ‰, where as the δ^{60}Ni isotopic compositions of other sediment samples measured thus far range between 0.00 ‰ and +0.5 ‰. It therefore seems that the uptake of Ni to marine ferromanganese crusts, and thus sorption to birnessite, is accompanied by isotopic fractionation. Based on the fact that sorption of Ni to ferromanganese crusts is a

major sink for Ni in seawater, and appears to impart a significant isotopic fractionation, these results suggest that this sorption process might have a significant influence on the Ni isotopic composition of seawater. To date however, Ni isotopic fractionation associated with the uptake of Ni to birnessite has never been measured experimentally and quantified in the laboratory.

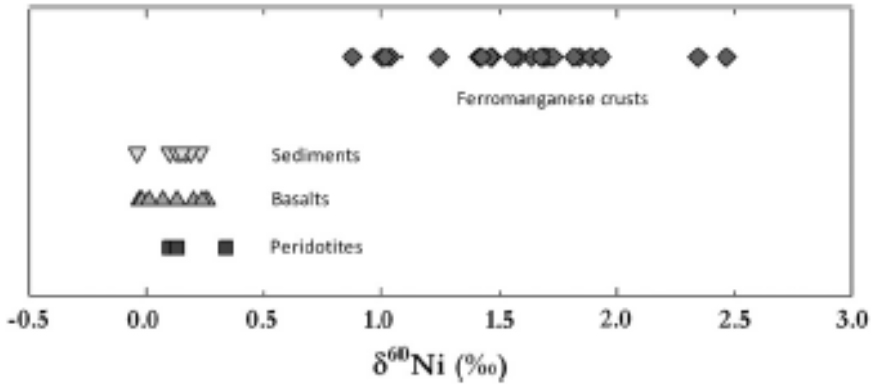

Figure 2.7 Summary of the δ^{60}Ni Isotopic composition of marine ferromanganese crust samples compared to the Ni isotopic composition of of geologiccal samples (from Gall et al., 2013).

Considering the fact that in ferromanganese-rich marine sediments Ni is found almost exclusively incorporated into the birnessite structure, then the heavy δ^{60}Ni isotopic composition measured in marine ferromanganese crusts seem to agree with stable isotope theory for equilibrium isotope fractionation (e.g. Schauble, 2004). Specifically, theory predicts that the heavy metal isotope should be enriched in the shortest and thus strongest bonding environment, which in this case should be provided via incorporation into the phyllomanganate structure. Positive isotope fractionations may also indicate a change in coordination environment during sorption. For example, in the case of Zn, which is 6-fold coordinated in seawater and 4-fold coordinated when sorbed to the birnessite surface, marine ferromanganese crust samples have been shown to display a heavy Zn isotopic composition of around 1.0 ‰ compared to deep seawater which displays a Zn isotopic composition of 0.5 ‰ (Little et al., 2014). Studies to date do not indicate a change in Ni coordination environment associated with sorption to the birnessite surface however (Peacock and Sherman, 2007a,b). Typically, Ni displays 6-fold coordination in solution, 6-fold

coordination when sorbed to the birnessite surface and 6-fold coordination when incorporated to the birnessite structure (Peacock and Sherman, 2007b). As such the large positive Ni isotope compositions of ferromanganese crusts are unlikely to be attributable to a change in Ni coordination during sorption.

The situation is complicated further as a result of a recent study by Cameron and Vance (2014), who present the first Ni isotope data for seawater and for the dissolved riverine load. Firstly, the study shows unequivocally that the Ni isotopic composition of the world's oceans is strikingly homogeneous, both in terms of depth and in terms of spatial variability. For example, the reported isotopic composition of seawater collected from the Atlantic, Pacific and the Southern Oceans is equal to +1.44 ‰ with standard deviations of only +/- 0.15 ‰. With these values in hand, we now see that these measured isotope compositions are very similar to the Ni isotopic compositions measured for marine ferromanganese crusts (Gall et al., 2013), and subsequently appear to suggest that the uptake of Ni to ferromanganese crusts may not after all be accompanied by a significant isotopic fractionation.

In contrast to seawater, the Ni isotopic compositions measured for the dissolved load of 8 major rivers (including the Amazon, Brahmaputra and the Nile) show large variations in their Ni isotopic compositions that range between +0.29 ‰ and 1.39 ‰. Despite the large variability of these results, the crucial point from this dataset is that all of the isotopic values measured for the dissolved riverine load are lighter than the isotopic composition of seawater (Cameron and Vance, 2014) and marine ferromanganese-rich crusts (Gall et al., 2013). The results of the study therefore highlight a significant mass balance issue with respect to the oceanic Ni budget. As the dissolved riverine load provides a major source of isotopically light Ni to ocean, the only way to account for the heavy Ni isotope composition of seawater and ferromanganese crusts would be to identify one or even several other sources that supply isotopically heavy Ni to the worlds oceans. An alternative explanation would be the existence of a missing Ni sink that is isotopically light with respect to its isotopic composition (Cameron and Vance, 2014). At present neither have been identified.

Chapter 3

Methods

In the following chapter the experimental and analytical methods used during this project are described in detail. In some cases the descriptions presented here may overlap with the methods described in results chapters 4, 5 and 6. This has been done so that each individual chapter remains self-explanatory. The methods described in this chapter are:

3.1 Laboratory based methods.

3.1.1 Synthesis of c-disordered birnessite

C-disordered hexagonal birnessite with a 7 Á inter-layer spacing was synthesized following the redox method of Villalobos et al. (2003). The reaction follows equation 3.1.

$$2KMnO_4 + 3MnCl_2 + 4NaOH \rightarrow 5MnO_2 + 4NaCl + 6H_2O$$

(Eq. 3.1)

Briefly, 320 mL of a 0.196 M $KMnO_4$ solution was added slowly to 360 mL of a 0.51 M NaOH solution. Then 320 mL of a 0.366 M $MnCl_2$ solution was added slowly to the above mixture whilst stirring vigorously. The resulting suspension was left to settle for approximately 4 hr. The supernatant was then removed and discarded. The remaining slurry was subsequently centrifuged at 3200 g for 30 min. All resulting supernatants were discarded. After centrifugation, the wet slurry was mixed with 800 mL of 1 M NaCl and shaken for 45 min. The suspension was centrifuged and the supernatant discarded. This process was repeated 4 times. For the last 1 M NaCl wash the pH was adjusted to pH 8 via the drop-wise addition of 1 M NaOH and the suspension shaken overnight. After centrifuging, the resulting paste was combined with Milli-Q grade (MQ) water, shaken for 1 hr and centrifuged at 3200 g for 10 min. This wash cycle was repeated 10 times, 1x for 1 hr, 8x for 0.5 hr and 1x overnight. Following the final wash, the suspension was dialyzed for 3 days in 43 x 27 mm cellulose dialysis tubing, which was placed in a 5 L beaker containing approximately 4 L of MQ water.

3.1.2 Transformation of c-disordered birnessite to todorokite

C-disordered birnessite was transformed to todorokite following a method adapted from Feng et al. (2004) and Feng et al. (2010). Approximately 45-50 g of the previously prepared c-disordered birnessite slurry (section 3.1.1) was suspended in 3 L of 1 M $MgCl_2$ and stirred moderately for 18 hr at room temperature. The resulting suspension was then centrifuged to a wet paste. This produced a 10 Å Mg-exchanged birnessite intermediate. This was re-suspended in approximately 700 mL of 1 M

$MgCl_2$ in a 1 L round bottom flask fitted with a glass condenser. The suspension was stirred continuously and heated to and kept at reflux (100 °C) using a combined heating mantle with magnetic stirrer. Suspension aliquots (approximately 75 mL) were taken at time intervals of 3, 6, 9, 12, 24 and 48 hr. Each suspension aliquot was cooled in a water bath to room temperature before centrifuging at 3200 g for 10 min. All samples were washed extensively in 18.2 MΩ MQ water. After 72 hr the reflux was stopped, the suspension was cooled to room temperature and the above washing procedure was repeated to give the final time series sample of 72 hr. All samples were oven dried at 30 ^{o}C prior to analysis.

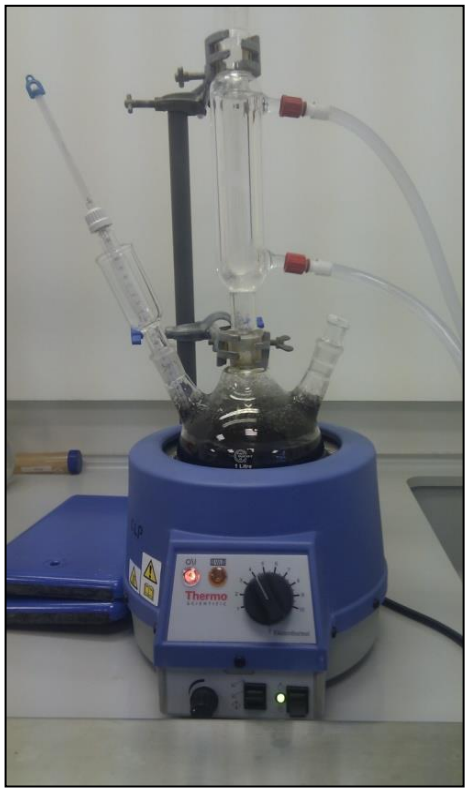

Figure 3.1 Experimental setup used during the transformation of the 10 Å Mg-exchanged birnessite intermediate to todorokite, and during the transformation of a Ni-sorbed 10 Å phyllomanganate to todorokite.

3.1.3 Co-precipitation of c-disordered birnessite in the presence of Ni.

A Ni-sorbed c-disordered hexagonal birnessite (approx 1 wt% Ni) was synthesized following the modified method of Villalobos et al. (2003) as discussed above in section 3.1.1.

Briefly, 320 mL of a 0.196 M $KMnO_4$ solution was added slowly to 360 mL of 0.51 M NaOH solution. Subsequently, 3.41 g of $Ni(NO_3)_2$ was added to 320mL of a 0.366 M $MnCl_2$ solution and added slowly to the above mixture whilst stirring vigorously at room temperature. After 30 minutes 5x 1 mL suspension aliquots were extracted in order to determine the amount of c-disordered birnessite precipitated. Approximately 35 g of mineral was precipitated in total. The mineral suspension was then left to settle for ~4 hr, after which the remaining supernatant was subsequently discarded and the wet mineral slurry centrifuged at 3200 g for 30 min. After centrifugation, the wet slurry was washed by mixing with 1 M NaCl, shaken for 45 min and re-centrifuged at 3200 g for 10 min. This process was repeated 4 times, and on the last wash the pH was adjusted to pH 8 and the suspension was shaken overnight. After the NaCl washes, the slurry was combined with Milli-Q water (MQ), shaken for 1 hr and centrifuged at 3200 g for 10 min. This wash cycle was repeated 10 times, 1x for 1 hr, 8x for 0.5 hr and 1x overnight. After centrifuging, the paste was combined with MQ water, shaken for 1 hr and centrifuged at 3200 g for 10 min. The wash cycle was repeated 10 times, 1x for 1 hr, 8x for 0.5 hrs and 1x overnight. One bottle was sacrificed (i.e. roughly ¼ of total mineral precipitated), retaining the solid for analysis (approximately 8 g).

3.1.4 Transformation of Ni incorporated c-disordered birnessite to todorokite

Ni incorporated c-disordered birnessite was transformed to todorokite using the method adapted from Feng et al. (2004) and Feng et al. (2010) as described above in section 3.1.2. During the current experimental procedure the suspension was left to age at 100 °C for an extended period of 4 weeks, during which suspension aliquots (approximately 75 mL) were extracted from the reaction vessel at time periods of 3, 6, 12, 24, 48 and 72 hr, 1, 2 and 4 weeks. Samples were left to age for an extended period of time as preliminary investigations indicated that the transformation was substantially slower when compared to the Ni free system. All solid samples were washed extensively in 18.2 MΩ MQ water before oven drying at 30 ^{o}C.

3.1.5 Synthesis of reference Manganese Oxide phases

Additionally, a suite of synthetic Mn oxide phases including, Na-birnessite (Tc Na-birnessite), crystalline hexagonal birnessite (Hx-birnessite), δMnO_2 and crystalline todorokite were synthesized and used as reference standards during X-ray absorption spectroscopy (XAS) analysis. All solid samples were crushed to a fine powder prior to analysis.

3.1.5.1 Triclinic Na-birnessite

Poorly crystalline, Tc Na-rich birnessite was prepared as a precursor to synthetic Hx-Birnessite. The preparation of the Na-birnessite precursor was undertaken using the oxidation method of Liu et al (2002). A mixed solution was prepared by dissolving 14.4 g of NaOH in 600 mL of 3 % H_2O_2. This solution was then added to 300 mL of a 0.3 M solution of $Mn(NO_3)_2.6H_2O$. The mixture was stirred vigorously at room temperature (~25 ºC) for approximately 10 min and the resulting precipitate was left undisturbed in the reaction vessel for 72 hr. The supernatant liquor was then siphoned off and the precipitate washed thoroughly in the centrifuge with MQ water until the pH of the supernatant stabilized at around pH 3-4.

3.1.5.2 Crystalline hexagonal birnessite

Synthetic hexagonal birnessite (Hx-Birnessite) was obtained by suspending the washed Na-birnessite precipitate in 0.1 M $NaNO_3$ and adjusting the pH of the suspension to around pH 2 via the dropwise addition of 1 M HNO_3 (similar to the method of Silvester et al., 1997). The mineral suspension was stirred continuously for 4 hr at room temperature and the resulting Hx-birnessite precipitate was washed thoroughly in the centrifuge until the supernatant remained clear. The product was subsequently separated from the supernatant and air-dried at room temperature.

3.1.5.3 δMnO_2

Poorly crystalline δMnO_2 was synthesized following the redox method of Villalobos et al. (2003). The synthesis procedure for δMnO_2 differs from that of c-disordered birnessite (section 3.1.1) only in the fact that a higher stoichiometric ratio of Mn (VII)/Mn(II) is used during the precipitation of δMnO_2 (Villalobos et al., 2003). Briefly, 1280 mL of a 0.19 M $KMnO_4$ solution was prepared and subsequently added slowly to 1440 mL of a 0.48 M of NaOH solution, during which the solution was stirred vigorously. Then 1280 mL of a 0.29 M $MnCl_2.4H_2O$ solution was prepared and added slowly (over approximately 30 min) to the previously prepared mixed solution of $KMnO_4$ and NaOH whilst stirring vigorously. The suspension was left to settle for approximately 4 hr, before the supernatant was siphoned off. The pH of the supernatant measured approximately pH 7. The remaining mineral suspension was evenly distributed between 4 PPCO centrifuge bottles and centrifuged at 3200 g for 30 min. All resulting supernatants were discarded. At this stage the washing procedure conducted during the synthesis of c-disordered birnessite was repeated. In this case, the pH after the final wash was adjusted to pH 8 via the dropwise addition of 1 M NaOH.

3.1.5.4 Highly crystalline todorokite

Highly crystalline todorokite was synthesized following the method of Feng et al. (1995). In the first step, a Na-rich triclinic birnessite phase was prepared following the method described in section 3.1.5.1. After leaving the fresh Na-rich birnessite precipitate to settle for approximately 1 hr, the supernatant was discarded and the solid phase washed extensively in 18.2 MΩ MQ water. A Mg-exchanged birnessite phase was obtained by dispersing approximately 10 g of the wet Na-birnessite slurry in 1 L of 1 M $MgCl_2$. The suspension was stirred moderately for 24 hr at room temperature. The solid phase was subsequently filtered and washed in MQ water. The above ion exchange and washing procedure was repeated 3 times in total. Highly crystalline todorokite was obtained by placing the wet Mg-birnessite slurry into a Teflon-lined, stainless steel reaction vessel, with 10 mL of MQ water before autoclaving at 140 °C and autogeneous pressure for approximately 48 hr. After 48 hr the reaction vessel was left to cool to room temperature, the todorokite suspension was filtered and the solid washed in MQ water and left to air dry.

3.1.6 Determination of average Mn oxidation state via potentiometric titration

The average Mn oxidation states (AOS) of the c-disordered birnessite, 10 Å phyllomanganate intermediate phase and all reflux products synthesized in chapter 4 was determined by the multi-step chemical titration method of Ligane and Karplus (1946) and Gaillot (2002) as follows:

Prior to analysis, a 0.02 M $KMnO_4$ solution was prepared by dissolving 3.06 g of $KMnO_4$ in 1L of 18.2 MΩ MQ water, which had previously been boiled and degassed using zero grade N_2. This solution was stored in the dark for approximately three weeks, before being filtered through a 0.2 µm filter paper to remove any impurities and particulate Mn. The filtered $KMnO_4$ solution was subsequently stored in a brown reagent bottle to prevent the photo reduction of Mn (VII) to Mn (III/IV). In order to determine the precise concentration of the prepared $KMnO_4$ solution, the solution was standardized against a standard solution of oxalic acid. Briefly, 20 mL of a 0.05 M oxalic acid solution was pipetted into a 250 mL conical flask, along with 2 mL of 2 M sulphuric acid. The flask was subsequently warmed on a hot plate to 60 – 80 °C before titration against the $KMnO_4$ solution.

In the first step, a 0.02 M Mohr salt solution ($(NH_4)_2Fe(SO_4)_2{\cdot}6H_2O$)) was prepared and titrated against the $KMnO_4$ solution prepared in the initial step descrbed above, in order to determine the concentration of Fe(II) in the Mohr salt solution. Briefly, 50 mL of the Mohr salt solution was pipetted into a conical flask and acidified with approximately 5 mL of concentrated sulphuric acid before titration against the $KMnO_4$ solution. In this step the average volume of titrant added at the endpoint = ($\mathbf{V_1}$). The end point of the titration was indicated by a change in the colour of the titrand from clear to light pink.

Redox couples are:

$KMnO_4/Mn^{2+}$ and Fe^{3+}/Fe^{2+}

Corresponding reactions are:

$MnO_4^- + 8\ H^+ + 5\ e^- \leftrightarrow Mn^{2+} + 4\ H_2O$

$5\ Fe^{2+} \leftrightarrow 5\ Fe^{3+} + 5\ e^-$

$MnO_4^- + 8\ H^+ + 5\ Fe^{2+} \leftrightarrow Mn^{2+} + 4H_2O + 5\ Fe^{3+}$

From the above reaction:

$n(Fe_{tot}) = 5n(MnO_4^-)$ as such, $n(Fe_{tot}) = 5CV_1$ (Eq. 3.2)

Where $n(Fe_{tot})$ and $n(MnO_4^-)$ are the moles of Iron and permanganate in the solution respectively, and C and V_1 correspond to the concentration of permanganate and the volume of permanganate added at the endpoint respectively.

In the second step, approximately 35 mg of finely ground Mn oxide mineral powder was reduced in exactly 50 mL of the standardized 0.02 M Mohr Salt solution. It is critical that the volume of Mohr salt used in this step is the same as that used in the first step. The mineral suspension was placed in an ultrasonic bath for up to 30 min in order to aid the reductive dissolution of the Mn oxide solid by the Fe^{2+} in the Mohr salt. Following the complete dissolution of the solid Mn oxide, the excess Fe^{2+} in the Fe/Mn oxide solution was titrated against the 0.02 M $KMnO_4$ solution. In this step, the titration was carried out at approximately pH 2 in order to avoid the precipitation of Fe^{3+}, which would substantially impede the accurate assessment of the titration endpoint. The exact volume of $KMnO_4$ required for the titration of the excess Fe^{2+} = (**V_2**). Again the end point was determined by a change in colour from clear to pink.

Redox couples are:

MnO_x/MnO^{2+} and Fe^{3+}/Fe^{2+}

Corresponding reactions are:

$$MnO_y + 2y\ H^+ + 2(y\text{-}1)\ e^- \leftrightarrow Mn^{2+} + y\ H_2O$$

$$\underline{2(y\text{-}1)\ Fe^{2+} \leftrightarrow 2(y\text{-}1)\ Fe^{3+} + 2(y\text{-}1)\ e^-}$$

$$MnO_y + 2(y\text{-}1)\ Fe^{2+} + 2y\ H^+ \leftrightarrow Mn^{2+} + 2(y\text{-}1)\ Fe^{3+} + yH_2O$$

From the above reaction:

$$2(y\text{-}1)\ n(Mn) = 2(y\text{-}1)\ n(MnO_y) = n(Fe_{react}) = n(Fe_{tot}) - n(Fe_{excess}) \qquad \text{(Eq. 3.3)}$$

Where n = the moles of different species.

The redox couples for the titration of the excess Fe^{2+} are the same as those in the first step. As such, V_2 is the volume of permanganate solution added at the endpoint:

$$n(Fe_{excess}) = 5n(MnO_4^-)_{titre} + n(Fe_{excess}) = 5CV_2 \qquad \text{(Eq. 3.4)}$$

and

$$2(y\text{-}1)\ n(MnO_x) = 5CV_1 - 5CV_2 = 5C(V_1 - V_2) \qquad \text{(Eq. 3.5)}$$

The third step in the titration procedure involves the determination of the amount of Mn^{2+} formed in step 2 by performing a back-titration of the excess Fe^{2+} generated in the previous step. Approximately 8 g of sodium pyrophosphate ($Na_4P_2O_7.10H_2O$) was dissolved in 100 mL of MQ water in a separate beaker. This pyrophosphate solution was subsequently added to the reduced Mn oxide solution obtained at the end of the second step. The pH of the mixture was adjusted to pH 6.5 by the careful dropwise addition of concentrated sulphuric acid, before titration against the 0.02 M $KMnO_4$ solution. Due to the bright pink/red color of the pyrophosphate complex, the equivalence point in this final step was determined by potentiometric titration. All potentiometric titrations were undertaken using a Metrohm automated titration suite equipped with a combined platinum ring conductivity electrode. The exact volume of $KMnO_4$ added at the equivalence point = (**V_3**).

Redox couples are:

MnO_4^-/Mn^{2+} and $Mn^{2+} + 3H_2P_2O_7^{2-}/Mn(H_2P_2O_7)_3^{3-}$

Corresponding reactions are:

$MnO_4^- + 8\ H^+ + 5e^- \leftrightarrow Mn^{2+} + 4H_2O$

$5Mn^{2+} + 15\ H_2P_2O_7^{2-} \leftrightarrow 5Mn\ (H_2P_2O_7)_3^{3-} + 5e^-$

$Mn^{2+} + MnO_4^- + 8\ H^+ + 15\ H_2P_2O_7^{2-} \leftrightarrow 5Mn(H_2P_2O_7)_3^{3-} + 4H_2O$

From the above reaction:

$n(Mn^{2+}) = 4n(MnO_4^-) = 4CV_3$ (Eq. 3.6)

Again n is equal to the moles of the different species and V_3 is the volume of $KMnO_4$ added at the equivalence point.

In addition,

$n(Mn^{2+}) = n(MnO_y) + n(MnO_4^-)_{titre}$ (Eq. 3.7)

By combining equations (3.4), (3.6) and (3.7):

$n(MnO_Y) = 4CV_3 – CV_2$ (Eq. 3.8)

By then combining equations (3.5) and (3.8):

$5C(V_1 – V_2) / 2(y – 1) = C(4V_3 – V_2)$ (Eq. 3.9)

Then finally:

$$2y = 2+5\ (V_1 - V_2) / (4V_3 - V_2) \qquad \text{(Eq. 3.10)}$$

Where 2y is equal to the average Mn oxidation state.

3.1.7 Ni Isotope fractionation during sorption to hexagonal birnessite

The following sorption experiments were designed in order to determine whether the uptake of Ni to hexagonal birnessite is accompanied by isotopic fractionation. The results and implications of this work are presented and discussed in chapter 6.

Ni isotope fractionation during the sorption of aqueous Ni (II) to synthetic hexagonal birnessite (c-disordered birnessite) was investigated using a series of 18 unique sorption experiments. Experiments were performed in duplicate, at 4 different Ni loadings (12, 120, 820 and 1640 μg Ni), 2 different pH values (pH 5 and pH 8) and for 3 different time durations (48 hr, 1 week and 4 week). A detailed summary of the experimental parameters used in each individual experiment is presented in chapter 6. The target Ni concentrations used in the experiments were estimated based on previous Ni sorption experiments (Peacock and Sherman, 2007; Peacock, 2009).

For the sorption samples a Ni (II) stock solution was prepared at 1000 mg/L $[Ni]_{total}$ from $Ni(NO_3)_2.6H_2O$ and a 0.1 M NaCl solution was prepared for use as a background electrolyte. Individual sorption experiments were prepared in 250 mL polycarbonate bottles at either 12, 120, 820 or 1640 μg $[Ni]_{total}$ by adding 0.01, 0.1, 0.8 or 1.6 mL of Ni stock solution to 0.01 g of mineral in 199.99, 199.90, 199.20 and 198.40 mL of NaCl respectively. The total volume of solution in each experiment was equal to 200 mL, giving a solid/solution ratio in each individual experiment of 0.05 g/L.

The resulting mineral suspensions were shaken and the initial pH recorded after stabilization to two decimal places. All pH measurements were calibrated to ±0.05 pH units using Whatman NBS grade buffers. The pH was then adjusted to the desired pH (either pH 5 or pH 8) via the drop wise addition of HNO_3/NaOH (various concentrations). All samples were subsequently sealed and shaken at room temperature (25 °C) for the required time period (48 hr, 1 week or 4 week). After shaking, the final suspension pH was recorded and the solid mineral was carefully separated from the solution using a vacuum filtration kit.

Samples were subsequently sent to the University of Oxford for sample purification and Ni isotope analysis. All of the sample purification procedures and subsequent Ni isotope analyses were conducted by Louise Gall at the Department of Earth Sciences, University of Oxford. A full outline of the procedure is presented in Gall et al. (2012), although a brief overview is provided below.

Prior to Ni isotope analysis all solid samples were first digested in a 6 M HCl solution and placed on a hot plate overnight, while all solution samples were first evaporated to dryness and re-dissolved in 6 M HCl. Sample aliquots were subsequently taken and analyzed for their respective Ni concentrations using an ICP-MS equipped with a quadrupole mass filter.

Following sample digestion all samples were treated with what is known as the double-spike method. The double-spike technique is a well established method proposed by Dodson (1963), that allows for the correction of mass fractionations that may occur during the chemical purification of the analyte and during sample analysis (e.g. Siebert et al., 2001; Albarede and Beard, 2004; Rudge et al., 2009). Essentially, the technique involves measuring the relative amounts of four isotopes in a sample, two of which have been enriched via the addition of isotopic spikes (Rudge et al., 2009). Typically the isotopic double-spike is a mixture of two of the minor isotopes (Bullen et al., 2011). As Ni has five stable isotopes, ^{58}Ni, ^{60}Ni, ^{61}Ni, ^{62}Ni, and ^{64}Ni, with respective natural abundances of 68.0769%, 26.2231%, 1.1399%, 3.6345%, and 0.9256% (Gramlish et al., 1989), the isotopes chosen for the double-spike method were ^{61}Ni and ^{62}Ni. These two isotopes were chosen over ^{64}Ni due to the fact that there is potential for interference from ^{64}Zn on ^{64}Ni. The purified Ni spikes used for the current analyses were supplied by Oak Ridge National Laboratory.

Following the double-spiking procedure the samples were again evaporated to dryness before being re-dissolved in a mixture of HCl, di-ammonium citrate ($(NH_4)_2C_6H_6O_7$) and NH_4OH.

Subsequently, a 3-stage ion-exchange chromatography procedure was employed in order to isolate Ni from any elements within the sample matrix that may cause interference during analysis. Briefly, the first separation step involves separating Ni from any s-block elements (e.g. K, Ca and Mg) within the sample matrix via complexation. In this step ammonia forms a strong complex with the Ni in solution and binds strongly to the column resin (AG50W-X4 cation exchange resin), conversely the s-block elements are complexed by the citrate and subsequently

eluted first from the column. The Ni-ammonium complex was removed from the resin and eluted from the column using a 3 M HCl solution.

In the second step, the sample was re-dissolved in a mixed solution of HCl, oxalic acid and H_2O_2. The resulting solution was loaded onto a second ion-exchange column before two separate solutions of oxalic acid-HCl and HCl-acetone were added to the column. The addition of the oxalic acid-HCl mixture eluted any trivalent cation species from the column, whereas addition of the HCl-acetone mixture eluted any remaining divalent species from the column, with the exception of Ni. Ni was finally eluted from the column via complexation with a dimethylglyoxamine ($CH_3C(NOH)C(NOH)CH_3$) (DMG) solution.

The third and final step served to ensure the complete separation of Ni from any Fe species that may have been added to the sample matrix. The samples were dissolved in a mixture of HCl and H_2O_2 before being loaded onto third exchange column (AG1-X8). In this step any Fe remaining in the sample matrix was retained on the column while Ni was immediately eluted.

The Ni isotopic compositions of all the purified solutions were subsequently analyzed using a Nu instruments Nu Plasma-HR multi-collector inductively coupled plasma mass spectrometer (MC-ICPMS). All of Ni isotope ratios presented in chapter 6 are reported in δ notation as the ratio $^{60}Ni/^{58}Ni$ relative to the Ni isotope standard SRM 986 (NIST) according to equation 3.11.

$$\delta^{60}\text{Ni} = \left(\frac{(^{60}Ni/^{58}Ni)_{sample}}{(^{60}Ni/^{58}Ni)_{standard}} - 1 \right) X\ 1000$$

(Eq. 3.11)

3.2 Spectroscopic and analytical tools.

This section gives a brief overview of the spectroscopic and analytical tools used in this thesis.

3.2.1 Powder X-ray diffraction (XRD)

X-ray diffraction (XRD) is a non-destructive technique, routinely used for the structural characterization of polycrystalline samples. When a focused beam of X-rays of known wavelength are generated and passed through a crystalline sample they will be diffracted at specific angles (θ) determined by the distance between adjacent lattice planes (e.g., Greaves, 1995). The exact angles at which the x-rays are diffracted are mathematically related to structural arrangement by the Bragg equation:

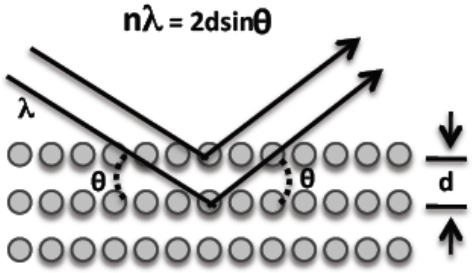

Figure 3.2 Where n is an integer representing the order of reflection, λ is the wavelength of the x-ray beam; d is the distance between adjacent planes of atoms and θ is the angle of the incident x-rays.

The d-spacings, which are unique to a specific sample, can thus be calculated from the Bragg equation and the diffraction patterns compared to a set of standard reference patterns, such as those published on the ICDD (International Centre for Diffraction Data) database (e.g., Wenk and Bulakh, 2004). In addition to phase identification, it is possible to gain information on structural properties of a sample, including residual lattice strain and the degree of structural order, as well as semi-quantitative information on the relative proportions of different minerals in multiphase systems. XRD data can also be used to calculate the average crystallite size through the application of the Scherer formula:

$$d = K\lambda / (B \cos q)$$

(Eq. 3.12)

Where d is crystallite size, K is the Scherer constant (shape factor), λ is the wavelength of the x-rays, B is the peak width at the FWHM of the selected peak (measured in radians) and q is the Bragg angle (in radians).

Typically, if the crystallites are free from strain or do not contain a high proportion of defects then peak broadening should only be an artefact of crystallite size, with potential contributions from the diffractometer. The contribution of instrumental broadening can be deciphered by analysing a standard powder sample of a crystalline material. For example, in the current work the Si (111) reflection was used to determine the effect of instrumental broadening. Calculation of crystallite size is not without its limitations and is generally restricted to crystallites <100 nm in size. Care must also be taken to avoid potential orientation effects (i.e. in this case crystallites will not satisfy the Bragg conditions). The effects of preferred orientation can be easily avoided by rotating the sample during analysis (e.g., Wenk and Bulakh, 2004).

The XRD instrumentation used for the analysis of all samples in this work was a Bruker D8 X-ray diffractometer equipped with CuKα radiation (λ = 1.5418) and a LynxEye detector. Tube voltage and current was approximately 40 kV and 40 mA respectively. XRD was used for analysis of finely ground powder samples, which were obtained during experiments presented in chapter 4 and chapter 5. In an attempt to minimize the effects of background fluorescence during data collection, the window width of the detector was reduced from 0.14 mm to 0.08 mm during the analysis of all samples.

3.2.2 Transmission electron microscopy (TEM)

Transmission electron microscopy (TEM) is a high resolution bulk diffraction and imaging technique that essentially generates a two-dimensional black and white image of a sample, with achievable resolutions down to ~0.2 nm. At these ultra-high resolutions it is possible to characterize a sample in terms of its structure, texture and crystallinity, crystallite size, particle morphology and particle distribution (e.g., Wenk and Bulakh, 2004).

TEM images are generated under high vacuum conditions by transmitting a focused beam of high-energy electrons, which have been accelerated to several hundred keV towards a sample surface. Essentially, electrons that are not scattered are transmitted through the sample where they hit a fluorescent screen underneath the microscope, on which a shadow image of the sample is generated. Contrast in an image is generated as a result of the interaction of the accelerated electrons with the sample. Areas of the image that appear darker are too dense for the electron beam to pass through the sample. Conversely, lighter areas of the image are areas in which the electrons have been transmitted through the sample without being scattered.

For all work presented in chapters 4 and 5 TEM imaging was performed on finely ground powder samples. Samples were loaded onto individual holey carbon TEM grids. All TEM imaging was performed at 200 kV on a Philips CM200 FEGTEM. Images were processed using the Image J software program. All distance measurements were determined in Image J. Prior to measurements images were spatially calibrated in order to measure actual distance in nm as opposed to distance in pixels in Image J using the scale bar presented on each individual TEM image.

3.2.3 Scanning electron microscopy (SEM)

A scanning electron microscope (SEM) uses electrons as opposed to light to generate a magnified three-dimensional image of a specimen. To acquire an SEM image a high-energy beam of electrons are focused and accelerated at ~ 30-200 keV towards a sample and scanned across its surface (e.g., Hochella et al., 1995). As the electrons penetrate the surface layers of a specimen they may interact with the sample in a number of ways. For example, electrons may undergo elastic scattering, generating high energy backscattered electrons during which, little to no energy is transferred from the incident electron to the sample, hence the electron retains much of its original intensity.Conversley, electrons may also be in-elastically scattered, during which, the energy of the incident electron is transferred to the sample. In this case the energy of the emitted electron is significantly reduced, giving rise to low energy secondary electrons.The resulting secondary electrons and backscattered electron signals are collected by a detector where they are amplified and subsequently displayed as an image on a monitor screen. SEM allows the collection of a wide variety of information on the physical and chemical characteristics of a

specimen, including surface topography, morphology, composition and electrical conductivity (e.g., Hochella et al., 1995).

All SEM images presented in this work were collected using an El Quanta 650 FEG-SEM, with imaging performed at 20 keV. Prior to analysis, finely crushed powdered samples were loaded onto individual aluminium stubs and left to air dry before the application of a platinum coating.

3.2.4 Inductively coupled plasma-optical emission spectroscopy (ICP-OES)

Inductively couples plasma-optical emission spectroscopy (ICP-OES) is a popular analytical technique used to measure the concentration of trace-species in aqueous solution. Typically, aqueous samples are aspirated by a nebuliser into an argon gas plasma reaching temperatures up to ~10,000K (e.g. Hou and Jones, 2000). The intense heat of the plasma causes analyte particles to undergo atomisation, ionisation and excitation. Once in an excited state the atoms relax and emit photons at specific wavelengths that are unique to the specific element of interest. Because the emitted radiation is polychromatic it is then passed through a monochromator where the wavelengths are separated, before being converted to an electrical signal that is amplified and subsequently measured by the detector (e.g. Hou and Jones, 2000). The response of an unknown sample is compared to the response of a range of standard solutions of known concentration. ICP-OES is particularly useful for the analysis of geochemical samples as the intense temperature of the argon plasma enables elemental detection limits down to the ppb level.

All ICP-OES measurements presented in chapter 5 were conducted by Robert Knight at the Trace Element Laboratory in the Department of Chemistry at the University of Hull, using an Optima 5300 DV Inductively Coupled Plasma-Optical Emission Spectrometer. For initial storage all samples were diluted 1:1 with 1 % HNO_3. For analysis samples were further diluted (10x) and analyzed in triplicate. For calibration standards, Ni and Mn solutions were prepared at 10, 20 and 30 ppm. In an attempt to improve the accuracy of the measurements and account for spectral interferences as a result of the concentrated background electrolyte (1 M $MgCl_2$,), all standards and calibration blanks were matrix matched.

3.2.5 Fourier transform infra-red spectroscopy (FTIR)

Fourier transform infrared spectroscopy (FTIR) is a widely used, non-destructive analytical technique, which involves passing a beam of infrared radiation through a sample. In short, an IR spectrum records the energy that molecular species absorb IR radiation, which is measured in wavenumbers. The absorption of IR radiation is associated with a vibrational mode of a particular molecule or bond (Wenk and Bulakh, 2004). The infrared region of the electromagnetic spectrum spans a range of 12800-30 cm^{-1} which is generally divided into three distinct regions: the far 400-30 cm^{-1}, mid 4000-400 cm^{-1} and near 12800-4000 cm^{-1}. In the context of the current work the mid IR region is of primary interest, as the vibrational frequencies of the MnO_6 octahedral units in layer-type and tunnel-type Mn oxides differ most in this region (Julien et al., 2003; Kang et al., 2007).

In the current study, FTIR spectroscopy was performed on finely crushed powdered samples using a Thermo Scientific iS10 FTIR spectrometer equipped with an attenuated total reflection (ATR) diamond crystal. Each spectrum presented in chapter 4 was an average of 32 scans with a spectral resolution of 1 cm^{-1}.

3.2.6 Brunauer-Emmett-Teller surface area analysis (BET)

BET is a relatively cheap and reliable method of estimating the reactive surface area of a solid sample, by essentially measuring the amount of gas (X) required to cover both the external mineral surface and internal pore space at a given relative pressure (P/P_0) according to the BET equation (3.13).

$$\frac{1}{X\left(\left(P_0/P\right)-1\right)} = \frac{1}{X_mC} + \frac{C-1}{X_mC}\left(\frac{P}{P_0}\right)$$

(Eq. 3.13)

Where C is the BET constant and X_m is the capacity of a monolayer, which corresponds to the exact volume of gas adsorbed at standard pressure and temperature conditions (i.e. 1 atm and 273 K). Typically, N_2 is used as the adsorbate gas, however, in some cases other gases such as Ar or CO_2 may also be used. The

relative pressure at which adsorption is measured is typically less than atmospheric pressure and is achieved by creating partial vacuum conditions

The specific surface area of a range of synthetic Mn oxide samples described in chapters 4 and 5 were measured using the BET-N_2 method. Measurements were conducted in duplicate using an automated Gemini V2365 system (Micromeritics Instrument Corp.). Prior to analysis finely ground powdered samples were dried and degassed in previously weighed sample tubes for 24 hr at room temperature using a Micromeritics smartprep 065 degassing unit. Sample degassing ensures the removal of any water, or contaminant gases associated with the mineral surface. This procedure is vital in order to ensure the measurement of accurate and precise surface area values. When thorough degassing is not achieved the specific surface area may appear reduced due to the fact that the mineral surface is already covered with previously adsorbed gas molecules. During the degassing procedure 2 clean and empty balance tubes are connected to the Gemini V2365 apparatus in order to allow the determination of the saturation pressure (P_0). Once the saturation pressure has been determined, one of the empty balance tubes is removed and replaced with a sample tube containing the degassed sample which is subsequently evacuated down to a specified pressure. A Dewar vessel containing nitrogen gas is then raised towards the sample tubes. N_2 gas is then admitted to the sample tube to acertain the lowest relative pressure and the volume of adsorbed gas (X) is measured. Measurements are repeated by incrementally admitting known amounts of N_2 gas to the sample tube at increasingly higher P/P_o values. The exact amount of gas adsorbed to the sample surface is calculated from difference measurements taken between the sample tube and the balance tube.

3.3 Synchrotron based Methods

3.3.1 X-ray Absorption Spectroscopy (XAS)

X-ray absorption spectroscopy (XAS) is a bulk technique that can provide unique structural and compositional information on a sample, including oxidation state, structural order and the exact mechanistic details of the nature of surface complexes (Manceau et al., 1992; Brown et al., 1995). Due to its element-selectivity and sensitivity to low element concentrations (<1 wt.%), XAS is an ideal technique for

studying the sorption of trace-metal species at the mineral-water interface. Furthermore, the short range nature of the XAS signal means that the technique is not limited to use on highly crystalline materials, but may be used on poorly ordered samples, such as δMnO_2 and compositionally complex natural samples, including marine ferromanganese-rich precipitates.

In simple terms XAS is primarily concerned with how X-rays are absorbed by an atom at energy levels near to or greater than the core-level binding energy of a particular atom of interest (e.g. De Groot, 2001; Zubavichus and Slovokhotov 2001; Newville, 2004). Measuring the X-ray absorption coefficient (μ) as a function of X-ray energy (e) gives information on the probability of X-ray absorption according to Beers Law:

$$I = I_0 e^{-\mu t}$$

(Eq. 3.14)

Where I is the intensity of X-rays transmitted through a sample, I_0 is the intensity of the incident X-rays and t is equal to the thickness of the sample, as shown in figure 3.3.

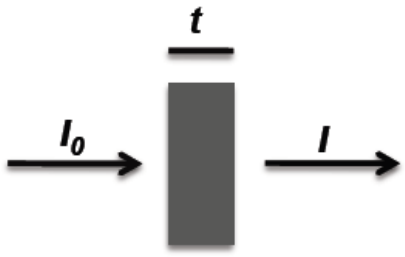

Figure 3.3 During XAS measurements a monochromatic beam of X-rays of intensity $\boldsymbol{I_0}$ are passed through a sample of thickness $\boldsymbol{t}$. The transmitted beam has an intensity $\boldsymbol{I}$.

X-rays generated by synchrotron radiation are extremely intense and tuneable over a broad spectral range by simply adjusting the wavelength of the X-ray source. When incident X-rays are tuned to an energy equal to that of the binding energy of a core-level electron in a particular sample, there will be a substantial rise in X-ray absorption, along with a simultaneous drop in the intensity of the transmitted X-rays. This feature is termed the absorption edge and corresponds directly to the energy required to excite and eject a deep core-level electron from the atom of interest, leaving a core-hole. The ejected photoelectron subsequently radiates away from the

central absorber as a wave, where it interacts and backscatters from surrounding atoms (Greaves, 1995). The backscatter generated creates interference between the outgoing and reflected photoelectron wave, and in turn this interference influences the probability of adsorption of X-ray photons and the emission of decay fluorescent photons. As such, X-ray photon absorption will vary depending on the immediate coordination environment of the atom of interest (e.g. De Groot, 2001; Zubavichus and Slovokhotov 2001; Newville et al., 2004).

An example of a typical X-ray absorption spectrum is presented in Figure 3.3 in which the X-ray absorption coefficient is plotted as a function of increasing energy. The spectrum is generally separated into two distinct regions, the near-edge structure (X-ray absorption near edge structure, XANES) and the extended fine structure (extended x-ray absorption fine structure, EXAFS). As highlighted in Figure 3.4, the XANES region typically occurs within 50 eV of the absorption edge whereas the EXAFS region extends above the absorption edge.

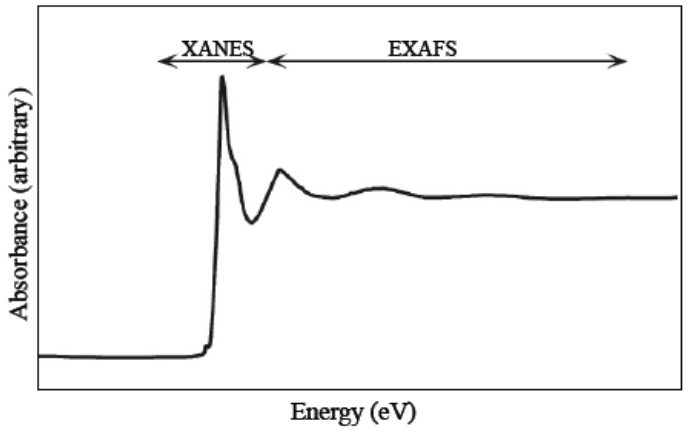

Figure 3.4 A typical X-ray absorption spectrum, highlighting the XANES region typically within 50 eV of the absorption edge and the EXAFS region which extends from several hundred eV to > 1000 eV above the absorption edge.

XAS experiments may be performed in two different modes, either transmission or fluorescence. Each mode essentially differs in the type of particle that is detected. The collection of data in transmission mode is preferred for concentrated samples (i.e. those containing >10 wt. % of the element of interest). The absorption coefficient is measured by measuring the intensity of the x-ray beam that is transmitted through the sample according to equation 3.15:

$$\mu(E)t = -\ln(I_0/I)$$

(Eq. 3.15)

Care must be taken when collecting XAS measurements in transmission mode to ensure that the sample surface is uniform and that the sample is not too thick. In the latter case there will not be enough transmission through the sample and thus no signal will be detected for I.

Conversely, samples that contain low concentrations of the element of interest (i.e. ppm levels or below) are generally collected in fluorescence mode (Newville et al., 2004). This is often the preferred method for the study of sorption processes at the mineral-water interface. In fluorescence mode, the absorption coefficient is measured by monitoring the intensity of the X-ray fluorescence that is emitted by higher-shell electrons as they relax into the core-hole left by the ejected photoelectron according to equation 3.16:

$$\mu(E) \propto I_f/I_0$$

(Eq. 3.16)

3.3.1.1 Extended X-ray Absorption Fine Structure Spectroscopy (EXAFS)

As discussed previously, the variation in X-ray photon absorption creates a decaying oscillatory wave known as the EXAFS that is generally observed from 50-1000 eV above the absorption edge. EXAFS spectroscopy serves as a powerful structural probe that can provide a variety of information on the immediate coordination environment of the central absorber (typically up to ~6 Å in oxides) (Brown et al., 1995; Zubavichus and Slovokhotov, 2001). Following background subtraction and normalization of the collected EXAFS, data is typically presented in two forms. Firstly, EXAFS data may be plotted in so-called *k*-space as the normalized EXAFS ($\chi(k)$) to produce an oscillating spectrum. In this case the data is often weighted by k^x, where x may equal 1, 2 or 3. Weighting the EXAFS data gives rise to enhanced oscillations at high *k* values. The frequency of the oscillations give valuable information on inter-atomic distances, as the frequency is inversely proportional to the distance between the absorbing atom and any neighbouring backscattering atoms. Whereas the amplitude and scattering profiles of the oscillations provide information

on the type and number of backscatterers surrounding the central absorber (Brown et al., 1995; Vlaic and Olivi, 2004). In addition, data is also presented as a Fourier transform (FT) of the EXAFS signal. Taking a FT of the EXAFS, transforms the data from *k*-space into *R*-space, producing a pseudo-radial distribution function (RDF) that yields information on the local structure surrounding the target atom. EXAFS presented in this form are often more useful for visualizing the information than the oscillating *k*-weighted EXAFS spectrum. Typically, the FT possesses several peaks, which correspond to either one or several atomic shells surrounding the central absorbing atom, the exact position of the peaks in the FT are usually shifted by approximately 0.5 Å due to a phase shift (Manceau et al., 1992). An example of a typical EXAFS spectrum along with the corresponding FT of the EXAFS signal is presented in Figure 3.5.

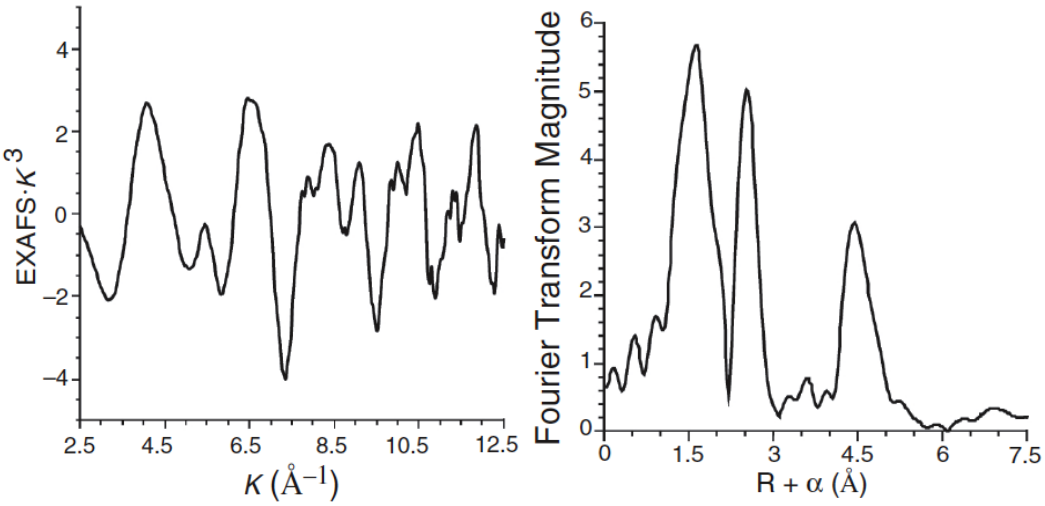

Figure 3.5 Typical normalized *k*-weighted EXAFS spectrum along with the corresponding Fourier transform of the EXAFS, where R + a indicates the phase shift (from Penner-Hahn, 1999).

3.3.1.2 EXAFS data collection

All bulk EXAFS spectroscopy data presented in chapters 4 and 5 was collected on beamline B18 at Diamond Light Source (DLS) Ltd. During data collection, storage ring energy was 3.0 GeV and the beam current was approximately 200 mA.

EXAFS data described in chapter 4 was collected in transmission mode at the Mn K-edge (6.539 keV) using a Ge 9-element detector. For EXAFS measurements, dry Mn oxide powders were diluted with cellulose nitrate and pressed into pellets. In order to minimize beam damage during data collection 2 EXAFS spectra were recorded at a single x,y point before moving to a new point to record a further 2 spectra. Up to 6 spectra were collected for each sample.

EXAFS data presented in chapter 5 was acquired in fluorescence mode at the Ni K-edge (8.333 keV). For measurement, samples were presented to the X-ray beam as dry powders pressed into pellets. In order to minimize beam damage during data collection 4 spectra were recorded at a single x,y point before moving to a new point to record a further 4 spectra. A total of 36 spectra were collected for each sample.

3.3.2 Micro-XAS and micro XRF

The collection of micro-XAS (μ-XAS) data follows essentially the same principles as bulk XAS except that, in the case of μ-XAS, measurements are made on a micron-size scale. By using a set of focusing optics to focus a beam of synchrotron radiation down to just a few microns in diameter, it is possible to collect XAS data at very precise locations within a heterogeneous sample. This is particularly useful when analysing natural sediment samples including marine ferromanganese-rich precipitates. These sediments display a high degree of heterogeneity in terms of their mineralogy that often varies spatially on the micron scale. Conversely, by measuring the intensity of characteristic X-ray fluorescence at various locations in a sample it is possible to produce detailed elemental maps that highlight the distribution and/or the correlation of certain elements within a sample. Both μ-XAS and μ-XRF are highly complementary and are often used in conjunction with each other. For example, it is possible to select discrete points of interest for μ-XAS analysis based on the data collected from the μ-XRF.

3.3.2.1 Micro-XAS and micro XRF data collection

Micro-focus X-ray fluorescence (μ-XRF) elemental maps (for Mn, Fe and Ni) and μ-EXAFS (at the Ni and Mn-K edges) presented in chapter 5 were collected at Diamond Light Source (DLS) Ltd on beamline I18. During data collection, storage

ring energy was 3.0 GeV and the beam current was approximately 200 mA. Samples were presented to the X-ray beam as ~30 μm thick self-supported thin sections, held between Kapton tape. Data was acquired in fluorescence mode (at the Ni K-edge) or transmission mode (at the Mn K-edge). Test scans indicated that there was no photo-redox or visible beam damage on the samples after 6 EXAFS scans up to k = 14 $Å^{-1}$. Nevertheless, in order to minimize beam damage 4 spectra were collected at a single x,y point before moving to a new point to record a further 4 spectra, collecting a total of up to 9 spectra (9 for Ni K-edge and 4 for Mn K-edge).

μ-XRF maps were collected at 8.4 keV with a pixel size of 10x10 μm and a count time of 1 sec per pixel. Maps were deadtime corrected and registered using custom beamline software. Maps were use to identify points of interest (POI) for collection of Ni and Mn μ-EXAFS. For μ-EXAFS the beam spot was ~2x3 μm.

Chapter 4

Nucleation and growth of todorokite: Implications for trace-metal cycling in marine sediments

The following chapter is adapted from a manuscript published in the journal *Geochimica et Chosmochimica Acta.*

4.1 Introduction

Manganese oxides are ubiquitous in oxic marine sediments and play a fundamental role in the biogeochemical cycling of trace elements in the ocean (e.g., Goldberg, 1954; Cronan, 1976; Burns and Burns, 1979; Post, 1999; Peacock and Sherman, 2007a; Sherman and Peacock, 2010; Spiro et al., 2010). Specifically, in addition to their ubiquity, they have large surface areas and are highly reactive, and so through coupled sorption and redox reactions are able to exert a strong control on the speciation, mobility and bioavailability of trace metals and micronutrients (e.g., Post, 1999).

In oxic marine sediments the main Mn-bearing phases are birnessite, buserite and todorokite (e.g., Burns and Burns, 1977). These minerals are all mixed Mn(III/IV) oxides, but birnessite and buserite are phyllomanganates (layer-type), consisting of sheets (layers) of edge-sharing MnO_6 octahedra, whereas todorokite is a tectomanganate (tunnel-type), consisting of triple chains of edge-sharing MnO_6 octahedra that share corners to form 3D tunnels. In birnessite and buserite, individual phyllomanganate sheets are stacked and separated by a hydrated interlayer region, which is partially filled with water molecules and a variety of cations to balance negative charge generated within the octahedral layers. Birnessite interlayers contain a single layer of water molecules resulting in an interlayer spacing of ~7 Å and, for example, Na^+ interlayer cations, while buserite interlayers contain a double layer of water molecules resulting in an interlayer spacing of ~10 Å and, for example, Mg^{2+} interlayer cations. In ideal todorokite, the tunnels have a square cross-section that measures three octahedra wide each side (Burns et al., 1985; Post and Bish, 1988; Post et al., 2003). In this case the tunnels equate to ~10x10 Å. In the marine

environment, todorokite tunnels are typically occupied by hydrated Mg^{2+} ions (e.g., Bodeï et al., 2007), whereas in more rarely occurring terrestrial todorokites, other large cations such as Ba^{2+} are thought to concentrate in the tunnel positions (e.g., Xu et al., 2010). The 7 and 10 Å phyllomanganates often display a number of structural and physiochemical variations, most notably possessing either triclinic or hexagonal symmetry, where hexagonal symmetry results from ordered vacancies in the manganese octahedral sites (Drits et al., 1997). In addition, these minerals can also exhibit varying degrees of disorder in the stacking of the phyllomanganate sheets along the c-axis, creating a continuum between turbostratic vernadite that consists of randomly orientated sheets (where the synthetic analogue is δMnO_2), to c-disordered phases that display some degree of sheet stacking, to highly crystalline phases in which sheets are ordered over several hundreds of angstroms (e.g., Villalobos et al., 2003). Natural marine birnessite is most commonly identified as a hexagonal, poorly crystalline phase, with either incoherent (vernadite) or semi-coherent (c-disordered birnessite) sheet stacking (e.g., Calvert and Price, 1970; Jauhari, 1987; McKenzie, 1989; Peacock and Sherman, 2007b; Grangeon et al., 2008). Furthermore, this suite of phyllomanganates also show variations in the proportion of Mn(III)/Mn(IV) within the layers. In vernadite Mn is predominantly present in the +4 oxidation state (e.g., Villalobos et al., 2003), while c-disordered and more crystalline phases contain a higher proportion of structural Mn(III) (e.g., Villalobos et al., 2003; Livi et al., 2011).

In the natural environment Mn(III/IV) oxides are thought to form via the microbial oxidation of Mn(II) (e.g., Brouwers, 2000; Francis et al., 2001; Bargar et al., 2000, 2005; Villalobos et al., 2003; Tebo et al., 2005; Webb et al., 2005a, b; Saratovsky et al., 2006; Spiro et al., 2010). However, although todorokite is often found intimitely associated with vernadite and both 7 and 10 Å semi-coherently stacked phyllomanganates (here collectively termed poorly crystalline phyllomanganates) in marine ferromanganese precipitates (e.g., Burns and Burns, 1978a, b; Siegel and Turner, 1983; Usui and Terashima, 1997; Banerjee et al., 1999; Bodeï et al., 2007; Peacock and Moon, 2012) it is thought to only form during the transformation of a 10 Å phyllomanganate under diagenetic and low temperature hydrothermal conditions (e.g., Burns and Burns, 1978b). Accordingly, marine ferromanganese precipitates that have precipitated directly from the water column (hydrogenetic) are typically rich in poorly crystalline phyllomanganates, those that have precipitated at the sediment-seawater interface (diagenetic) contain both poorly crystalline phyllomanganates and todorokite in variable proportions reflecting the influence of sediment pore-waters on individual precipitates, while those that have

precipitated below the sediment-seawater interface in close proximity to hydrothermal fluids are generally todorokite rich (e.g., Burns and Burns, 1977).

Despite the close association of poorly crystalline phyllomanganates and todorokite in natural marine precipitates, the exact crystallization pathway and formation mechanism of todorokite from these minerals in natural environments is still unclear. This is due at least in part to the fact that the X-ray diffraction patterns of 10 Å phyllomanganate and todorokite overlap at key peaks, and in natural precipitates todorokite is also often poorly crystalline and typically found intermixed with a variety of other poorly crystalline oxyhydroxides (e.g., Usui et al., 1997; Banerjee et al., 1999; Bodeï et al., 2007; Peacock and Moon, 2012). As such it can be very difficult to elucidate the detailed spectral, structural and morphological information necessary to determine precisely how poorly crystalline phyllomanganates transform into todorokite. The precise crystallization pathway and transformation mechanism are important however because the speciation, mobility and bioavailability of trace metals and micronutrients scavenged by the primary, authigenic phases will ultimately depend on whether these species are retained in the neo-formed todorokite or released back to sediment pore-waters and potentially then to seawater during the transformation. Notably, Bodeï et al. (2007) perform a range of high-resolution analyses, including X-ray diffraction, X-ray absorption spectroscopy and transmission electron microscopy, on a marine manganese concretion from hemipelagic sediments, and propose that todorokite forms in these settings via the dissolution-recrystallization of a single- to bi-layered hexagonal vernadite precursor (with an interlayer spacing equal to 7 Å) to a multi-layered and semi-coherently stacked Mg-rich vernadite intermediate (with 10 Å d-spacing), which then undergoes a topotactic transformation to todorokite.

In keeping with current knowledge of todorokite formation in the natural environment, the only known route to preparing synthetic todorokite involves the transformation of a phyllomanganate precursor, via either high temperature and pressure hydrothermal treatment (e.g., Giovanoli et al., 1975; Golden et al., 1986; Shen et al., 1993; Feng et al., 1995, 1998; Tian et al., 1997; Vileno et al., 1998; Luo et al., 1999; Malinger et al., 2004; Liu et al., 2005) or a refluxing process at atmospheric pressure, designed to better simulate todorokite formation in natural environments (Feng et al., 2004; Cui et al., 2006, 2008, 2009a). In all of the studies above, successful transformation required either an initial phyllomanganate precursor, or a phyllomanganate intermediate, possessing some degree of c-axis sheet stacking and an expanded (10 Å) interlayer region. More recently, Feng et al. (2010) synthesized a

todorokite-like phase from a biogenic poorly crystalline hexagonal birnessite (most similar to δMnO_2), via a mild reflux procedure (atmospheric pressure, 100 ^oC), developed to better represent marine diagenetic and mild hydrothermal conditions while still achieving transformation on an observable time scale (investigated over 48 hr). In general agreement with Bodeï et al. (2007), Feng et al. (2010) propose that their biogenic precursor transforms to a triclinic phyllomanganate intermediate (with a 10 Å d-spacing), which then undergoes topotactic transformation to a todorokite-like product. Due to the poorly crystalline nature of the biogenic precursor, both the intermediate and the todorokite-like product are similarly poorly crystalline, which prevented a more detailed evaluation of the crystallization pathway and transformation mechanism.

Here I synthesize todorokite from a c-disordered hexagonal birnessite via a mild reflux procedure. The birnessite precursor is analogous to marine birnessite and displays sufficient sheet stacking along the c-axis for identification of key spectral, structural and morphological features in the precursor, intermediate and transformation products. Similarly to Feng et al. (2010), the mild reflux procedure provides a reasonable representation of marine diagenetic and mild hydrothermal conditions, while still achieving transformation on an observable time scale. The initial c-disordered birnessite, intermediate phyllomanganate and subsequent transformation products are extensively characterized using X-ray diffraction (XRD), Fourier transform infrared spectroscopy (FTIR), BET surface area analysis, scanning electron microscopy (SEM), high-resolution transmission electron microscopy (HR-TEM) and extended X-ray absorption fine structure spectroscopy (EXAFS). Through careful and combined analyses of these results I provide new insight into the crystallization pathway of todorokite formation from birnessite, and propose the first detailed mechanism for todorokite formation in the marine environment. In addition, I discuss the implications of the formation mechanism for the fate and mobility of trace metals and micronutrients sequestered by marine Mn oxides.

4.2 Methods

4.2.1 Preparation of hexagonal birnessite precursor

A c-disordered hexagonal birnessite phase with an interlayer spacing of ~7 Å was synthesized following the method of Villalobos et al. (2003). The method is described in detail in chapter 3.

4.2.2 Transformation of Hexagonal Birnessite to Todorokite

C-disordered hexagonal birnessite was transformed to todorokite following a method adapted from Feng et al. (2004, 2010). The method is outlined in the methods chapter (Chapter 3).

4.2.3 Characterization of Precursor, Intermediate and Reflux Products

Powder X-ray diffraction (XRD) patterns were collected using a Bruker D8 diffractometer, operating at 40kV/40mA and equipped with CuKα radiation (λ = 1.5418) and a LynxEye detector. Samples were analyzed over a range of 2-80 $^{o}2\theta$ with a 0.010 step size and step time of 155 sec. Fourier transform infrared (FTIR) spectroscopy was performed on powdered samples using a Thermo Scientific iS10 FTIR spectrometer equipped with an attenuated total reflection (ATR) diamond crystal. Each spectrum was an average of 32 scans with a resolution of 1 cm^{-1}.

Scanning electron microscopy (SEM) and transmission electron spectroscopy (TEM) images were collected at the Leeds Electron Microscopy and Spectroscopy center in the Institute for Materials Research at the University of Leeds. For imaging, finely crushed powder samples were suspended in methanol and dispersed via sonication. For SEM imaging, all samples were loaded onto individual aluminium stubs and left to air dry. A platinum coating was applied to all samples prior to imaging which was performed at 20 kV using an EI Quanta 650 FEGESEM. For TEM imaging, samples were loaded onto individual holey carbon TEM grids. Imaging was performed at 200 kV on a Philips CM200 FEGTEM.

The average Mn oxidation state (AOS) of all synthesized Mn oxides was determined by potentiometric titration (Ligane and Karplus, 1946; Gaillot, 2002). This

method is described in detail in chapter 3, but briefly, 35 mg of finely ground mineral powder was reduced in 50 mL of a previously standardized 0.02 M $(NH_4)_2Fe(SO_4)_2$ (Mohr Salt) solution. The suspension was placed in an ultrasonic bath for up to 30 min to aid reduction. The resulting solution was then titrated against a standardized 0.02 M $KMnO_4$ solution at pH 2 to avoid the precipitation of Fe^{3+}. After this, 8 g of sodium pyrophosphate was dissolved in 100 mL of MQ water and added to the previous Mn oxide solution. The amount of reduced Mn^{2+} formed in the reduction step was determined by a second titration against the standardized 0.02 M $KMnO_4$ solution, this time the mixture was adjusted to pH 6.5-6.6 via the drop-wise addition of concentrated sulfuric acid. Due to the strong color of the pyrophosphate complex, the equivalence point in this second titration was determined by potentiometric titration. Potentiometric titrations were undertaken using an automated titrator equipped with a combined platinum ring conductivity electrode. Reported AOS values are the average of three separate titrations for each sample, with standard deviations calculated based on the triplicate measurements.

The specific surface area of all samples was measured in duplicate using the BET-N_2 method using a Gemini V2365 system (Micromeritics Instrument Corp.). Samples were dried and degassed for 24 hr at room temperature. Reported BET values are ±5 %.

In addition to the above analyses, extended X-ray absorption fine structure (EXAFS) spectra for the c-disordered birnessite precursor, Mg-exchanged phyllomanganate intermediate and subsequent reflux products at the Mn K-edge (6.539 keV) were collected. Spectra were collected on station B18 at Diamond Light Source (DLS) Ltd. During data collection, storage ring energy was 3.0 GeV and the beam current was approximately 200 mA. EXAFS data were collected from up to 6 transmission mode scans using a Ge 9-element detector. Test scans indicated no photo-reduction after 6 scans to k = 14 $Å^{-1}$. Nevertheless, in order to minimize beam damage 2 EXAFS spectra were recoded at a single x,y point before moving to a new point to record a further 2 spectra.

For EXAFS measurements, dry powders were diluted with cellulose nitrate and pressed into pellets. Energy calibration was achieved by assigning the first inflection point of Au (L3) foil to 11.919 keV. EXAFS data reduction was performed using ATHENA (Ravel and Newville, 2005) and PySpline (Tenderholt et al., 2007). ATHENA was used to calibrate from monochromator position (millidegrees) to energy (eV) and to average multiple spectra from individual samples. PySpline was used to

perform background subtraction where the pre-edge was fit to a linear function and the post-edge background to two 2nd-order polynomial segments.

4.2.4 Preparation of Reference Mn Oxides

A Triclinic Na-birnessite (Tc-Na-birnessite), crystalline hexagonal birnessite (Hx-birnessite), c-disordered hexagonal birnessite (as above), all with an interlayer spacing of ~7 Å, δMnO_2 and crystalline todorokite were prepared and used as references during the above analyses. Tc-Na-birnessite was prepared following the oxidation method of Liu et al., (2002), Hx-birnessite was prepared by acidification of the Tc-Na-birnessite suspension (Drits et al., 1997; Silvester et al., 1997; Lanson et al., 2000; Liu et al., 2002) and δMnO_2 was synthesized following the protocols of Villalobos et al. (2003). A todorokite with high crystallinity was prepared by hydrothermal treatment of a Mg-substituted Tc-Na-birnessite suspension, following the method of Feng et al. (1995). Synthesis procedures for the Tc-Na-birnessite, Hx-birnessite, poorly crystalline δMnO_2 and todorokite are detailed in chapter 3. Mineral identity and purity of the references were confirmed by XRD analysis of randomly orientated powder samples.

4.3 Results

4.3.1 X-ray Diffraction

C-disordered birnessite displays basal reflections at ~7 Å [001] and ~3.5 Å [002] (for reference pattern see turbostratic birnessite, Drits et al., 1997), while for Mg-exchanged phyllomanganate these appear at ~10 Å [001] and ~5 Å [002] (for reference pattern see that of buserite JCPDS-32-1128). Exchange of Mg^{2+} ions into the interlayer of ~7 Å birnessite expands this region to ~10 Å. Both phases also have two *hk0* reflections (or *hk* bands) at ~2.4 Å [100] and ~1.4 Å [110]. These are due to diffraction within the phyllomanganate sheets. In common with 10 Å phyllomanganate, the tectomanganate todorokite has peaks at ~10 Å [001] and ~5 Å [002], and peaks at ~2.4-2.5 Å [21-1] and [210], and ~1.4 Å [020]. As such, it can be difficult to distinguish todorokite from 10 Å phyllomanganate using XRD (e.g., Burns et al., 1983, 1985; Giovanoli, 1985; Bodeï et al., 2007; Saratovsky et al., 2009; Feng et al., 2010). However, in contrast to 10 Å phyllomanganates, todorokite has characteristic peaks at 2.22 Å [21-2], 1.90 Å [31-2], 1.74 Å [21-4] and 1.54 Å [21-5] (JCPDS-38-475). In addition, the peak at ~2.4 Å [21-1] is prominent and the peak at ~2.5 Å is evident as a characteristic splitting of the ~2.4 Å phyllomanganate peak region when 10 Å phyllomanganate and todorokite are mixed. Compared to 10 Å phyllomanganate, todorokite also has a characteristic splitting of the ~5 Å peak to reveal a peak at ~4.3 Å, and displays a characteristic loss of symmetry and splitting of the ~1.4 Å peak.

XRD patterns for the c-disordered birnessite, Mg-phyllomanganate intermediate and all subsequent reflux products synthesized in the current study are presented in Figure 4.1. Firstly, c-disordered birnessite shows 4 broad peaks at ~7.2 Å, ~3.6 Å, ~2.4 Å and ~1.4 Å originating from the [001], [002], [100] and the [110] reflections, respectively. After suspension of the c-disordered birnessite in 1 M $MgCl_2$ the basal spacing is expanded from ~7 Å to ~10 Å as indicated by the presence of both the ~9.6 Å [001] and ~4.8 Å [002] peaks in the Mg-phyllomanganate intermediate (Fig. 4.1). These peaks are more intense than those of the c-disordered birnessite precursor suggesting that the ion-exchange process enhances the crystallinity and long range ordering of the sheets.

The *d*100/*d*110 peak intensity ratios for the c-disordered birnessite and Mg-phyllomanganate intermediate are 2.44/1.41 and 2.43/1.41 respectively, which equate to ~ $\sqrt{3}$ which is in good agreement with diffraction data from Villalobos et al. (2003) for c-disordered birnessite and indicates that the Mn layers have hexagonal symmetry

with *a* = *b* = 2.83 Å (Drits et al., 1997). The ~1.4 Å peak is symmetrical in both the precursor and intermediate phases further indicating that these possess hexagonal symmetry (Drits et al., 2007). In both the precursor and intermediate phases the ~2.4 Å peak exhibits a degree of asymmetry on the high-angle side. This feature is typical of phyllomanganates that lack significant long-range ordering of the sheets (Villalobos et al., 2006). By contrast, triclinic birnessite (JCPDS-23-1046) shows a characteristic splitting of the peaks at ~2.4 Å and ~1.4 Å, lending the ~1.4 Å peak region in particular a distinctive asymmetry (e.g., Drits et al., 1997).

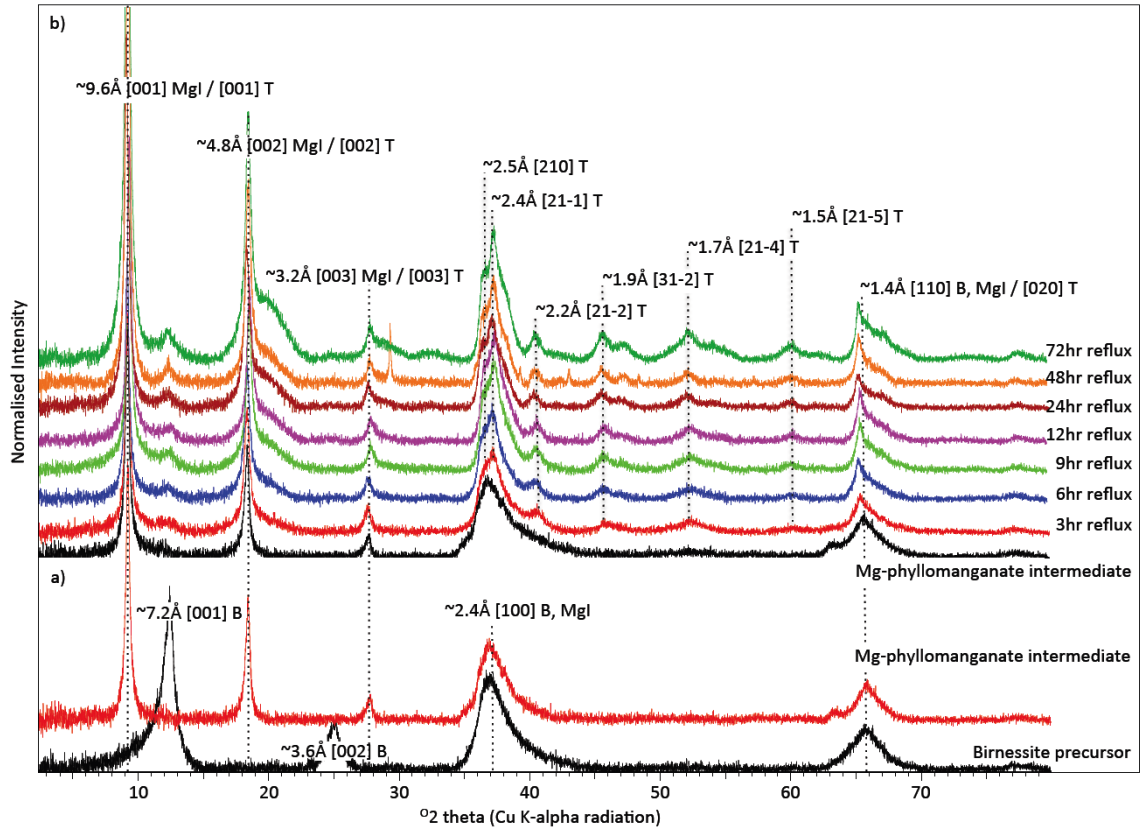

Figure 4.1 X-ray diffraction patterns: a) c-disordered birnessite precursor and Mg-exchanged phyllomanganate intermediate and b) Mg-exchanged phyllomanganate intermediate (repeated from Fig. 4.1a) and all subsequent reflux products. Characteristic X-ray diffraction peaks are labelled for c-disordered birnessite (B), Mg-exchanged phyllomanganate intermediate (MgI) and todorokite product (T) (based on Drits et al., 1997 for turbostratic birnessite, JCPDS-32-1128 for buserite and JCPDS-38-475 for todorokite).

Over the course of the reflux four distinct changes are visible in the XRD patterns (Fig. 4.1). Firstly, the appearance of four broad peaks at ~2.2 Å, ~1.9 Å, ~1.7 Å and ~1.5 Å indicates that transformation of the 10 Å phyllomanganate to todorokite has begun by 3 hr reflux. As the reflux progresses, these peaks become sharper and more intense indicating the progressive formation of todorokite. Secondly, the peak at ~2.4 Å has split by 3 hr reflux to reveal two peaks in this region at ~2.45 and 2.41 Å, where the peak at ~2.45 Å becomes more prominent with time. Thirdly by 3 hr reflux, the peak at ~5 Å begins to broaden on the high-angle side, developing into a broad shoulder at ~4.3 Å, with two separate peaks distinguishable after 48 hr reflux. Finally, the ~1.4 Å peak shows a significant loss of symmetry as the reflux proceeds. These three later changes are those expected during the transformation of 10 Å phyllomanganate to todorokite (Feng et al., 2004) and are consistent with transformation having begun by 3 hr reflux.

4.3.2 Fourier Transform Infra-Red Spectroscopy

FTIR spectra for c-disordered birnessite, Mg-phyllomanganate intermediate and a selection of the subsequent refluxed products are presented in Figure 4.2. For FTIR of Mn oxides, a broad peak at ~760 cm^{-1} is typically assigned to an asymmetrical Mn-O stretching vibration, corresponding to corner-sharing MnO_6 octahedra (Julien et al., 2004). This absorption band is absent in phyllomanganate (layer-type) Mn oxides and is therefore unique to those that possess a tectomanganate (tunnel-type) structure (Julien et al., 2004). FTIR spectroscopy can therefore conclusively distinguish between the layer-type intermediate phase and the tunnel-type todorokite product. Figure 4.2 shows that the characteristic peak is apparent in the refluxed product after 3 hr of reflux (as highlighted by the dashed line in Fig. 4.2), which is consistent with the XRD data that also indicates the presence of todorokite by this time point (Fig. 4.1). The presence of the 760 cm^{-1} peak in the FTIR spectrum is consistent with a transition from edge- to corner-sharing MnO_6 octahedra, expected during the transformation of birnessite to todorokite (Julien et al., 2004; Kang et al., 2007). The increasing intensity of this peak with time indicates that more todorokite is present within the matrix as the transformation proceeds.

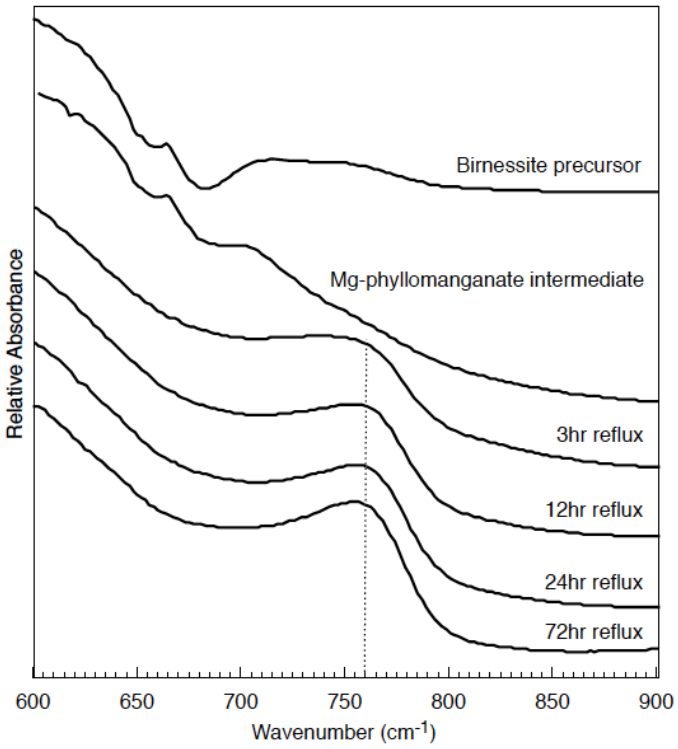

Figure 4.2 Fourier transform infrared powder absorption spectra of c-disordered birnessite precursor, Mg-exchanged phyllomanganate intermediate, and reflux products at 6 hr, 12 hr, 24 hr and 72 hr reflux.

4.3.3 Electron Microscopy

SEM images of the c-disordered birnessite show that the precursor material has a plate-like morphology typical of phyllomanganate Mn oxides (Fig. 4.3a). Individual birnessite crystallites appear to be randomly oriented and aggregated into larger particles measuring approximately 200-300 nm in diameter (not shown). After 6 hr reflux the overall morphology has evolved and small fibrous needles (<0.2 μm) of todorokite can be seen intergrown within the platy birnessite matrix (Fig. 4.3b). After 72 hr of reflux treatment, the mineralogy is dominated by elongated fibres (> 2.0 μm) of crystalline todorokite (Fig. 4.3c). In addition, these fibres appear to be aggregated into a dense network of fibres resulting in an overall plate-like morphology (Fig. 4.3d).

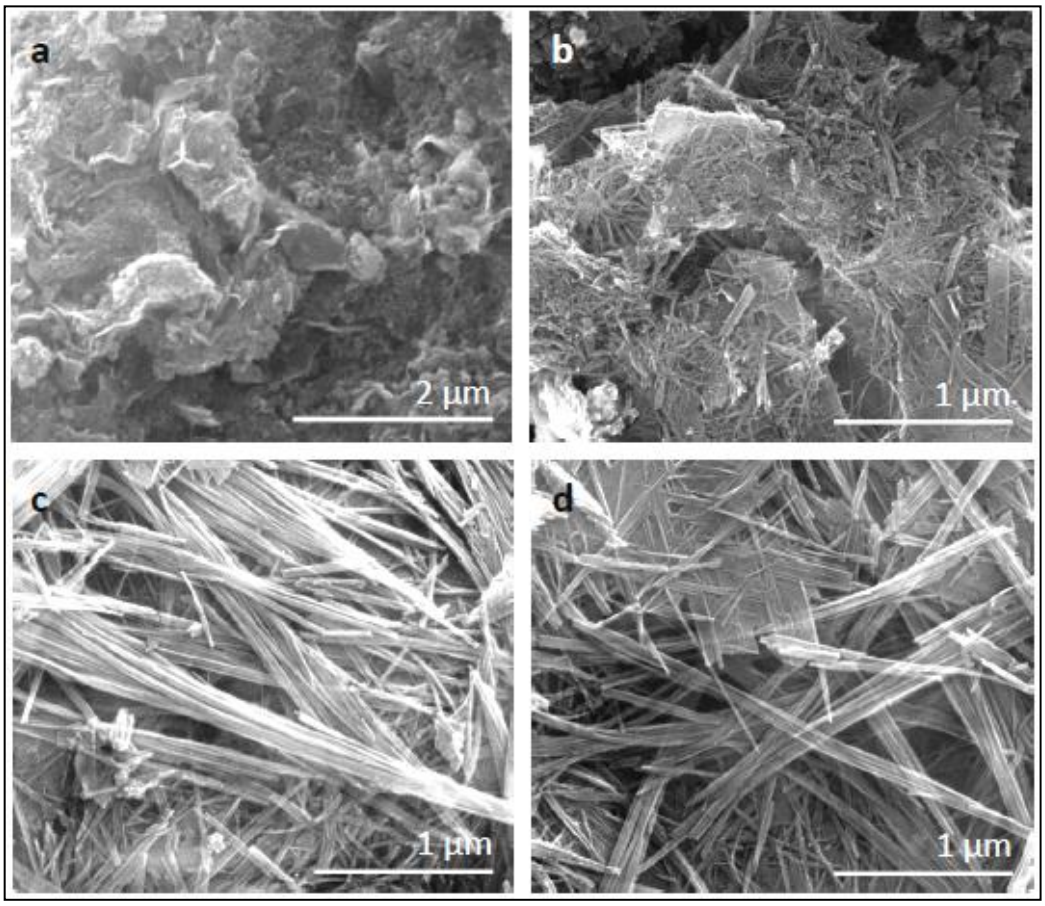

Figure 4.3 Scanning electron micrographs: a) c-disordered birnessite precursor, and reflux products at b) 6 hr reflux, c-d) 72 hr reflux.

HR-TEM images are presented in Figure 4.4. The prominent feature of both the c-disordered birnessite precursor (Fig. 4.4a, b) and the Mg-phyllomanganate intermediate (Fig. 4.4c, d) is the repetition of the [001] lattice planes (space group p63/mmc), from which it can be inferred that the individual phyllomanganate layers are reasonably well stacked over at least 50 Å. The measured interlayer of the c-disordered birnessite is equal to ~5.6 Å, while the Mg-phyllomanganate is equal to ~8.6 Å (Fig. 4.4b, d), neither of which are consistent with the 7.2 Å and 9.6 Å *d*-spacing's determined via XRD (Fig. 4.1). However, it has been reported that phyllomanganate layers are susceptible to collapse under the high vacuum conditions required for TEM work. For example, Post and Veblen (1990) report layer collapse in 7 Å K^+ birnessite to ~6.0 Å. It is evident from Figure 4.4e that after approximately 1.5 hr reflux the layers of the Mg-phyllomanganate have become substantially rumpled and distorted in areas equivalent to several square nanometres. In corroboration with SEM observations (Fig. 4.3), TEM images taken after 6 hr reflux (Fig. 4.4f) show a significant change in particle morphology. Primary particles of todorokite that measure

~ 8-10 nm wide and that are elongated longitudinally along the [010] direction (space group p2/m; i.e., along the direction of tunnel growth) some 200 nm in length (Fig. 4.4f) are observed. On close inspection at 6 hr reflux, these primary particles appear to be aggregating together laterally across the [100] direction, resulting in the formation of substantially wider todorokite laths that measure approximately 20-30 nm in diameter, which is equivalent to the aggregation of 2-3 primary todorokite particles (Fig. 4.4f). The extent of lateral particle aggregation over the duration of the experiment is highlighted in Figure 4.4, where significant lateral aggregation is observed from 6 hr reflux (image 4.4f; laths on average ~ 20-30 nm wide), to 48 hr reflux (image 4.4g; laths on average ~ 50-100 nm wide) to 72 hr reflux (image 4.4h; laths on average ~100-150 nm wide). In addition to lateral aggregation, the particles also continue to elongate along the [010] direction as the reflux proceeds (from 6 to 24 to 72 hr, images Fig. 4.4f, i and h, respectively). It is difficult to determine from these images whether particle-particle aggregation along the [010] makes any contribution to todorokite growth as, unlike across the [100] direction, the observation of particle-particle boundaries is less clear. However, after 24 hr reflux, crystalline laths up to 600 nm in length ([010] direction) are observed extending from central regions of overlapping todorokite laths (Fig. 4.4i). The central regions of overlapping laths are aligned with each other at 120°. This dense network of fibres gives rise to the formation of large aggregates of todorokite that exhibit a plate-like morphology. The size of these plate-like aggregates appears to increase with increased reflux time and, after 72 hr, plates of todorokite measuring approximately 500 x 550 nm are observed (Fig. 4.4j). This plate-like growth morphology is typical of todorokite found in both marine and terrestrial settings (Turner et al., 1982; Siegel and Turner 1983; Bodeï et al., 2007; Xu et al., 2010).

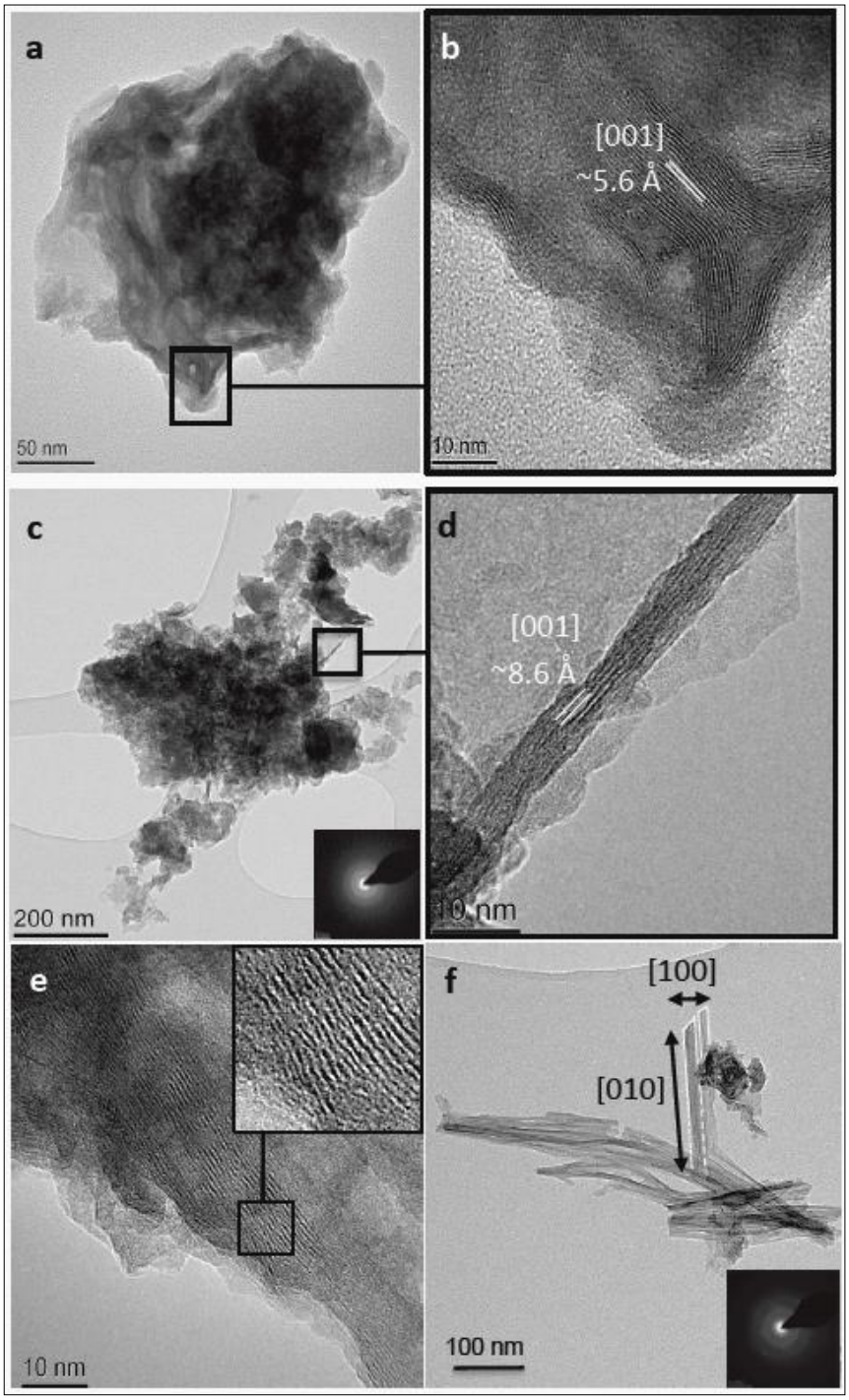

Figure 4.4 Transmission electron micrographs of: (a - b) c-disordered birnessite precursor and (c – d) Mg-exchanged phyllomanganate intermediate with b) and d) highlighting the repetition of the [001] lattice planes, (e) reflux product at 1.5 hr showing rumpling and distortion of the phyllomanganate layers, (f) reflux product at 6 hr showing primary particles of todorokite (white outlines) elongated longitudinally along [010] and aggregating laterally across [100] to form todorokite laths.

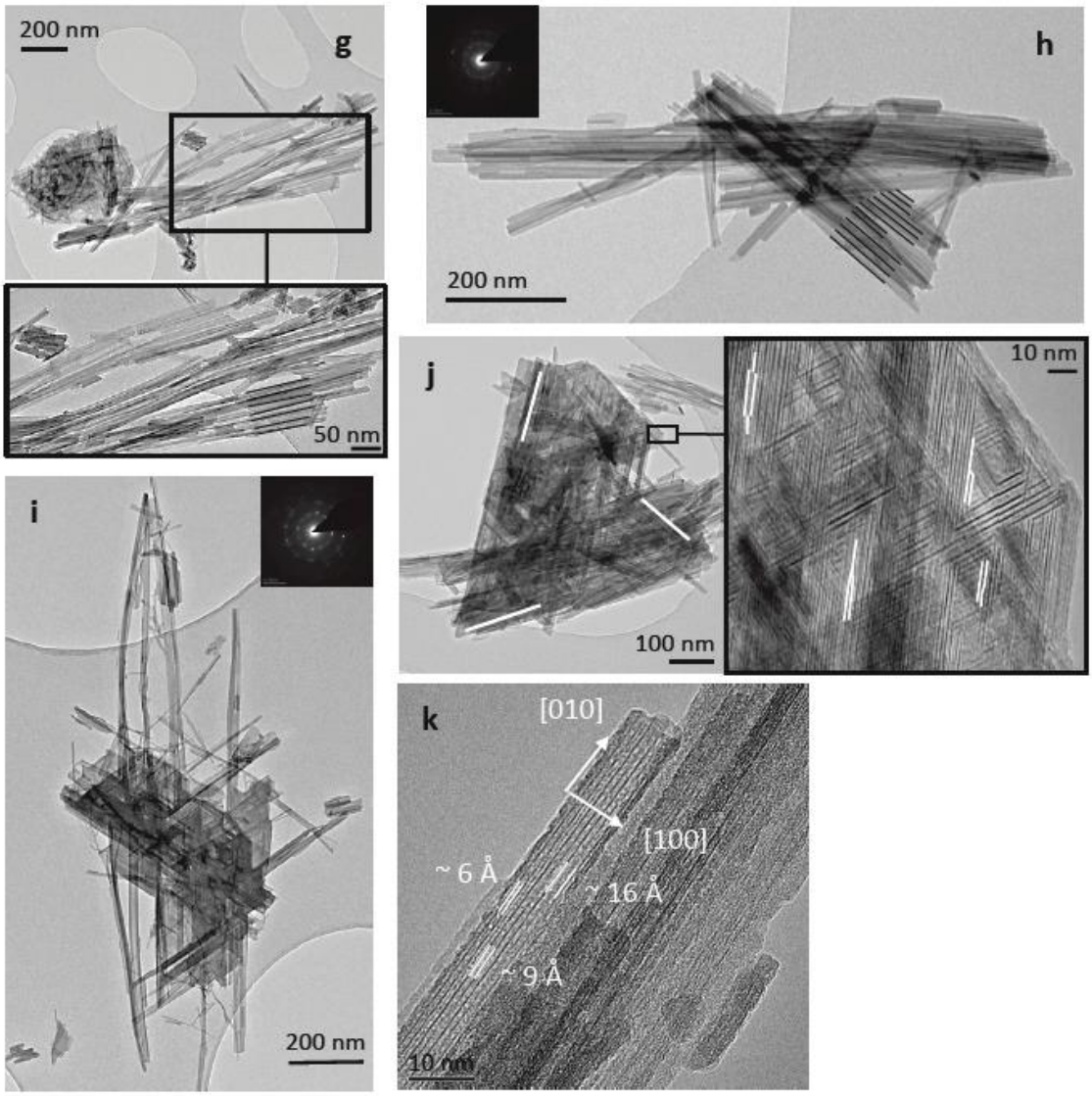

Figure 4.4 (*continued)* (g) reflux product at 48 hr showing todorokite laths ~ 50-100 nm wide (black lines highlight primary particle aggregation), (h) reflux product at 72 hr showing todorokite laths ~ 100-150 nm wide (black lines highlight primary particle aggregation), (i) reflux product at 24 hr showing crystalline laths of todorokite elongated along [010] with laths overlapping and aligned at 120°, (j) reflux product at 72 hr showing todorokite with a plate-like morphology with plates comprised of aligned overlapping laths, also showing in the enlarged area a number of linear dislocations along the direction of tunnel growth (highlighted with white lines), (k) reflux product at 72 hr showing heterogeneous todorokite tunnel dimensions.

HR-TEM images (Fig. 4.4k, j) also reveal that the todorokite product contains a number of structural defects. Specifically, the todorokite tunnels highlighted in Figure 4.4k display widths across the [100] direction of ~ 6 Å, 9 Å and 16 Å, approximately corresponding to tunnels that are (3x2), (3x3) and (3x4) MnO_6 octahedra wide. Tunnel-width inconsistencies are commonly observed in todorokite (Turner et al., 1982; Feng et al., 2004; Bodeï et al., 2007; Xu et al., 2010). In addition to heterogeneous tunnel dimensions, the images also reveal the presence of a substantial number of linear dislocations along the direction of tunnel growth (Fig. 4.4j).

4.3.4 Physiochemical Characterization

BET surface area and pH measurements for c-disordered birnessite, the Mg-phyllomanganate intermediate and all subsequent reflux solids and solutions, respectively, are presented in Table 4.1 and displayed graphically in Figure 4.5. The measured N_2 BET surface areas of the c-disordered birnessite and Mg-phyllomanganate intermediate are 103.7 m^2/g and 104.9 m^2/g, respectively. After 3 hr of reflux treatment the surface area has decreased to 78.82 m^2/g and shows little variation during the first 12 hr, with all measured values falling within the 5 % error range of the technique. The measured surface area then peaks at 95 m^2/g at 24 hr, after which there is a subsequent drop to 69.95 m^2/g at 48 hr, ending with 65.82 m^2/g at 72 hr. The pH values of the reflux solutions at 3 hr until 24 hr show little variation, averaging at 4.85 pH units. At 48 hr there is an increase in pH to 5.10, which further increases to 5.51 pH units at 72 hr reflux. An increase in solution pH towards the end of the reflux procedure is consistent with the observations of Feng et al. (2010).

Sample	Surface Area (m^2/g)[a]	Reflux Soln. pH[b]
C-disordered birnessite	103.7	N/A
Mg-phyllomanganate	104.9	N/A
3hr-Reflux	78.82	4.80
6hr-Reflux	82.47	4.85
9hr-Reflux	76.24	4.85
12hr-Reflux	75.36	4.86
24hr-Reflux	94.81	4.89
48hr-Reflux	69.95	5.10
72hr-Reflux	65.82	5.51

Table 4.1 Specific surface area of the solid products and pH of the reflux solution for the c-disordered birnessite precursor, Mg-phyllomanganate intermediate and all subsequent reflux products. [a]All surface area measurements are ±5%. [b]All pH measurements are ± 0.05 pH units.

The Mn AOS in c-disordered birnessite is 3.78±0.04. This value is in good agreement with Villalobos et al. (2003) for c-disordered birnessite and indicates that the precursor contains a significant proportion of Mn(III). After exchange in 1 M $MgCl_2$ the AOS is 3.75±0.04, while after 72 hr reflux the final todorokite product has an AOS of 3.79±0.004. The results of the oxidation state titrations indicate that within error there is no significant change in the net Mn AOS as the transformation proceeds.

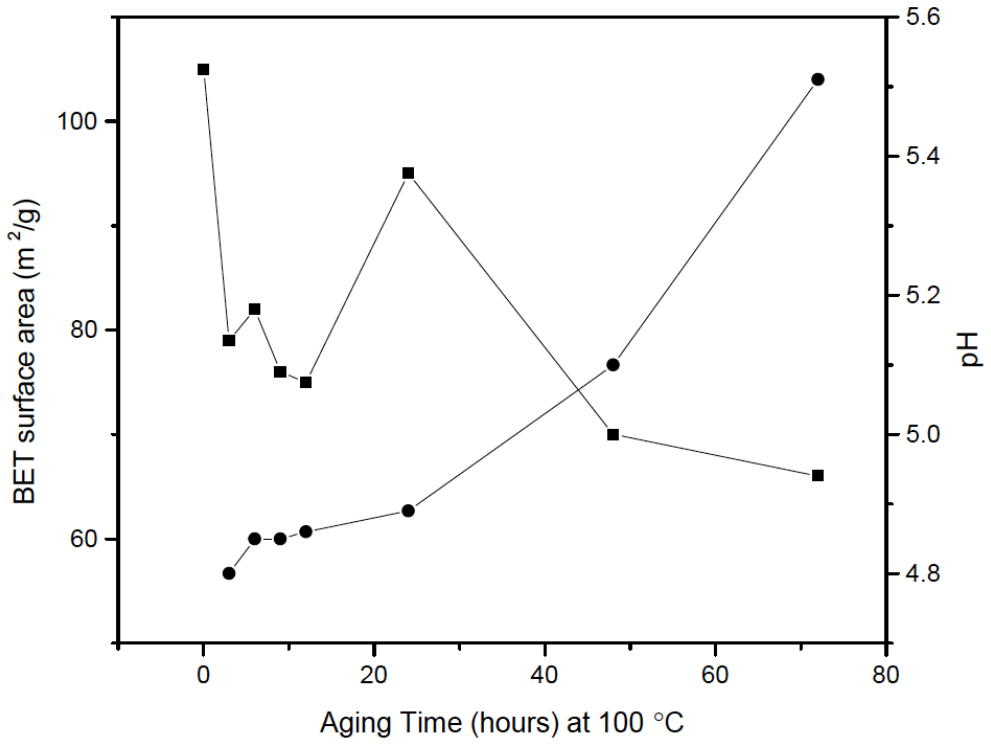

Figure 4.5 Specific surface area of the solid products and pH of the reflux solution for the reflux time series. The first surface area measurement shown on the plot is the Mg-exchanged phyllomanganate intermediate at 0 hr aging time; pH measurements start at 3 hr reflux. ■ Symbols indicate surface area values and ● symbols indicate measured pH values. For exact values see Table 4.1.

4.3.5 X-ray Absorption Spectroscopy

Mn K-edge EXAFS of the reference Mn oxides, c-disordered birnessite, Mg-phyllomanganate intermediate and early stage reflux products are shown in Figure 4.6. Mn EXAFS spectroscopy is sensitive to Mn-O and Mn-Mn interatomic distances, and MnO_6 polyhedral linkages (e.g., Manceau and Combes, 1988). Information on sample mineralogy and crystallinity can therefore be obtained by comparing sample spectra to a suite of standard Mn oxide reference spectra (e.g., Manceau et al., 2002). In agreement with previous studies, the Mn oxide reference spectra show clear differences in *k*-space in the (6.5 – 9.5 $Å^{-1}$) indicator region (e.g., Webb et al., 2005a). This region is sensitive to the amount and ordering of Mn(IV) and Mn(III) in the sheets of phyllomanganates (δMnO_2, c-disordered birnessite, Hx-birnessite and Tc-Na-birnessite) and to the tunnel dimension in tectomanganates (todorokite) (e.g., Manceau and Combes, 1988; McKeown and Post, 2001). In particular, the *k*-space peaks at ~6.7, 8 and 9.2 $Å^{-1}$ appear sharper and more intense for layered vs. tunnel structures (e.g., Webb et al., 2005a). This is evident when comparing the phyllomanganate (δMnO_2 and Hx-birnessite) to the tectomanganate (high crystalline todorokite) reference spectra. For layered structures, these indicator features also appear sharper and more intense with an increase in coherent stacking of the layers along the c-axis, i.e., from δMnO_2, to c-disordered birnessite, to Hx-birnessite (e.g., Webb et al., 2005a). As expected, the collected EXAFS spectra show that the c-disordered birnessite precursor and Mg-phyllomanganate intermediate, have c-axis ordering that is intermediate between turbostratic δMnO_2 and highly crystalline Hx-birnessite (Fig. 4.6). In addition, in agreement with XRD data, the Mg-phyllomanganate intermediate displays slightly sharper and more intense indicator peaks than the c-disordered birnessite precursor, confirming that the ion-exchange process enhances the c-axis ordering of the Mn octahedral layers. In addition, Mn K-edge EXAFS can also be used to conclusively distinguish between phyllomanganates with triclinic and hexagonal symmetry, where triclinic phases exhibit a splitting of the indicator peak at ~8 $Å^{-1}$ while hexagonal phases do not (Webb et al., 2005). In this respect the EXAFS spectra confirm that the c-disordered birnessite precursor has hexagonal symmetry, in agreement with XRD data (Fig. 4.1) and as expected for c-disordered birnessite synthesized following the method of Villalobos et al. (2003). The spectra also show that the Mg-phyllomanganate intermediate and early-stage reflux products, shown until 3 hr reflux (by which time, rumpling of the phyllomanganate

layers at 1.5 hr has been observed (Fig. 4.4e)), similarly possess hexagonal symmetry.

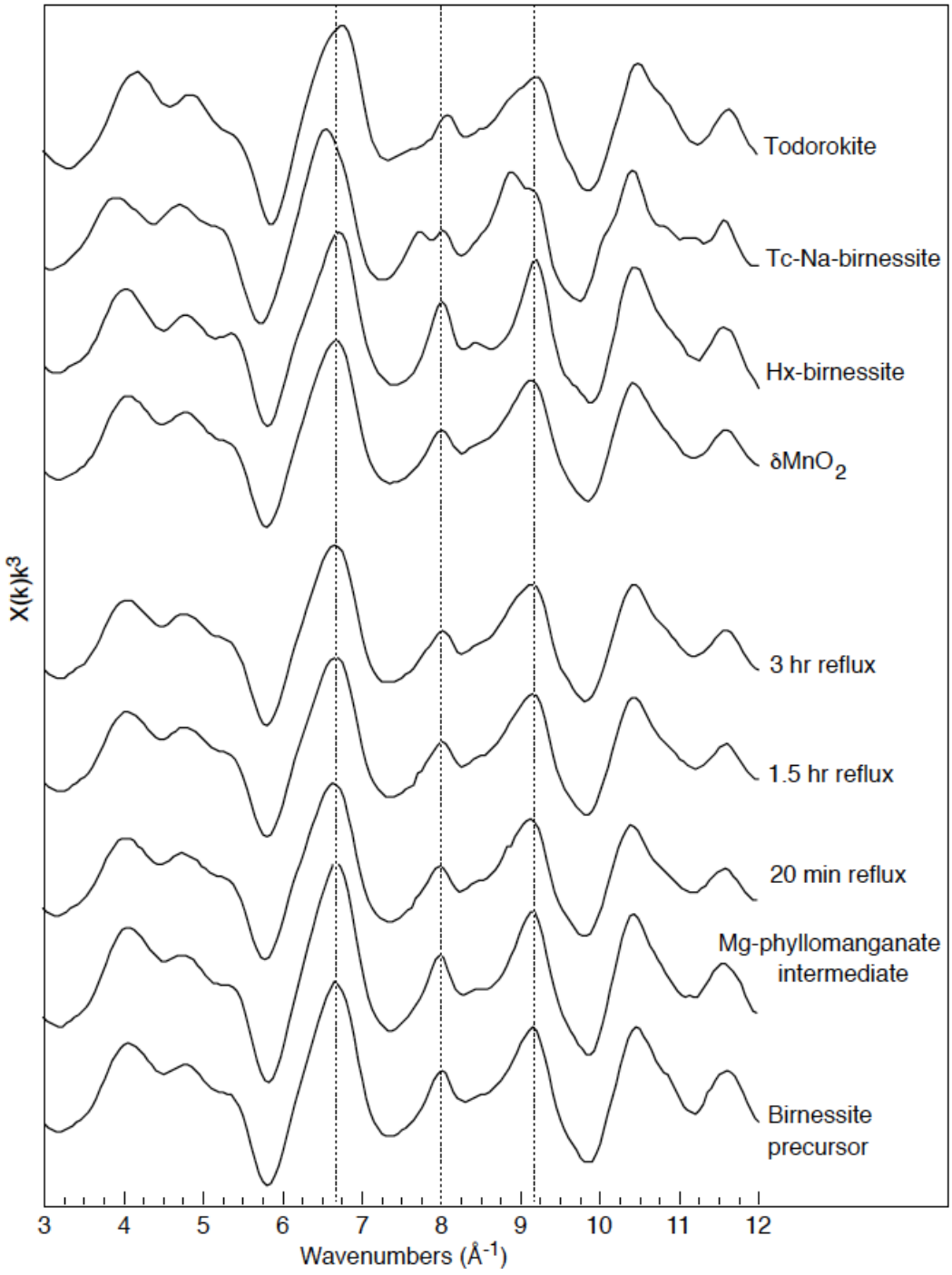

Figure 4.6 Mn K-edge EXAFS for Mn oxide reference compounds and the c-disordered birnessite precursor phase, Mg-exchanged phyllomanganate intermediate and reflux products at 20 min, 1.5 hr and 3hr reflux. Vertical dashed lines mark the positions of the k-space indicator regions at ~6.7, 8 and 9.2 Å-1.

4.4 Discussion

4.4.1 Mechanism of Todorokite Formation in the Marine Environment

It is widely agreed that the formation of todorokite in the marine environment is a complex multistage process (Burns and Burns, 1978a,b; Siegel and Turner, 1983; Golden et al., 1986; Shen et al., 1993; Feng et al., 2004; Bodeï et al., 2007; Feng et al., 2010). The exact formation mechanism of todorokite in marine diagenetic and hydrothermal settings has remained unclear due to this complexity, and because it is often found intermixed with other poorly crystalline oxyhydroxide minerals (Usui et al., 1997; Banerjee et al., 1999; Bodeï et al., 2007). Todorokite was initially synthesized by Golden et al. (1986), however subsequent confirmation of this synthesis has often proved challenging (Siegel and Turner, 1983; Golden et al., 1986; Shen et al., 1993; Ching et al., 1999; Feng et al., 2004; Cui et al., 2006; Cui et al., 2008; Cui et al., 2009; Feng et al., 2010).

The current experimental study presents the first detailed description of the crystallization pathway and mechanism of todorokite formation from birnessite. I show that this reaction pathway involves a four-stage process beginning with todorokite nucleation, then crystal growth to form todorokite primary particles, followed by their self-assembly and oriented growth, culminating in a traditional crystal ripening processes. Each of these stages in the crystallization process is described in detail below.

4.4.1.1 Todorokite nucleation

Previous studies have recognized that the ordering of the birnessite layers over at least several tens of angstroms is fundamental for the eventual formation and pillaring of the todorokite tunnel walls (e.g., Bodeï et al., 2007). In the current work HR-TEM images of the birnessite precursor and 10 Å phyllomanganate intermediate indicate that the individual phyllomanganate layers are reasonably well stacked over at least 50 Å (Fig. 4.4b, d). It has also been suggested that the presence of structural Mn(III) within the birnessite layers is an important prerequisite for todorokite formation (Bodeï et al., 2007; Cui et al., 2008). Specifically, distortion of the Mn(III) octahedra due to the Jahn-Teller effect results in the elongation and thus weakening of the Mn^{3+}-O bonds along the z-axis. It is at this structural weak point, between the Mn^{3+}-O-Mn^{4+} bonds that run parallel to the [010], that the phyllomanganate layers are thought to be

most susceptible to rumpling (Bodeï et al., 2007; Cui et al., 2008). It is believed that this kinking of the layers leads to the formation of the todorokite tunnel walls within the volume of the phyllomanganate interlayer (Bodeï et al., 2007; Cui et al., 2008). Potentiometric titration of the birnessite precursor and 10 Å phyllomanganate intermediate confirm that these two phases contain a significant proportion of Mn(III), with AOS of 3.78 and 3.75, respectively. The proposed rumpling of the phyllomanganate layers is directly observed at 1.5 hr reflux. Specifically, HR-TEM images indicate that the layers of the 10 Å intermediate have become distorted in localized areas some tens of square nanometers in size (Fig. 4.4e). This suggests that the rearrangement of the phyllomanganate sheets, and thus the nucleation of todorokite, proceeds within local domains relatively rapidly after the start of reflux treatment. Furthermore, Cui et al. (2006) investigate the transformation of birnessite to todorokite over a wide temperature range from 40 to 140 ^{o}C, and show that the transformation is significantly enhanced at and above 100 ^{o}C. In parallel, Bodeï et al. (2007) suggest that elevated temperatures increase the kinetics of the 10 Å intermediate transformation. With this new data I suggest specifically that the kinking of the 10 Å phyllomanganate layers, and thus the key step in the nucleation of todorokite, is thermally induced. The temperature dependence of todorokite nucleation then at least partly explains the prevalence of todorokite over phyllomanganates in hydrothermal marine ferromanganese precipitates (as documented by, for example, Burns and Burns (1977)).

Based on the literature to date and the new data presented here, it is clear that there are two major prerequisites for the formation of crystalline todorokite directly from 10 Å phyllomanganate. Firstly, the 10 Å phase must contain enough structural Mn(III) to allow the kinking of the phyllomanganate layers. Secondly, the 10 Å phase must also display at least semi-coherent c-axis ordering, so that as the phyllomanganate layers kink, there are sufficient adjacent layers for the cross-linking todorokite tunnel walls to form. The absence of one or both of these prerequisites results in the synthesis of a variety of layer-type and tunnel-type Mn oxide products. For example, Feng et al. (2010) use a biogenic phyllomanganate precursor with AOS 3.8±0.3 but incoherent (turbostratic) c-axis ordering, and are able to produce only a very poorly crystalline nanoscale todorokite-like product; these authors also report a failed attempt to synthesize todorokite from an acid birnessite with semi-coherent c-axis ordering but an AOS of 3.96±0.02. Similarly, Bodeï et al. (2007), using a turbostratic 10 Å phyllomanganate, produce a mixture of primary 7 Å birnessite and jianshuite/Mg-chalcophanite and secondary poorly crystalline todorokite. It has also

been suggested that triclinic symmetry in the 10 Å phyllomanganate intermediate might be another prerequisite for todorokite formation (Feng et al., 2010), i.e., that during the formation of todorokite from hexagonal 7 Å birnessite, there is a transition from hexagonal symmetry in the precursor to triclinic symmetry in the intermediate phase. However, I have shown from both XRD (Fig. 4.1) and Mn K-edge EXAFS spectroscopy data (Fig. 4.6), that both the precursor and intermediate phases possess hexagonal symmetry. Furthermore, there is no evidence for the appearance of a triclinic phyllomanganate during the early stages of todorokite nucleation. It therefore appears that todorokite can form via a hexagonal pathway and triclinic symmetry is not a prerequisite for todorokite formation.

4.4.1.2 Formation of todorokite primary particles

Following the formation of the proposed todorokite nucleation sites by 1.5 hr reflux, FTIR data (Fig. 4.2) confirms that by 3 hr reflux there is some degree of structural transition from edge-sharing to corner-sharing MnO_6 octahedra as indicated by the appearance of the broad shoulder at ~760 cm^{-1} in the FTIR spectrum (Julien et al., 2004; Kang et al., 2007). In turn this is consistent with XRD data (Fig. 4.1) at 3 hr reflux, which shows the presence of characteristic todorokite peaks between 2.4 Å and 1.5 Å. Notably, there is a distinct increase in asymmetry of the initially symmetrical 10 Å intermediate [110] reflection as it evolves into the todorokite [020] reflection, with this trend towards asymmetry beginning by 3 hr reflux. The growth and narrowing of the todorokite [020] reflection reflects todorokite growth along the [010] direction, i.e., along the direction of tunnel growth.

I capture the first visual evidence of todorokite crystallization at 6 hr reflux with the clear presence of small and poorly crystalline primary particles of todorokite in the TEM images (Fig. 4.4f). Interestingly, these primary particles are elongated along the [010] direction, measuring up to 200 nm in length (Fig. 4.4f). By comparison, the width of these particles along the [100] direction is significantly smaller, measuring between 8 and 10 nm. The widths of the todorokite particles are comparable to the crystallite size (calculated from Scherer analysis) of the 10 Å phyllomanganate intermediate particles i.e. ~8 nm along the [100] direction. I suggest that following the nucleation of todorokite within the phyllomanganate layers, the todorokite particles grow preferentially along the [010] direction with the width of the particles controlled by the crystallite size of the phyllomanganate intermediate i.e. ~8 nm. Due to the

difference in both size and morphology between the 10 Å phyllomanganate and todorokite, I suggest that the todorokite primary particles grow along the [010] via dissolution of the 10 Å phyllomanganate followed by precipitation of crystalline todorokite. This is consistent with the drop in surface area measured between the 10 Å phyllomanganate intermediate and the reflux product at 3 hr.

4.4.1.3 Self-assembly and oriented growth

It is evident on close inspection (Fig. 4.4f) that at 6 hr reflux some of the initially formed primary particles of todorokite are orientated and aggregated together laterally across the [100] direction resulting in the formation of substantially wider todorokite laths (20-30 nm wide). It is possible to make out several particle-particle boundaries between laterally aggregating primary particles (Fig. 4.4f). However, similarly early on in the transformation it is difficult to identify any particle-particle boundaries along the length of tunnel growth. This suggests that primary particle aggregation is occurring exclusively in the lateral direction. The data therefore indicates that following the formation of acicular todorokite, the primary crystallites aggregate via attachment of the [100] faces i.e., via an oriented attachment-type mechanism. This is again consistent with the drop in surface area from the 10 Å phyllomanganate intermediate to the 3 hr reflux product. Analysis of the HR-TEM data shows that there is little variation in the widths of individual todorokite primary particles from the early stages of particle nucleation (widths on average ~ 8 nm) to the end of the reflux treatment (widths on average ~ 5-15 nm). This indicates that lateral oriented attachment of todorokite particles is a key particle growth mechanism throughout the duration of the reflux treatment. The progressive attachment of todorokite primary particles is consistent with the overall drop in surface area from the 3 hr to 72 hr reflux products (Fig. 4.5). The maximum surface area value measured at 24 hr reflux may therefore be an anomaly. The self-assembly and lateral aggregation of primary particles in an Mn oxide system has also been observed by Portehault et al. (2007) during the formation of cryptomelane. They find that cryptomelane-type MnO_2 nanowires synthesized under mild hydrothermal conditions form via the lateral “side to side” aggregation of primary nanorods.

Oriented attachment (OA) refers to the self-assembly and oriented growth of primary particles to form larger secondary particles. First described by Penn and Banfield (1998a), OA is a spontaneous crystal growth mechanism, whereby primary

crystallites align and eventually aggregate together at specific surfaces that share similar crystallographic dimensions. The resulting secondary particles are larger and thus ultimately more thermodynamically stable due to the overall reduction in surface free energy (Penn and Banfield, 1998a, b). In recent years the importance of this non-classical growth mechanism has become increasingly apparent and a growing number of studies have shown that under varying experimental conditions a diverse range of geochemically important mineral phases such as Fe oxides, TiO_2, ZnS and $CaSO_4$ form via OA-based growth mechanisms (Penn and Banfield, 1998a; Penn and Banfield, 1999; Banfield et al., 2000; Gilbert et al., 2003; Huang et al., 2003; Waychunas et al., 2005; Burrows et al., 2012; Van Driessche et al., 2012). In addition, the growth of materials by OA has also been shown to provide a route for the formation of a variety of structural defects (Penn and Banfield et al., 1998a, b; Penn et al., 2001). For example, it is understood that prior to attachment, particles may often misalign, ultimately leading to the offset of lattice planes between adjoining particles. This misalignment leads to the incorporation of both linear- and edge-type dislocations at particle-particle boundaries (Penn and Banfield, 1998a; Banfield et al., 2000; Penn et al., 2001) such as those observed in the microstructure of the neo-formed todorokite samples (Fig. 4.4j).

Notably, in addition to the formation of todorokite laths, I also observe that individual laths are oriented specifically in three distinct directions at 60°/120° to each other (Fig. 4.4j) to form large aggregates of todorokite with a plate-like morphology. This trilling pattern is a characteristic growth morphology of todorokite that has been widely described in both natural and synthetic samples (Seigel and Turner, 1983; Golden et al., 1987; Feng et al., 2004; Bodeï et al., 2007; Xu et al., 2010). I suggest that this morphology arises due to the assembly and subsequent attachment of adjacent layers of elongated todorokite laths, on the [001] faces. Because of the pseudo-hexagonal structure within the Mn-O layers of the todorokite, adjacent layers can attach with a 60°/120° angle between the layers and still provide structural continuity, with each stacked layer having elongated crystallites aligned in one direction.

In summary, I suggest that the formation of todorokite from birnessite proceeds via the initial formation of local nano-domains of todorokite within the 10 Å phyllomanganate interlayer, leading to the formation of primary todorokite particles that grow from solution exclusively along the [010] direction. These primary particles then self-assemble laterally across the [100] direction via OA to form significantly larger and more crystalline secondary todorokite laths. Todorokite laths may undergo

further assembly, to form stacked layers, in which laths of todorokite may attach at angles of 60º, 120º or 240º in order to retain structural continuity. This process is presented visually in Figure 4.7. To my knowledge this is the first study to observe primary todorokite particles and capture their self-assembly and oriented growth during todorokite formation.

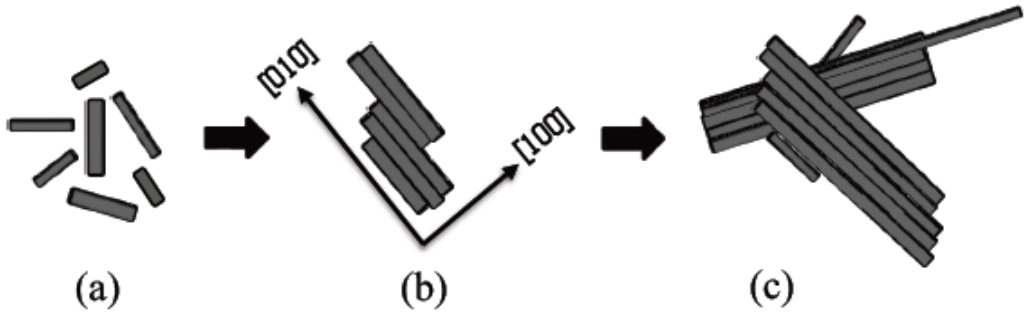

Figure 4.7 Simplified 2D model for the growth of todorokite: a) primary todorokite particles, b) oriented attachment of primary todorokite particles to form larger and more stable secondary todorokite laths, and c) further aggregation of todorokite laths to form todorokite with a plate-like morphology.

In order to robustly relate this formation and growth mechanism to the formation of todorokite in the marine environment, it is necessary to consider the role of artificial reflux treatment on the overall transformation process. For example, it has been shown that the growth of materials via hydrothermal routes typically favours OA-type growth (Penn and Banfield 1999; Gilbert et al., 2003). Importantly however, the morphological growth features observed in these synthetic samples throughout the reflux process are highly comparable to those seen in natural marine todorokite. As such, while the refluxing process necessarily accelerates the transformation rate, the overall formation and growth mechanism does not appear to have been fundamentally altered.

4.4.1.4 Crystal Ripening

In many instances experimental observations have shown that growth by OA usually dominates during the early stages of crystallization, and subsequently gives way to traditional ripening-based growth during the final stages of crystallization (Waychunas et al., 2005; Zhang et al., 2009). I therefore suggest that the neo-formed todorokite phase will likely undergo further growth from solution as a result of Ostwald-ripening processes during the later stages of the reflux, once any remaining birnessite has been transformed. However, owing the overlap of key peaks in the diffraction patterns of the 10 Å intermediate phase and the final todorokite product it is difficult to elucidate when the transformation is complete, and thus when all birnessite is consumed and ripening occurs. That said the significant decrease in surface area at 48 hr and 72 hr reflux is consistent with crystal ripening.

4.4.1.5 Potential implications for Trace Metal Cycling in Marine Sediments

It is well understood that the sequestration of dissolved trace metals to Mn oxide phases, and in particular to the phyllomanganate birnessite, exerts a strong control on the concentration of metals in seawater (e.g., Goldberg, 1954; Cronan, 1976; Burns and Burns, 1979; Post, 1999; Peacock and Sherman, 2007a; Sherman and Peacock, 2010; Spiro et al., 2010). In particular, recent work shows that sorption equilibrium between marine birnessite and the micronutrients Ni and Cu helps explain measured concentrations of these metals in the modern global oceans (Peacock and Sherman, 2007a; Sherman and Peacock, 2010). Mechanistically, Ni and Cu are sequestered from seawater and strongly bound to birnessite (e.g., Manceau et al., 2007a; Peacock and Sherman, 2007a; Peacock, 2009; Sherman and Peacock 2010), where at the pH of seawater and marine sediment porewaters, these metals then become variably progressively incorporated into the birnessite structure with time (Peacock, 2009; Peña et al., 2010; Sherman and Peacock, 2010). In natural marine birnessite, Ni is found entirely structurally incorporated (Peacock and Sherman, 2007b) while Cu only partially incorporates, likely because Cu(II) is Jahn-Teller distorted while Ni(II) is not (Sherman and Peacock, 2010). Jahn-Teller distortion sterically hinders Cu(II) incorporation into Mn(IV)-rich birnessite.

In the context of the current study, it is traditionally thought that Ni and Cu incorporated into birnessite might aid its transformation to todorokite (Burns and Burns, 1978; Burns and Burns, 1979; Usui, 1979; Takematsu et al, 1984). Subsequent work suggests specifically that the incorporation of heterovalent cations,

including Mn(III), Ni(II) and Cu(II), is necessary to kink the 10 Å phyllomanganate layers (Bodeï et al., 2007). For Mn(III) at least, the current work supports this assertion and shows that the kinking of the 10 Å phyllomanganate layers leads to the nucleation of todorokite primary particles. However, despite the role of Mn(III) in the crystallization of todorokite, it has been noted that natural todorokite typically contains significantly less Ni and Cu than the 10 Å phyllomanganate from which it crystallized (Siegel and Turner, 1983; Bodeï et al., 2007). For example, Siegel and Turner (1983) report 10 Å phyllomanganate with 3.8% NiO and 2.8% CuO while the neo-formed todorokite contains only 0.2% NiO and 1.5% CuO. While these studies do not explain the overall lower amounts of metal impurities in neo-formed todorokites, Siegel and Turner (1983) do suggest that higher Cu concentrations in todorokite reflect the Jahn-Teller distortion of Cu(II), and thus incorporated Cu(II) (and specifically the strained Cu^{2+}-O-$Mn^{3/4+}$ bond) is more favourable for kinking of the phyllomanganate layers and thus formation of Cu-bearing todorokite.

Having determined a four-stage nucleation and growth mechanism for the formation of todorokite, I can potentially shed new light on the role of trace metal impurities in the precursor birnessite phase, and their ultimate fate, during transformation to todorokite. I suggest that, in fact, only incorporated heterovalent cations with Jahn-Teller distortion will likely facilitate the initial kinking of the 10 Å phyllomanganate layers and thus promote the nucleation of todorokite and the subsequent formation of todorokite primary particles. It follows that for Ni-rich 10 Å phyllomanganates (where Ni(II) is not Jahn-Teller distorted), and in particular those with low structural Mn(III) and/or Cu(II) content, Ni(II) might retard the transformation of birnessite to todorokite, and/or be lost to solution in order that transformation can proceed, both of which potentially explain the prevalence of Ni-poor todorokites in the natural environment. Studies investigating the role of trace metal impurities during growth by OA are extremely limited, especially for cases where growth by OA is accompanied by phase transformation or vice versa. Kim et al. (2008) indicate that metal(loids) adsorbed to goethite nanoparticle surfaces substantially disrupt growth via OA, by essentially blocking attachment and aggregation interfaces. These authors conclude that if nanoparticle growth by OA is to proceed, impurities at aggregation interfaces must either be incorporated into the mineral structure away from attachment surfaces or desorbed into solution. As the Mn octahedral layers in both birnessite and 10 Å phyllomanganate are only a single octahedron thick, impurities incorporated into the mineral structure are effectively still present at aggregation interfaces. If non Jahn-Teller distorted impurities are lost to solution then the

diagenesis of birnessite potentially provides a source of these metals to marine sedimentary pore-waters and subsequently a benthic flux of micronutrients to seawater.

4.5 Summary and Conclusions

The current study provides the first detailed mechanism for the formation and growth of todorokite from birnessite in the marine environment. Specifically, I present evidence for a four-stage process that can be summarized as:

1. Nucleation of todorokite: Todorokite tunnel walls form within the phyllomanganate interlayers via kinking of the layers, these nano-domains then provide a nucleation site for todorokite primary particle formation.

2. Primary particle formation: Primary todorokite particles grow from solution via dissolution-recrystallization, specifically along the direction of tunnel growth ([010] direction).

3. Oriented attachment of primary particles: Simultaneous with their growth from solution, the primary particles align and attach perpendicular to the direction of tunnel growth ([100] direction) via oriented attachment, to form todorokite laths.

4. Ripening: Once the birnessite is consumed, further growth from solution occurs via traditional Ostwald-ripening type processes.

I propose there are two prerequisites for the formation of todorokite from 10 Å phyllomanganate. Firstly, the 10 Å phyllomanganate must contain a significant proportion of structural Mn(III) which, due to its Jahn-Teller distortion, facilitates kinking of the layers. Secondly, the 10 Å phyllomanganate must also display semi-coherent c-axis ordering, so that as the layers kink, there are sufficient adjacent layers for the formation of the todorokite tunnel walls. Both of these factors are necessary for the nucleation of todorokite and subsequent formation of todorokite primary particles.

Based on these prerequisites it follows that, contrary to traditional thinking, only structural cation impurities with Jahn-Teller distortion should aid the formation and growth of todorokite. As such, I predict that structural cation impurities without Jahn-Teller distortion (e.g., Ni) might retard the transformation of birnessite to todorokite and/or be lost to solution during this diagenetic process.

Chapter 5

Fate and mobility of Ni during the transformation of birnessite to todorokite

The following chapter is adapted from a manuscript currently in the final stages of preparation for submission to *Geochimica et Cosmochimica Acta.*

5.1 Introduction

The phyllomanganates birnessite and buserite, together with the tectomanganate todorokite, are the dominant Mn-bearing minerals in oxic marine sediments, where they are typically found as poorly crystalline and intermixed nanoparticulate phases (e.g., Goldberg, 1954; Burns and Burns, 1977; Banerjee et al., 1999; Post 1999). Birnessite and buserite in particular are highly reactive and through coupled sorption and redox reactions exert a strong control on the concentration, speciation and bioavailability of trace metals and micronutrients in seawater (e.g., Post et al., 1999). The poorly crystalline phyllomanganates present in marine ferromanganese precipitates are typically enriched in trace metals such as Ni, Cu and Zn by ~ 10^6 over their respective concentrations in seawater (e.g., Arrhenius, 1963; Koschinsky and Hein, 2003). Specifically with regard to Ni, hydrogenetic ferromanganese crusts and diagenetic ferromanganese nodules typically contain between ~0.2 and 1 bulk wt% Ni, respectively (e.g., Koschinsky and Halbach, 1995), resulting from a sorption equilibrium between birnessite and Ni which helps control the concentrations of this micronutrient in the modern global oceans (Peacock and Sherman, 2007a).

In oxic marine sediments however, the poorly crystalline phyllomanganates transform into todorokite during oxic diagenesis and under mild hydrothermal conditions. In the case of Ni, previous work shows that Ni is readily sequestered from seawater to birnessite via surface complexation both above and below Mn octahedral vacancy sites present on the birnessite [001] surface (space group P63/mmc) (e.g., Manceau et al., 2007a, b; Peacock and Sherman, 2007a.b; Peacock, 2009; Peña et

al., 2010). Subsequent to this initial sequestration, with aging and under pH conditions relevant to the marine environment, surface complexed Ni progressively migrates into the birnessite crystal lattice to become structurally incorporated (Peacock, 2009), and in natural marine ferromanganese precipitates, Ni is found entirely incorporated into birnessite and buserite (e.g., Peacock and Sherman, 2007b). Despite our understanding of Ni sequestration by birnessite and buserite, the fate and mobility of Ni and other micronutrients during the transformation of these phases into todorokite remains unclear. Work presented in chapter 4 of this thesis on the mechanism of todorokite nucleation and growth suggests that, contrary to current understanding, trace metals like Ni might retard the transformation of birnessite to todorokite and be released to marine sedimentary pore-waters during this diagenetic process, thus potentially providing a benthic flux of these micronutrients to seawater. A complete knowledge of the controls on Ni concentrations and isotopic compositions in seawater is important, not only for our understanding of the modern marine biogeochemical Ni cycle (e.g., Cameron and Vance, 2014), but also for the interpretation of palaeo Ni signatures recorded in marine sedimentary archives (e.g., Konhauser et al., 2009).

As outlined previously, in the natural environment Mn(III/IV) oxides are thought to form via the microbial oxidation of Mn(II) (e.g., Brouwers, 2000; Francis et al., 2001; Bargar et al., 2000, 2005; Villalobos et al., 2003; Tebo et al., 2005; Webb et al., 2005a, b; Saratovsky et al., 2006; Spiro et al., 2010). However, although todorokite is often found intimitely associated with turbostratic phyllomanganate (termed vernadite) and both 7 Å (birnessite) and 10 Å (buserite) semi-coherently stacked phyllomanganates (here all collectively termed poorly crystalline phyllomanganates) in marine ferromanganese precipitates (e.g., Burns and Burns, 1978a, b; Siegel and Turner, 1983; Usui and Terashima, 1997; Banerjee et al., 1999; Bodeï et al., 2007; Peacock and Moon, 2012) it is thought to only form during the transformation of a phyllomanganate during oxic sediment diagenesis and under low temperature hydrothermal conditions (e.g., Burns and Burns, 1978b). Indeed, observations from both natural ferromanganese samples and experiments largely support this assertion. For example, marine ferromanganese precipitates are generally classified into 3 genetic types, in order to reflect their respective modes of accretion and dominant Mn oxide mineralogy. Ferromanganese precipitates classified as hydrogenetic precipitate slowly from ambient seawater and are typically rich in poorly crystalline phyllomanganate phases. Conversely, those formed at the sediment-seawater interface are classified as diagenetic and typically contain varying mixtures of both poorly crystalline phyllomanganates and todorokite, reflecting the influence of

diagenetic sediment pore-waters on individual precipitates. Todorokite is typically prevalent in marine ferromanganese precipitates formed in close proximity to hydrothermal fluids (e.g., Burns and Burns, 1977). Moreover, all todorokite synthesis procedures to date involve the transformation of a phyllomanganate via either high temperature and pressure hydrothermal treatment (e.g., Giovanoli et al., 1975; Golden et al., 1986; Shen et al., 1993; Feng et al., 1995, 1998; Tian et al., 1997; Vileno et al., 1998; Luo et al., 1999; Malinger et al., 2004; Liu et al., 2005) or a more mild refluxing process at atmospheric pressure, designed to better simulate todorokite formation in natural environments (e.g., Feng et al., 2004, 2010; Cui et al., 2006, 2008, 2009a).

Classically, the transformation of birnessite to todorokite is described as a topotactic process, during which some of the morphological features and structural elements of the precursor phyllomanganate phase are preserved in the neo-formed todorokite product (e.g., Bodeï et al., 2007; Feng et al., 2010). Structural incorporation of heterovalent cations, including Cu(II) and Ni(II), is thought to aid transformation (Burns and Burns, 1978; Burns and Burns, 1979), as is the presence of structural Mn(III) where, because of its Jahn-Teller distortion, Mn^{3+}-O-Mn^{4+} bonds that run parallel to the [010] (space group P2/m) should be relatively weak and most susceptible to topotactic rearrangement (Bodeï et al., 2007; Cui et al., 2008). However, the specific mechanistic details of the transformation were largely unclear.

In the previous chapter of this thesis I report a new four-stage nucleation and growth model for the formation of todorokite in the marine environment, during which large crystalline laths of todorokite are formed via an aggregation-dominated pathway. Initially, it was found that todorokite tunnel walls form within the phyllomanganate interlayers via a thermally-induced kinking of the layers, and these nano-domains act as nucleation sites for the formation of todorokite primary particles, some 8-10 nm wide and up to 100 nm in length. In agreement with previous work (e.g., Bodeï et al., 2007), I suggested that for successful todorokite formation, the phyllomanganante layers must be spaced ~10 Å apart, closely matching the eventual tunnel dimensions of the neo-forming todorokite (where ideal todorokite consists of triple chains of edge-sharing MnO_6 octahedra that share corners to form 3D tunnels equating to ~10x10 Å (Burns et al., 1985; Post and Bish, 1988; Post et al., 2003)). Additionally, I suggested that a significant proportion of structural Mn(III) which, due to its Jahn-Teller distortion facilitates kinking of the phyllomanganate layers, and semi-coherent *c*-axis ordering, so that as the layers kink there are sufficient adjacent layers for the formation of the todorokite tunnel walls, are also prerequisite for todorokite formation. The primary

particles grow from solution via dissolution-recrystallization, exclusively along the direction of tunnel growth ([010] crystallographic direction). These initially formed primary crystallites then assemble spontaneously via oriented attachment (OA), attaching at crystal faces perpendicular to the direction of tunnel growth ([100] crystallographic direction), to form large acicular laths of todorokite measuring up to 150 nm wide and 500 nm in length. Lateral attachment of the primary todorokite particles is accompanied by continuous growth from solution along the [010] direction. Further coalescence of the todorokite laths, via the attachment of the [001] surfaces, give rise to large stacked plates of todorokite, in which individual laths are oriented specifically at 120^{O} to each other in order to preserve structural continuity between each stacked layer.

While this new growth model explains many of the unique morphological and structural features observed in natural todorokites, it also raises important questions about the long-term sequestration of trace metals during phyllomanganate transformation and todorokite crystal growth via this non-classical OA-based growth pathway. In addition to todorokite, there is now a diverse and rapidly growing catalogue of mineral phases known to grow via OA, including TiO_2, Cu and Fe (hydr)oxides, ZnS, cryptomelane-type Mn oxide and $CaSO_4$ (Penn and Banfield, 1998a; Penn and Banfield, 1999; Banfield et al., 2000; Gilbert et al., 2003; Huang et al., 2003; Waychunas et al., 2005; Portehault et al., 2007; Burrows et al., 2012; Van Driessche et al., 2012; Frandsen et al., 2014). Many of these mineral phases are ubiquitous in natural soils and sediments and play important roles in the biogeochemical cycling of aqueous trace metals, yet to date there have been few detailed studies investigating the effects of OA type-growth on the retention of surface sorbed or structurally incorporated trace metal impurities. This is particularly true for cases where crystal growth by OA is accompanied by a phase transformation. Indeed there is now increasing evidence to suggest that there is an intimate link between the two processes. For example, Frandsen et al. (2014) found that the formation and growth of large (15x150 nm) hematite (α-Fe_2O_3) spindles under hydrothermal conditions, was induced by the alignment and orientated attachment of small (<5 nm in diameter) akaganeite (β-FeOOH) nanorods. Change in phase stability, due to the increase in particle size as a result of akaganeite particle aggregation was found to favor transformation to hematite. Specifically the authors suggest that the interface between aggregating akaganeite particles may serve as ideal sites for the nucleation of hematite. Further conversion of the remaining akaganeite particles to hematite was

found to occur upon contact of the akaganeite particles with the newly formed hematite spindle surfaces.

Previously, I proposed that contrary to traditional understanding, only structurally incorporated heterovalent Jahn-Teller active cations will promote the nucleation of todorokite and the subsequent formation of todorokite primary particles, as only cations with distorted metal-O bonds along the *z*-axis will produce relatively weak metal-O-Mn^{4+} linkages running parallel to the [010] which facilitate layer kinking and initial formation of the todorokite tunnel walls. I suggest that for Ni-rich phyllomanganates (where Ni(II) is not Jahn-Teller distorted), and in particular those with low structural Mn(III) and/or Cu(II) content (where Mn(III) and Cu(II) are Jahn-Teller distorted), Ni(II) might retard the transformation of birnessite to todorokite, and be released to solution, in order that transformation can proceed. Indeed, it has been noted that natural todorokite typically contains less Cu and, in particular, substantially less Ni than the 10 Å phyllomanganate from which it crystallized (Siegel and Turner, 1983; Bodeï et al., 2007).

Considering the few studies to investigate the fate of sorbed trace metals during OA-type crystal growth, Kim et al. (2008) find that the progressive adsorption of As(V), Cu(II), Zn(II) and Hg(II) onto nanoparticulate goethite disrupts growth via OA, by essentially blocking attachment and aggregation interfaces. These authors conclude that if nanoparticle growth by OA is to proceed, impurities at aggregation interfaces must either be structurally incorporated into the mineral structure away from attachment surfaces or desorbed into solution. However, because the Mn octahedral layers in poorly crystalline phyllomanganates are only a single octahedron thick, impurities incorporated into the mineral structure are effectively still present at aggregation interfaces. Similarly, a more recent investigation finds that the growth rate of goethite nanorods via OA is inhibited due to the association of NO_3^{2-} with the aggregating crystal faces (Burrows et al., 2012). As such there is recent evidence to suggest that trace metal impurities might retard transformation and/or be desorbed into solution in mineral systems that grow via an OA-type pathway.

In order to determine the effect of Ni on todorokite nucleation and growth, and investigate the fate and mobility of Ni sequestered by birnessite during its transformation into todorokite, todorokite has been synthesized from a Ni-sorbed c-disordered hexagonal birnessite, via a mild reflux procedure. The Ni-sorbed birnessite precursor is analogous to marine birnessite and crucially displays sufficient ordering of the phyllomanganates sheets along the c-axis to enable the identification of key

spectral, structural and morphological features in the precursor c-disordered birnessite, 10 Å phyllomanganate intermediate and transformation products.

The initial c-disordered birnessite, intermediate phyllomanganate and subsequent transformation products have been extensively characterized using X-ray diffraction (XRD), transmission electron microscopy (TEM) and BET surface area analysis, while the fate and mobility of Ni during the conversion of birnessite to todorokite is determined via Ni K-edge extended X-ray absorption fine structure spectroscopy (EXAFS), transmission electron microscopy-energy dispersive spectroscopy (TEM-EDS) and inductively coupled plasma optical emission spectrometry (ICP-OES). In addition, μ-X-ray fluorescence (μ-XRF) and μ-EXAFS have been employed in order to determine the dominant Mn oxide mineralogy and Ni mineralogical phase associations in three genetically distinct natural marine ferromanganese precipitates, namely a hydrogenetic ferromanganese crust sample, a diagenetic marine ferromanganese nodule and a hydrothermal–type ferromanganese precipitate. With careful and combined analysis of this work I asses the effect of sorbed Ni on the transformation of birnessite to todorokite, and use these findings to shed new light on the fate and mobility of Ni in oxic marine sediments.

5.2 Methods

5.2.1 Preparation of Ni-sorbed hexagonal birnessite precursor

Ni sorbed c-disordered hexagonal birnessite with an interlayer spacing of ~7 Å and ~1.0 wt% Ni was synthesized following a modified method of Villalobos et al. (2003). Briefly, 320 mL of a 0.196 M $KMnO_4$ solution was added slowly to 360 mL of 0.51 M NaOH solution. Subsequently, 3.41 g of $Ni(NO_3)_2$ was added to 320 mL of a 0.366 M $MnCl_2$ solution and added slowly to the above mixture whilst stirring vigorously at room temperature. After 30 min 5x 1 mL suspension aliquots were taken in order to quantify the amount of mineral precipitated. The mineral suspension was then left to settle for ~4 hr. Meanwhile, 3x aliquots of the supernatant solution were extracted, filtered through 0.2 µm syringe filters and retained for Ni and Mn analysis via inductively coupled plasma optical emission spectroscopy (ICP-OES). ICP-OES analysis was conducted at the Trace Element Laboratory in the Department of Chemistry at the University of Hull; using an Optima 5300 DV ICP-OES. Sample standard deviation is calculated based on measurement of the 3 separate supernatant aliquots.

The remaining supernatant was subsequently discarded and the wet mineral slurry centrifuged at 3200 g for 30 min. After centrifugation, the wet slurry was washed by mixing with 1 M NaCl, shaken for 45 min and re-centrifuged at 3200 g for 10 min. This process was repeated 4 times, and on the last wash the pH was adjusted to pH 8 and the suspension was shaken overnight. After the NaCl washes, the slurry was combined with Milli-Q water (MQ), shaken for 1 hr and centrifuged at 3200 g for 10 min. This wash cycle was repeated 10 times, 1x for 1 hr, 8x for 0.5 hr and 1x overnight. Approximately ¼ of the total resulting wet paste was sacrificed for X-ray diffraction (XRD), transmission electron microscopy (TEM), BET and extended X-ray absorption fine structure (EXAFS) analyses. After drying the wet paste overnight in the oven at 30 ^{o}C, the sample was ground to a fine powder, before dissolving 0.01g of the mineral in 3 M HCl heated on a hot plate for approximately 2 hr in order to determine the total concentration of Ni sequestered to the solid product by ICP-OES as above. Accordingly, the Ni-doped c-disordered birnessite was found to contain ~1.0 wt % Ni.

5.2.2 Transformation of Ni sorbed hexagonal birnessite to todorokite

The Ni-sorbed c-disordered hexagonal birnessite was subsequently transformed to todorokite following the method outlined in the methods chapter (chapter 3). Briefly, the remaining wet paste Ni-sorbed c-disordered birnessite was suspended in an ~ 4L of 1 M $MgCl_2$ and stirred moderately for 18 hr at room temperature. The resulting suspension was then centrifuged to a wet paste. This produced a Ni-sorbed phyllomanganate intermediate with an interlayer spacing of ~10 Å. The Ni-sorbed phyllomanganate intermediate was then re-suspended in approximately 800 mL of 1 M $MgCl_2$ in a 1 L round bottom flask fitted with a glass condenser. The suspension was stirred continuously and heated to and kept at 100 °C using a combined heating mantle with magnetic stirrer. The suspension was left to age for a period of 4 weeks, during which time, suspension aliquots (~75 mL) were extracted from the reaction vessel at time intervals of 3, 6, 12, 24, 48 and 72 hr, 5 days, and 1, 2 and 4 weeks. Each suspension aliquot was cooled in a water bath to room temperature before centrifuging at 3200 g for 10 min. Supernatant solutions were collected and the pH measured (calibrated to ±0.05 pH units with Whatman NBS grade buffers). Triplicate aliquots of each supernatant solution were also filtered through 0.2 µm syringe filters and retained for Ni and Mn ICP-OES as described above. All solid samples were washed extensively in 18.2 MΩ.cm MQ water and oven dried at 30 ^{o}C prior to analysis. After 4 weeks the reflux was stopped, the suspension was cooled to room temperature and the above procedure was repeated to obtain the final solution and solid samples.

5.2.3 Natural Ferromanganese-rich Samples

A hydrogenetic marine ferromanganese crust sample (237KD; Pacific Ocean; location: 09^{o}18'N, 146^{o}03'W; water depth: 4830 m), a diagenetic marine ferromanganese nodule sample (Nod-P-1; Pacific Ocean; location: 14^{o}50'N, 124^{o}28'W; water depth: 4300 m) and a hydrothermal marine precipitate sample (D17-1-IV; Lau Basin; location: 22^{o}17.78'S, 176^{o}38.89'W; water depth: 2063-1965 m) were supplied by J.R. Hein (United States Geological Survey). From each sample, a small section (roughly 20 mm in length and perpendicular to the growth layers, 15 mm wide and 5 mm deep) was cut from the upper 0-60 mm of the bulk sample, using a wafering saw. From the cut sections a small amount of material was extracted using a micro drill, ground to a fine powder and dissolved in 6 M HCl, and then analysed for

bulk Ni content by ICP-OES (as above). Bulk Ni contents for the hydrogenetic, diagenetic and hydrothermal samples are ~0.4, 0.5 and 0.07 wt.% Ni, respectively. The sections were subsequently encased in high purity resin and self-supported ~30 μm thick polished sections were prepared for μX-ray fluorescence (μXRF) and μEXAFS. Micro thin sections were prepared by Bob Jones and John Ford at the National Oceanography Centre, Southampton. Previously reported chemical analyses of the hydrogenetic, diagenetic and hydrothermal samples give bulk Mn:Fe ratios of 1.9, 5 and 114, respectively, which are within the ranges expected for ferromanganese precipitates assigned to these different genetic types (Rehkämper et al., 2002).

5.2.4 Characterization of Precursor, Intermediate and Reflux Products

Powder XRD patterns were collected using a Bruker D8 diffractometer, operating at 40kV/40mA and equipped with CuKα radiation (λ = 1.5418) and a LynxEye detector. Samples were analyzed over a range of 2-90 $^{o}2\theta$ with a 0.009^{o} step size and step count time of 7 sec. Data evaluation was undertaken using the DIFFRAC plus EVA software package. For XRD analysis of natural ferromanganese samples, distinctly Mn-rich regions of the samples (i.e. dark brown/black areas) were chosen for analysis to avoid obviously Fe-rich areas.

TEM images were collected at the Leeds Electron Microscopy and Spectroscopy center in the Institute for Materials Research at the University of Leeds. For imaging, finely crushed powder samples were suspended in methanol and dispersed via sonication. Samples were then loaded onto individual holey carbon TEM grids and allowed to dry at room temperature. Imaging was performed at 200 kV on a Philips CM200 FEGTEM. EDS data was collected at several points of interest using the TEM. The wt% of Ni identified at each specific point of interest was measured using a standardless procedure.

2.2.5 X-ray Absorption and Fluorescence Spectroscopy

In addition to the above analyses, Ni K-edge (8.333 keV) EXAFS spectra were collected for the c-disordered birnessite precursor, Mg-exchanged phyllomanganate intermediate and subsequent reflux products. Micro-focus μXRF elemental maps (for

Mn, Fe and Ni) and μEXAFS (at the Ni and Mn-K edges (6.539 keV)) were also collected for the natural ferromanganese samples. Spectra were collected at Diamond Light Source (DLS) Ltd on station B18 (synthetic samples) and I18 (natural samples).

During data collection, storage ring energy was 3.0 GeV and the beam current was approximately 200 mA. Samples were presented to the X-ray beam as dry powders pressed into pellets (synthetic samples), or as ~30 μm thick self-supported thin sections (natural samples), held between Kapton tape. Data was acquired in fluorescence mode (Ni K-edge) or transmission mode (Mn K-edge). Test scans indicated that there was no photo-redox or visible beam damage on the samples after 6 EXAFS scans to k = 14 $Å^{-1}$. However, in order to minimize beam damage 4 spectra were recorded at a single x,y point before moving to a new point to record a further 4 spectra, collecting a total of 36 spectra (for Ni K-edge of the synthetic samples) or up to 9 spectra (9 for Ni K-edge and 4 for Mn K-edge of the natural samples). μXRF maps were collected at 8.4 keV with a pixel size of 10x10 μm and a count time of 1 sec per pixel. Maps were deadtime corrected and registered using custom beamline software. XRF maps were use to identify points of interest (POI) for collection of Ni and Mn μEXAFS. For μEXAFS the beam spot was ~2x3 μm. Energy calibration was achieved by assigning the first inflection point of Au (L3) foil to 11.919 keV.

EXAFS data reduction was performed using ATHENA (Ravel and Newville, 2005) and the Ni spectra were fit using DL_EXCURV (Tomic et al., 2005). Spectra were fit in k-space over 3 – 12 $Å^{-1}$, with no Fourier filtering during data analysis, and the fitting included full multiple scattering as coded in EXCURV98 (Binsted, 1998). Multiple scattering calculations require specification of the full three dimensional structure of the Ni coordination environment (i.e., bond angles in addition to bond lengths). This was done using hypothetical model clusters with either C_1 or C_3 symmetry, for various different Ni local coordination geometries, including Ni sorbed at Mn octahedral vacancy sites present in the phyllomanganate layers (Peacock and Sherman, 2007a), Ni structurally incorporated into the phyllomanganate layers (Peacock and Sherman, 2007a,b) and Ni sorbed to todorokite (Fig. 5.5). Several reference compounds were used to help fit the EXAFS spectra, namely a synthetic Ni-sorbed c-disordered birnessite where Ni is surface adsorbed at the vacancy sites, a natural Ni-incorporated poorly crystalline phyllomanganate where Ni is structurally incorporated, and two Ni-sorbed todorokite samples prepared at 24 hr and 1 wk contact times respectively (for further details of the reference compounds see section 2.2.6). Reference spectra were fit by the refinement of a single model cluster. Where appropriate, the sample spectra were fit by linear combination of different model

clusters as coded in EXCURV98 (Binsted, 1998). Linear combination was performed over the *k*-range 3 – 12 $Å^{-1}$ with a linear combination of the k^3-weighted Chi(*k*) for each cluster. In the linear combinations only the Fermi Energy (EF) and relative site occupancies were optimized. For all fits, the number of independent data points (N_{ind}) was determined using Stern's rule (Stern, 1993) as $2\Delta k\Delta R/\pi + 2$ (Booth and Hu, 2009) where Δk and ΔR are the range in *k* and *R*-space actually fitted. The number of fitted parameters (N_{par}) was determined as the total number of parameters optimized during the various model refinements and was always less than N_{ind}.

The quality of the fits provided by the different model clusters was assessed using the EXAFS R-factor and the reduced Chi^2 function, which provides an absolute index of the goodness of the fit (and so can be used for comparing fit quality between fits where N_{pars} is not equivalent; all as coded in EXCURV98 (Binsted, 1996, 1998)). Typical errors associated with EXAFS modelling over the *k*-range used here are 15 % and 25 % for first and second shell coordination numbers, respectively, ±0.02 and 0.05 Å for first and second shell distances, respectively, and 15 % and 25 % for first and second shell Debye–Waller factors, respectively (Binsted, 1998). The errors associated with the optimized site occupancies for the linear combination fits were evaluated for each fit by assuming that manual changes to the optimized site occupancies were not significant until they generated >10 % increase in the reduced Chi^2 function (Peacock, 2009; Moon and Peacock, 2012). The error on an optimized site occupancy is therefore quoted as the difference between the optimized site occupancy and the site occupancy value incrementally determined to generate a 10 % increase in reduced Chi^2.

In addition to principal linear combination in DL_EXCURV, all linear combination fits of the Ni spectra were checked in ATHENA. Linear combination fitting was also performed for some of the Mn spectra recorded for the natural ferromanganese samples in ATHENA. In these cases fitting was done with a linear combination of Chi(*k*) over the *k*-range 3 – 12 $Å^{-1}$, using the δMnO_2 and todorokite reference spectra. The errors reported are those generated in ATHENA, i.e., 1-sigma error bars assuming the only source of noise is statistical noise (Ravel, 2009). As EXAFS experiments are very rarely dominated by statistical noise, these errors are conservative. For two-component mixtures such as those used here, the error on the fits is typically estimated at ±10 % of the fitted value (e.g., Kim et al., 2000). Given the fact that the reference spectra for δMnO_2 and todorokite are similar over the indicator

region, and that the natural samples show somewhat reduced data quality compared to these, ±10 % is still likely a conservative error estimate.

2.2.6 Reference compounds

In addition, a range of Ni free synthetic Mn oxides were prepared using the methods described in the methods section (Chapter 3) and used as references during the above analyses The references used in the current work include triclinic Na-birnessite (Tc-Na-birnessite), crystalline hexagonal birnessite (Hx-birnessite), c-disordered hexagonal birnessite, all with an interlayer spacing of ~7 Å, δMnO_2 and crystalline todorokite. Mineral identity and purity was confirmed by XRD analysis of randomly orientated powder samples.

The Ni-sorbed Mn oxides used as references during the EXAFS analysis included a Ni-sorbed c-disordered birnessite, a Ni-incorporated natural poorly crystalline phyllomanganate, and Ni-sorbed todorokite. For the Ni-sorbed c-disordered birnessite (where the mineral was prepared as above following the method of Villalobos et al., 2003) and Ni-sorbed todorokite (with todorokite prepared as described in chapter 4 of this thesis via the method of Feng et al., 2004) a Ni^{2+} stock solution was prepared at 100 ppm from $Ni(NO_3)_2.6H_2O$ and a NaCl background electrolyte at 0.1 M. Individual sorption experiments were prepared at 15 ppm $[Ni]_{total}$ by adding 4 mL of Ni stock to 0.1 g of mineral in 21 mL of background electrolyte, giving a solid/solution ratio of 4 g/L. Suspension pH was adjusted to pH ~5 and ~8 for the c-disordered birnessite and todorokite experiments, respectively, via the dropwise addition of HNO_3/NaOH and recorded after stabilization to two decimal places. The c-disordered birnessite experiment was left for 24 hr, while two todorokite experiments were prepared and left for 24 hr and 1 week, during which time the pH of each sample was periodically checked and adjusted as necessary using HNO_3/NaOH. The samples were subsequently centrifuged at 3000 g for 5 minutes to produce wet pastes for EXAFS analysis.

The Ni-incorporated natural poorly crystalline phyllomanganate is catalogued as hydrogenetic ferromanganese crust sample 5DSR8 (Pacific Ocean; location: 04°09'S, 174°54'W; water depth: 1585 m) from Chu (2004), and was sourced from the National Oceanography Centre, Southampton as a dry powder. No further preparation was performed.

5.3 Results

5.3.1 Transformation of Ni-sorbed Hexagonal birnessite to todorokite

5.3.1.1 X-ray diffraction

XRD patterns for the Ni-sorbed c-disordered birnessite precursor, Ni-sorbed 10 Å phyllomanganate intermediate and all subsequent reflux products are presented in Figure 5.1. The c-disordered birnessite precursor shows 4 broad peaks at ~7.2 Å, ~3.6 Å, ~2.4 Å and ~1.4 Å, corresponding to the [001], [002], [100] and the [110] reflections, respectively (Villalobos et al., 2003). Following suspension of this phase in 1 M $MgCl_2$, the inter-layer spacing is expanded from ~7 Å to ~10 Å as indicated by the appearance of peaks at ~9.6 Å, ~ 4.8 Å and ~ 3.2 Å ([001] [002] and [003] basal reflections, respectively) in the 10 Å phyllomanganate (Fig. 5.1). In agreement with the work presented previously in chapter 4, these peaks are more intense than those of the c-disordered birnessite precursor suggesting that the ion-exchange process enhances the crystallinity and long range ordering of the sheets. The *d*100/*d*110 peak intensity ratios of the c-disordered birnessite and 10 Å phyllomanganate are close to √3 (at 2.42/1.41 and 2.40/1.41, respectively), which is again in good agreement with the study of Villalobos et al. (2003) for c-disordered birnessite and indicates that both phases have hexagonal layer symmetry with $a = b = 2.83$ Å (Drits et al., 1997). In addition, for both phases, the symmetrical shape of the ~1.4 Å peak further indicates hexagonal layer symmetry (Drits et al., 1997), and the slight degree of asymmetry on the high angle side of the ~2.4 Å peak, is common to phyllomanganates that lack significant periodic ordering of the sheets (Villalobos et al., 2006). By contrast, triclinic birnessite (JCPDS-23-1046) shows a characteristic splitting of the peaks at ~2.4 Å and ~1.4 Å, lending the ~1.4 Å peak region in particular a distinctive asymmetry (e.g., Drits et al., 1997).

Over the course of the reflux there is little evidence for the formation of todorokite during the first 24 hrs (Fig. 5.1). This is in sharp contrast to the transformation of Ni-free c-disordered birnessite, during which characteristic todorokite peaks at ~2.2 Å, ~1.9 Å, ~1.7 Å and ~1.5 Å are observed by 3 hrs reflux. In the current study, the only observable changes over the 3 hr time period are a decrease in the intensity of the ~9.6 Å, ~ 4.8 Å and ~ 3.2 Å peaks. This likely reflects a reduction in the crystallinity of the 10 Å phyllomanganate due to some degree of dissolution-recrystallization occurring during the initial reflux stages. These peaks are

markedly more intense after 6 hr reflux likely reflecting a relative increase in crystallinity by this time point.

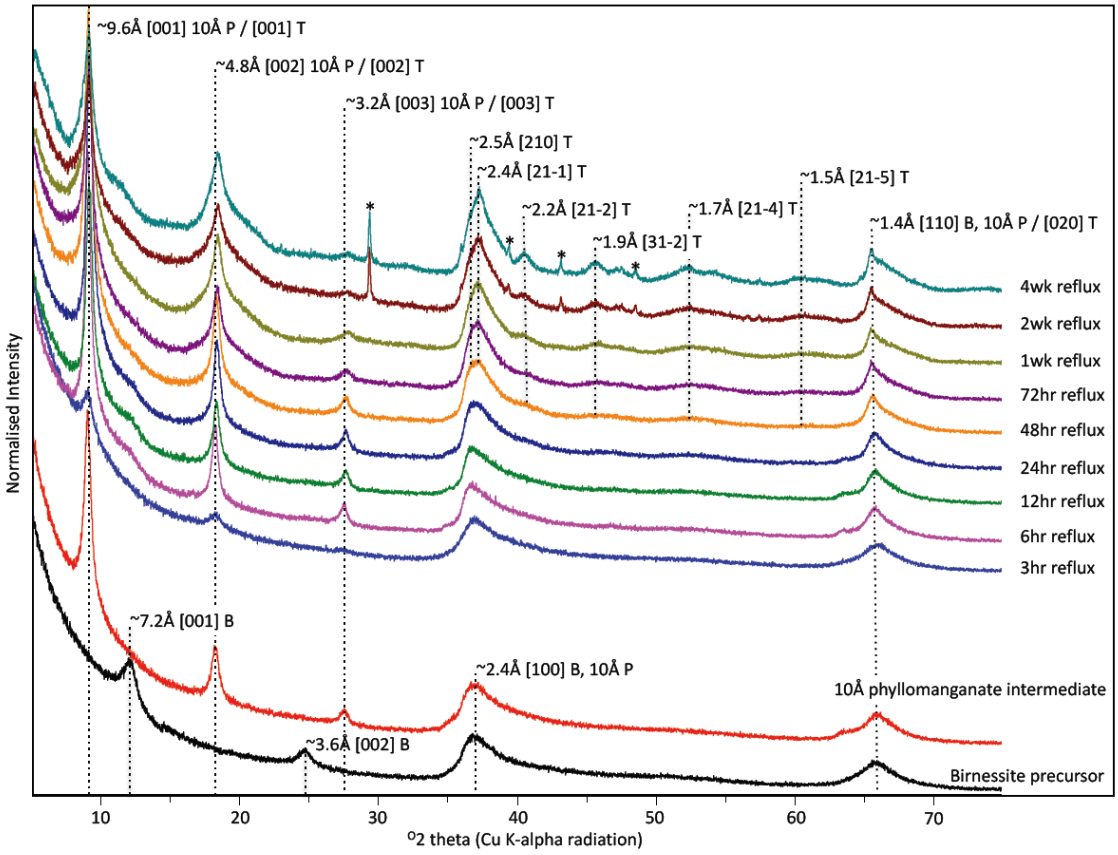

Figure 5.1 X-ray diffraction patterns for the Ni-sorbed c-disordered birnessite precursor, Ni-sorbed 10 Å phyllomanganate intermediate and subsequent reflux products. Characteristic X-ray diffraction peaks are labelled for c-disordered birnessite (B), 10 Å phyllomanganate intermediate (10Å P) and todorokite product (T) (based on Drits et al., 1997 for turbostratic birnessite, JCPDS-32-1128 for buserite and JCPDS-38-475 for todorokite). The * symbol indicates residual $MgCl_2$.

The four distinct changes in the XRD patterns, expected during the transformation of birnessite to todorokite, only start to become visible by 48 hr reflux (Fig. 5.1). Firstly, by 48 hr reflux additional broad peaks are observed at ~2.2 Å, ~1.9 Å and ~1.7 Å, and a broad hump at ~1.5 Å, indicating that transformation of the 10 Å phyllomanganate to todorokite has begun by this time point (Feng et al., 2004). As the reflux proceeds these peaks become sharper and more intense indicating the

progressive formation of todorokite. Secondly, by 48 hr reflux the peak at ~2.4 Å has begun to split to reveal a shoulder at ~2.45 Å, which becomes more prominent with time. Thirdly, the peak at ~5.0 Å has begun to broaden, developing into a broad shoulder on the high-angle side at ~4.3 Å. Fourthly, by 48 hr reflux the peak at ~1.4 Å has started to become progressively asymmetrical. These later three changes are those expected during the transformation of 10 Å phyllomanganate into todorokite (Feng et al., 2014) and indicate that transformation has begun by 48 hr reflux.

5.3.1.2 Transmission electron microscopy

TEM images are presented in Figure 5.2, and highlight the gradual transformation the 10 Å phyllomanganate into todorokite over the first 2 wks of reflux. Firstly, the 10 Å phyllomanganate has a rumpled plate-like morphology, where the edges of the phyllomanganate sheets measure ~50 – 70 Å wide (Fig. 5.2a, inset).

Repetition of the [001] lattice planes (space group p63/mmc) indicates that the individual phyllomanganate layers are reasonably well stacked over at least 30 Å. In agreement with previous work, the measured interlayer of the 10 Å phyllomanganate is equal to ~8.2 Å (Fig. 5.2b), which although inconsistent with that measured via XRD (9.6 Å; Fig. 5.1) is consistent with the partial collapse of the phyllomanganate layer under the high vacuum conditions of the TEM (e.g. Post and Veblen, 1990).

At 6 hr reflux the morphology of the imaged samples is still dominated by the platy 10 Å phyllomanganate phase. However, small primary particles of todorokite measuring ~ 6 – 10 nm wide across the direction of tunnel growth ([100] direction) and elongated longitudinally along the direction of tunnel growth ([010] direction) are also visible within the sample matrix (Fig. 5.2c, d). The lattice fringes of these particles are poorly defined, indicating that they are poorly crystalline. In the previous chapter, characteristic todorokite XRD peaks were present by 3 hr reflux and I was able to visually identify the presence of todorokite primary particles by 6 hr. The poor crystallinity of the todorokite primary particles in this Ni-doped system likely accounts for the lack of characteristic todorokite peaks in the XRD at the same approximate time point.

At 24 hr reflux, the mineralogy is still dominated by the 10 Å phyllomanganate phase, however, it is evident that the todorokite primary particles have begun to form platy todorokite aggregates measuring ~200 x 200 nm (Fig. 5.2e), in particular, large acicular laths of todorokite measuring on average ~250 nm in length (along the direction of tunnel growth, [010] direction) and ~70 nm wide (across the direction of tunnel growth, [100] direction) (Fig. 5.2f). These todorokite laths are assembled from a number of smaller primary particle building blocks that vary in length but measure consistently between ~ 8 – 10 nm wide. With increasing reflux time, these secondary todorokite laths increase in size, particularly in the longitudinal direction, and after 1 wk large todorokite laths, measuring on average ~ 460 nm long and ~ 70 nm wide (Fig. 5.2g) dominate the sample morphology.

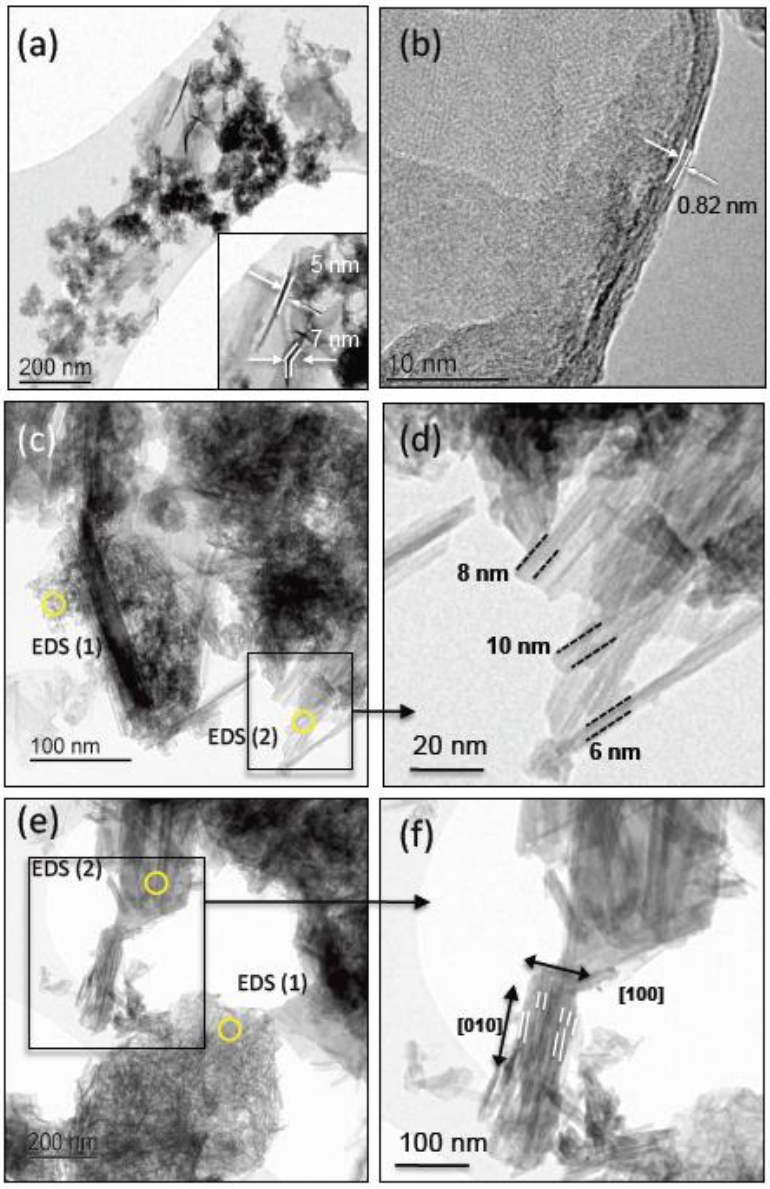

Figure 5.2 Transmission electron micrographs of: (a-b) Ni-sorbed 10 Å phyllomanganate precursor with image (a) highlighting the plate-like birnessite morphology and thick phyllomanganate sheet edges, and (b) highlighting the 10 Å phyllomanganate intermediate interlayer spacing. Images (c-d) show the product after 6 hrs of reflux treatment, where (c) highlights the birnessite dominated mineralogy of the sample matrix and (d) highlights the formation of poorly crystalline todorokite primary particles, which are elongated along the [010] direction and relatively uniform in size (6-10 nm) across the [100] direction, (e-f) shows the product after 24 hrs of reflux treatment with (e) highlighting the mixed birnessite/todorokite mineralogy and (f) highlighting the formation of poorly crystalline plate-like todorokite, and the formation of large secondary todorokite laths, formed via the lateral aggregation of todorokite primary particle building blocks.

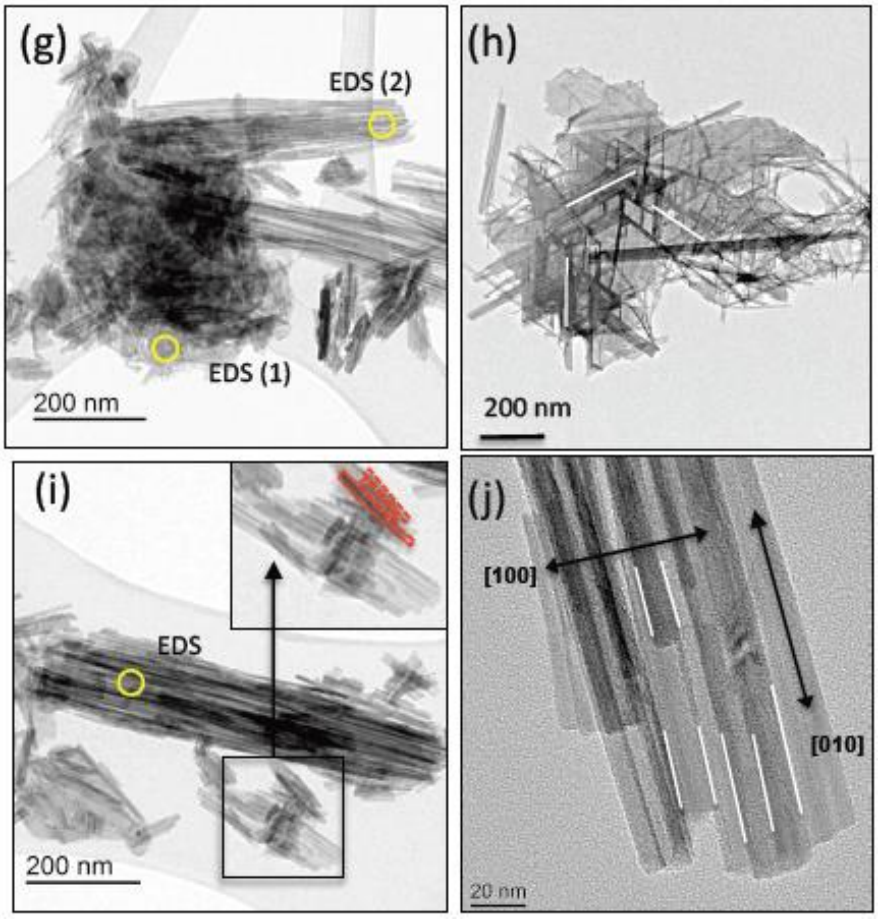

Figure 5.2 (*continued*) TEM Images (g-h) show the product after 1 week of aging and indicates that the mineralogy is largely dominated by todorokite and (h) the (i-j) product after 2 weeks of aging (i) Red lines highlight the lateral aggregation of primary todorokite particles and (j) highlights the relatively uniform widths of the individual todorokite primary particles after 2 weeks of reflux treatment. Yellow circles in images (c), (e), (g) and (i) indicate the position of EDS analysis, where the circle is equal to the approximate size of the analyzed area. For approximate wt % of Ni detected at the selected EDS points, please refer to Table 5.1.

The lattice fringes of the todorokite laths are notably more defined by 1 wk reflux, indicating an increase in the crystallinity of the neo-formed todorokite phase with time. At this same time point, it is also apparent that individual todorokite laths are aligned with each other at 120° to form large aggregates of todorokite that exhibit a plate-like morphology (Fig. 5.2h). These large todorokite plates (>1000 nm x 500 nm), are orientated in three distinct directions, are arranged into stacked layers along the [001] direction (Fig. 5.2h). At 2 wk reflux, there is no observable 10 Å

phyllomanganate or phyllomanganate-like phase within the sample matrix, indicating that by this time point the 10 Å phyllomanganate has undergone essentially complete transformation into todorokite (Fig. 5.2i). In addition, by 2 wk the average size of the secondary todorokite laths has increased further to ~700 nm long and ~150 nm wide (Fig. 5.2i).

Comparison of the TEM images over 2 weeks of reflux shows that the individual todorokite primary particles vary in length ([010] direction), while in contrast, particle widths ([100] direction) remain consistent at on average ~6 – 10 nm wide (Fig. 5.2d, f, i). The progressive formation of todorokite laths some ~700 nm long ([010] direction) and ~150 nm wide ([100] direction) is consistent with the growth mechanism identified in the previous chapter for todorokite formed in a Ni-free system, where longitudinal growth of primary particles and secondary laths is dominated by growth from solution, via dissolution-recrystallisation, while lateral growth of the todorokite laths is dominated by the oriented-attachment (OA) of primary particles along the [100] crystal faces.

EDS data collected at 6 and 24 hr, and 1 and 2 wk reflux, for selected points (marked on Fig. 5.2, where point 1 is always on the platy 10 Å phyllomanganate matrix and point 2 on the todorokite matrix) is presented in Table 5.1. From 6 hr to 1 wk reflux, despite the progressive formation of todorokite, EDS shows that, in the measured sample points, sequestered Ni is associated with the platy 10 Å phyllomanganate fraction of the sample matrix and there is no detectable Ni associated with the poorly crystalline todorokite primary particles or secondary todorokite laths (Table 5.1). After 2 wk reflux, when there is no observable 10 Å phyllomanganate or phyllomanganate-like phase within the sample matrix, EDS shows that there is still no detectable Ni associated with todorokite, despite measuring several points on a number of different todorokite laths and plate-like aggregates (all typified by the 2 wk EDS point, Fig. 5.2i, Table 5.1). It is important to note that while this data can be used for relative comparison of Ni concentrations between measured points, it is not used for the quantitative measure of absolute Ni concentrations in the current study.

Sample	Cu (wt%)	C (wt%)	Mn (wt%)	O (wt%)	Mg (wt%)	Ni (wt%)	sum (wt%)
6 hr EDS (1)	50.7 (0.7)	21.1 (0.8)	16.3 (0.4)	10.9 (0.6)	0.7 (0.1)	0.4 (0.1)	100.1
6 hr EDS (2)	51.9 (0.8)	25.9 (0.8)	12.5 (0.4)	8.9 (0.5)	0.7 (0.1)	0	99.9
24 hr EDS (1)	26.8 (0.4)	0	41.4 (0.5)	28.9 (0.6)	2.0 (0.1)	1.0 (0.1)	100.1
24 hr EDS (2)	22.3 (0.3)	0	35.5 (0.4)	39.5 (0.5)	2.6 (0.1)	0	99.9
1 wk EDS (1)	32.4 (0.5)	0	34.4 (0.5)	30.1 (0.7)	2.2 (0.2)	0.9 (0.1)	100
1 wk EDS (2)	37.0 (0.6)	4.6 (0.5)	31.5 (0.6)	25.3 (0.7)	1.7 (0.2)	0	100.1
2 wk EDS	31.8 (0.4)	14.0 (0.5)	28.4 (0.4)	24.2 (0.5)	1.7 (0.1)	0	100.1

Table 5.1 HR-TEM EDS data for EDS spot measurements made on a selection of the reflux products. Positions of spot analyses are shown on Figure 3. Numbers in the parentheses below the measured values are the errors on each measurement.

5.3.1.3 Physiochemical characterization

The absolute measurements of Ni wt% in the c-disordered birnessite, 10 Å phyllomanganate intermediate and all subsequent reflux products are presented in Table 5.2. Surface area measurement for the 10 Å phyllomanganate intermediate and all subsequent reflux products, and the corresponding concentrations of Ni and Mn in the reaction solution are presented in Table 5.3 and Figure 5.4. pH measurements of the reaction solutions are also presented in Table 5.3. The absolute concentration of Ni associated with the solid phase shows little variation from the c-disordered birnessite precursor to the 10 Å phyllomanganate intermediate, and subsequently over the first 72 hr of reflux, with the c-disordered birnessite containing 0.92±0.002 wt% Ni and the 72 hr reflux sample containing 0.98±0.010 wt% Ni (Table 5.2). By 1 wk reflux the concentration of Ni associated with the solid phase drops to 0.80±0.011 wt% Ni and by 2 wk reflux there is a pronounced drop to 0.45±0.001 wt% Ni (Table 5.2). By 4 wk reflux the final todorokite product contains 0.54±0.003 wt% Ni. Overall

there is a ~50 % reduction in the concentration of Ni sequestered to the solid product over the duration of 4 wk reflux (Table 5.2).

The N_2 BET surface area of the 10 Å phyllomanganate is 102.3 m^2/g, which is highly comparable to previous work for the measured surface area of Ni-free 10 Å phyllomanganate (e.g. Villalobos et al., 2003). At 3 hr reflux there is a reduction in surface area to 84 m^2/g, which then shows little variation during the first 12 hr, with all measured values falling within the 5 % error range of the technique. At 24 hr reflux surface area is 97 m^2/g, peaking at 48 hr reflux at 99 m^2/g. A second and more substantial drop in surface area to ~37 m^2/g occurs by 1 wk reflux. The surface area then continues to decrease to 28 m^2/g by 2 wk reflux and 20 m^2/g by the full 4 wk reflux. Overall an ~80 % reduction in surface area is observed over the duration of the 4 wk reflux (Fig. 5.3). The observed overall decrease in surface area is highly comparable to the trends observed during the transformation of a Ni-free 10 Å phyllomanganate, and is consistent with an increase in particle size due to the formation and growth of large todorokite laths and plates, via the orientated attachment of considerably smaller todorokite primary particles.

Sample	**wt% Ni[a]**
c-disordered birnessite	0.92±0.002
10Å phyllomanganate	1.03±0.005
3hr reflux	0.96±0.007
6hr reflux	1.07±0.010
12hr reflux	1.00±0.004
24hr reflux	1.04±0.003
48hr reflux	0.99±0.009
72hr reflux	0.98±0.010
1wk reflux	0.80±0.011
2wk reflux	0.45±0.001
4wk reflux	0.54±0.003

Table 5.2 Total wt% Ni in solid samples. [a] error is standard deviation of 3 measurements made on separate sample aliquots

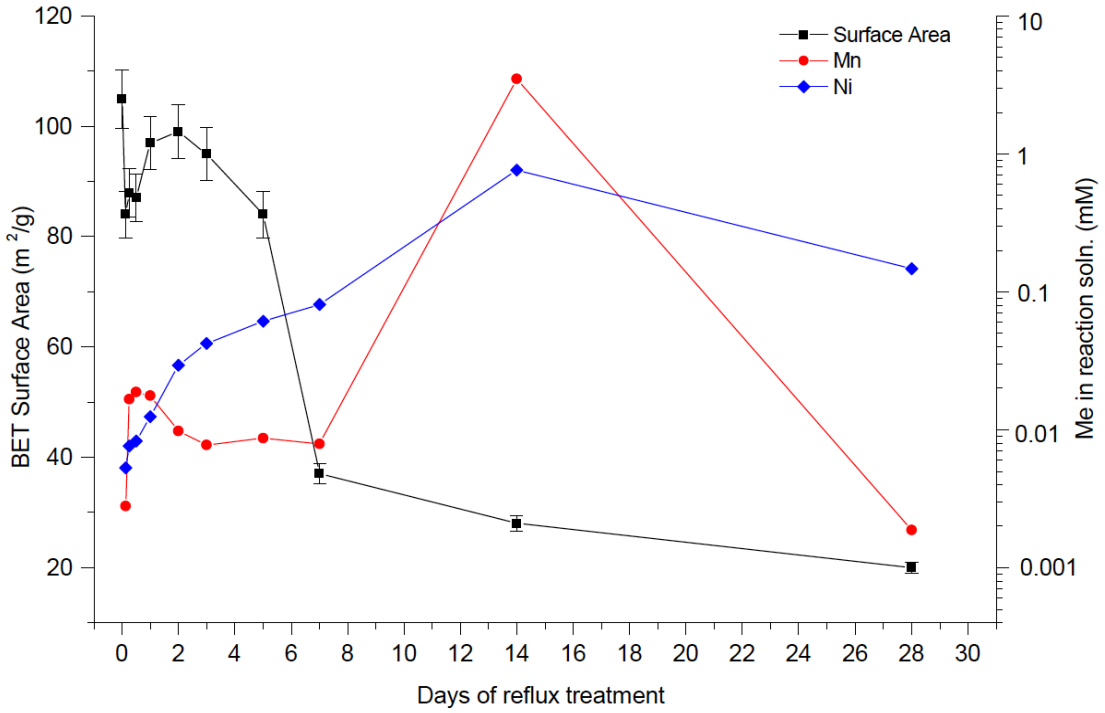

Figure 5.3. Surface area of the solid reflux products and the [Ni] and [Mn] in the reflux solution as a function of reflux time. The first surface area measurement shown on the plot is the Ni-sorbed 10 Å phyllomanganate intermediate at 0 hr reflux; measurements of Ni and Mn in the reaction solution start at 3 hr reflux. For exact values see Table 5.3.

The dissolved concentrations of Mn and Ni in the reaction solution at 3 hr reflux are 0.003 mM and 0.004 mM, respectively (Table 5.3, Fig. 5.3). At 6 hr reflux there is a relatively sharp increase in $[Mn]_{soln}$ to 0.017 mM, which then remains fairly consistent between 6 hr and 24 hr, after which there is a decrease in $[Mn]_{soln.}$ to 0.010 mM at 48 hr reflux, which again then remains approximately consistent between 48 hr and 1 wk reflux. Up to and including 1 wk reflux, $[Ni]_{soln}$ shows a substantial but relatively steady increase from 0.006 mM at 6 hr reflux to 0.054 mM at 1 wk reflux. By 2 wk reflux there is a notable release of Mn (3.5 mM) and Ni (0.4 mM) into the reaction solution (Table 5.3, Fig. 5.3). After 2 wk reflux there is a large decrease in $[Mn]_{soln}$, with $[Mn]_{soln}$ at 4 wk reflux comparable to that at 3 hr reflux (0.002 mM), while for $[Ni]_{soln}$ there is a less pronounced decrease to 0.093 mM at 4 wk reflux.

pH measurements of the cooled reaction solution show a slight increase in solution pH from ~5.29 to 5.93 over the first 72 hr of reflux. The pH of the reaction solution subsequently remains relatively stable until a more substantial drop in pH occurs from pH ~5.81 to ~4.84 at 1 wk reflux and then from pH ~4.84 to ~4.26 at 4 wk reflux (Table 5.3).

Sample	Surface Area[a] (m^2/g)	Ni (mM)[b]	Mn (mM)[b]	pH[c]
0	102	N/A	N/A	N/A
3 hr	84	$0.004 \pm 8.1 \times 10^{-5}$	$0.003 \pm 3.8 \times 10^{-5}$	5.29
6 hr	88	$0.006 \pm 5.2 \times 10^{-4}$	$0.017 \pm 4.2 \times 10^{-4}$	5.47
12 hr	87	$0.007 \pm 8.1 \times 10^{-4}$	$0.019 \pm 6.5 \times 10^{-4}$	5.49
24 hr	97	$0.010 \pm 2.2 \times 10^{-4}$	$0.018 \pm 3.3 \times 10^{-4}$	5.56
48 hr	99	$0.021 \pm 3.9 \times 10^{-4}$	$0.010 \pm 3.2 \times 10^{-4}$	5.93
72 hr	95	$0.030 \pm 5.7 \times 10^{-4}$	$0.008 \pm 2.1 \times 10^{-4}$	5.95
5 day	84	$0.042 \pm 9.6 \times 10^{-4}$	$0.009 \pm 3.3 \times 10^{-4}$	5.82
1 wk	37	$0.054 \pm 1.1 \times 10^{-3}$	$0.008 \pm 1.9 \times 10^{-4}$	5.81
2 wk	28	$0.414 \pm 6.8 \times 10^{-3}$	$3.508 \pm 1.2 \times 10^{-2}$	4.84
4 wk	20	$0.093 \pm 3.8 \times 10^{-4}$	$0.002 \pm 5.6 \times 10^{-3}$	4.26

Table 5.3. Specific surface area of the solid products, and Ni and Mn concentrations and pH of the reflux solutions for the 10 Å phyllomanganate intermediate (time 0) and all subsequent reflux products. [a]All surface area measurements are ±5%. [b]All reported errors are the standard deviation as determined from triplicate measurements. [c]All pH measurements are ± 0.05 pH units.

5.3.1.4 Ni K-edge X-ray absorption spectra of the reference compounds

Ni K-edge EXAFS and Fourier transforms of the EXAFS for the reference compounds are shown in Figure 5.4 and EXAFS fits are summarized in Table 5.4. Visual inspection of the Ni-sorbed c-disordered birnessite and Ni-incorporated natural poorly crystalline birnessite reference spectra indicate that the Ni local coordination environment is very similar to that found previously for Ni sorbed to hexagonal birnessite, where Ni is located above Mn octahedral vacancy sites present in the phyllomanganate layers (Peacock and Sherman, 2007a,b; Peacock, 2009; Pena; Manceau), and Ni-rich marine ferromanganese precipitates were Ni is found entirely structurally incorporated into the phyllomanganate layers, by filling vacancy sites and/or isomorphically substituting for Mn present in the mineral lattice (Peacock and Sherman, 2007a,b; Peacock, 2009). In agreement with this previous work, the best fits to the Ni-sorbed and Ni-incorporated reference spectra are provided by optimization of the model clusters representing Ni-sorbed above vacancy sites and Ni-incorporated into the phyllomanganate layers, respectively (Fig. 5.5, Table 5.4).

In contrast to Ni sorbed on and incorporated into birnessite, there has been very little work to determine the crystal-chemical mechanism of Ni uptake by todorokite. Theoretically, trace metals could sorb to todorokite via outer-sphere surface complexation, where Ni might be located in the todorokite tunnels (e.g., Pakarinen et al., 2010), or via inner-sphere surface complexation, where Ni could adsorb to Mn(OH) sites present at the edges of the triple chains that form the todorokite framework, akin to Ni adsorption on triclinic birnessite in which there are no Mn octahedral vacancy sites (Peacock and Sherman, 2007a) and at high Ni loading on hexagonal birnessite when the vacancy sites are saturated (Manceau et al., 2007a). Sorbed as an outer-sphere complex, the Ni-sorbed todorokite EXAFS spectrum would resemble that of Ni^{2+}(aq) where Ni is surrounded by 6 O at ~2.04±0.02 Å. Adsorbed at the Mn(OH) sites, the Ni-sorbed todorokite spectrum would likely reflect Ni adsorbed as a tridentate corner-sharing complex, as per Ni adsorbed on triclinic birnessite with 2 Mn at ~3.05±0.05 Å (Peacock and Sherman, 2007a).

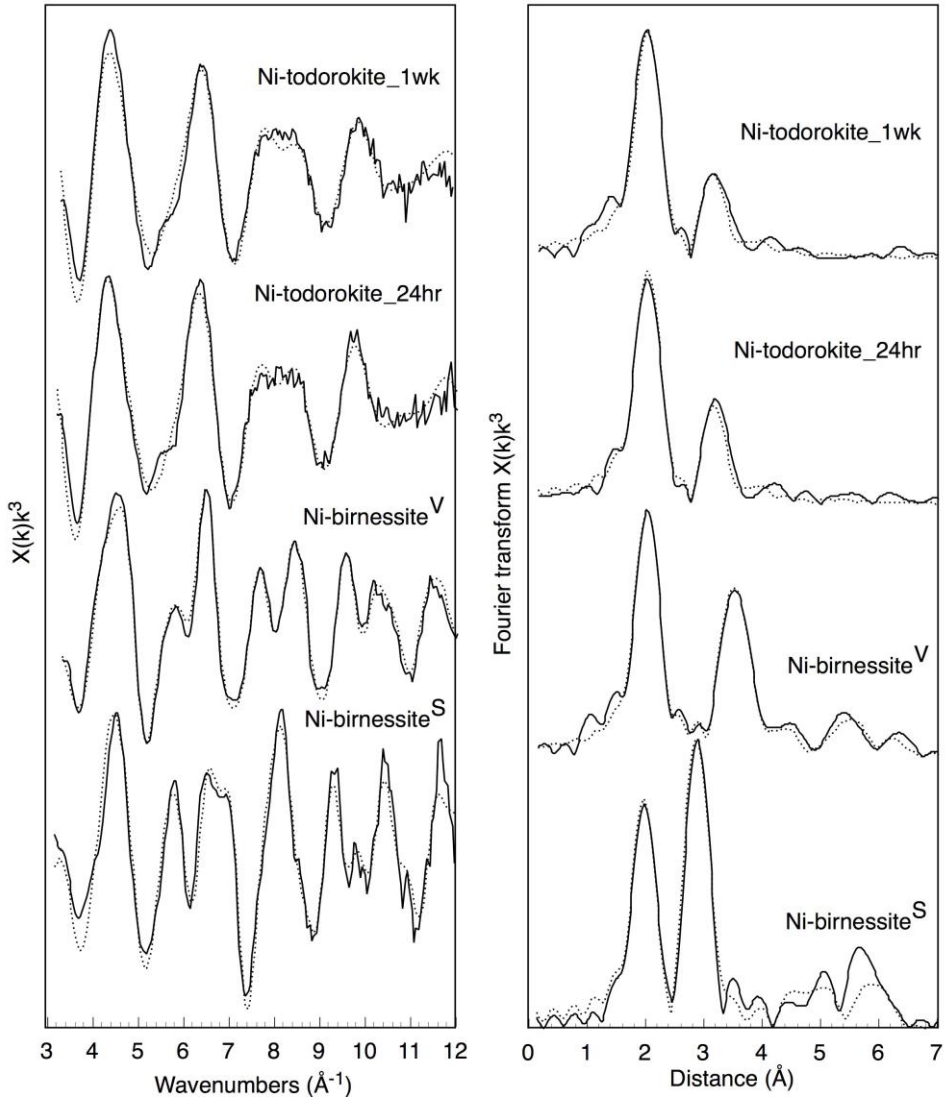

Figure 5.4. Ni K-edge EXAFS and the corresponding Fourier transforms of the EXAFS for the reference compounds. Ni-birnessite^{S} is a Ni-incorporated natural poorly crystalline birnessite; Ni-birnessite^{V} is a synthetic c-disordered birnessite with Ni sorbed above the Mn octahedral vacancy sites, Ni-todorokite_24hr and Ni-todorokite_1wk are synthetic todorokite samples equilibrated at pH 8 with 15 ppm $[Ni]_{total}$ in 0.1 M NaCl for 24 hrs and 1 week respectively. Solid lines are data, dotted lines are fits.

To my knowledge, there are currently no EXAFS spectra for Ni structurally incorporated into todorokite, but Ni is expected to exclusively occupy the Mn sites at the edges of the triple chains (Post and Bish, 1988; Post et al., 2003; Bodeï et al., 2007), which would yield an Ni coordination environment consisting of 6 O at ~2.04 Å,

4 edge-sharing Mn at ~2.87 – 2.91 Å and 4 corner-sharing Mn at ~3.48 – 3.50 Å (Bodeï et al., 2007). Visual inspection of the todorokite sorption spectra at 24 hr and 1 wk contact time show the Ni local coordination environment is very similar in both spectra and most similar to Ni adsorbed on triclinic birnessite where Ni forms tridentate corner-sharing surface complexes (Peacock and Sherman, 2007a). Accordingly the best fits to these spectra are provided by the cluster representing Ni tridentate corner-sharing to Mn(OH) sites present at the edges of the todorokite triple chains, with 6 O at ~2.00 – 2.11 Å and 2 Mn at ~2.98 – 3.10 Å. It should be noted that the fits were improved (from reduced Chi^2 ~18 to ~15, Table 5.4) by allowing a slight distortion of the Ni octahedron, evident as a very minor deviation of the spherical coordinates of the surface binding O atoms from exact octahedral coordination (O_1, O_4 and O_6, Table 5.4). The fits could not be improved by including any other Ni coordination environments.

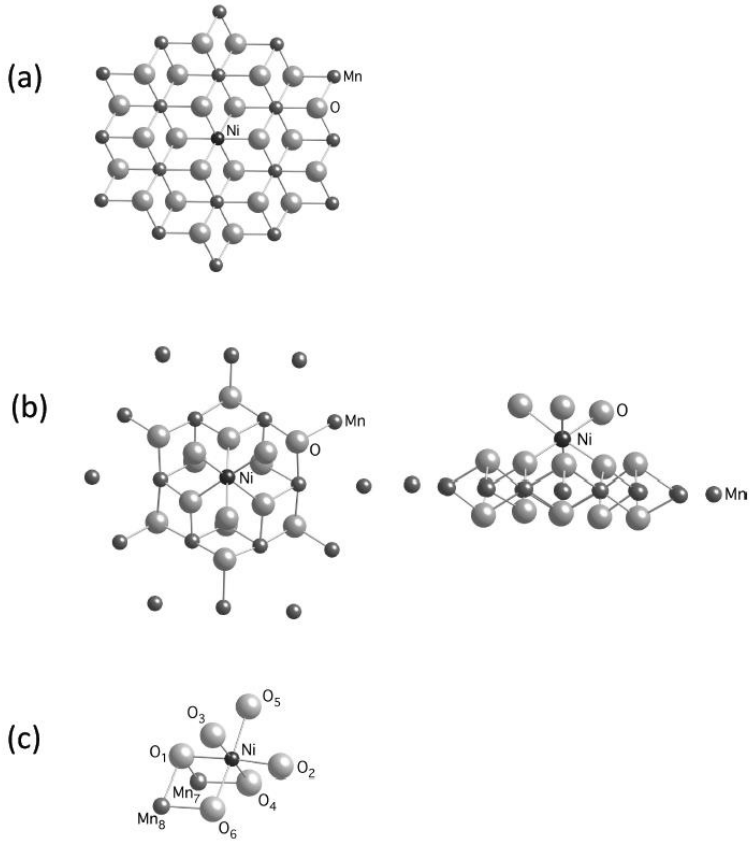

Figure 5.5. Molecular clusters used to model EXAFS spectra of (a) Ni surface adsorbed above Mn octahedral vacancy sites present in the layers of a hexagonal phyllomanganate, (b) Ni structurally incorporated into the layers of a phyllomanganate, and (c) Ni surface sorbed to todorokite as a tridentate corner-sharing complex.

Shell	*N*	*R* (Å)	2σ² (Å²)	*θ*	*φ*	EF	R (%)	Reduced Chi²
Ni-structurally incorporated natural birnessite (Ni-birnessite^{S})								
Ni_0	*1*	0	0	*0*	*0*	1.43	18.1	17.6
O_1	*3*	2.01	0.012	*47*	*0*			
O_2	*3*	2.04	0.011	*136*	*180*			
Mn_3	*3*	2.88	0.012	*90*	*270*			
Mn_4	*3*	2.85	0.013	*90*	*90*			
Mn_5	*3*	5.94	0.006	*90*	*270*			
Mn_6	*3*	4.94	0.01	*90*	*180*			
Mn_7	*3*	5.05	0.012	*90*	*0*			
Mn_8	*3*	5.9	0.005	*90*	*90*			
O_9	*3*	3.33	0.016	*105*	*0*			
O_{10}	*3*	3.58	0.009	*75*	*180*			
O_{11}	*3*	4.47	0.006	*75*	*100*			
O_{12}	*3*	4.45	0.009	*105*	*45*			
O_{13}	*3*	4.51	0.004	*100*	*80*			
O_{14}	*3*	4.65	0.011	*75*	*135*			
Ni-sorbed c-disordered birnessite (Ni-birnessite^{V})								
Ni_0	*1*	0	0	*0*	*0*	3.45	13.9	10.4
O_1	*3*	2.08	0.011	*60*	*270*			
O_2	*3*	2.01	0.01	*120*	*90*			
O_3	*3*	3.26	0.004	*150*	*270*			
Mn_4	*3*	3.53	0.005	*125*	*0*			
Mn_5	*3*	3.42	0.004	*126*	*180*			
O_6	*3*	4.35	0.004	*136*	*90*			
O_7	*3*	3.61	0.005	*110*	*270*			
Mn_8	*3*	5.38	0.004	*110*	*90*			
Mn_9	*3*	5.54	0.005	*110*	*270*			
Mn_{10}	*3*	6.01	0.004	*110*	*0*			
Mn_{11}	*3*	5.82	0.004	*110*	*180*			
Ni-sorbed todorokite 24 hr (Ni-todorokite_24hr)								
Ni_0	*1*	0	0	*0*	*0*	-1.15	19.6	14.6
O_1	*1*	2.05	0.01	94	358			
O_2	*1*	2	0.011	*90*	*180*			
O_3	*1*	2.06	0.012	*90*	*90*			
O_4	*1*	2.06	0.01	*90*	272			
O_5	*1*	2.1	0.007	*0*	*0*			
O_6	*1*	2.03	0.007	176	*0*			
Mn_7	*1*	3	0.012	*90*	*315*			
Mn_8	*1*	3.1	0.009	*135*	*0*			
Ni-sorbed todorokite 1 wk (Ni-todorokite_1wk)								
Ni_0	*1*	0	0	*0*	*0*	0.68	20.4	15.8
O_1	*1*	2.05	0.01	94	358			
O_2	*1*	2	0.011	*90*	*180*			
O_3	*1*	2.06	0.013	*90*	*90*			
O_4	*1*	2.06	0.011	*90*	272			
O_5	*1*	2.11	0.007	*0*	*0*			
O_6	*1*	2.03	0.008	176	*0*			
Mn_7	*1*	2.98	0.011	*90*	*315*			
Mn_8	*1*	3.1	0.007	*135*	*0*			

Table 5.4. EXAFS fits for Ni sorbed and incorporated reference compounds, fit by refinement of a single model cluster. Where *N* is the number of atoms in a shell. *R*, *θ* and *φ* are the Interatomic distance and spherical coordinates of the prototype atom in each shell with either C_1 or C_3 symmetry. $2\sigma^2$ is the Debye–Waller factor. EF is the correction to the Fermi energy value assigned in ATHENA. Values in italics were held constant during refinement.

5.3.1.5 Ni K-edge X-ray absorption spectra of the experimental samples

Ni K-edge EXAFS and Fourier transforms of the EXAFS for the experimental samples are shown in Figure 5.6 and EXAFS fits are summarized in Tables 5.5. and 5.6. Spectra for the birnessite precursor and 10 Å phyllomanganate intermediate are visually very similar to those in previous work where Ni is sorbed in two distinct coordination environments, namely, adsorbed as a surface complex above Mn octahedral vacancy sites and also structurally incorporated into the phyllomanganate layers (Peacock and Sherman, 2007a; Peacock, 2009). When Ni is present as a structurally incorporated species in addition to a vacancy site adsorbed complex, the spectral shape of the characteristic *k*-space features for Ni adsorbed at vacancy sites, at ~6 and 8 $Å^{-1}$ (see the Ni-sorbed c-disordered reference spectrum (Fig. 5.4)), are modified towards the shape of these features for Ni incorporated into the phyllomanganate layers (see the Ni-incorporated natural phyllomanganate reference spectrum (Fig. 5.4)). Specifically, the feature at ~6 $Å^{-1}$ deepens to produce a clear splitting of the ~5.5 – 7 $Å^{-1}$ oscillation, while the feature at ~8 $Å^{-1}$ shoals resulting in a single peak for the ~7.5 – 9 $Å^{-1}$ oscillation, both as a function of the amount of structurally incorporated Ni (Peacock, 2009).

The presence of Ni as both vacancy site surface complexes and structurally incorporated species is manifest in the Fourier transform as two next-nearest Mn neighbour distances represented by peaks at ~3.5 and 2.9 Å, respectively, whose relative amplitudes reflect the proportion of the total Ni occupying vacancy sites vs. structurally incorporated positions (Peacock, 2009). Accordingly, the best fits to the birnessite precursor and 10 Å phyllomanganate intermediate spectra are provided by a linear combination of the Ni-sorbed c-disordered birnessite and Ni-incorporated natural phyllomanganate reference spectra (Fig. 5.4, Table 5.5). Specifically, the birnessite precursor is found to contain ~54±4 % Ni adsorbed above vacancy sites and ~46±4 % Ni structurally incorporated, while the 10 Å phyllomanganate intermediate contains ~38±4 % Ni at vacancy sites and ~62±4 % Ni incorporated. The increase in the proportion of structurally incorporated Ni from the birnessite precursor to the 10 Å phyllomanganate intermediate is consistent with the observed increase in long range order between our precursor an intermediate phases (Fig. 5.1). Partial dissolution-recrystallization during the Mg ion exchange process is likely to favor some structural incorporation of surface adsorbed species.

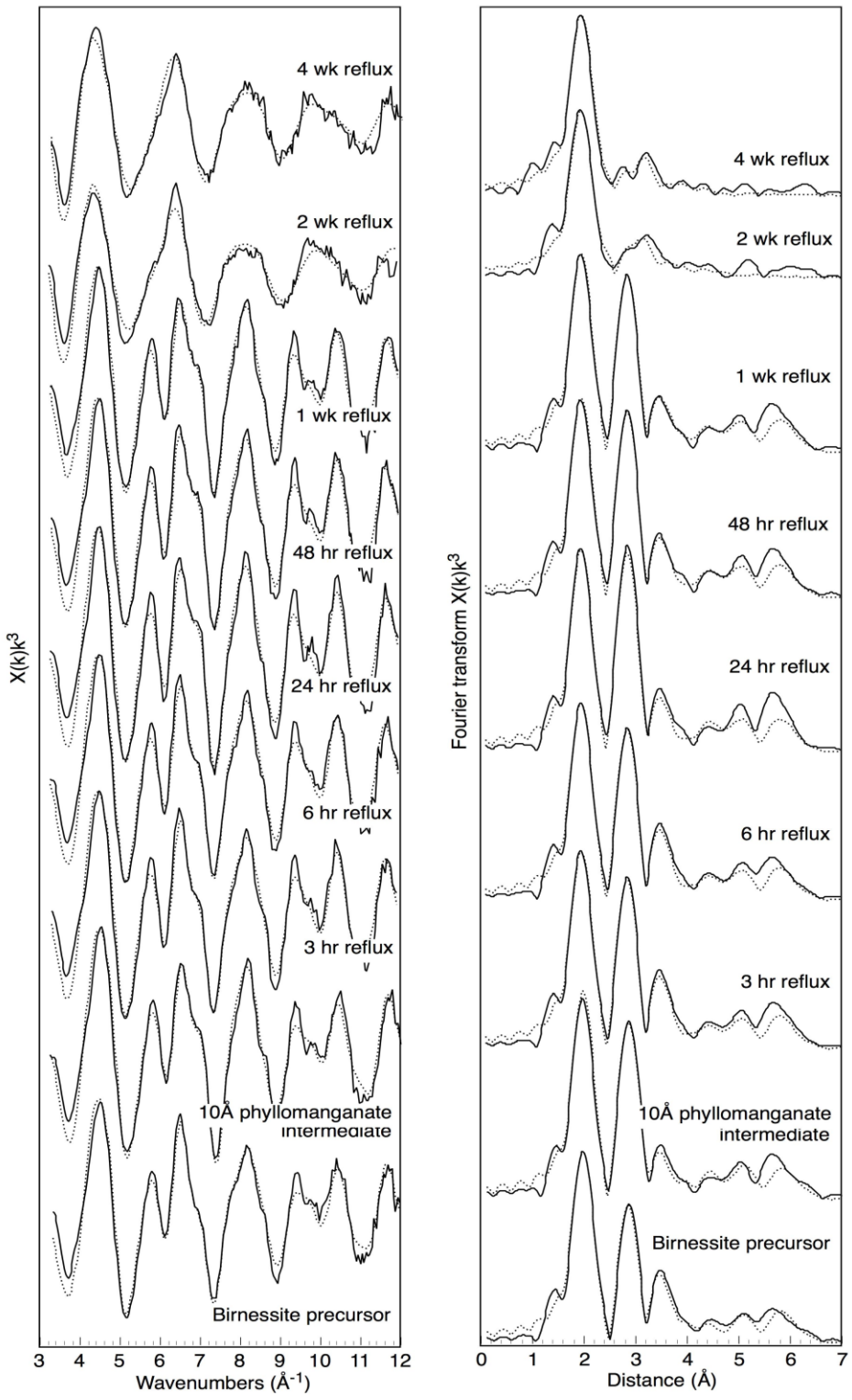

Figure 5.6. Ni K-edge EXAFS and Fourier transforms of the EXAFS for the experimental samples including Ni-sorbed c-disordered birnessite precursor, Ni-sorbed 10 Å phyllomanganate intermediate and subsequent reflux products at 3 hr, 6 hr, 24 hr, 48 hr, 1 week, 2 week and 4 week. Solid lines are data and dotted lines are fits.

The reflux spectra are visually very similar to the birnessite precursor and 10 Å phyllomanganate intermediate, and remarkably similar to each other up to and including 1 wk reflux (Fig. 5.6). In the first instance, these observations indicate that the Ni local coordination environment in the reflux samples is likely similar to that in the precursor and intermediate samples, and that this environment does not significantly change throughout the reflux to 1 wk. In particular, these reflux spectra do not resemble the reference spectra for Ni-sorbed todorokite (Fig. 5.4). Neither is there any indication that a significant proportion of the Ni has become structurally incorporated into the neo-forming todorokite. In this latter scenario, one would expect a change in the amplitude of the characteristic spectral features resulting from edge- and corner-sharing Mn. Specifically, if a significant proportion of the Ni originally associated with the 10 Å phyllomanganate was incorporated into the neo-forming todorokite then the amplitude of the spectral features at ~6 and 8 $Å^{-1}$ in *k*-space, which manifest as Ni-Mn distances at ~2.9 and 3.5 Å in *R*-space, should change somewhat to reflect the fact that the local coordination environment of the Ni now includes 6 Mn at ~2.9 Å and 2 Mn at ~3.5 Å, as expected for Ni coprecipitated with a phyllomanganate, and also 4 Mn at ~2.9 Å and 4 Mn at ~3.5 Å, as expected for Ni incorporated into todorokite (Bodeï et al., 2007). While this change in the Ni local coordination environment would not produce significant changes in the expected Ni-Mn interatomic distances, and the absolute changes in the number of Mn next-nearest neighbours would be difficult to resolve, the fact that the amplitude of these key spectral features, and in fact the entire spectral signature, remains so remarkably consistent from 3 hr to 1 wk reflux is a strong indication that Ni remains sequestered by the 10 Å phyllomanganate intermediate as the reflux proceeds, despite the fact that XRD (Fig. 5.1) and TEM (Fig. 5.2) data show that a significant amount of neo-formed todorokite is present in the sample matrix by 48 hr reflux.

In agreement with these observations, the best fits to the spectra for 3 hr to 1 wk reflux are provided by a linear combination of the Ni-sorbed c-disordered birnessite and Ni-incorporated natural phyllomanganate reference spectra, as per the birnessite precursor and 10 Å phyllomanganate intermediate samples (Fig. 5.4, Table 5.4). Specifically, the total Ni sorbed, ~40 % is adsorbed above the vacancy sites with ~60 % structurally incorporated, with no significant change in these proportions when comparing the reflux samples to the 10 Å phyllomanganate intermediate, or each other.

The 2 wk and 4 wk reflux spectra are visually very different to the birnessite precursor, 10 Å phyllomanganate intermediate and the reflux spectra up to and including 1 wk (Fig. 5.6).

In contrast to the previous reflux samples, these spectra are visually similar to the reference spectra for Ni-sorbed todorokite (Fig. 5.4), where Ni is found in tridentate corner-sharing configuration, with 6 O at ~2.00 – 2.11 Å and 2 Mn at ~2.98 – 3.10 Å. There is no obvious visual evidence for Ni-Mn edge- or corner-sharing distances at ~2.9 Å or ~3.5 Å indicative of Ni structurally incorporated into a phyllomanganate (~2.9 Å), adsorbed above vacancy sites on a phyllomanganate (~3.5 Å), or structurally incorporated into todorokite (~2.9 and 3.5 Å). Accordingly the best fits to these spectra are provided by the molecular cluster representing Ni tridentate corner-sharing surface complexes with 6 O at ~1.98 – 2.10 Å and 2 Mn at ~2.94 – 3.11 Å. The fits could not be improved by including any other Ni coordination environments. Because the Mn(OH) sites present at the edges of the todorokite triple chains and those at the edges of a phyllomanganate layer essentially provide the same local coordination environment for sorbed trace metals, the presence of Ni tridentate corner-sharing configuration could indicate that Ni is newly associated with the neo-formed todorokite or in fact still associated with the 10 Å phyllomanganate intermediate, albeit via a different sorption mechanism compared to the previous reflux samples. However, the fact that no 10 Å phyllomanganate intermediate is detected in the 2 wk reflux samples (TEM, Fig. 5.2i, j) indicates that the solid-associated Ni at 2 wk and 4 wk reflux is most likely sorbed to neo-formed todorokite.

Sample	**EF**	***N* Ni^S**	***N* Ni^V**	**R (%)**	**Reduced Chi^2**
Birnessite precursor	3.46	0.46±0.04	0.54±0.04	23.3	2.9
10Å phyllomanganate intermediate	0.51	0.62±0.04	0.38±0.04	21.3	2.2
3 hr reflux	2.43	0.58±0.04	0.42±0.04	22.5	2.6
6 hr reflux	1.81	0.59±0.04	0.41±0.04	21.5	2.2
12 hr reflux	0.62	0.62±0.04	0.39±0.04	21.6	2.1
24 hr reflux	2.13	0.70±0.05	0.30±0.05	24.4	2.7
48 hr reflux	2.21	0.65±0.04	0.35±0.04	23.5	2.7
72 hr reflux	1.80	0.61±0.04	0.39±0.04	23.4	2.5
5 day reflux	0.83	0.59±0.04	0.41±0.04	22.1	2.2
1 wk reflux	1.44	0.62±0.04	0.38±0.04	23.3	2.5

Table 5.5. EXAFS fits for the birnessite precursor, 10 Å phyllomanganate intermediate and all reflux products up to 1 wk, fit by linear combination of reference spectra. EF is the correction to the Fermi energy value assigned in ATHENA. *N* NiS is the number of Ni atoms (Ni site occupancy) for reference spectrum Ni-structurally incorporated natural birnessite (Ni-birnessite^S). *N* Ni^V is the number of Ni atoms (Ni site occupancy) for reference spectrum Ni-sorbed c-disordered birnessite (Ni-birnessite^V). In the linear combination analysis, *N* Ni^S + *N* Ni^V was constrained to equal 1.

Shell	***N***	***R* (Å)**	**2σ^2 (Å^2)**	***θ***	***φ***	**EF**	**R (%)**	**Reduced Chi^2**
2 wk reflux								
Ni_0	*1.0*	0.00	0.000	*0*	*0*	0.10	20.1	13.5
O_1	*1.0*	1.98	0.005	*94*	*358*			
O_2	*1.0*	2.06	0.011	*90*	*180*			
O_3	*1.0*	2.10	0.012	*90*	*90*			
O_4	*1.0*	2.09	0.011	*90*	*272*			
O_5	*1.0*	2.04	0.011	*0*	*0*			
O_6	*1.0*	2.05	0.007	*176*	*0*			
Mn_7	*1.0*	2.95	0.011	*90*	*315*			
Mn_8	*1.0*	3.11	0.009	*135*	*0*			
4 wk reflux								
Ni_0	*1.0*	0.00	0.000	*0*	*0*	2.15	13.7	8.1
O_1	*1.0*	1.98	0.005	*94*	*358*			
O_2	*1.0*	2.06	0.012	*90*	*180*			
O_3	*1.0*	2.05	0.013	*90*	*90*			
O_4	*1.0*	2.10	0.012	*90*	*272*			
O_5	*1.0*	2.06	0.012	*0*	*0*			
O_6	*1.0*	2.05	0.007	*176*	*0*			
Mn_7	*1.0*	2.94	0.013	*90*	*315*			
Mn_8	*1.0*	3.11	0.008	*135*	*0*			

Table 5.6. EXAFS fits for the samples after 2 wk and 4 wk reflux. Samples fit by refinement of a single model cluster. *N* is the number of atoms in a shell. *R*, *θ* and *φ* are the interatomic distance and spherical coordinates of the prototype atom in each shell with either C_1 or C_3 symmetry. $2\sigma^2$ is the Debye–Waller factor. EF is the correction to the Fermi energy value assigned in ATHENA. Values in italics were held constant during refinement.

5.3.2 Natural Ferromanganese Samples

5.3.2.1 Bulk XRD

Bulk XRD patterns for the hydrogenetic ferromanganese crust, diagenetic ferromanganese nodule and hydrothermal ferromanganese precipitate are presented below in Figure 5.7.

The Mn mineralogy of the hydrogenetic crust (Fig 5.7,a) and diagenetic nodule (Fig 5.7,b) is dominated by very poorly crystalline phyllomanganates, usually termed vernadite in natural samples (JCPDS-15-604) and δMnO_2 in synthetic analogues. In this phase the phyllomanganate sheets are turbostratic and thus the XRD peaks at ~10 Å [001] and ~5 Å [002] for 10 Å phyllomanganate (buserite), and ~7 Å and ~3.5 Å for 7 Å phyllomanganate (birnessite), are very weak or absent, and only broad *hk0* reflections (or *hk* bands) at ~2.4 Å [100] and ~1.4 Å [110] are clearly evident. In both samples extremely weak and broad peaks at ~9.8 Å and ~4.8 Å are indexed as the [001] and [002] reflections of 10 Å phyllomanganate (buserite JCPDS-32-1128). The presence of very poorly crystalline phyllomanganate in the hydrogenetic and diagenetic ferromanganese samples agrees with previous reports for these ferromanganese precipitate genetic types (e.g., Peacock and Sherman, 2007b). In particular, the presence of poorly crystalline 10 Å phyllomanganate in diagenetic ferromanganese precipitates is often reported in natural samples, where it is thought to have formed during mild dissolution-recrystallization of poorly crystalline 7 Å phyllomanganate (e.g., Bodeï et al., 2007).

In both the hydrogenetic and diagenetic samples the ~2.5 Å peak exhibits a slight degree of asymmetry on the high-angle side. As discussed previously, this feature is common to phyllomanganate phases that lack significant periodic ordering of the phyllomanganate sheets (e.g. Villalobos et al., 2006; Manceau et al., 2007b). In addition, the *d*100/*d*110 peak intensity ratios for both the hydrogenetic and diagenetic samples approximately equal $\sqrt{3}$ indicating that the phyllomanganate layers have hexagonal symmetry with $a = b = 2.83$ Å (Drits et al., 1997). Other much sharper diffraction peaks in the hydrogenetic sample are identified as hydroxyapatite ($Ca_5(PO_4)_3(OH)$) (based on JCPDS-9-0432) (Fig. 5.7a), while sharp peaks at ~4.25, ~3.35, ~2.28, ~1.81 and ~1.67 Å in the diagenetic sample are identified as a crystalline quartz phase (based on JCPDS-46-1045) (Fig. 5.7b).

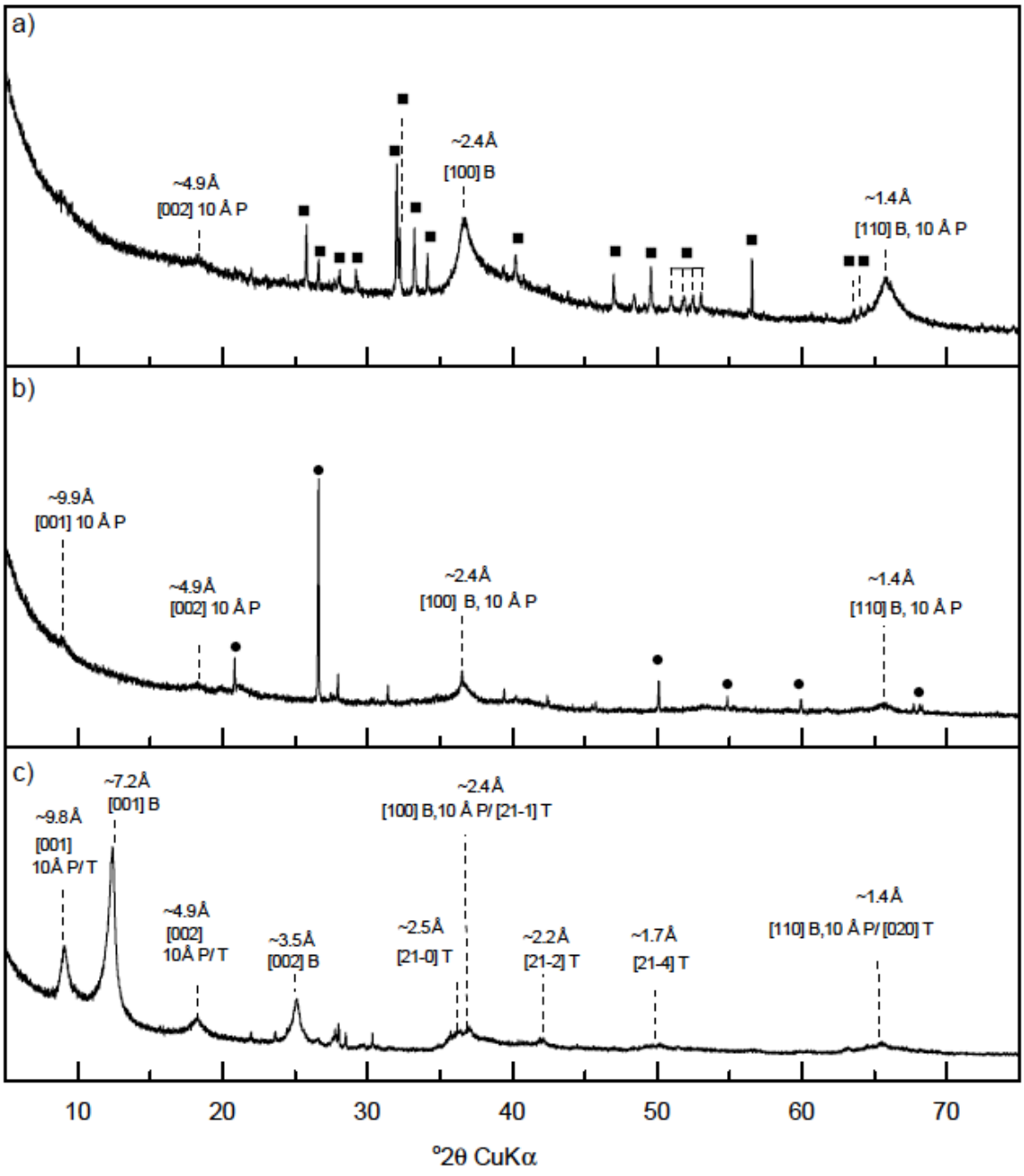

Figure 5.7 Bulk powder X-ray diffraction patterns for (a) the hydrogenetic ferromanganese crust collected from the Pacific ocean (b) the diagenetic ferromanganese nodule from the Pacific Ocean and (c) the hydrothermal marine precipitate, collected from the Lau Basin. X- ray diffraction peaks are labelled for phyllomanganate (P) and todorokite (T) (based on JCPDS-15-604 for vernadite, Drits et al., 1997 for turbostratic birnessite, JCPDS-32-1128 for buserite and JCPDS-38-475 for todorokite). The ■ symbol denotes hydroxyapatite ($Ca_5(PO_4)_3(OH)$), while the ● symbol denotes quartz (identification of the peaks are based on JCPDS cards 9-0432 and 46-1045, respectively).

The hydrothermal sample consists of mixed 7 and 10 Å phyllomanganate and todorokite phases. Specifically, XRD peaks are evident at ~7.2 Å [001] and 3.5 Å [002], belonging to 7 Å phyllomanganate (for reference pattern see turbostratic birnessite, Drits et al., 1997), and ~9.8 Å [001] and ~4.8 Å [002], belonging to 10 Å phyllomanganate (buserite JCPDS-32-1128), but in addition, characteristic todorokite peaks at ~2.2 Å [21-2] and ~1.7 Å [21-4] are also present. It should be noted that the peak region at ~2.4 Å is split resulting in a peak at ~2.5 Å, as expected when 10 Å phyllomanganate and todorokite are mixed (i.e. as reported in chapter 4 of this thesis). The presence of characteristic todorokite peaks and the splitting of the ~2.4 Å peak region allow the identification of todorokite despite the presence of 10 Å phyllomanganate (where the highest intensity peaks due to the [001] and [002] reflections overlap in these two phases). The relatively high intensity of the ~7.2 Å [001] and ~3.5 Å [002] peaks for 7 Å phyllomanganate (and to some extent the ~10 Å [001] and ~5 Å [002] peaks for 10 Å phyllomanganate, noting that these peaks also result from todorokite) indicates that the phyllomanganate sheets are significantly more ordered than in the hydrogenetic and diagenetic samples.

5.3.2.3 μ-XRF elemental mapping

Two-colour and tri-colour μXRF maps of the distribution of Fe (green), Mn (blue) and Ni (red) in the natural ferromanganese samples are presented in Figure 5.8, with scatter plots of the normalized fluorescence counts between Fe-Mn, Mn-Ni and Fe-Ni in Figure 5.9. The relatively pure green and blue colours of the Fe- and Mn-rich areas of the Fe-Mn maps indicate that Fe and Mn are strongly spatially segregated and anti-correlated in the scanned areas of all 3 samples (Fig. 5.8a, c, e). This spatial distribution of Fe and Mn is observed at every probed spatial scale in natural ferromanganese precipitates (e.g., Manceau et al., 2004). Pearson correlations for the Fe-Mn normalized fluorescence count plots are r = -1.5, -0.34 and 0.13 for the hydrogenetic, diagenetic and hydrothermal samples (Fig. 5.9a, d, g), respectively, supporting the observed lack of correlation.

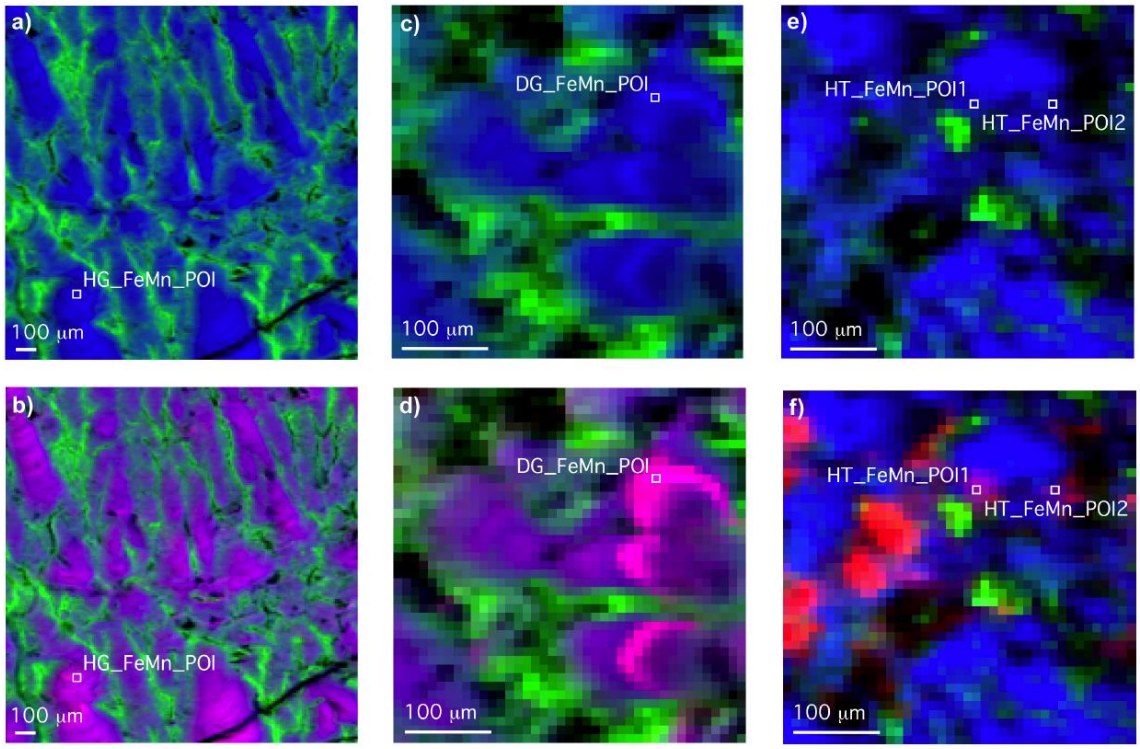

Figure 5.8. μ-XRF elemental maps showing the distribution of Mn (blue), Fe (green) and Ni (red) in (a-b) the hydrogenetic ferromanganese crust sample collected from the Pacific Ocean, (c-d) the diagenetic ferromanganese nodule from the Pacific Ocean and (e-f) the hydrothermal ferromanganese precipitate from the Lau Basin. Pixel size is 10x10 μm, and total map area for the hydrogenetic sample is 1700x1700 μm, and for the diagenetic and hydrothermal samples is 400x400 μm. Points of interest (POI) subject to μ-EXAFS analysis are also shown.

On adding Ni (red) to both the hydrogenetic and diagenetic samples, the Mn-rich areas of the samples turn to varying shades of magenta (blue + red), while those that are Fe-rich remain bright green (green + red = yellow) (Fig. 5.8b, d). This colour mixing indicates that the majority of the Ni is spatially associated and positively correlated with the Mn-rich fraction in the scanned areas. Pearson correlations for the Mn-Ni and Fe-Ni plots are r = 0.94 and -0.69 for the hydrogenetic sample (Fig. 5.9b, c) and r = 0.83 and -0.36 for the diagenetic sample (Fig. 5.9e, f), respectively, supporting the observed correlations. By contrast, on adding Ni (red) to the hydrothermal sample, there is little change in the colours of the Mn- (blue) or Fe- (green) rich areas (Fig. 5.8f). Instead, small, intense red areas appear in the center left region of the map that show little spatial correlation with either the Mn- or Fe-rich fractions. This is further reflected in the lack of correlation evident in the Mn-Ni and

Fe-Ni plots (Pearson correlations are r = -0.28 and 0.17, respectively; Fig. 5.9h,i). Therefore, in the hydrothermal ferromanganese sample, the majority of the Ni appears to be predominantly concentrated in an unidentified mineral phase.

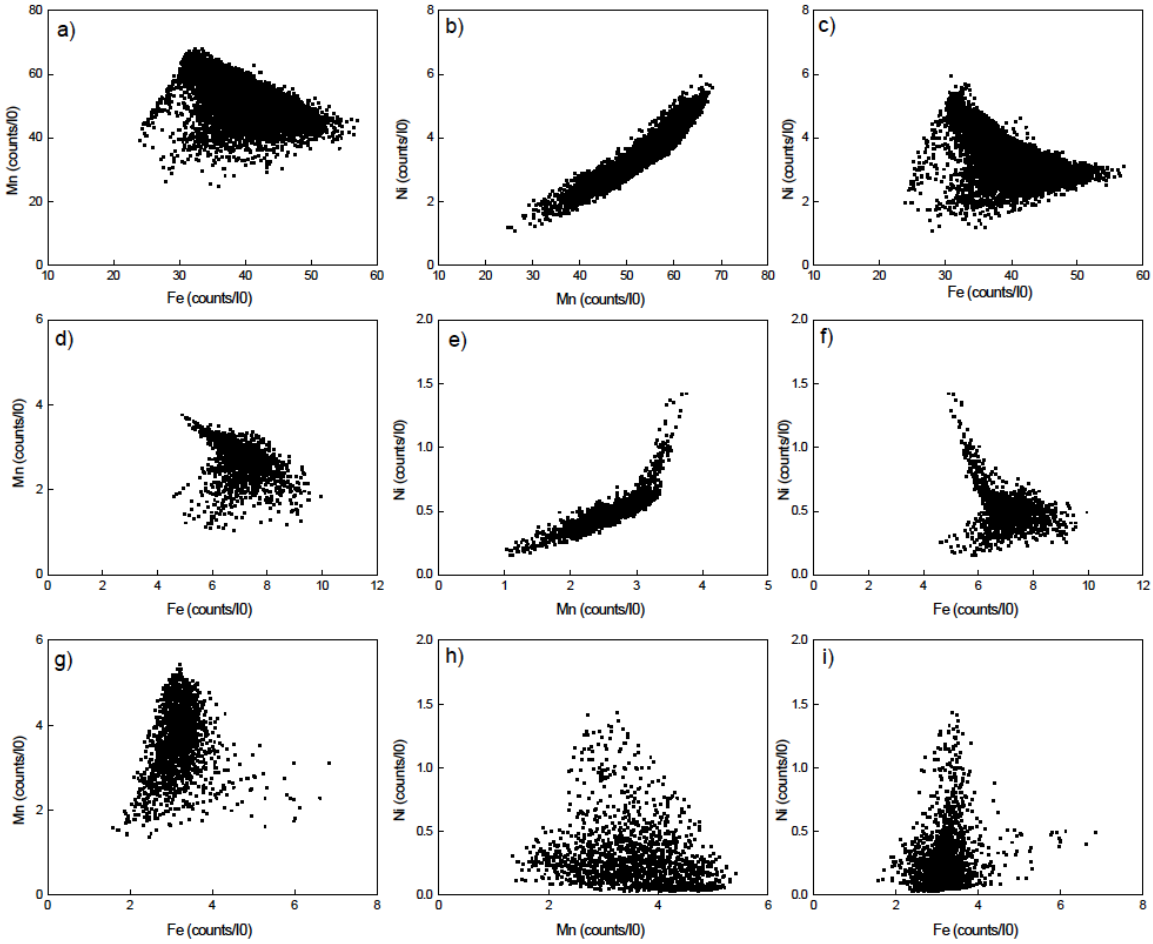

Figure 5.9. Scatter plots displaying normalized fluorescence counts between Mn-Fe, Ni-Mn, and Ni-Fe, for (a-c) the hydrogenetic ferromanganese crust sample collected from the Pacific Ocean, (d-f) the diagenetic ferromanganese nodule from the Pacific Ocean, and (g-i) the hydrothermal ferromanganese precipitate from the Lau Basin.

The µXRF maps presented in Figure 5.8 were also used to select 4 physically discrete and chemically defined points of interest (POI) that were subject to µEXAFS. For this investigation, the primary areas of interest were those enriched in Mn and Ni. The chosen POI are highlighted in Figure 5.8.

5.3.2.4 μ-EXAFS

Mn K-edge EXAFS of the Mn oxide reference compounds and μEXAFS of the natural ferromanganese samples are shown in Figure 5.10. Mn EXAFS spectroscopy is sensitive to Mn-O and Mn-Mn interatomic distances, and MnO_6 polyhedral linkages (e.g., Manceau and Combes, 1988). Information on sample mineralogy and crystallinity can therefore be obtained by comparing sample spectra to a suite of standard Mn oxide reference spectra (e.g., Manceau et al., 2002).

In agreement with previous studies, the Mn oxide reference spectra used in the current study show clear differences in *k*-space in the (6.5 – 9.5 $Å^{-1}$) indicator region (e.g., Webb et al., 2005a). This region is sensitive to the amount and ordering of Mn(IV) and Mn(III) in the sheets of phyllomanganates (δMnO_2, Hx-birnessite and Tc-Na-birnessite) and to the tunnel dimension in tectomanganates (todorokite) (e.g., Manceau and Combes, 1988; McKeown and Post, 2001). For layered structures, the *k*-space peaks at ~6.7, 8 and 9.2 $Å^{-1}$ appear sharper and more intense with an increase in coherent stacking of the layers along the c-axis, i.e., from the δMnO_2 to Hx-birnessite (e.g., Webb et al., 2005a). For tunnel structures, these indicator features are less sharp and intense, and significantly broader, with a notable increase in the background of the region between ~7.4 – 8.7 $Å^{-1}$, and the shoulder at ~5.5 $Å^{-1}$ also appears less pronounced, compared to layered structures (e.g., Webb et al., 2005a). These differences are evident when comparing the phyllomanganates (δMnO_2 and Hx-birnessite) to the tectomanganate (high crystalline todorokite) reference spectra. In agreement with XRD data presented in Figure 5.7, the spectra for the hydrogenetic and diagenetic samples are most similar to the reference spectrum for poorly crystalline phyllomanganate δMnO_2. Also in agreement with the XRD data, the spectra recorded at two separate POI for the hydrothermal sample, have features attributable to todorokite. Specifically, compared to the hydrogenetic and diagenetic samples, the features at ~6.7, 8 and 9.2 $Å^{-1}$ are less sharp and intense, and also broader.

Given that the bulk XRD data shows that the phyllomanganate present in the hydrothermal sample is in fact more ordered than that found in the hydrogenetic and diagenetic samples, then the reduced intensity and sharpness, along with the broadening, of these indicator peaks is most likely due to the presence of todorokite rather than a very poorly crystalline phyllomanganate phase. Furthermore, the

background of the region between ~7.4 – 8.7 $Å^{-1}$ is significantly elevated, and the shoulder at ~5.5 $Å^{-1}$ is also somewhat less pronounced, compared to the hydrogenetic and diagenetic samples.

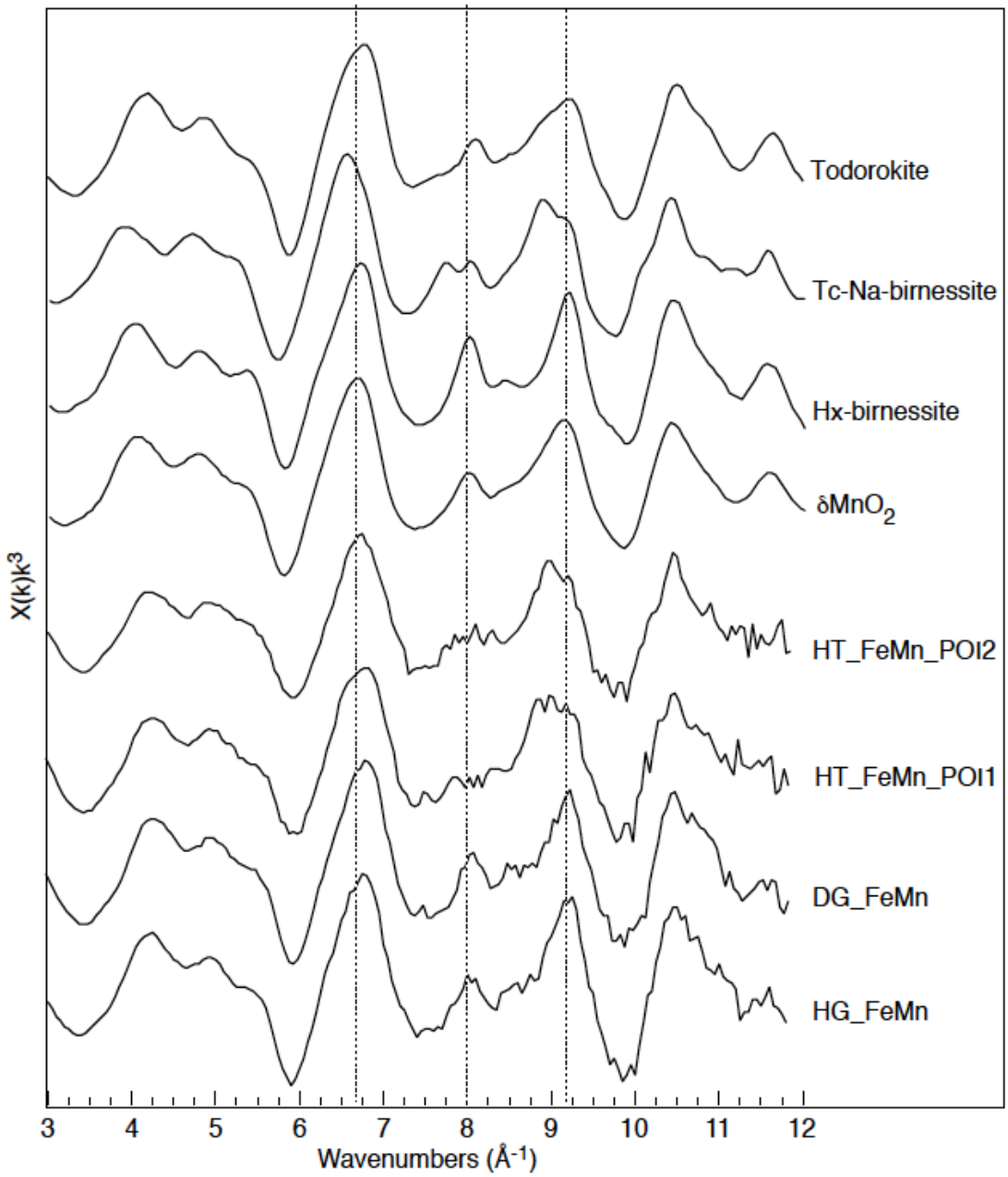

Figure 5.10 Mn K-edge EXAFS for the selected POI in the natural samples. The hydrogenetic, diagenetic and hydrothermal samples are labelled here as HG_FeMn, DG_FeMn and HT_FeMn, respectively. Dashed vertical lines indicate key *k*-space indicator regions at ~6.7, 8 and 9.2 $Å^{-1}$.

Ni K-edge μEXAFS of the natural ferromanganese samples are shown in Figure 5.11 and the fits are summarised in Table 5.7. For the hydrothermal sample at POI2 the Ni concentration was too low to generate a useable EXAFS spectrum. Spectra for the hydrogenetic and diagenetic samples, containing predominantly poorly crystalline phyllomanganate, and the hydrothermal sample at POI1, containing both phyllomanganate and todorokite, are visually most similar to the reference spectrum for Ni structurally incorporated into a natural phyllomanganate (Fig. 5.5).

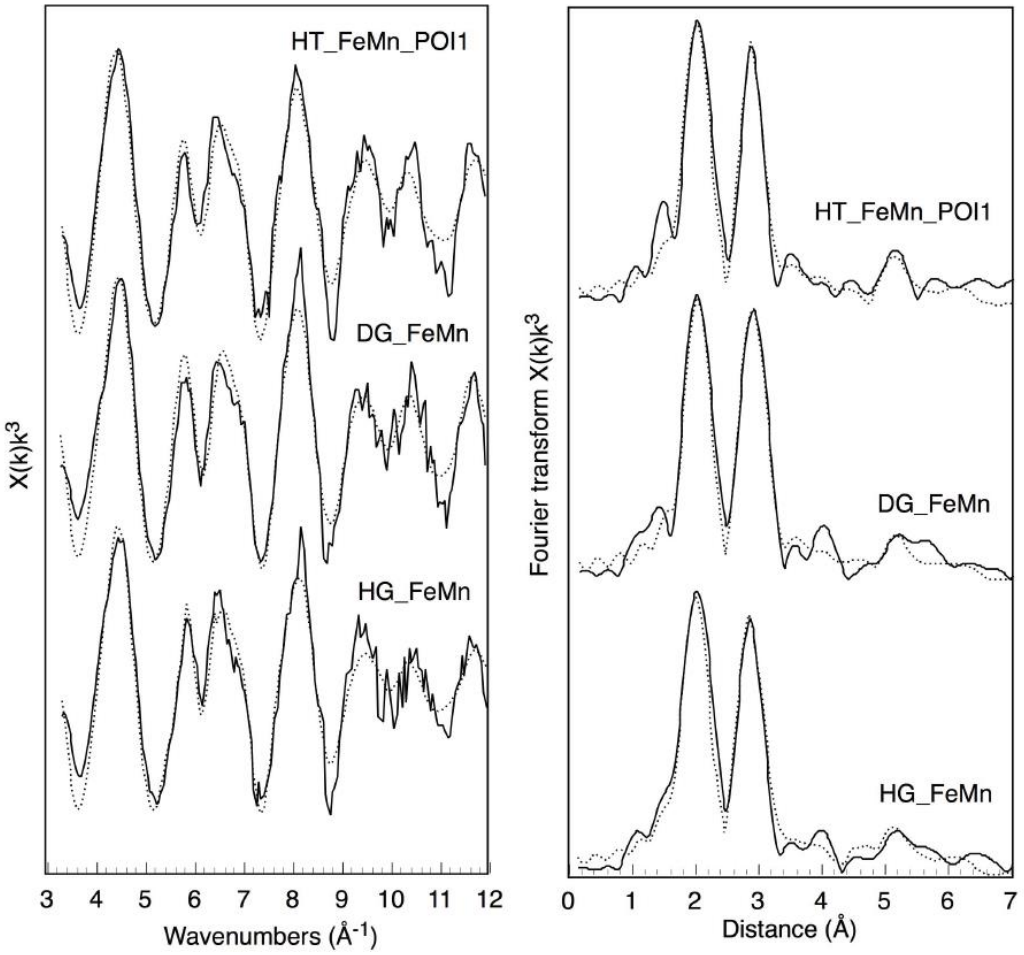

Figure 5.11 Ni K-edge EXAFS and the corresponding Fourier Transforms of the EXAFS for the natural hydrogenetic, diagenetic and hydrothermal samples, labeled here as HG_FeMn, DG_FeMn and HT_FeMn respectively. Solid lines are data, dotted lines are fits.

In particular, pronounced splitting of the spectral feature at ~6 $Å^{-1}$ and a single peak at ~8 $Å^{-1}$ is observed as expected for Ni incorporated into the phyllomanganate layers (Manceau et al., 2007b; Peacock and Sherman, 2007a,b; Peacock, 2009). In all spectra, the splitting of the feature at ~6 $Å^{-1}$, and the amplitude of the

corresponding peak in the Fourier transform at ~2.9 Å, is not as pronounced or as intense, respectively, as that observed in the Ni-incorporated natural phyllomanganate reference spectrum. In this sense the natural ferromanganese *k*-space spectra also resemble the experimental samples up to and including 1 wk reflux (Fig. 5.6), where Ni is both structurally incorporated in, and surface adsorbed to, a phyllomanganate (section 5.3.1.5). However, in the natural ferromanganese spectra, no significant peak in the Fourier transform at ~3.5 Å corresponding to Ni surface adsorbed at the vacancy sites is observed.

As for the Ni-incorporated natural phyllomanganate reference spectrum, the very minor peak at ~3.5 Å is fit by multiple scattering occurring in the near-coordination environment about the Ni atom (Mn-O and Mn-Mn at ~2.9 Å). Accordingly, the best fits to the natural ferromanganese samples are provided by the cluster representing Ni incorporated into the layers of a phyllomanganate (Fig. 5.11, Table 5.5). Inclusion of Ni in any other local coordination environments (e.g., surface adsorbed to a phyllomanganate (using the Ni-sorbed c-disordered reference spectrum), sorbed to todorokite (using one of the Ni-sorbed todorokite reference spectra)) did not improve the fits. Complete structural incorporation of Ni into the layers of natural marine phyllomanganates agrees with previous work for other Ni-rich hydrogenetic and diagenetic ferromanganese precipitates (Peacock and Sherman, 2007b).

Importantly, in the hydrothermal sample containing both phyllomanganate and todorokite, despite the fact our µXRF indicates that the majority of the sequestered Ni is associated with an unidentified phase, there is still a spectral signature for a minority of Ni structurally incorporated into a phyllomanganate at POI1, and there is no evidence to indicate that Ni is adsorbed or incorporated by the co-located todorokite. This suggests that, in agreement with the experimental results up to an including 1 wk reflux, in sediments where both phyllomanganate and todorokite are present, the majority of the solid-phase Ni is preferentially sequestered to the phyllomanganate phase.

Shell	*N*	*R* (Å)	$2\sigma^2$ (Å^2)	*θ*	*φ*	EF	R (%)	Reduced Chi^2
HG_FeMn								
Ni_0	*1*	0	0	*0*	*0*	2.34	25.2	29
O_1	*3*	2.02	0.012	*47*	*0*			
O_2	*3*	2.08	0.011	*136*	*180*			
Mn_3	*3*	2.93	0.015	*90*	*270*			
Mn_4	*3*	2.85	0.012	*90*	*90*			
Mn_5	*3*	5.99	0.01	*90*	*270*			
Mn_6	*3*	4.96	0.011	*90*	*180*			
Mn_7	*3*	5.08	0.01	*90*	*0*			
Mn_8	*3*	5.88	0.009	*90*	*90*			
O_9	*3*	3.31	0.01	*105*	*0*			
O_{10}	*3*	3.53	0.01	*75*	*180*			
O_{11}	*3*	4.52	0.008	*75*	*100*			
O_{12}	*3*	4.45	0.01	*105*	*45*			
O_{13}	*3*	4.55	0.01	*100*	*80*			
O_{14}	*3*	4.65	0.013	*75*	*135*			
DG_FeMn								
Ni_0	*1*	0	0	*0*	*0*	1.3	20.8	22.7
O_1	*3*	2.04	0.015	*47*	*0*			
O_2	*3*	2.06	0.009	*136*	*180*			
Mn_3	*3*	2.86	0.015	*90*	*270*			
Mn_4	*3*	2.9	0.017	*90*	*90*			
Mn_5	*3*	6	0.009	*90*	*270*			
Mn_6	*3*	4.95	0.014	*90*	*180*			
Mn_7	*3*	5.08	0.01	*90*	*0*			
Mn_8	*3*	5.89	0.009	*90*	*90*			
O_9	*3*	3.3	0.009	*105*	*0*			
O_{10}	*3*	3.49	0.013	*75*	*180*			
O_{11}	*3*	4.54	0.008	*75*	*100*			
O_{12}	*3*	4.42	0.011	*105*	*45*			
O_{13}	*3*	4.57	0.009	*100*	*80*			
O_{14}	*3*	4.64	0.013	*75*	*135*			
HT_FeMn								
Ni_0	*1*	0	0	*0*	*0*	3.14	24.3	27.4
O_1	*3*	2.01	0.01	*47*	*0*			
O_2	*3*	2.06	0.01	*136*	*180*			
Mn_3	*3*	2.94	0.018	*90*	*270*			
Mn_4	*3*	2.84	0.013	*90*	*90*			
Mn_5	*3*	6	0.011	*90*	*270*			
Mn_6	*3*	4.96	0.011	*90*	*180*			
Mn_7	*3*	5.09	0.01	*90*	*0*			
Mn_8	*3*	5.91	0.01	*90*	*90*			
O_9	*3*	3.36	0.014	*105*	*0*			
O_{10}	*3*	3.5	0.01	*75*	*180*			
O_{11}	*3*	4.49	0.012	*75*	*100*			
O_{12}	*3*	4.5	0.012	*105*	*45*			
O_{13}	*3*	4.55	0.012	*100*	*80*			
O_{14}	*3*	4.65	0.012	*75*	*135*			

Table 5.7 EXAFS fits for natural ferromanganese samples, fit by refinement of a single model cluster. *N* is the number of atoms in a shell. *R*, *θ* and *φ* are the interatomic distance and spherical coordinates of the prototype atom in each shell with either C_1 or C_3 symmetry. $2\sigma^2$ is the Debye–Waller factor. EF is the correction to the Fermi energy value assigned in ATHENA. Values in italics were held constant during refinement.

5.4 Discussion

5.4.1 The Effect of Sorbed Ni on the Transformation of Birnessite to Todorokite

In the previous chapter of this thesis I report a four-stage nucleation and growth model, beginning with todorokite nucleation, then crystal growth from solution to form todorokite primary particles, followed by their self-assembly and oriented growth via oriented attachment (OA) to form crystalline todorokite laths, culminating in traditional crystal ripening. In this Ni-free system, characteristic XRD peaks for todorokite are seen by 3 hr reflux, todorokite primary particles are observed with HR-TEM by 6 hr reflux, and the oriented attachment of these particles to form crystalline todorokite laths is similarly evident by 6 hr reflux, with highly crystalline laths several tens of nanometers in length evident by 24 hr reflux.

In the system investigated here, I transform a Ni-sorbed 10 Å phyllomanganate where, of the total Ni sorbed (~1 wt% Ni), ~60 % is structurally incorporated into the phyllomanganate crystal lattice with the remaining ~40 % surface adsorbed at Mn octahedral vacancy sites present in the phyllomanganate layers (Table 5.5). However, despite the presence of sorbed Ni, I find no evidence to suggest that this trace metal impurity has a significant effect on the growth mechanism of todorokite. HR-TEM images clearly show that the large acicular laths of todorokite present by 24 hr reflux are composed of considerably smaller todorokite primary particle building blocks. Specifically, individual todorokite primary particles are elongated along the direction of tunnel growth ([010] direction) by varying degrees, but measure consistently between 6-10 nm wide across the direction of tunnel growth ([100] direction) over the entire duration of the reflux (from 6-10 nm wide after 6 hr (Fig. 5.2f) to ~8-10 nm wide after 2 wk reflux (Fig. 5.2j)). Moreover, these nano-sized primary particles are crystallographically aligned and aggregated together across the direction of tunnel growth via the attachment of the [100] crystal faces. Both the width and the length of these secondary todorokite laths continues to increase with increasing reflux time, from ~70 x 250 nm at 24 hr, to ~100 x 450 nm at 1 wk and ~100 x 750 nm after 2 wk (Figs. 5.2e,g,i, respectively). These observations indicate that the formation of secondary acicular todorokite laths can be directly attributed to the simultaneous aggregation of primary todorokite crystallites across the [100] direction and their growth from solution along the [010] direction. The homogeneous widths of the todorokite primary particles over the course of the reflux indicates that these particles grow exclusively from solution along the [010] direction. All of the

above observations are comparable and consistent with observations from chapter 4, and show that the mechanism and pathway of todorokite formation from a Ni-doped phyllomanganate does not significantly differ from a Ni-free phyllomanganate, proceeding via crystal growth from solution to form todorokite primary particles, followed by their self-assembly and oriented growth via OA.

Despite the fact that sorbed Ni has no significant effect on the growth mechanism of todorokite, I find evidence to show that this metal impurity has a notable effect on the growth rate of this neo-formed phase. In contrast to the Ni-free system, where characteristic XRD peaks for todorokite are seen by 3 hr reflux, these same peaks are not seen until the 48 hr time point in the Ni-doped experiment (Fig. 5.1; where peaks may be present at any time point between the 24 and 48 hr scans). Characteristic todorokite morphology is evident in the HR-TEM by 6 hr reflux, but these primary particles are only a minor component of the overall sample matrix, which is still dominated by platy phyllomanganate. Furthermore, the todorokite primary particles have very poorly defined lattice fringes, indicating poor crystallinity (Fig. 5.2). The fact these primary particles are only a minor component of the sample matrix and are poorly crystalline may account for the absence of characteristic todorokite XRD peaks at this time point (Fig. 5.1). The crystallinity of the todorokite formed after 2 wk reflux, and with further reflux up to 4 wk, is also reduced (Fig. 5.2), compared to that formed by 72 hr in the Ni-free system. As such, compared to the Ni-free system investigated in the previous chapter, the results presented here show that Ni, sorbed to birnessite at concentrations equivalent to those found in natural marine ferromanganese precipitates, significantly retards the rate of todorokite formation, and in addition reduces the crystallinity of the neo-formed todorokite phase.

To date there has been little work on the effect of sorbed trace metal impurities on the growth of minerals by OA, especially for cases where growth via OA is accompanied by a phase transformation or vice versa. Surface adsorbed metal(loids), including Cu(II), Zn(II), As(V) and Hg(II) (Fuller et al., 1993; Waychunas et al., 1993; Myneni et al., 1997; Kim et al., 2008), have been shown, or at least predicted, to substantially disrupt nanoparticle aggregation and growth. Specifically, it is suggested that surface adsorption of metal(loids) can result in a passivation of the nanoparticle surface, through either modification of surface charge or alteration of surface structure and/or composition, which inhibits aggregation-type growth processes (Fuller et al., 1993; Waychunas et al., 1993; Myneni et al., 1997; Kim et al., 2008). Kim et al. (2008) suggest that for growth via OA to proceed, surface adsorbed metal(loid)

impurities must either be structurally incorporated into the mineral matrix, away from particle attachment and aggregation interfaces, or desorbed into solution.

In the case of phyllomanganates, the Mn octahedral layers are only a single Mn octahedron thick, and, as such, structurally incorporated impurities are essentially still present at attachment interfaces. Based on these previous studies, and given the fact that todorokite growth proceeds via OA in both the Ni-free (i.e. chapter 4 of this thesis) and Ni-doped systems, then the observed retardation in the rate of todorokite formation in the Ni-doped experiment is likely attributable, at least in part, to the presence of both a structurally incorporated and surface adsorbed metal impurity. In addition, and with specific reference to Ni, the Ni octahedron is not Jahn-Teller distorted. Elongation of the metal-O bonds along the z-axis in Mn(III) creates a strain on the Mn^{3+}-O-Mn^{4+} bonds that run parallel to the [010], which aids the kinking of the phyllomanganate layers and thus the nucleation of todorokite within the phyllomanganate matrix (Bodeï et al., 2007; Cui et al., 2008). Indeed, the presence of sufficient structural Mn(III), which facilitates phyllomanganate layer kinking, together with semi-coherent c-axis ordering, so that as the layers kink there are sufficient adjacent layers to form the todorokite tunnel walls, are prerequisites for todorokite formation. In the previous chapter of this thesis it was predicted that structurally incorporated cation impurities without Jahn-Teller distortion, such as Ni, might retard the transformation of birnessite to todorokite, by essentially retarding phyllomanganate layer kinking and thus the formation of todorokite primary particles. Overall, the observed reduction in the rate of todorokite formation in the Ni-doped system can be attributed to a retardation in the rate of todorokite primary particle formation, specific to a metal impurity without Jahn-Teller distortion, and a more general disruption to growth via OA, as a result of a metal impurity at attachment interfaces.

In summary, I have shown for the first time that, contrary to traditional understanding, the presence of sorbed Ni does not aid the transformation of birnessite to todorokite and in fact retards todorokite formation, and substantially reduces the crystallinity of the neo-formed todorokite phase.

5.4.2 The Fate and Mobility of Ni During the Transformation of Birnessite to Todorokite

In addition to predicting that structurally incorporated metal impurities without Jahn-Teller distortion, such as Ni, should retard the transformation of birnessite to todorokite, I also postulated in the previous chapter that such impurities, both structurally incorporated and surface adsorbed at aggregation interfaces, may be lost to solution in order to facilitate todorokite growth via OA. It is now clear that during the transformation of Ni-doped birnessite to todorokite, over the course of the 4 wk reflux, there is a ~50 % reduction in solid-associated Ni (Table 5.2).

Taking all of the analyses together, I am able to provide a coherent picture for the fate and mobility of Ni during the transformation of Ni-doped birnessite to todorokite. Up to and including 1 wk reflux, Ni EXAFS and HR-TEM EDS data shows that all detectable, solid-associated Ni is sorbed to the phyllomanganate phase (Fig.5.6 and Table 5.1, respectively), despite the progressive formation of todorokite within the sample matrix (Fig. 5.2). However, by 1 wk reflux, absolute concentrations for solid-associated Ni indicate that ~20 % of the total sorbed Ni is released to solution (Table 5.2). This initial release might be understood in light of our four-stage growth mechanism, together with the surface area measurements and the relative trends in the Mn and Ni solution data, which show more variability during this time frame. Akin to the Ni-free system, there is also an initial drop in surface area evident at 3 hr reflux, which then remains relatively constant until at least 12 hr reflux (Table 5.3). This is accompanied by a sharp release of Mn, and a more gradual release of Ni (Fig. 5.3).

In agreement with the work presented for the Ni-free system, the drop in surface area during the early stages of the transformation is consistent with the formation and growth of todorokite primary particles along the direction of tunnel growth, via dissolution of the 10 Å phyllomanganate followed by precipitation of todorokite, where the difference in both size and morphology between the two phases drives the dissolution-recrystallisation process. The concurrent release of Mn and Ni is then consistent with this dissolution-recrystallization. Up to 1 wk reflux, the overall decrease in surface area, the relative stabilization of solution Mn yet the continued increase in solution Ni, are then consistent with the growth of the todorokite primary particles via an OA-type growth mechanism. A shift from a dissolution-recrystallization dominated growth mechanism to growth dominated by aggregation is typical of nanoparticle systems that undergo growth by OA (e.g., Waychunas et al., 2005). However, although one specific growth mechanism may dominate at any given point,

the two growth processes are likely to be occurring simultaneously throughout the transformation (e.g.Waychunas et al., 2005; Kim et al., 2008). In this case, aggregation of the primary particles, with minor dissolution-recrystallisation, is consistent with the overall decrease in surface area yet relatively minor change in solution Mn. Conversely the continued increase in solution Ni is consistent with its release during ongoing minor dissolution, and its desorption from attachment interfaces in order for aggregation to proceed (Kim et al., 2008), during which time there is a progressive transformation of the high-affinity phyllomanganate phase into one in which we see no detectable Ni (Fig. 5.6 and Table 5.1). By 2 wk reflux the absence of observable phyllomanganate in the HR-TEM, the relatively minor decrease in surface area towards the final value at 4 wk reflux, yet the relatively significant increase in solution Mn and Ni, are consistent with the dissolution of the remaining birnessite by this time point. In the absence of the phyllomanganate phase, EXAFS now show that all detectable, solid-associated Ni is sorbed to the neo-formed todorokite as a tridentate surface complex (Fig. 5.6), however, absolute concentrations for solid-associated Ni show that only ~50 % of the initially sequestered Ni is associated with this solid phase (Table 5.2). By 4 wk reflux, the substantial decrease in solution Mn is consistent with ripening-type growth of the neo-formed todorokite, commencing after all the phyllomanganate is consumed, while the relatively minor decrease in solution Ni likely reflects some further adsorption of Ni to the todorokite phase.

Principally the experimental results presented here indicate that in a system dominated by todorokite as the end product of diagenesis, a significant fraction of the Ni originally sequestered to birnessite is released to marine sedimentary porewaters during the birnessite to todorokite transformation, while the remaining solid-associated Ni is sorbed to todorokite via surface complexation, as opposed to structural incorporation, and is therefore also subject to remobilization. Overall the marine diagenesis of birnessite is a source of Ni to sedimentary porewaters and thus potentially provides a benthic flux of Ni to seawater.

5.4.3 Ni Speciation in Natural Ferromanganese-rich Marine Sediments

Analysis of the natural marine ferromanganese precipitates is consistent with the new model mechanism for the transformation of birnessite to todorokite, and the resulting fate of Ni during this OA-type process. Specifically, in the hydrothermal

sample containing both phyllomanganate and todorokite, akin to the experimental samples up to and including 1 wk reflux, the Ni associated with Mn-rich phases is preferentially sequestered to the phyllomanganate phase, with no evidence that Ni is surface adsorbed or structurally incorporated by the co-located todorokite (Fig. 5.8, 5.11). These observations agree with those made previously for natural intermixed ferromanganese precipitates, where neo-formed todorokite typically contains substantially less Ni than the 10 Å phyllomanganate from which it crystallized (Siegel and Turner, 1983; Bodeï et al., 2007).

5.6 Summary and Conclusions

The current study provides the first detailed understanding of the effect of sorbed Ni on the transformation of birnessite to todorokite in the marine environment, and the fate and mobility of this micronutrient during this diagenetic process. Specifically,

1. Sorbed Ni significantly retards the transformation of birnessite to todorokite and reduces the crystallinity of the neo-formed todorokite phase, but does not alter the mechanism and pathway of todorokite formation, compared to a Ni-free system. The inhibitory effect of sorbed Ni on todorokite formation can be attributed to i) a retardation in the rate of todorokite primary particle formation, where the presence of non Jahn-Teller distorted Ni within the phyllomanganate matrix is unfavourable for phyllomanganate layer kinking and thus inhibits todorokite nucleation and subsequent formation of primary particles, and ii) a disruption to growth via oriented attachment, where sorbed Ni blocks primary particle attachment and aggregation interfaces. The fact that sorbed Ni retards the transformation process is contrary to current knowledge, where it is understood that Ni should aid the transformation of birnessite to todorokite.

2. Sorbed Ni is released to solution during the transformation of birnessite to todorokite. Desorption of Ni can be attributed to its release to solution during i) dissolution of the phyllomanganate phase and its recrystallization into todorokite, leading to the growth of the todorokite primary particles along the direction of tunnel growth ([010] direction), and ii) desorption from attachment

and aggregation interfaces in order that growth via oriented attachment can proceed, leading to the growth of stable secondary todorokite laths.

3. In systems tending towards todorokite as the final product of diagenesis, up to half of the Ni originally sequestered by the phyllomanganate phase is released to solution, while the remaining solid-associated Ni is sorbed to todorokite via surface complexation and is therefore subject to remobilization. Overall the marine diagenesis of birnessite is a source of Ni to sedimentary porewaters and thus potentially provides a benthic flux of Ni to seawater.

Chapter 6

Ni stable isotope fractionation during experimental sorption to hexagonal birnessite.

6.1 Introduction

The majority of transition metal elements are now recognized as biologically active elements, with unique biological roles as essential metal cofactors in metalloenzymes or as structural elements in proteins (Morel et al., 2003). As a result, many transition metal stable isotope systems are becoming increasingly developed as a means of investigating the biogeochemical cycling of key micronutrient trace-metals in both modern and ancient seawater, and to understand biogeochemical processes on the early Earth (e.g. Anbar and Rouxel, 2007; Konhauser et al., 2009). However, in contrast to some of the other stable isotope systems, such as Mo (e.g. Barling et al., 2004; Wasylenki et al., 2011), Zn (e.g. Pokrovsky et al., 2005; Little at al., 2014) and Tl (e.g. Rehkämper et al., 2002; Nielson et al., 2004; Peacock and Moon, 2012; Nielsen et al., 2013), the Ni isotope system has been substantially slower to develop. However, Ni has recently generated significant interest as a biogeochemical tracer as it is now recognized as an important bioessential trace-metal, required as a key nutrient for primary productivity in photosynthetic algae (Frausto de Silva and Williams, 2001; Dupont et al., 2010), and in addition, as a unique enzyme cofactor in the metabolism of methanogenic archea (Thauer et al., 1998; Cameron et al., 2009). Thus Ni concentrations and Ni isotopic compositions recorded in marine sediments offer significant potential as a tracer for both modern and ancient biogeochemical processes (e.g. Cameron et al., 2009; Konhauser et al., 2009). For example, a recent study by Konhauser et al. (2009) highlights a significant decrease in Ni concentrations measured in banded iron formations that were deposited over the Achaean, which is interpreted as an equally significant decline in concomitant oceanic Ni. Considering the unique biological role of Ni, it is believed that a catastrophic decline in oceanic Ni concentrations could have stifled methanogenic activity on the early Earth, which in turn is thought to have aided the progressive oxygenation of the atmosphere (Konhauser et al., 2009).

As detailed in previous chapters, one of the primary controls on the modern day oceanic Ni budget is uptake to marine ferromanganese-rich precipitates, and to date, chemical and spectral analyses conducted on these sediments, including sequential leaching experiments and XAS have revealed that Ni is strongly correlated with the Mn oxide fraction (e.g., Goldberg, 1954; Lei and Boström, 1995; Koschinsky and Halbach 1995; Koschinsky and Hein 2003; Peacock and Sherman, 2007b). Specifically, Ni is found exclusively associated with the poorly crystalline Mn oxide birnessite (δMnO_2), where it is found almost entirely incorporated into the birnessite structure (Manceau et al., 2007b; Peacock and Sherman, 2007a). The incorporation of Ni into the birnessite crystal lattice is thought to be primarily a function of the rearrangement of Ni sorbed above and below manganese octahedral vacancy sites on the birnessite [001] surface, with time (Peacock and Sherman, 2007a; Peacock, 2009). In particular, marine ferromanganese precipitates classified as hydrogenetic provide an excellent repository for trace-metal chemical and isotopic information primarily because they precipitate extremely slowly from ambient seawater (~1 mm/Myr), and are largely free from any diagenetic input, and thus the inherent complexities associated with early diagenetic processes.

A recent study investigating the global variability of Ni isotopic signatures recorded in a variety of hydrogenetic marine ferromanganese crusts, found that these sediments were significantly heavier with respect to their δ^{60}Ni isotopic composition than any other geological samples reported in the literature to date (Gall et al., 2013). The Ni isotopic compositions of the ferromanganese crust samples ranged between +0.7 ‰ and +2.5 ‰, with no apparent trend between different ocean basins. In contrast, the δ^{60}Ni isotopic compositions of all other reported samples ranged between -0.1 ‰ and +0.3 ‰ (Cameron et al., 2009; Gall et al., 2012). However, in order to develop these Ni isotopic records as either palaeo proxies or marine biogeochemical tracers, a detailed mechanistic understanding of the processes that control these isotope fractionations is required. At present, the magnitude and the variability of the Ni isotopic compositions recorded in marine ferromanganese crusts have not been explained.

Theoretically, the sorption of Ni to the birnessite surface and its subsequent incorporation into the birnessite structure could invoke some degree of isotopic fractionation, leading to the somewhat heavier isotopic composition of marine ferromanganese crusts (+0.7 ‰ - +2.5 ‰ (Gall et al., 2013)) relative to modern seawater, which is homogeneous with respect to its Ni isotopic composition at around

+1.44 ± 0.15 ‰ (Cameron and Vance, 2014). According to stable isotope theory, equilibrium isotope fractionations are generally sensitive to three major factors, namely temperature, the difference in mass between isotopes, and differences in bond stiffness, and as a general rule, the heavy isotope typically accumulates in the strongest bonding environment (e.g. Schauble, 2004). In the current example, the uptake of the free Ni^{2+} ion to the birnessite surface and its incorporation into the birnessite crystal structure over time should theoretically provide the strongest bonding environment. In addition, it is also predicted that species, which undergo the greater change in coordination environment during sorption, should exhibit larger isotopic fractionations. To the author's knowledge, the potential isotopic fractionation of Ni during its sorption to Mn oxides has not been investigated.

Isotopic fractionation specifically associated with sorption to the birnessite surface has been recognized for a variety of other systems, including Zn (Pokrovsky et al., 2005), Mo (Barling and Anbar, 2004; Wasylenki et al., 2011), and Tl (Peacock and Moon, 2012; Nielsen et al., 2013). From these studies, both Mo and Tl have been shown to undergo a change in oxidation state during sorption to the birnessite surface. While Zn does not take part in redox reactions during sorption to birnessite, the uptake of Zn to birnessite is accompanied by pH-dependent isotope fractionation. It should be noted that although in many instances the sorption of trace-metal species to birnessite, and indeed other oxy (hydr)oxide minerals, is accompanied by isotope fractionation, fractionation is highly element specific and is not necessarily a given (Bullen, 2011). For example, experimental studies have shown that isotopic fraction during the sorption of Cd to Mn oxide phases is negligible, particularly under high ionic strength conditions (e.g. Wasylenki et al., 2009; Horner et al., 2010).

In order to investigate the potential isotopic fractionation of Ni during its sorption to birnessite, several laboratory sorption experiments were performed on synthetic c-disordered hexagonal birnessite (analogous to natural marine birnessite) under varying physiochemical conditions. If indeed the sorption of Ni^{2+} to birnessite is accompanied by an isotopic fractionation, both the direction and the magnitude of the fractionation are of primary interest.

6.3 Experimental methods

6.3.1 Mineral preparation and characterization

Synthetic c-disordered hexagonal birnessite analogous to natural marine birnessite was synthesized following the redox method of Villalobos et al. (2003). This method is outlined in detail in chapter 3. Briefly, 320 mL of a 0.196 M $KMnO_4$ solution was added slowly to 360 mL of a 0.51 M NaOH solution. Then 320 mL of a 0.366 M $MnCl_2$ solution was added slowly to the above mixture whilst stirring vigorously. The resulting suspension was left to settle for approximately 4 hr. The supernatant was then removed and discarded. The remaining slurry was subsequently centrifuged at 3200 g for 30 min. The supernatant was again removed and discarded. After centrifugation, the wet slurry was mixed with 800 mL of 1 M NaCl and shaken for 45 min. The suspension was centrifuged and the supernatant discarded. This process was repeated 4 times. For the last 1 M NaCl wash the pH was adjusted to pH 8 via the drop-wise addition of 1 M NaOH and the suspension shaken overnight. After centrifuging, the resulting paste was combined with Milli-Q grade (MQ) water, shaken for 1 hr and centrifuged at 3200 g for 10 min. This wash cycle was repeated 10 times, 1x for 1 hr, 8x for 0.5 hr and 1x overnight. Following the final wash, the suspension was dialyzed for 3 days in 43 x 27 mm cellulose dialysis tubing, which was placed in a 5 L beaker containing approximately 4 L of MQ water.

Mineral identity and purity was subsequently confirmed by powder X-ray diffraction (XRD) (Fig. 6.1), using a Bruker D8 diffractometer equipped with CuKα radiation (λ = 1.5418) and a LynxEye detector. Samples were analyzed over a range of 5-70^o 2θ with a 0.010 step size and step time of 155 sec.

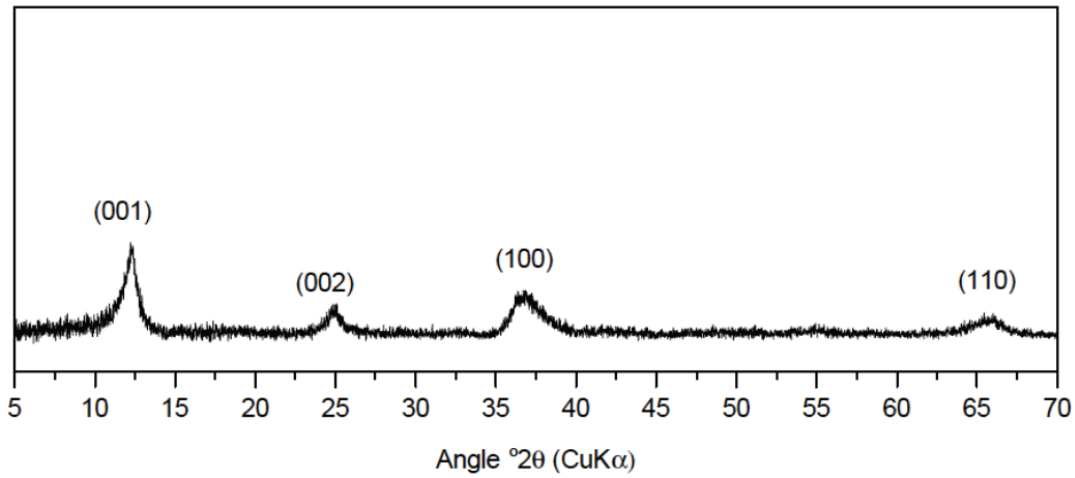

Figure 6.1 Powder XRD pattern for the synthetic c-disordered hexagonal birnessite used during the current study, showing the [001], [002], [100] and [110] reflections, which correspond to the d-spacings of ~7 Å, ~3.6 Å, ~2.4 Å and ~1.4 Å respectively of a hexagonal birnessite phase.

6.3.2 Preparation of Ni adsorption samples

Nickel isotope fractionation during the sorption of aqueous Ni^{2+} to synthetic c-disordered hexagonal birnessite was investigated using a series of 18 unique sorption experiments. Experiments were performed in duplicate, at 4 different initial Ni concentrations (12, 120, 820 or 1640 µg $[Ni]_{total}$), 2 different pH intervals (pH 5 and pH 8), and for 3 different time durations (48 hr, 1 week and 4 week). A detailed summary of the experimental parameters used in each individual sorption experiment is provided in Table 6.1. The target Ni concentrations used in the experiments were estimated based on previous Ni sorption experiments (Peacock and Sherman, 2007a). It should be noted that no sorption experiments were conducted at pH 8 for low Ni loadings (i.e. 12 and 120 µg $[Ni]_{total}$). Previously conducted sorption edge experiments at these Ni concentrations (Fig. 6.2) show that at high pH regimes all of the Ni in solution is sorbed to the birnessite surface after 48 hr equilibration. As such, under these experimental conditions it is anticipated that there will not be sufficient Ni remaining in solution for Ni isotope analysis, and thus no measurable isotope fractionation.

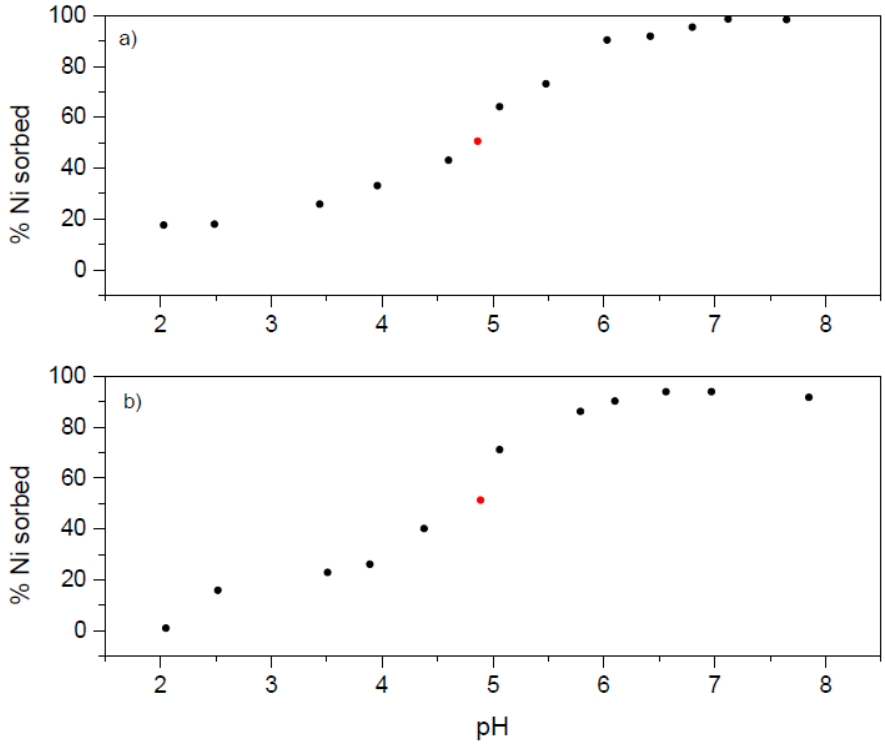

Figure 6.2 pH sorption edge experiments for Ni^{2+} on synthetic c-disordered birnessite (0.05 g/L) as a function of pH, at 25 °C, after equilibration for 48 hr with (a) 12 µg $[Ni]_{total}$ and (b) 120 µg $[Ni]_{total}$. Experiments were conducted using 0.1 M NaCl as a background electrolyte solution. Black dots are data points, while red dots mark the approximate positions of the isotope experiments.

Sample	pH	Duration	$[Ni]_{stock}$ ($\mu g/g$)	$NaCl_{0.1M}$ (mL)	MnO_2 (g)	$[Ni]_{total.}$ ($\mu g/g$)	$[Ni]_{total.}$ (μg)	$[Ni]_{sorbed}$ (wt%) at 100%	$[Ni]_{solid.}$ (%)	$[Ni]_{solid.}$ (μg)	$[Ni]_{soln.}$ (%)	$[Ni]_{soln.}$ (μg)
$1A_1$	5	48 hr	1000	200	0.01	0.06	12	0.1	60	7.2	40	4.8
$1A_2$	5	48 hr	1000	200	0.01	0.06	12	0.1	60	7.2	40	4.8
$2A_1$	5	48 hr	1000	200	0.01	0.59	118	1	60	71	40	47
$2A_2$	5	48 hr	1000	200	0.01	0.59	118	1	60	71	40	47
$3A_1$	5	48 hr	1000	200	0.01	4.11	822	8	10	82	90	740
$3A_2$	5	48 hr	1000	200	0.01	4.11	822	8	10	82	90	740
$3B_1$	8	48 hr	1000	200	0.01	4.11	822	8	40	329	60	493
$3B_2$	8	48 hr	1000	200	0.01	4.11	822	8	40	329	60	493
4A1	5	48 hr	1000	200	0.01	8.22	1644	16	10	164	90	1480
$4B_1$	8	48 hr	1000	200	0.01	8.22	1644	16	40	658	60	986
$4B_2$	8	48 hr	1000	200	0.01	8.22	1644	16	40	658	60	986
$5A_1$	5	1 wk	1000	200	0.01	0.06	12	0.1	60	7.2	40	4.8
$5A_2$	5	1wk	1000	200	0.01	0.06	12	0.1	60	7.2	40	4.8
$6A_1$	5	1 wk	1000	200	0.01	0.59	118	1	60	71	40	47
$7A_1$	5	1 wk	1000	200	0.01	4.11	822	1	10	82	90	740
$8B_1$	8	1 wk	1000	200	0.01	4.11	822	8	40	329	60	493
$8B_2$	8	1 wk	1000	200	0.01	4.11	822	8	40	329	60	493
$9A_1$	5	1 wk	1000	200	0.01	8.22	1644	16	10	164	90	1480
$9A_2$	5	1 wk	1000	200	0.01	8.22	1644	16	10	164	90	1480
$10B_1$	5	1 wk	1000	200	0.01	8.22	1644	16	40	658	60	986
$10B_2$	8	1 wk	1000	200	0.01	8.22	1644	16	40	658	60	986
$11A_1$	5	4 wk	1000	200	0.01	0.06	12	0.1	60	7.2	40	4.8
$11A_2$	5	4 wk	1000	200	0.01	0.06	12	0.1	60	7.2	40	4.8
$12A_1$	5	4 wk	1000	200	0.01	0.59	118	1	60	71	40	47
$12A_2$	5	4 wk	1000	200	0.01	0.59	118	1	60	71	40	47
$13A_1$	5	4 wk	1000	200	0.01	4.11	822	8	10	82	90	740
$13A_2$	5	4 wk	1000	200	0.01	4.11	822	8	10	82	90	740
$13B_2$	8	4 wk	1000	200	0.01	4.11	822	8	40	329	60	493
$14A_1$	5	4 wk	1000	200	0.01	8.22	1644	16	10	164	90	1480
$14A_2$	5	4 wk	1000	200	0.01	8.22	1644	16	10	164	90	1480
$14B_1$	8	4 wk	1000	200	0.01	8.22	1644	16	40	658	60	986

Table 6.1 Experimental parameters used for each individual sorption experiment. The letter (A or B) next to the sample number represents the pH of the experiment, where *A* corresponds to the experiments conducted at pH 5 and *B* corresponds to experiments conducted at pH 8. The subscript (1 or 2) denotes the sample repeat. All sorption experiments were performed in duplicate however, during sample separation a small number of samples were lost.

For the sorption experiments a Ni^{2+} stock solution was prepared at 1000 mg/L from $Ni(NO_3)_2.6H_2O$ and a 0.1 M NaCl solution was prepared for use as a background electrolyte. Individual sorption experiments were prepared in 250 mL polycarbonate bottles at either 12, 120, 820 or 1640 µg $[Ni]_{total}$ by adding 0.01, 0.1, 0.8 or 1.6 mL of Ni stock solution to 0.01 g of c-disordered birnessite in 199.99, 199.90, 199.20 and 198.40 mL of NaCl respectively. The total volume of solution in each experiment was equal to 200 mL, giving a solid/solution ratio in each individual experiment of 0.05 g/L. The resulting mineral suspensions were shaken and the initial pH recorded after stabilization to two decimal places. All pH measurements were calibrated to ±0.05 pH units using Whatman NBS grade buffers. The pH was then adjusted to the desired pH (pH 5 or pH 8) via the drop wise addition of HCl/NaOH. The samples were subsequently sealed and shaken at room temperature (25 °C) for

the required time period (48 hr, 1 week or 4 week). After shaking, the final suspension pH was recorded and the solid mineral was separated from the solution using a vacuum filtration kit.

For each individual experiment, both the solid mineral and the corresponding reaction solution were analyzed for their respective concentrations of Ni using a quadrupole ICP-MS, while the ^{60}Ni isotopic composition of the solid phases and the corresponding solutions were analyzed using a muliticollector-ICP-MS (MC-ICP-MS).

All ICP-MS analyses presented in this work have been conducted by Louise Gall, at the University Oxford, UK. The details of sample preparation, sample purification, and subsequent isotope analysis are outlined in the methods section (chapter 3). Ni isotope ratios presented in the current work are reported as the ratio ^{60}Ni/^{58}Ni relative to the Ni isotope standard SRM 986 (NIST):

$$\delta^{60}\text{Ni} = \left(\frac{(^{60}\text{Ni}/^{58}\text{Ni})_{\text{sample}}}{(^{60}\text{Ni}/^{58}\text{Ni})_{\text{standard}}} - 1 \right) \text{X } 1000$$

6.4 Results

The results presented here provide the first insight into Ni isotope fractionation associated with the sorption of Ni to synthetic c-disordered birnessite. A full summary of the results are tabulated in Table 6.2 and presented graphically below in Figure 6.3, where the isotopic offset between the $\delta^{60}Ni_{soln\text{-}solid}$ has been plotted against the fraction (%) of Ni sorbed to the solid birnessite samples, as a function of time, initial Ni loading and pH.

It should be noted that where possible the isotopic composition of both the solid c-disordered birnessite and the corresponding reaction solution were analyzed. However, during the chemical separation procedure, prior to Ni isotope analysis, some of the solution samples (mainly from the low Ni concentration experiments) were lost. The high Na content of the sample matrix (i.e. from the 0.1 M NaCl-

background electrolyte solution) produced a Na-OH precipitate during the first ion-exchange step (see methods chapter), which blocked the columns.

Experimental parameters				Solid phase analysis				Solution analysis			
Sample	pH	Duration	$[Ni]_{total.}$ (μg)	[Ni] (µg)	[Ni] (%)	$\delta^{60}Ni$(‰)	±2 s.d.	[Ni] (µg)	[Ni] (%)	$\delta^{60}Ni$(‰)	±2 s.d.
$1A_1$	5	48 hr	12	7.7	64	-0.451	0.048	2.4	20		-
$1A_2$	5	48 hr	12	8	67	-0.342	0.017	1.8	15		-
$2A_1$	5	48 hr	118	61	52	-1.017	0.017	53	45		-
$2A_2$	5	48 hr	118	57	49	-1.044	0.039	55	47		-
$3A_1$	5	48 hr	822	166	20	-1.742	0.055	630	77	0.530	0.050
$3A_2$	5	48 hr	822	176	21	-1.735	0.038	629	77	0.533	0.041
$3B_1$	8	48 hr	822	484	59	-0.634	0.074	331	40	0.942	0.059
$3B_2$	8	48 hr	822	425	52	-0.632	0.048	329	40	0.946	0.031
4A1	5	48 hr	1644	403	24	-1.946	0.085	1376	84	0.379	0.084
$4B_1$	8	48 hr	1644	572	35	-0.933	0.034	985	60	0.625	0.048
$4B_2$	8	48 hr	1644	525	32	-1.025	0.008	1060	64	0.564	0.680
$5A_1$	5	1 wk	12	9.9	83	-0.081	0.051	0.7	6		-
$5A_2$	5	1wk	12	7	58	-0.178	0.026	1.4	12		-
$6A_1$	5	1 wk	118	44	37	-0.678	0.092	53	45		-
$7A_1$	5	1 wk	822	239	29	-0.979	0.063	562	68	0.452	0.740
$8B_1$	8	1 wk	822	373	45	-0.625	0.080	250	30		-
$8B_2$	8	1 wk	822	328	40	-0.646	0.052	250	30		-
$9A_1$	5	1 wk	1644	226	14	-1.239	0.070	1345	82	0.277	0.048
$9A_2$	5	1 wk	1644	250	15	-1.252	0.049	1340	82	0.285	0.014
$10B_1$	8	1 wk	1644	431	26	-1.025	0.051	910	55	0.829	0.052
$10B_2$	8	1 wk	1644	433	26	-1.104	0.062	925	56	0.858	0.050
$11A_1$	5	4 wk	12	7.8	65	-0.417	0.070	3.5	29		-
$11A_2$	5	4 wk	12	6.9	57	-0.457	0.054	3.5	29		-
$12A_1$	5	4 wk	118	63	53	-0.692	0.053	55	47		-
$12A_2$	5	4 wk	118	58	49	-0.835	0.103	60	51		-
$13A_1$	5	4 wk	822	130	16	-1.210	0.045	665	81	0.286	0.025
$13A_2$	5	4 wk	822	160	19	-1.279	0.041	645	78	0.352	0.036
$13B_2$	8	4 wk	822	444	54	-0.518	0.030	288	40	0.778	0.093
$14A_1$	5	4 wk	1644	194	12	-1.283	0.053	1432	87	0.190	0.040
$14A_2$	5	4 wk	1644	325	20	-1.315	0.038	1425	87	0.202	0.042
$14B_1$	8	4 wk	1644	625	38	-0.897	0.028	955	58	0.647	0.054

Table 6.2 Summary of results of the Ni isotope analysis of the solid c-disordered birnessite and the corresponding reaction solutions. The letter (A or B) next to the sample number represents the pH of the experiment, where *A* corresponds to the experiments conducted at pH 5 and *B* corresponds to experiments conducted at pH 8. The subscript (1 or 2) denotes the sample repeat. The symbol [Ni] % is the amount of Ni associated with the solid/solution fractions as a percentage of the total Ni added to each individual experiment.

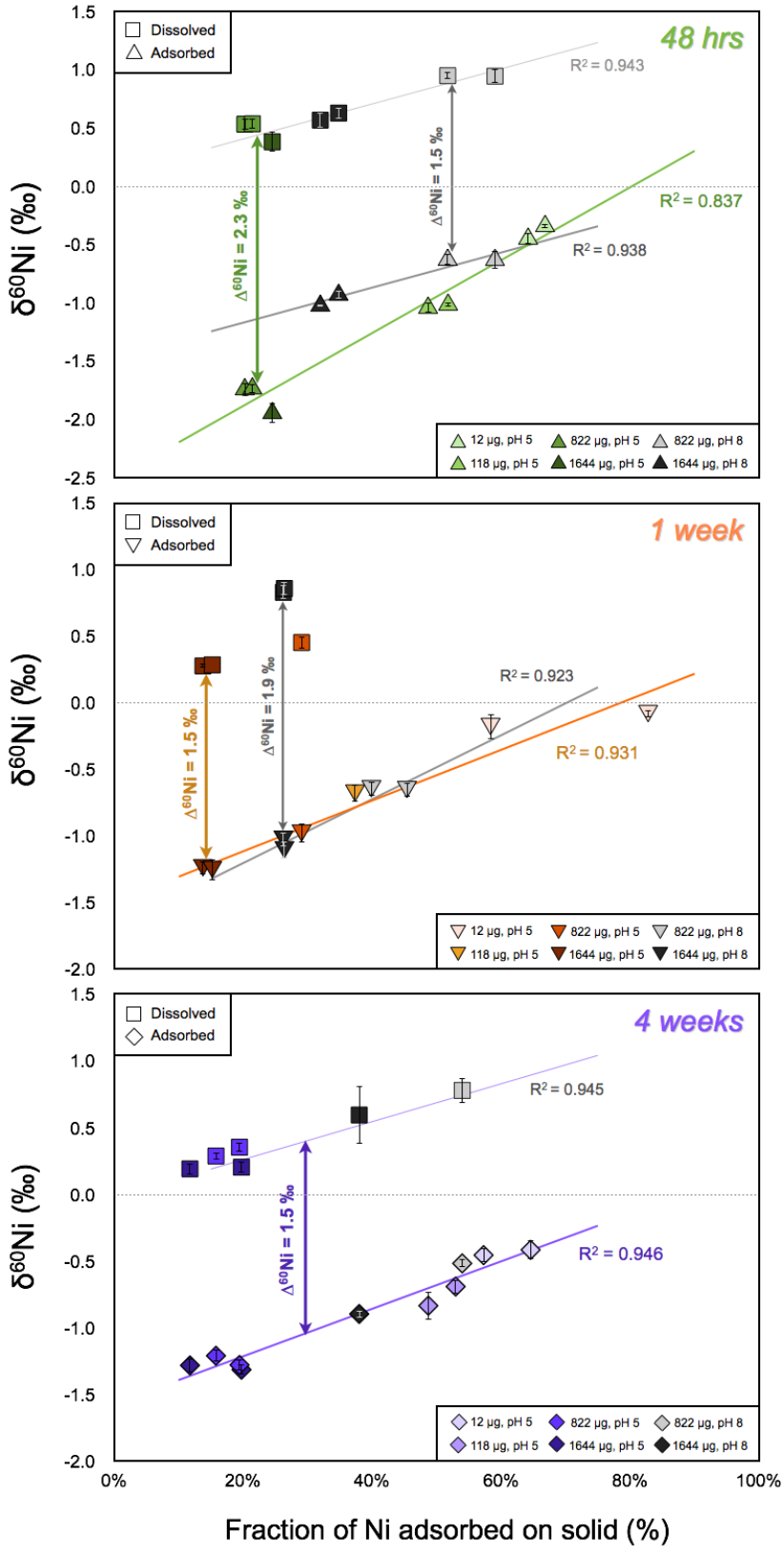

Figure 6.3 Plot showing the δ^{60}Ni isotopic composition of the solid-solution pairs versus the fraction of Ni sorbed to synthetic c-disordered birnessite ([Ni] %), as a function of pH, equilibration time and initial Ni loading ($[Ni]_{total}$ µg).

As highlighted previously, both the solid birnessite and the corresponding reaction solutions were analyzed via ICP-MS for their respective Ni concentrations prior to Ni isotope analysis. It can be seen from comparison of the experimental parameters in Table 6.1 and the results presented in Table 6.2, that for the most part, the concentrations of Ni sorbed to the solid c-disordered birnessite phase are consistent with those estimated based on previous sorption edge experiments for Ni on synthetic hexagonal birnessite (Peacock and Sherman, 2007a).

The first point to note from visual analysis of Figure 6.3 is that regardless of the experimental conditions, the sorption of Ni to synthetic c-disordered birnessite is accompanied by isotopic fractionation, during which, the solid birnessite phase is preferentially enriched in the light Ni isotope, leaving the remaining solution isotopically heavy. In addition, the measured data for all of the solid-solution pairs plot on single parallel lines. This linear relationship is highly indicative of a closed system equilibrium isotopic exchange (e.g. Barling and Anbar, 2004) between aqueous Ni and Ni sorbed to the birnessite surface, as opposed to a uni-directional kinetic isotope effect. The linear relationship between δ^{60}Ni values of the solution samples and the δ^{60}Ni values of the corresponding solid samples also indicates that mass balance has been maintained in the system.

6.4.1 Effect of Absolute Amount of Ni Sorbed

It is evident from visual analysis of Fig 6.3 that regardless of sample equilibration time the isotopically heaviest solid-solution pair is also the experiment with the highest fraction of Ni sorbed, ([Ni] %) and, as such, all three individual plots display a positive correlation between the measured δ^{60}Ni values and the fraction of Ni sorbed to birnessite. It is important to note however, that the fraction of Ni sorbed to the birnessite solid ([Ni] %) is actually inversely correlated to the absolute amount of Ni sorbed ([Ni] μg), at fixed pH (either pH 5 or pH 8; see Table 6.2). Accordingly, as the fraction of Ni sorbed to the birnessite surface increases ([Ni] %), the absolute amount of Ni sorbed to the solid birnessite phase decreases ([Ni] μg), and this in turn appears to give rise to a heavier δ^{60}Ni isotopic composition in the solid phase. This trend is evident in both pH regimes, and at all sample equilibration times (Figure 6.3). For clarity, the trend between the absolute amount of Ni sorbed to the birnessite and the δ^{60}Ni isotopic composition of the solid phase is illustrated below in Figures 6.4 - 6.6. Data is presented as the average amount of Ni sorbed Vs the average δ^{60}Ni

isotopic composition of the solid phase, where the averages are calculated as the average of the two sample repeats.

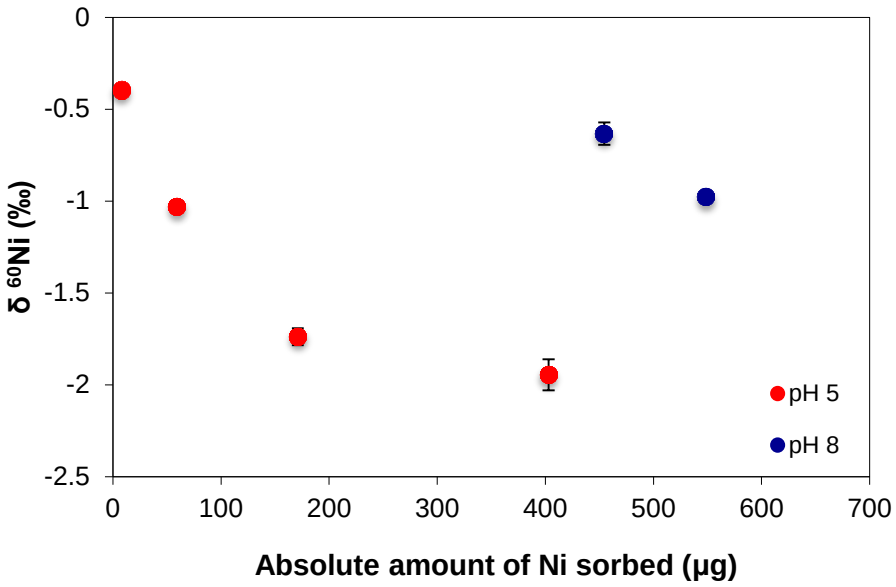

Figure 6.4 The average δ^{60}Ni isotopic composition of the solid c-disordered birnessite phase as a function of average absolute Ni sorbed after 48 hr equilibration at pH 5 and pH 8.

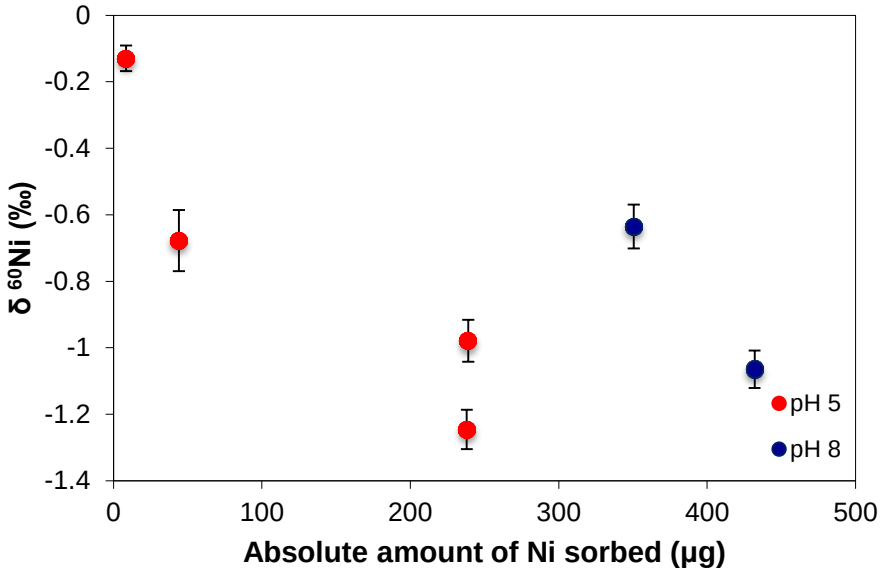

Figure 6.5 The average δ^{60}Ni isotopic composition of the solid c-disordered birnessite phase as a function of average absolute Ni sorbed after 1 week equilibration at pH 5 and pH 8.

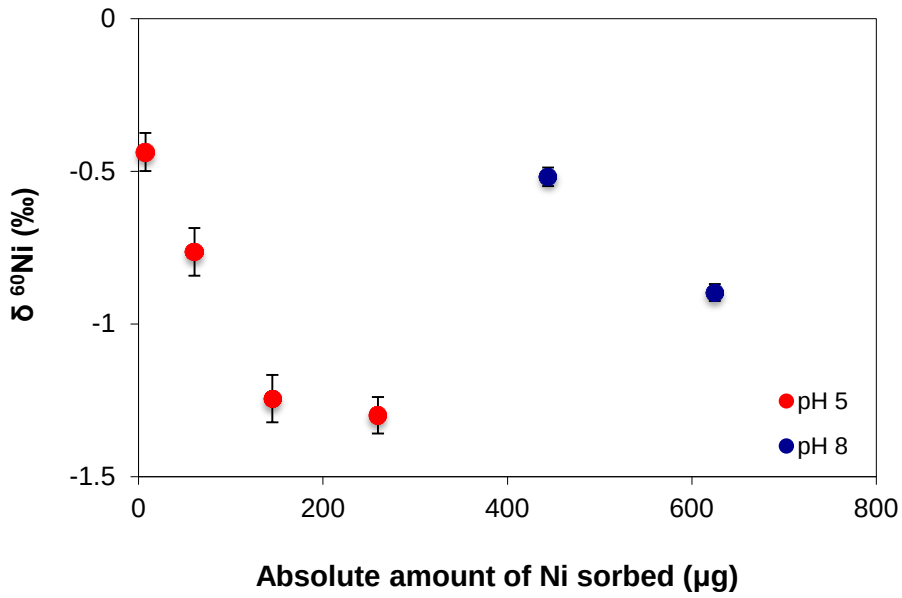

Figure 6.6 The average δ^{60}Ni isotopic composition of the solid c-disordered birnessite phase as a function of average absolute Ni sorbed after 4 week equilibration at pH 5 and pH 8.

Figure 6.4 highlights the relationship between the average absolute amount of Ni sorbed to the birnessite and the average δ^{60}Ni isotopic composition of this phase after 48 hr equilibration at both pH 5 and pH 8. Considering first the experiments performed at pH 5 (in red) and at the lowest absolute Ni sorbed, the average amount of Ni sorbed is ~7.8 µg, and the corresponding average δ^{60}Ni isotopic composition is ~ -0.45 ‰. In comparison, at the maximum absolute Ni sorbed achieved in these experiments, the average amount of Ni sorbed is considerably higher at ~403 µg and the average isotopic composition is substantially lighter at ~ -1.95 ‰. Similarly, analysis of the samples equilibrated at pH 8 (in blue) show that at the lowest absolute Ni sorbed an average of ~455 µg Ni is sorbed, which exhibits an average isotopic composition of ~ -0.63 ‰, while at the maximum absolute Ni sorbed achieved, ~548 µg of Ni is sorbed, which again displays a significantly lighter average isotopic composition at ~ -0.98 ‰.

The drift towards heavier δ^{60}Ni isotopic compositions in the solid phase with a decrease in the absolute amount of Ni sorbed is also apparent regardless of sample equilibration time. For example, Figure 6.6 displays the average absolute amount of Ni sorbed along with the average δ^{60}Ni isotopic compositions of the solid phase after the full 4 week equilibration period. Again, at pH 5 the lowest average amount of Ni

sorbed is ~7.4 μg, and the corresponding average δ^{60}Ni isotopic composition is ~ -0.45 ‰; while at the highest absolute Ni sorbed, an average of ~330 μg Ni is sorbed, which accordingly displays a substantially lighter average δ^{60}Ni isotopic composition at ~ -1.35 ‰. Again, the lowest average amount of Ni sorbed to the solid phase after equilibration at pH 8 for 4 weeks is ~444 μg, and the corresponding δ^{60}Ni isotopic composition of the solid phase is ~ -0.52 ‰, while at the highest absolute Ni sorbed of ~625 μg the average δ^{60}Ni isotopic composition of the solid is again lighter at approximately ~ -0.89 ‰.

In summary, the results presented above suggest that lower amounts of Ni sorbed to the solid birnessite surface are more favourable for a c-disordered birnessite phase with a heavier δ^{60}Ni isotopic composition.

6.4.2 Effect of solution pH

In general, the results presented in Table 6.2 and Figure 6.3 show that the fraction of Ni sorbed to the birnessite surface ([Ni] %) is higher at pH 8 compared to pH 5 at comparable initial Ni loadings ($[Ni]_{total}$ μg). For example, for samples equilibrated for 48 hr with initial Ni loadings of 822 μg $[Ni]_{total,}$ ~20 % of the total Ni is sorbed at pH 5 (samples $3A_1$ and $3A_2$), while in comparison, ~55 % of the total Ni is sorbed at pH 8 (samples $3B_1$ and $3B_2$). These results are comparable and consistent with trends observed for Ni uptake to synthetic hexagonal birnessite (e.g. Peacock and Sherman, 2007a).

Considering only the absolute amount of Ni sorbed from previous section (6.4.1), then the general overarching trend suggests that lower [Ni] sorbed to the birnessite give rise to a more positive δ^{60}Ni isotopic composition of the solid c-disordered birnessite phase. Importantly however, when looking at these trends as a function of pH (i.e. red vs blue data points) the trend line of the data from the pH 8 experiments presented in Figures 6.4 - 6.6 and in Figure 6.7 is almost always above that of the experiments conducted at pH 5. As such, the solid birnessite samples from the experiments conducted at pH 8 display a heavier δ^{60}Ni isotopic composition, despite the fact that in individual experiments conducted at fixed initial Ni loadings there is inevitably more Ni sorbed at pH 8. Essentially, it appears that in order to drive the δ^{60}Ni isotopic composition of the solid c-disordered birnessite phase towards heavier values, and thus in turn towards a δ^{60}Ni isotopic composition more

representative of marine ferromanganese crusts, low concentrations of Ni should be sorbed to the birnessite surface. Importantly however, it appears from these experiments that this must be achieved by having a low initial Ni loading in each individual experiment as opposed to low pH conditions.

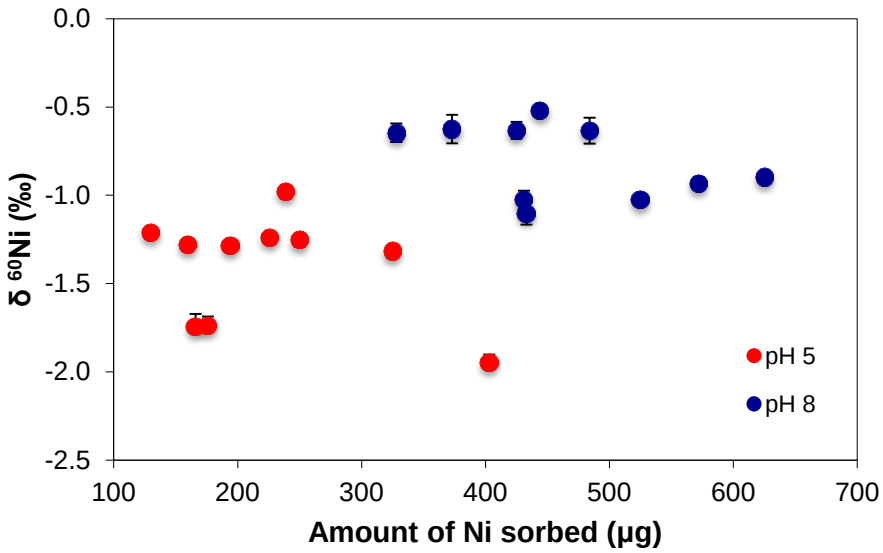

Figure 6.7 The δ^{60}Ni isotopic composition of the solid c-disordered birnessite phase as a function of pH.

6.4.3 Effect of sample equilibration time

It is evident from analysis of Table 6.2 and Figure 6.3 that the first set of samples (i.e. samples $1A_1$–$4B_2$), which were left to equilibrate for 48 hr, show a variation in δ^{60}Ni isotopic composition of the birnessite between -1.95 ‰ and -0.34 ‰, and in δ^{60}Ni remaining in solution between 0.38 and 0.95 ‰. The second set of sorption experiments (i.e. samples $5A_1$–$10B_2$), which were left to equilibrate for 1 week, show a variation in δ^{60}Ni on the birnessite between -1.25 ‰ and -0.08 ‰, with δ^{60}Ni in solution varying between 0.28 ‰ and 0.86 ‰. The final set of samples, which were equilibrated for 4 weeks (samples $11A_1$ -$14B_1$), show the smallest range of δ^{60}Ni values of all of the three sample sets. The δ^{60}Ni values measured for the birnessite vary between -1.32 ‰, and -0.42 ‰, while δ^{60}Ni values for the solution vary from 0.19 ‰ to 0.78 ‰.

In addition, it is also apparent from the data presented in Table 6.2 and Figure 6.3 that the samples equilibrated for 48 hr show a notable difference between the experiments performed in each pH regime. For example, experiments conducted at pH 5 show an isotopic fractionation between the solution and solid (i.e. $\delta^{60}Ni_{soln\text{-}solid}$) of 2.3 ‰, while the experiments conducted at pH 8 show a significantly smaller fractionation between the solution and solid of only 1.5 ‰. A $\delta^{60}Ni_{soln\text{-}solid}$ of 1.5 ‰ is also displayed by the experiments performed for 1 week and 4 weeks, where by this point, differences in the magnitude of the fractionation as a function of pH are no longer evident with both the pH 5 and pH 8 samples plotting on the same correlation lines (Figure 6.3).

The results tabulated in Table 6.2 also indicate that the solid samples at pH 8 show a slight drift towards heavier average $\delta^{60}Ni$ isotopic compositions with an increase in equilibration time. This relationship is apparent regardless of initial Ni loading and is highlighted below in Figure 6.7.

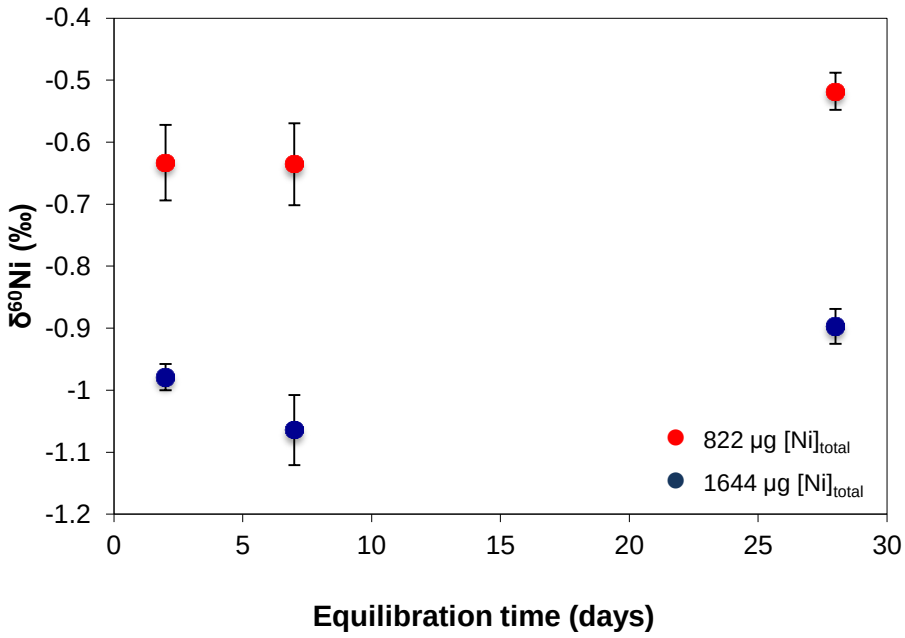

Figure 6.8 The average $\delta^{60}Ni$ isotopic composition of the solid c-disordered birnessite phase as a function of equilibration time at pH 8. µg $[Ni]_{total}$ is the amount of Ni initially added to each experiment.

The average δ^{60}Ni isotopic composition of the birnessite at initial loadings of 822 μg $[Ni]_{total}$ is ~ -0.63 ‰, and within error, the isotopic composition of the solid remains the same until at least 1 week. By 4 weeks the average δ^{60}Ni isotopic composition has become heavier at ~ -0.51 ‰. Similarly, at loadings of 1644 μg $[Ni]_{total}$ the isotopic composition of the solid after 48 hr is ~ -0.98 ‰, and is not significantly different within error after 1 week, but by 4 weeks the solid is isotopically heavier at ~ -0.89 ‰.

In contrast, experiments performed at pH 5, display a slightly different behaviour as a function of equilibration time. Firstly, it is apparent from Table. 6.2 and Figure 6.8 below that the experiments prepared with the lowest initial Ni loadings of 12 μg and 118 μg $[Ni]_{total}$ display average δ^{60}Ni isotopic compositions for the birnessite of ~ -0.39‰ and ~ -1.1‰ respectively, after 48 hr. By 1 week, solid samples from both these initial Ni loadings are slightly heavier at ~ -0.17 ‰ and ~ -0.67 ‰, respectively. By 4 weeks solid samples from both initial Ni loadings are marginally lighter than the solid phase after 1 week, but heavier than the average isotopic composition after just 48 hr at -0.44 ‰ and -0.76 ‰ respectively.

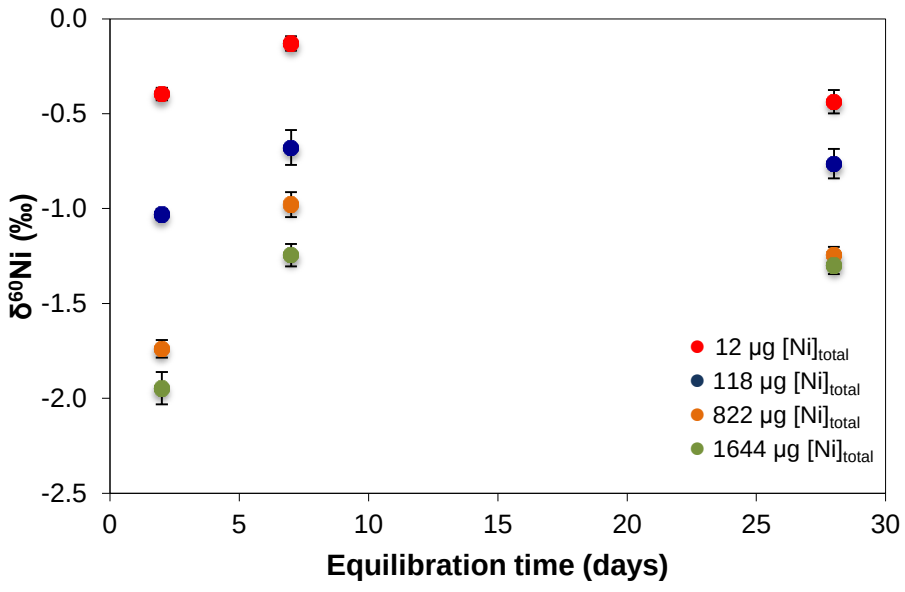

Figure 6.9 The average δ^{60}Ni isotopic compositions of the solid c-disordered birnessite phase as a function of equilibration time and initial Ni loadings at pH 5. μg $[Ni]_{total}$ relates to the amount of Ni initially added to each experiment.

Samples prepared at higher initial Ni loadings of 822 μg and 1644 μg $[Ni]_{total}$ follow a similar trend, in that the solid samples equilibrated for 4 weeks are heavier with respect to their δ^{60}Ni isotopic compositions than those equilibrated for just 48 hr at the same initial Ni loadings.

In summary, all of the experiments conducted in the current study show that the sorption of Ni to synthetic c-disordered hexagonal birnessite is accompanied by an isotopic fractionation, during which sorption of the light Ni isotope is unequivocally favored, thus leaving the remaining in solution isotopically heavy. In addition, the magnitude of the isotope effect between the solid-solution pairs is particularly large at 1.5 ‰.

The experiments also reveal that the δ^{60}Ni isotopic composition of the solid c-disordered birnessite phase and the corresponding solutions are sensitive to all experimental parameters, namely, initial Ni loading / absolute amount of Ni sorbed to the solid, pH and sample equilibration time. It appears based on these results that relatively low absolute amount of Ni sorbed on the solid (conversely relatively high fraction of Ni sorbed from a dilute, as opposed to more concentrated, solution), higher solution pH and increased equilibration time are favorable for a c-disordered birnessite phase with a heavier δ^{60}Ni isotopic composition.

6.5 Discussion

Experimental data for mass-dependent stable isotope fractionations is rare for many transition metal isotope systems, and the current study provides the first data set for Ni isotope fractionation during the sorption of aqueous Ni to synthetic c-disordered hexagonal birnessite.

Isotopic analysis of the both the solid birnessite and the corresponding reaction solutions shows that regardless of experimental conditions, the sorption of Ni to c-disordered birnessite is accompanied by isotopic fractionation, during which the synthetic birnessite phase is preferentially enriched in the light Ni isotope, thus leaving the remaining solution isotopically heavy. While some degree of isotopic fractionation during sorption was expected, the direction of the isotopic fractionation is somewhat surprising, because, if sorption does indeed impart an isotopic signature, then stable isotope fractionation theory predicts that the heavy Ni isotope should be preferentially

concentrated in the stronger bonding environment, which in turn is usually provided by the solid phase. In addition, the magnitude of the fractionation measured between the solid-solution pairs in this study ($\delta^{60}Ni_{solid\text{-}soln}$ of 1.5 ‰) is unexpectedly large. Finally, the results presented in this work are somewhat inconsistent with the heavy Ni isotopic compositions (+0.7 ‰ - +2.5 ‰) recorded in natural ferromanganese crusts (Gall et al., 2013). Considering the fact that modern global seawater exhibits a Ni isotopic composition of +1.44 ± 0.15 ‰ (Cameron and Vance, 2014), and assuming that this has not changed significantly over the Cenozoic during crust deposition, then a significant proportion of the global crusts that have been measured appear to be heavy with respect to seawater (those with isotopic compositions more than +1.44 ± 0.15 ‰), with isotopic fractionations ($\delta^{60}Ni_{solid\text{-}soln}$) up to ~ 1 ‰.

Equilibrium stable isotope fractionation describes the partial separation of isotopes between two or more substances that are in, or are approaching, chemical equilibrium. As mentioned previously, according to stable isotope theory there are a set of general qualitative chemical rules governing equilibrium stable isotope fractionations, which can be used to make predictions about the magnitude and direction of isotope fractionation between two separate substances (Schauble, 2004). In the first instance, equilibrium isotope fractionations usually decrease as temperature increases, and, all else being equal, fractionations are typically largest for light elements and for isotopes with very different masses (e.g., Schauble, 2004). In addition to these rules, a further consideration of equilibrium thermodynamics provides a means to predict which substances will be enriched in heavy isotopes in a given geochemical system. In equilibrium thermodynamics, all systems essentially strive to achieve their lowest energy state. Because chemical bonds involving heavier isotopes have a lower ground state energy than otherwise identical bonds involving lighter isotopes of the same element, then during equilibrium isotope fractionation the heavy isotope will tend to concentrate in the substance that confers the lowest ground state energy for that particular bond, i.e., in the substance that confers the strongest bonding environment. This process is well demonstrated for the isotope exchange of ^{18}O and ^{16}O between liquid water and water vapour:

$$H_2{}^{16}O\ (l) + H_2{}^{18}O\ (g) \Leftrightarrow H_2{}^{18}O\ (l) + H_2{}^{16}O\ (g)$$

(Eq. 6.1)

where at, or approaching, chemical equilibrium, ^{18}O concentrates in the stronger O-H bonds of liquid water phase relative to the weaker O-H bonds of the vapour phase.

The formation of strong bonding environments, i.e., strong chemical bonds, essentially correlates with several physico-chemical properties, including high oxidation state in the element of interest and low coordination number (Schauble, 2004). Thus with a choice of bonding environment between substance *A* with element *E* in low oxidation state, and substance *B* with element *E* in high oxidation state, the heavier isotopes will tend to concentrate in substance *B*, all else being equal. Similarly, with a choice of bonding environment between substance *A* with element *E* in high coordination, and substance *B* with element *E* in low coordination, the heavier isotopes will again typically concentrate in substance *B*. In general these rules for equilibrium isotope fractionation predict that large equilibrium fractionations are most likely to occur at low temperature between substances with significantly different oxidation states, coordination numbers, bonding partners and/or electronic configurations (Schauble, 2004).

The isotopic fractionation of Zn as a result of sorption to marine ferromanganese crusts is a perhaps a more relevant example of an isotope system that follows the rules of stable isotope theory as outlined above. For example, the free Zn^{2+} ion in seawater is present as the VI-fold $[Zn(H_2O)_6]^{2+}$ complex (e.g. Turner et al., 1981; Little et al., 2014). However, the sorption of Zn^{2+} to the birnessite surface is accompanied by a reduction in coordination environment to a IV-fold coordinated complex. Accordingly, marine ferromanganese crusts are heavy with respect to their Zn isotopic composition at around +0.9 - +1.5 ‰, compared to the isotopic composition of Zn in seawater at +0.5 ‰ (Marechél et al., 2000; Little et al., 2014). In comparison, the Ni^{2+} ion is also largely present in seawater as the VI-fold coordinated $[Ni(H_20)_6]^{2+}$ complex (Byrne, 2002), however, experimental EXAFS data have shown, that unlike Zn, Ni remains in VI-fold coordination during complexation above and below Mn octahedral vacancy sites on the birnessite [001] surface, and also during its subsequent incorporation into the birnessite structure (Peacock and Sherman, 2007a; Peacock, 2009). In addition, the sorption of Ni to the birnessite surface is not accompanied by a change in oxidation state, nor is there a change in bonding partner, as the free Ni^{2+} ion is directly bound to oxygen in both seawater and at the birnessite surface. In light of the above discussion on stable isotope theory, and considering the crystal chemistry of Ni during sorption to birnessite, it is perhaps incorrect to assume that the heavy Ni isotope should concentrate in the solid birnessite phase. What is more clearly demonstrated by stable isotope theory is the fact that any fractionation associated with the sorption of Ni to birnessite should theoretically be relatively small, compared to the Zn stable isotope system for example, where significant changes in

Zn bonding environment occur on Zn sorption. As such, the large 1.5 ‰ separation between δ^{60}Ni for the solid-solution pairs reported in this study is difficult to explain in the context of stable isotope theory and experimental evidence on the mechanism of Ni sorption to birnessite.

With respect to the direction of the isotope fractionations measured in the current experimental study, it should be considered that an alternative process other than sorption to birnessite could be responsible for the heavy Ni isotopic compositions measured in natural ferromanganese precipitates (Gall et al., 2013). In light of recent research investigating the isotopic composition of Cu in marine ferromanganese crusts (Little et al., 2014), it is evident that significant attention should be paid to the role of organic Ni-binding ligands in controlling the speciation and isotopic composition of Ni in seawater. Recent isotopic measurements conducted on an array of ferromanganese crust samples have shown that these precipitates are isotopically light with respect to their Cu isotopic compositions at -0.3 ‰ to -0.5 ‰ relative to the Cu isotopic composition of seawater +0.9 ‰ (Little et al., 2014), despite the fact that theory predicts enrichment in the heavy isotope. In seawater, the free Cu^{2+} ion is present as the V-fold coordinated $[Cu(H_2O)_5]^{2+}$ complex, however, during sorption to birnessite in marine ferromanganese crusts Cu^{2+} may be present as either a III-fold or IV-fold coordinated complex (Sherman and Peacock, 2010; Little et al., 2014). In a similar manor to the Zn isotope system, the reduction in coordination environment during sorption to marine ferromanganese crusts should lead to a heavy Cu isotopic composition in the solid phase. It has been suggested by Little et al. (2014) that because approximately 99 % of all dissolved Cu^{2+} in seawater is complexed by a group of strong class 1 organic ligands (e.g. Moffet and Dupont, 2007; Buck et al., 2012) that the Cu isotopic signatures recorded in marine ferromanganese crusts only reflect part of the isotopic separation between the sorbed and dissolved pools of Cu^{2+} in seawater. As such, it is suggested that the extent of any isotopic fractionation between the free Cu^{2+} ion and ligand-bound Cu in seawater must be quantified. In practice however, measuring the isotopic compositions of individual organic ligands in seawater is fraught with difficulty and theoretical predictions are often used as an alternative. Accordingly, recent *ab initio* calculations for both Cu-malonate and Cu acetohydroxaomate complexes, which are believed to be good synthetic analogues for humic acid and marine siderophore-type complexes, predict that these ligands should be enriched in the heavy Cu isotope by around +0.55 ‰ and +1.1 ‰, respectively (Sherman, 2013). Given these recent estimates, it appears that ligand bound Cu in seawater may be isotopically heavy, thus in turn leaving isotopically light

Cu^{2+} free to sorb to marine ferromanganese crusts (Little et al., 2014).

It is known, that the speciation of Ni in estuarine environments is strongly influenced by complexation to both fulvic and humic substances (Turner and Martino, 2006), however, the association of Ni with organic ligands in the deep ocean is less well understood. If for example, Ni-complexing ligands prove to exert a significant control on the isotopic composition of Ni in seawater, it could be the case that the light Ni isotope is preferentially bound to organic ligands, leaving the heavy isotope to sorb to ferromanganese crusts. Initial studies into the fractionation of Ni isotopes during complexation by organic molecules is promising, and computational calculations indicate that the uptake of Ni by organics in seawater may indeed preferentiality sequester the light Ni isotope (Fujii et al., 2011). In a scenario where strong Ni-binding ligands are absent from solution, such as the experimental setup employed in the current study, the uptake of the light Ni isotope to the mineral surface may be overwhelmingly favored.

Perhaps another important factor that should be given some consideration when assessing the results of this experimental study is the extent to which Ni is incorporated into the birnessite structure. As highlighted previously, in marine ferromanganese precipitates Ni is found exclusively incorporated into the birnessite structure (e.g. Bodeï et al., 2007; Manceau et al., 2007a,b; Peacock and Sherman, 2007a). Recent lab-based EXAFS studies show however, that the process of Ni incorporation occurs relatively slowly over time at circumneutral pH, via the rearrangement of surface sorbed Ni (Peacock, 2009). For example, it has been demonstrated experimentally that at pH 4 Ni is sorbed above and below octahedral vacancy sites on the birnessite surface after equilibration for 24 hr, whereas equilibration at pH 7 for the same time duration sees a shift from an entirely surface sorbed Ni complex to a birnessite with approximately 90 % of the total Ni sorbed to the surface and approximately 10 % structurally incorporated into the birnessite crystal lattice. Accordingly, the proportion of Ni incorporated into the birnessite structure continues to increase with prolonged equilibration at pH 7, and after 2.5 weeks approximately 70 % of the Ni was found to be surface sorbed, while the remaining 30 % was structurally incorporated (Peacock, 2009). Based on the results of this previous work, it is therefore not expected that Ni incorporation will occur under the conditions of the pH 5 experiments, regardless of equilibration time. As such, the isotopic signatures recorded in the low pH experiments (pH 5) should entirely reflect surface sorption. This is also likely to be the case at pH 8 after 48 hr equilibration

time, and even potentially for the 1 week experiments. A significant proportion of Ni incorporation would only be expected in the samples equilibrated for 4 weeks at pH 8 and therefore, theoretically at least, the Ni isotopic signal recorded in these samples should reflect a mix of surface sorption and structural incorporation, although the exact proportion is unknown.

Given the fact that Ni is found to be entirely incorporated into the birnessite structure in marine ferromanganese crusts (e.g. Manceau et al., 2007b; Peacock and Sherman 2007b), it may be the case that the heavy Ni isotopic signal recorded in these marine sedimentary archives, only manifests once all of the surface sorbed Ni is completely incorporated into the birnessite crystal lattice, or alternatively, when a critical ratio of surface sorbed vs incorporated Ni is reached. Indeed the current data set (Fig. 6.6, and Table 6.2) shows a trend towards lighter δ^{60}Ni isotopic compositions in the solid birnessite phase under low pH conditions (pH 5) where all surface complexation is expected to occur above and below octahedral vacancy sites. In contrast, at pH 8 and with increasing equilibration time, the δ^{60}Ni isotopic compositions of the solid phase, although still isotopically light relative to the reaction solution, are heavier compared to the isotopic compositions of the solid phase at pH 5 (e.g. Figs. 6.6, 6.7 and 6.8). The shift towards an isotopically heavier solid composition with both an increase in equilibration time and an increase in solution pH may potentially be the result of a progressive rise in the proportion of Ni incorporated into the birnessite crystal structure.

In order to test this assertion experimentally and thus potentially elucidate what balance of surface sorbed vs incorporated Ni might invoke a heavy isotopic signal, there is clearly a need for additional Ni sorption experiments over considerably longer time scales.

6.6 Summary and conclusions

The current study provides the first insight into Ni isotope fraction as a result of sorption to the Mn oxide birnessite. Results show that Ni isotopes are fractionated as a result of sorption to synthetic c-disordered hexagonal birnessite, during which, the solid birnessite phase is preferentially enriched in the light Ni isotope, leaving the remaining solution isotopically heavy. The results of the current experimental study highlight two major issues:

1. The direction of the measured isotope fractionations are somewhat inconsistent with measurements of the Ni isotopic compositions of natural marine ferromanganese precipitates, where a significant proportion of the precipitates measured are isotopically heavy at around with respect to the modern Ni isotopic composition of seawater.

2. The magnitude of the isotope effect i.e. $\delta^{60}Ni_{soln.}$ - $\delta^{60}Ni_{soln}$ = 1.5 ‰ is large considering the fact that Ni does not undergo a change in coordination environment, bonding partner or oxidation state during sorption to the birnessite surface, or during incorporation into the birnessite crystal structure.

Both the direction of the fractionation and the magnitude of the isotope effect are difficult to explain in the context of stable isotope theory. Although it appears based on the results of the current experimental study that relatively low absolute amount of Ni sorbed on the solid (conversely relatively high fraction of Ni sorbed from a dilute, as opposed to more concentrated, solution), high solution pH and increased equilibration time drive the solid phase towards heavier $\delta^{60}Ni$ isotopic composition, more like the isotopic composition of many marine ferromanganese precipitates with respect to contemporaneous seawater.

It also seems likely, based on recent studies on other transition metal isotope systems (e.g. Fujii et al., 2011; Sherman, 2013; Little et al., 2014), that the complexation of Ni by organic ligands in seawater could impart a significant influence on the Ni isotopic composition of seawater and thus in turn marine ferromanganese

crusts. As such, it would be instructive to perform similar experiments as those here but with the addition of a variety of strong organic complexes to the reaction solution. According to recent research (Fujii et al., 2011), certain organic Ni binding ligands present in seawater may favour the uptake of the light Ni isotope, thus leaving the heavy Ni isotope free to sorb to marine ferromanganese crusts.

Chapter 7

Summary and Future Work

7.1 Characterization of the transformation of birnessite to todorokite

Work presented in chapter 4 of this thesis provides the first detailed insight into the crystallization pathway and mechanism of todorokite formation from birnessite under conditions analogous to those found in marine diagenetic and hydrothermal settings. Knowledge of this transformation pathway is crucial for our understanding of the eventual fate and mobility of trace metals sequestered to the authigenic birnessite phase and, thus, for ultimately quantifying the role of marine ferromanganese precipitates in global trace element cycles.

In the current study, synthetic c-disordered hexagonal birnessite was transformed to todorokite via a mild hydrothermal treatment procedure, the transformation pathway was investigated and characterized as a time-series using a combination of XRD, FTIR, BET surface area analysis, SEM, HR-TEM and Mn K-edge EXAFS spectroscopy. As a result of the findings of this work I propose a new four-stage process for the transformation of birnessite to todorokite. Specifically I present evidence for: (i) the initial formation of local nano-domains of todorokite within the 10 Å phyllomanganate interlayer; (ii) the formation and growth of 8-10 nm wide primary todorokite particles, that grow from solution specifically along the [010] crystallographic direction (b* direction) by up to 200 nm; (iii) the lateral self-assembly of the initially formed primary todorokite crystallites across the [100] direction (a* direction) exclusively via the attachment of the [100] crystal faces, to form substantially larger and more crystalline secondary todorokite laths, which grow up to 150 nm wide and 600 nm in length; (iv) the further assembly and oriented aggregation of secondary todorokite laths to form stacked layers, in which individual laths of todorokite attach at angles 120º to each other, most likely in order to preserve structural continuity between each successive layer. The results and observations presented in chapter 4 are consistent with todorokite crystal growth via an oriented attachment-type growth mechanism, as opposed to growth solely from solution via traditional crystal ripening.

To my knowledge this is the first study to observe isolated primary todorokite particles and capture their apparent self-assembly and oriented growth during todorokite formation. Although the formation and subsequent growth of todorokite via an oriented attachment-type mechanism helps to explain many of the unique morphological and structural features observed in natural marine todorokite, this new mechanism of growth ultimately raises important questions about the retention of trace species during todorokite formation and growth.

Furthermore, in light of this work, and by considering previous studies investigating the transformation of birnessite to todorokite, I also suggest that there are two major prerequisites for the formation of crystalline todorokite directly from 10 Å phyllomanganate phase; (i) the 10 Å phyllomanganate must contain a sufficient amount of structural Mn(III) to allow the kinking/rearrangement of MnO_6 octahedra within the phyllomanganate layers and thus the formation of todorokite nucleation sites; (ii) the phyllomanganate sheets of the 10 Å phyllomanganate must also display some degree of semi-coherent ordering along the c-axis, so that as the phyllomanganate layers kink/rearrange, there are sufficient adjacent layers to allow for the formation of the todorokite tunnel walls. The absence of one or both of these prerequisites has been shown in previous studies to result in the formation of a variety of other layer-type and tunnel-type Mn oxides.

In order to hone the work presented here, there are several areas where further experiments would be beneficial. Firstly, in order to determine whether, and if so when, traditional crystal ripening occurs, one needs to determine at which point in the transformation all of the 10 Å phyllomanganate phase has transformed to todorokite. As discussed in chapter 4, this is very difficult to assess via analysis of the XRD patterns alone, as the 10 Å phyllomanganate intermediate and the neo-formed todorokite product share the same major diffraction features. In addition, the application of other complementary techniques such as SEM or TEM analysis is similarly inconclusive. It has however, been highlighted in the study of Feng et al. (2004) that todorokite is thermally stable up to temperatures reaching 400°C, while in contrast the 10 Å phyllomanganate intermediate (buserite), collapses back to a 7 Å phyllomanganate phase at temperatures above 140°C. As such, thermal decomposition experiments, coupled with XRD analysis, could be undertaken for the 10 Å phyllomanganate phase and the subsequent reflux products in order to determine at what point in the reaction all of the phyllomanganate has been consumed. This is crucial in order to eventually determine an overall rate law for the transformation process. To my knowledge, there is currently no kinetic data for the

transformation of birnessite to todorokite. The primary parameters needed to constrain the rate of transformation for any given reaction includes the %, fraction (α) or concentration of the product phase with time, at a fixed temperature and pressure. For the birnessite todorokite system investigated in the current study this could be determined experimentally using thermal decomposition experiments for example. With this data in hand it would then be possible to generate a series of plots displaying the % transformation vs time or fraction of transformation (α) vs time. This is useful if several parallel experiments were conducted at a range of different temperatures to gauge qualitatively how changes in the experimental conditions affect the overall reaction rate. In the case of the birnessite to todorokite transformation there are currently no data for either the rate (k) or the activation energy (E_a) of the transformation. The best approach to try and determine these parameters would firstly involve the application of the Avrami equation (Eq 7.1).

$$\alpha = 1 - \exp(-kt)^n$$

(Eq. 7.1)

Where α is the fraction transformed, k is the rate, t is time and *n* is a constant which depends on the mechanism. Linearizing the avrami equation yields equation 7.2 from which it is possible to obtain values for the rate of the reaction (k) (e.g.Putnis, 1992).

$$-\ln \ln(1-\alpha) = n \ln k + n \ln t$$

(Eq. 7.2)

A reaction/phase transformation whose kinetics conform to the avrami equation should give a rise to a straight line when –ln ln(α-1) is plotted against lnt. From the plot the slope of the line is equal to *n*, and the value at which the line intersects the y intercept is equal to n lnk.

Having obtained a value for the rate of the reaction it is subsequently possible to calculate the activation energy (E_a) for the overall transformation process of birnessite to todorokite from the Arrhenius equation (Eq. 7.3).

$$\ln k = \ln A - (E_a/RT)$$

(Eq. 7.3)

Where A is the pre-exponential factor (1/s), E_a is the activation energy (kJ/mol), R is the universal gas constant (8.314 J/mol K) and T is temperature in

degrees Kelvin. By subsequently constructing an Arrhenius plot of lnk vs 1/T the activation energy can be extracted from the slope of the plot, which corresponds directly to $-E_a / R$. While the point at which the extrapolated line of the slope crosses the y intercept is equal to ln A.

It would also be potentially beneficial to undertake future TEM analysis on the birnessite/todorokite system using a cryogenic TEM (cryo-TEM) setup, as this would circumvent any potential issues that may arise as a result of sample drying, such as the preservation of drying artefacts.

Finally, with a view to further understanding the formation and growth of todorokite in the marine environment, and fully testing the applicability of these experiments to the formation of todorokite in such a setting, it would be insightful to investigate the effect of ionic strength on the growth of todorokite via oriented attachment. Typically, in other systems that undergo growth via an oriented attachment-type pathway, the interaction of particles prior to a so called “attachment event” is often described by the DVLO (Derjaguin-Landau-Verwey-Overbeek) theory of inter-particle interaction. In short, the theory accounts for both electrostatic repulsion and weak van der Waals forces between approaching particles as a function of particle distance (e.g. Stumm, 1992; Mullaugh and Luther, 2011). It is well understood that increasing ionic strength suppresses the thickness of the electrical double-layer surrounding the mineral surface, thus in terms of OA-type crystal growth, increasing the ionic strength of the background electrolyte should theoretically lower the energy between two “approaching” particles (e.g. Zhang et al., 2008; Mullaugh and Luther, 2011; Burrows et al., 2012). Accordingly, DVLO theory predicts that increasing the ionic strength of the background electrolyte will not only increase the likelihood of particle-particle contact, but also accelerate the overall rate of growth via OA. As the todorokite synthesis procedure described in this thesis was conducted under particularly high ionic strength conditions, (1 M $MgCl_2$) it should at least be considered that the experimental conditions could have favored the growth of large todorokite laths via an OA-dominated pathway. Such effects have been demonstrated experimentally for other mineral systems, including the growth and aggregation of goethite nanorods and CdS nanoparticles (Mullaugh and Luther, 2011; Burrows et al., 2012). In the case of goethite, it was found that increasing the concentration of the background electrolyte from 0.1 mM to 80 mM $NaNO_3$ lead to a statistically significant increase in the growth rate constant (Burrows et al., 2012). While in the case of CdS nanoparticles, it was similarly found that increasing the ionic strength of the background electrolyte from 0.002 M to 0.032 M NaCl resulted in an increase in the

growth rate via OA (Mullaugh and Luther, 2011). In both cases however, the authors did note that increasing the ionic strength further to 0.5 M did not further enhance the rate of particle growth via OA.

7.2 The effect of Ni on the mechanism of formation and growth of todorokite

In light of the new four-stage mechanism for the transformation of birnessite and growth of todorokite identified in chapter 4, the work presented in chapter 5 of this thesis investigates the effect of Ni on the transformation of birnessite to todorokite. As natural marine birnessite is typically enriched in trace metals it is important to consider the effects of trace metal impurities on the transformation process. Accordingly, a Ni-rich c-disordered birnessite phase, containing approximately 1 wt % Ni was synthesized via a co-precipitation method, and subsequently transformed to todorokite over a 4 week period using the mild hydrothermal treatment procedure. The transformation pathway was fully characterized using XRD, TEM, ICP-OES and BET surface area analysis, while the distribution and phase association of Ni during the transformation was investigated using Ni *k*-edge EXAFS spectroscopy and TEM coupled with EDS.

The results presented in chapter 5 revealed that the incorporation of Ni into the precursor phyllomanganate phase and thus the 10 Å phyllomanganate intermediate inhibits transformation to todorokite. For example, XRD, BET surface area data and TEM images all show that that the formation and growth of todorokite is delayed, while the crystallinity of the neo-formed todorokite is reduced, in comparison to the Ni-free system. As predicted in chapter 4 and discussed further in chapter 5, it is likely that the nucleation of todorokite (i.e. the formation of the todorokite tunnel walls) within the 10 Å phyllomanganate interlayer is disrupted because Ni is a non Jahn-Teller active species. Therefore the Ni-rich 10 Å phyllomanganate layers are, to a certain extent, stabilized against topotactic rearrangement, which in turn disrupts and delays the formation of todorokite primary particles and their growth via the addition of ions from solution.

Crucially however, while the presence of both surface sorbed and structurally incorporated Ni in the 10 Å phyllomanganate structure appears to inhibit the overall rate of todorokite formation and the crystallinity of the neo-formed todorokite product,

there is no evidence to suggest that this sorbed Ni has a significant effect on the growth mechanism of todorokite via an oriented attachment-type pathway. It is evident from analysis of the TEM images presented in chapter 5 that following todorokite nucleation, primary todorokite particles exhibit direction specific growth from solution exclusively along the [010] direction, while large todorokite laths measuring up to 700 x 150 nm grow via the simultaneous attachment of the [100] primary particle crystal faces, and continued growth from solution along the [010] direction.

In order to further investigate the role of Jahn-Teller vs. non Jahn-Teller cations on the nucleation and growth of todorokite, similar experiments to those in this work are required, but using, for example, Cu-doped birnessite precursors, where Cu is Jahn-Teller distorted. Comparison of these experiments to the work reported in this thesis would help to further elucidate the effect of metal impurities on the rate and mechanism of transformation, and in turn determine the fate of the impurities as the transformation proceeds.

It would also be potentially useful to undertake the transformation of the 10 Å phyllomanganate to todorokite in smaller batch experiments, spiking each individual reaction solution with varying concentrations of Ni, in order to investigate the effect of entirely surface sorbed Ni on the aggregation of primary todorokite particles, and thus in turn the growth of large secondary todorokite laths. Based on the results presented in chapter 5, it would be expected that the sorption of Ni to the Mn(OH) sites along the edges of the neo-formed todorokite primary particles would be largely unfavourable for the growth of large todorokite laths via the orientated attachment of todorokite primary particles across the [100] direction.

7.3 The fate and mobility of Ni during the transformation of birnessite to todorokite

In chapter 5 of this thesis Ni K-edge EXAFS, TEM-EDS and Ni solution data were used to trace the distribution of Ni during the transformation of birnessite to todorokite. In the first instance, Ni K-edge EXAFS data show that the co-precipitation method used in the current study generates a Ni-rich c-disordered birnessite precursor phase, with ~60 % of the Ni incorporated into the birnessite structure and ~40% sorbed as an inner-sphere surface complex above and below octahedral vacancy sites on the birnessite [001] surface. Time-series EXAFS then shows that, as the reflux proceeds, Ni remains sequestered by the 10 Å phyllomanganate

intermediate as an incorporated and surface sorbed complex, despite the progressive formation and growth of todorokite within the sample matrix. However, at 2 wk reflux, there is a notable amount of both Ni and Mn present in the reflux solution. This dissolution likely occurs because there is a change in phase stability around this time in the reaction, as the relatively large neo-formed todorokite particles become dominant over the relatively small birnessite platelets. Some of the released Ni is subsequently sequestered to the neo-formed todorokite phase, where it is specifically sorbed to Mn(OH) sites at the edge of the todorokite triple chains as a tridentate corner-sharing complex. In this coordination environment, Ni is substantially more susceptible to remobilization than it would be if it were incorporated into the todorokite structure.

In total, approximately 50% of the total Ni associated with the 10 Å phyllomanganate phase was released into solution over the course of the transformation processes. Therefore, contrary to previous assumptions, the transformation of birnessite to todorokite does not appear to provide a direct route for the incorporation of (non Jahn-Teller) trace metals into the neo-formed todorokite structure. These results go some way to explaining why natural marine todorokites typically concentrate less Ni than the 10 Å phyllomanganate phase from which they apparently crystallized (Siegel and Turner, 1983; Bodeï et al., 2007).

Moreover, these results suggest that the oxic diagenesis of birnessite in marine sediments provides a source of Ni, and perhaps other trace metals, to marine sedimentary porewaters, thus potentially providing a benthic flux of trace metal micronutrients to seawater.

7.4 Extent of Ni isotope fractionation during sorption to birnessite

Hydrogenetic marine ferromanganese crusts have been shown to exhibit heavy Ni isotopic compositions up to ~ +2.5 ‰ (Gall et al., 2013), compared to the Ni isotopic composition of global seawater (Vance et al., 2014). At present, little is known about the fundamental processes that give rise to the heavy Ni isotopic composition measured in marine ferromanganese crusts, however, it has been demonstrated for a range of other transition metal systems that the sorption of these species to mineral surfaces can be a major driver of isotope fractionation (e.g. Barling et al., 2004; Wasylenki et al., 2011; Little et al., 2014). Thus it is plausible that the uptake of aqueous Ni from ambient seawater could account for the heavy Ni isotopic

composition of hydrogenetic marine ferromanganese precipitates. A mechanistic understanding of the fundamental processes that drive this fractionation is paramount for the development of the Ni isotope system as a biogeochemical tracer, and specifically, Ni isotopes may shed light on the birnessite to todorokite transformation process, Ni release into solution, and subsequent processes that govern whether Ni is ultimately released to seawater or retained in the sediments.

In order to determine whether the uptake of Ni to the phyllomanganate birnessite could account for the heavy Ni isotopic composition of marine hydrogenetic precipitates, a series of individual sorption experiments were conducted using a synthetic c-disordered hexagonal birnessite phase, at pH 5 and pH 8, for time durations of 48 hrs, 1 week and 4 weeks, and at 4 different initial Ni loadings.

The work conducted in chapter 6 of this thesis provides the first experimental data set for the fractionation of Ni isotopes during sorption to hexagonal birnessite, and show that the sorption of Ni to birnessite is accompanied by an equilibrium-based isotope fractionation, during which, the light Ni isotope is preferentially sorbed by the birnessite. Consequently, the corresponding reaction solution remained isotopically heavy. Enrichment of the synthetic birnessite phase in the light Ni isotope was evident regardless of Ni loading, sample equilibration time, or solution pH.

Clearly, the direction of the isotopic fractionations measured in this experimental system contradicts recent Ni isotope data collected from natural ferromanganese crusts, which show that these precipitates are distinctly enriched in the heavy Ni isotope. In addition to the direction of fractionation, the relatively large magnitude of the isotope effect (1.5 ‰) between the solid birnessite and the reaction solution is also particularly surprising. As detailed in chapter 6, isotope effects are often more pronounced when the sorbent species undergoes a change in coordination environment during sorption (e.g. in the case of Tl, Mo, Zn on hexagonal birnessite (Barling and Anbar, 2004; Wasylenki et al., 2011; Peacock and Moon, 2012; Nielsen et al., 2013)). However, aqueous Ni does not undergo a significant change in coordination during uptake from solution to the birnessite surface or during incorporation into birnessite vacancy sites, where it is found in 6-fold coordination (e.g. Peacock and Sherman, 2007a; Peacock, 2009).

Unfortunately I was unable to offer a conclusive explanation for either the light Ni isotopic composition of the birnessite phase or indeed the magnitude of the fractionation between the solid birnessite and the reaction solution. Notably however, the Ni isotopic composition of the birnessite solid and thus in turn the corresponding

solutions were sensitive to all three experimental parameters. Specifically, high pH, low amounts of Ni sorbed to the birnessite and increased equilibration time appeared to drive the Ni isotopic composition of the solid phase towards heavier isotopic values.

It is evident in light of these results, that a significant amount of further experimental work is required in order to determine the mechanistic processes responsible for the heavy Ni isotopic composition of marine ferromanganese precipitates. Specifically, I would recommend performing additional sorption experiments with pH, Ni loading and equilibration time, approaching those found in the marine system – i.e., at pH ~8, with Ni << 0.7 wt%, and for extended equilibration time. These experiments may also potentially elucidate whether the heavy Ni isotope signal recorded in ferromanganese crusts is a function of the proportion of Ni structurally incorporated into the birnessite structure. Certainly based on the results of recent sorption studies for Ni on hexagonal birnessite (e.g. Peacock, 2009) it is likely that at pH 5 the isotopic signal measured in these experiments reflects entirely Ni surface complexation over the octahedral Mn vacancy sites. Accordingly, an isotopic signal reflecting both a mixture of surface sorbed and incorporated Ni is only likely in the experiments equilibrated at pH 8 for 1 week and 4 weeks, and even in these experiments a larger proportion of the Ni is likely still sorbed to the birnessite surface, as opposed to Ni incorporated into the birnessite crystal lattice. Despite the fact there is no obvious change in the local co-ordination environment between surface sorbed and structurally incorporated Ni, the process of structural incorporation might impart an isotope fractionation that results in a heavier isotope signal for sorbed Ni.

Another promising avenue to explore with this work is the role of organic Ni-binding ligands in controlling the Ni isotopic composition of seawater, and thus in turn the isotopic composition of marine ferromanganese crusts. A recent combined experimental and theoretical study by Fujii et al. (2011), showed that during the equilibration of aqueous Ni with several organic complexes, including oxalic acid and a crown ether complex, the light Ni isotope was preferentially complexed by the organic ligands. In light of this previous study and the work conducted in chapter 6 of this thesis, it would be very insightful to conduct further bench top sorption experiments for Ni on hexagonal birnessite with the addition of several different organic Ni complexing agents, in order to investigate the Ni isotopic composition of the solid birnessite phase in the presence of organic Ni-binding ligands. Theoretically, if the complexation of the light Ni isotope is favoured by the organic ligands in solution, then the heavy Ni isotope should be free to sorb to the birnessite surface,

perhaps explaining the heavy isotope composition of natural marine ferromanganese precipitates that form in a system with abundant organic ligands.

References

Adams L. F, Ghiorse W. C. (1987) Characterization of extracellular $Mn2^{+}$ -oxidizing activity and isolation of an $Mn2^{+}$ -oxidizing protein from Leptothrix discophora SS-1. *J. Bacteriol.* **169**, 1279–1285.

Albarede F. and Beard B. (2004) Analytical methods for non-traditional isotopes. *Rev. Mineral. Geochem.* **55**, 113-152.

Anbar A. D. and Rouxel O. (2007) Metal stable isotopes in paleoceanography. *Ann. Rev. Earth Planet. Sci.* **35**, 717-746.

Andersen M. S., Nyvang V., Jakobsen R. and Postma D. (2005) Geochemical processes and solute transport at the seawater freshwater interface of a sandy aquifer. *Geochim. Cosmochim. Acta* **69**, 3979–3994.

Appelo C. A. J. and Postma D. (1996) From rainwater to groundwater. *In Geochemistry, Groundwater and Pollution* (ed.A. A. Balkema). Rotterdam, Brookfield.

Appelo C. A. J. and Postma D. (1999) A consistent model for surface complexation on birnessite (δ-MnO_2) and its application to a column experiment.*Geochim. Cosmochim*. *Acta*. **63**, 3039-3048.

Arrhenius G. (1963). Pelagic sediments. In: *Hill, M.N.* (Ed.), Sea, 3. Interscience, New York, pp 655–727.

Banerjee R., Roy S., Dasgupta S., Mukhopadhyay S. and Miura H.(1999) Petrogenesis of ferromanganese nodules from east of the Chagos Archipelago, Central Indian Basin, Indian Ocean. *Mar. Geol*. **157**, 145–158.

Banfield J. F., Welch S. A., Zhang H., Ebert T. T. and Penn R. L. (2000) Aggregation-based crystal growth and microstructure development in natural iron oxyhydroxide biomineralization products. *Science*. **289**, 751–754.

Bargar J. R., Tebo B. M., Villinski J. E. (2000) In situ characterization of Mn (II) oxidation by spores of the marine Bacillus sp. strain SG-1. *Geochim. Cosmochim*. *Acta* **64**, 2775–2778.

Bargar J. R., Tebo B. M., Bergmann U., Webb S. M., Glatzel P., Chiu V. Q. and Villalobos M. (2005) Biotic and abiotic products of Mn (II) oxidation by spores of the marine Bacillus sp. strain SG-1. *Am. Mineral*. **90**, 143–154.

Barling J. and Anbar A. D. (2004) Molybdenum isotope fractionation during adsorption by manganese oxides. *Earth. Planet. Sci. Lett.* **317**, 148-155. **217,** 315-329.

Bilinski H., Giovanoli R., Usui A. and Hanzel D. (2002) Characterization of Mn oxides in cemented streambed crusts from Pinal Creek, Arizona, USA, and I n hot-spring deposits from Yuno-Taki falls, Hokkaido, Japan. *Am. Mineral*. **87**, 580.

Binsted N., Pack M. J., Weller M. T. and Evans J. (1996) Combined EXAFS and powder diffraction analysis. *J. Am. Chem. Soc*. **118**, 10200–10210.

Binsted N. (1998) EXCURV98: The Manual. CLRC Daresbury Laboratory, Warrington, UK

Bodeï S., Manceau A., Geoffroy N., Baronnet A., Buatier, M. (2007). Formation of todorokite from vernadite in Ni-rich hemipelagic sediments. *Geochim. Cosmochim. Acta* **71**, 5698–5716.

Bonatti E., Kraemer T. and Rydell H. (1972) Classification and genesis of submarine Iron- manganese deposits. In: *Ferromanganese deposits on the ocean floor (eds. Horn D.)* Lamont Doherty Geological Observatory of Columbia University, Palisades, NY. pp.149-161

Booth C. H. and Hu Y-J. (2009) Confirmation of standard error analysis techniques applied to EXAFS using simulations. *J. Phys. Conf. Ser.* **190**.

Brindley G. W. and Brown G. (1980) Crystal Structures of Clay Minerals and their X-ray Identification. Mineralogical Society, London.

Brouwers G. J., Vijgenboom E., Corstjens P. L. A. M., De Vrind J. P. M., De Vrind-De Jong E. W. (2000): Bacterial Mn^{2+} Oxidizing Systems and Multicopper Oxidases: An Overview of Mechanisms and Functions. *Geomicrobiol. J*. **17:1**, 1-24.

Brown G. E., Parks G. A and O'Day P. A. (1995) Sorption at mineral-water interfaces: macroscopic and microscopic perspectives. In: *Mineral Surfaces* (eds. Vaughn D. J. and Pattrick R. A. D.) The Mineralogical Society series. **5**, 129-183.

Bruland K. (1980) Oceanographic distributions of cadmium, zinc, nickel, and copper In the North Pacific*. Earth. Planet. Sci. Lett*. **47**,176–198.

Bruland K. W. and Lohan M. C. (2003) Controls of Trace Metals in Seawater*. In Treatise on Geochemistry*, vol. 6 (ed. H. Elderfield). Elsevier, Amsterdam. pp. 23–47.

Buck K. N., Moffett J., Barbeau K. A., Bundy R. M., Kondo Y., Wu J. (2012) The organic complexation of iron and copper: an inter comparison of competitive ligand exchange–adsorptive cathodic stripping voltammetry (CLE-ACSV) techniques. *Limnol.Oceanogr*. Methods **10**, 496–515.

Bullen T. D. (2011) Stable Isotopes of Transition and Post-Transition Metals as Tracers in Environmental Studies. In: *Handbook of Environmental Isotope Geochemistry, Advances in Isotope Geochemistry* (ed. Baskaran M.) Springer-Verlag, Berlin, Heidelberg. pp. 177-203.

Burdige D.J. (1993). The biogeochemistry of manganese and iron reduction in marine sediments. *Earth. Sci. Rev*. **35**, 249– 284.

Burns R. G. and Burns V. M. (1977) Mineralogy of ferromanganese nodules. In *Marine Manganese Deposits* (ed. G. P. Glasby). Elsevier, Amsterdam.

Burns V. M. and Burns R. G. (1978a) Authigenic todorokite and phillipsite inside deep-sea manganese nodules. *Am. Mineral*. **63**, 827-831.

Burns V. M. and Burns R. G (1978b) Post-depositional metal enrichment processes inside manganese nodules from the north equatorial pacific. *Earth Planet. Sci. Lett*. **39**, 341-348.

Burns R. G., Burns V. M. and Stockman H. (1983) A review of the todorokite buserite problem: implications to the mineralogy of marine manganese nodules. *Am. Mineral*. **68**, 972–980

Burns R. G., Burns V. M. and Stockman H. (1985) The todorokite–buserite problem: further consideration. *Am. Mineral*. **68**, 972–980

Burrows N. D., Hale C. R. H., Penn R. L. (2012) Effect of ionic strength on the kinetics of crystal growth by orientated aggregation. *Cryst. Growth. Des.* **12**, 4787-797.

Byrne R. H., Kump L. R. and Cantrell K. J. (1988) The influence of temperature and pH on trace metal speciation in seawater. *Mar. Chem*. **25**, 163–181.

Byrne R. H. (2002) Inorganic speciation of dissolved elements in seawater: the influence of pH on concentration ratios. *Geochem. Trans*. **3**, 11-16.

Calvert S. E. and Price N. B. (1970) Composition of manganese nodules and manganese carbonates from Loch Fyne, Scotland. *Contrib. Mineral. Petrol.* **29**, 215-233.

Calvert S. E. and Pedersen T. F. (1993) Geochemistry of Recent oxic and anoxic marine sediments: Implications for the geological record. *Mar.Geol.* **113**, 67-88.

Cameron V., Vance D., Archer C., House C. H. (2009) A biomarker based on the stable isotopes of Ni. *Proc. Natl. Acad. Sci. U.S.A.* **106**,10944-10948.

Cameron V. and Vance D. (2014) Heavy nickel isotope compositions in rivers and the oceans. *Geochim. Cosmochim. Acta.* **128**, 195-211.

Cahyani V., Murase J., Ishibashi E., Asakawa S. and Kimura M. (2009) Phylogenetic positions of $Mn2^{+}$-oxidizing bacteria and fungi isolated from Mn nodules in rice field subsoils. *Biol. Fertil. Soils.* **45**, 337–346.

Ching S., Krukowska K. S. and Suib S. L. (1999) A new synthetic route to todorokite-type manganese oxides. *Inorg. Chim. Acta* **294**, 123–132.

Chukhrov F. V., Gorshkov A. I., Rudnitskaya Y. S., Berezovskaya V. V. and Sivtsov A. V. (1980a) Manganese minerals in clays: a review. *Clays Clay Miner.* **28**, 154–346.

Chukhrov F. V. and Gorshkov A. I. (1981) Iron and manganese oxide minerals in soils. *Trans. R. Soc. Edinb*. **72**, 195–200.

Chukhrov F. V., Sakharov B. A., Gorshkov A. I. , Drits V. A., and Dikov Y. P. (1985) Investiya Akademie Naukia, SSSR, Seriya GeologicheskayaCrystal structure of birnessite from the Pacific Ocean. *Intern. Geol. Rev.* **27,** 1082–1088 8, 66–73.

Crerar D. A. and Barnes H. L. (1974) Deposition of deep-sea manganese nodules. *Geochim. Cosmochim. Acta.* **38**, 279-300.

Cronan D. S. (1976) Basal metalliferous sediments from the eastern Pacific. *Bull. Geol. Soc. Amer.* **87**, 928-934.

Cui H. J., Feng X. H., He J. Z., Tan W. F. and Liu F. (2006) Effects of reaction conditions on the formation of todorokite at atmospheric pressure. *Clays Clay Miner*. **54**, 605–615.

Cui H. J., Liu X. W., Tan W. F., Feng X. H., Liu F. and Ruan H. D. (2008) Influence of Mn(III) availability on the phase transformation from layered buserite to tunnel-structured todorokite. *Clays Clay Miner*. **56**, 397–403.

Cui H. J., Qiu G. H., Feng X. H., Tan W. F. and Liu F. (2009) Birnessites with different average manganese oxidation states were synthesized, characterized, and transformed to todorokite at atmospheric pressure. *Clays Clay Miner*. **57**(6), 715–724.

De Groot F. (2001) High-resolution X-ray emission and X-ray absorption spectroscopy*. Chem. Rev.* **101**, 1779-1808.

Dick G. J., Lee Y. E. and Tebo B. M. (2006) Manganese(II)- oxidizing Bacillus spores in Guaymas Basin hydrothermal sediments and plumes. *Appl. Environ. Microbiol*. **72**, 3184–3190.

Dixon J. B. and Skinner H. C. W. (1992) Manganese minerals in surface environments. *In Biomineralization Processes of Iron and Manganese. Modern and Ancient Environments* (eds. H. C.W. Skinner and R. W. Fitzpatrick). CATENA Verlag, Cremlingen-Destedt, Germany.

Drits V. A., Silvester E., Gorshkov A. L., Manceau A. (1997) Structure of synthetic monoclinic Na-rich birnessite and hexagonal birnessite: I. Results from X- Ray Diffraction & Selected area electron diffraction. *Am. Mineral*. **82**, 946- 961.

Dupont C. L., Barbeau K., Palenik B. (2008) Ni up take and limitation in marine Synechococcus strains. *Appl and Environ Microbiol.* **74,** (1),23–31.

Dupont C. L., Buck K. N., Palenik B., Barbeau K. (2010) Nickel utilization in phytoplanktonic assemblages from contrasting oceanic regimes. *Deep-sea Res I.* **57**, 553-566.

Dymond J., Lyle M., Finney B., Piper D. Z., Murphy K., Conrad R. and Pisias N. (1984) Ferromanganese nodules from MANOP Sites H, S, and R-Control of Mineralogical and chemical composition by multiple accretionary processes. *Geochim. Cosmochim. Acta.* **48**, 931-949.

Fendorf S. E. and Zasoski R. J. (1992) Chromium (III) oxidation by δ-MnO_2.1. Characterization. *Environ.Sci.Technol*. **28**, 79-85.

Feng Q., Kanoh H., Miyai Y. and Ooi K. (1995) Metal ion extraction/insertion reactions with todorokite-type manganese oxide in the aqueous phase. *Chem. Mater*. **7**, 1722–1727.

Feng X. H., Tan W. F., Liu F., Wang J. B. and Ruan H. D. (2004) Synthesis of todorokite at atmospheric pressure. *Chem. Mater*. **16**, 4330–4336.

Feng X. H., Zhai L. M., Tan W. F., Lui F., He J. Z. (2007) Adsorption and redox reactions of heavy metals on synthesized Mn oxide minerals. *Environ. Pollut.* **147**, 366-373.

Feng X. H., Zhu M., Ginder-Vogel M., Ni C., Parikh S. J., Sparks D. L. (2010). Formation of nano-crystalline todorokite from biogenic Mn oxides. *Geochim. Cosmochim. Acta* **74**, 3232–3245.

Francis C. A. and Tebo B. M. (1999) Marine *Bacillus* spores as catalysts for oxidative precipitation and sorption of metals. *J. Mol. Microbiol. Biotechnol.* **1**, 71–78.

Francis C. A. and Tebo B. M. (2001) Diversity of *cumA* multicopper oxidase genes from Mn(II)-oxidizing and non-oxidizing Pseudomonasstrains. *Appl. Environ. Microbiol.* **67**, 4272–78.

Francis C. A., Co E. M., Tebo B. M. (2001). Enzymatic manganese (II) oxidation by a marine alpha-proteobacterium. *Appl. Environ. Microbiol.* **67,** (9), 4024-4029.

Francis C. A. and Tebo B. M. (2002) Enzymatic manganese(II) oxidation by metabolically dormant spores of diverse *Bacillus* species. *Appl. Environ. Microbiol.* 68:874–80

Frandsen C., Legg. B. L., Comolli. L. R., Zhang H., Gilbert B., Johnson E. and Banfield J. F. (2014) Aggregation-induced growth and transformation of β-FeOOH nanorods to micron-sized α-Fe_2O_3 spindles. *Cryst. Eng. Comm*

Frausto da Silva J. R. R. and Williams R. J. P. (2001) The Biological Chemistry of the Elements: The Inorganic Chemistry of Life, second ed. Oxford University Press, Oxford.

Friedl G., Wehrli B., and Manceau A. (1997) Solid phases in the cycling of manganese in eutrophic lakes: New insights from EXAFS spectroscopy. *Geochim. Cosmochim. Acta* **61**, 275–290.

Fujii T., Moynier F., Dauphas N., Abe M., (2011). Theoretical and experimental Investigation of nickel isotopic fractionation in species relevant to modern and ancient oceans. *Geochim. Cosmochim. Acta*. **75**, 469–482.

Fuller C. C., Davis J. A., Waychunas G. A. (1993) Surface-Chemistry of Ferrihydrite.2. Kinetics of Arsenate Adsorption and Coprecipitation. *Geochim. Cosmochim. Acta.* **57,** 2271-2282.

Gaillardet J., Viers J., Dupre B. (2003). Trace elements in river waters. *In:Treatise on Geochemistry. Surface and Ground Water, Weathering, and Soils.* **5**, 225–272.

Gaillot A-C. (2002) Caracterisation structurale de la birnessite: Influence du protocole de synthese. Ph.D thesis, Universite Joseph Fourier- Grenoble.

Gall L., Williams H. M., Siebert C. and Halliday A. N. (2012) Determination of mass-dependent nickel isotope compositions using double spiking and MC-ICPMS. J. Anal. Atom. Spectrom. 27, 137–145.

Gall L., Williams H. M., Siebert C., Halliday A. N., Herrington R. J., Hein J. R. (2013). Nickel isotopic compositions of ferromanganese crusts and the constancy of deep ocean inputs and continental weathering effects over the Cenozoic. *Earth. Planet. Sci. Lett.* **317**, 148-155.

Gilbert B., Zhang H., Huang F., Finnegan M. P., Waychunas G. A., Banfield J. F. (2003) Special phase transformation and crystal growth pathways observed in nanoparticles. *Geochem. trans.* **4,** 20-27.

Giovanoli R., Biirki P., Giuffredi M. and StummW. (1975b) Layer Structured Manganese Oxide Hydroxides. IV. The Buserite Group; Structure

Stabilization by Transition Elements. *Chimia*. **29**, 517-52.

Giovanoli R. (1985) A review of the todorokite-buserite problem: implications to the mineralogy of marine manganese nodules: disscusion. *Am. Mineral.* **70**, 202-204.

Glasby G. P. (2006) Manganese: predominant role of nodules and crusts. In Marine Geochemistry (eds. H. D. Schulz and M. Zabel). Springer, pp. 371–427.

Glover E. D. (1977) Characterization of marine birnessite. *Am. Mineral*. **62**, 278– 285.

Goldberg E. D. (1954) Marine geochemistry. I. Chemical scavengers of the sea. *J. Geol*. **62**, 249–265.

Golden D. C., Chen C. C. and Dixon J. B. (1987) Transformation of birnessite to buserite, todorokite and manganite under mild hydrothermal treatment. *Clays Clay miner.* **35**, 271-280.

Gramlish J., Machlan L., Barnes I., Paulsen P., (1989). Absolute isotopic abundance ratios and atomic weight of a reference sample of nickel. *J.Res.Natl.Inst.Stand.Tech*. **94**, 347–356**.**

Grangeon S., Lanson B., Lanson M., Manceau A., (2008) Crystal structure of Ni-sorbed synthetic vernadite: a powder X-ray diffraction study. *Mineral Mag*. **72**, 1279–1291.

Greaves G. N. (1995) New X-ray techniques and approaches to surface mineralogy. In: *Mineral Surfaces* (eds. Vaughn D. J. and Pattrick R. A. D.) The Mineralogical Society series. **5**, 87-128.

Green-Pedersen H., Jensen B. T., Pind N. (1997). Nickel adsorption on MnO_2, $Fe(OH)_3$, montmorillonite, humic acid and calcite: a comparative study. *Environ. Technol*. **18**, 807-815.

Halbach P., Scherhag C., Hebisch U. and Marchig V. (1981) Geochemical and mineralogical control of different genetic types of deep-sea nodules from the Pacific *Ocean. Miner. Deposita.* **16**, 59–64.

Hansel C. M. and Francis C. A. (2006) Coupled photochemical and enzymatic Mn(II) oxidation pathways of a planktonic Roseobacter-like bacterium. *Appl. Environ. Microb.* 72, 3543-3549.

Hastings D. and Emerson S. (1986) Oxidation of manganese by spores of a marine Bacillus: kinetic and thermodynamic considerations. *Geochim. Cosmochim. Acta.* **50**, 1819-1824.

Hein J. R., Koschinsky A., Halbach P., Manheim, F. T., Bau M., Kang J-K., and Lubick N. (1997): Iron and manganese oxide mineralizations in the Pacific. In: *Manganese mineralizations: Geochemistry of Terrestrial and Marine Deposits* (eds. K. Nicholson, J.R. Hein, B. Bühn and S. Dasgupta). Geological Society Special Publications. **199**, 123-138.

Hem J. D. (1981) Rates of Manganese oxidation in aqueous systems. *Geochim. Cosmochim. Acta.* **45**, 1369-1374.

Hochella M. F. (1995) Mineral surfaces: their characterization and their chemical, physical and reactive nature. In: *Mineral Surfaces* (eds. Vaughn D. J. and Pattrick R. A. D.) The Mineralogical Society series. **5**, 18-60.

Horner T. J., Schonbachler M., Rehkämper M., Nielsen S. G., Williams H., Halliday A. N., Xue Z. and Hein J. R. (2010) Ferromanganese crusts as archives of deep water Cd isotope compositions. *Geochem. Geophys. Geosys*. **11**, 1525-2027.

Hou X. and Jones B. T. (2000) Inductively coupled plasma/optical emission spectroscopy. In: *Encyclopedia of Analytical Chemistry*. (ed. R. A. Meyers) Wiley and Sons Ltd. 9468-9485.

Huang F., Zhang H and Banfield J. F (2003) The role of orientated attachment crystal growth in hydrothermal coarsening of Nano crystalline ZnS. *J. Phys. Chem B*. **107**, 10470-10475.

Jauhari P. (1987) Classification and inter-element relationships of ferromanganese nodules from the Central Indian Ocean Basin. *Marine Minerals*. **6**, 419-429.

Jones L. H. P. and Milne A. A. (1956) Birnessite, a new manganese oxide mineral from Aberdeenshire; Scotland. *Min Mag*. **31**, 283-288.

Joshima M. and Usui A. (1998) Magnetostratigraphy of hydrogenetic manganese crusts from Northwestern Pacific seamounts. *Marine Geol.* **146**, 53-62.

Julien C. M., Massot M., Poinsignon S. (2004) Lattice vibrations of manganese oxides part I. Periodic structures. *Spectrochim. Acta. A.* **60**, 689-700.

Kang L., Zhang M., Liu Z. H., Ooi K. (2007) IR spectra of manganese oxides with either layered or tunnel structure. *Spectrochim Acta*. **67**, 864-869.

Kim C. S., Brown G. E. and Rytuba J. J. (2000) Characterization and speciation of mercury-bearing mine wastes using X-ray absorption spectroscopy. *Sci. Tot. Environ*. **261**, 157–168.

Kim C. S., Lentini C. J., Waychunas G. A. (2008) Associations between iron oxyhydroxide nanoparticles growth and metal adsorption/structural incorporation. In Adsorption of Metals By *Geomedia II*: Variables, Mechanisms, and Model Applications, Barnett, M. (Ed.), Elsevier Academic Press, 478.

Konhauser K. O., Pecoits E., Lalonde S. V., Papineau D., Nisbet E. G., Barley M. E., Arndt N. T., Zahnle K. and Kamber B. S. (2009) Oceanic Ni depletion and a methanogen faminebefore the great oxidation event. *Nature.* **458**, 750-753.

Koschinsky A. and Halbach P. (1995) Sequential leaching of marine f erromanganese precipitates: genetic implications. *Geochim. Cosmochim. Acta*. **59**, 5113-5132.

Koschinsky A. and Hein J. R. (2003) Acquisition of elements from seawater by ferromanganese crusts: Solid phase associations and seawater speciation. *Marine Geol.* **198**, 331-351.

Krumbein W. E. and Jens K. (1981) Biogenic rock varnishes of the Negev Desert (Israel): An ecological study of iron and manganese transformation by cyanobacteria and fungi. *Oecologia*. **50**, 25-38

Kwon K. D., Refson K., Sposito G. (2009) On the role of Mn(IV) vacancies in the photoreductive dissolution of hexagonal birnessite. *Geochim. Cosmochim. Acta*. **73**, 4142-4150.

Kwon K. D., Refson K. and Sposito G. (2010) Surface complexation of Pb(II) by hexagonal birnessite nanoparticles. Geochim.Cosmochim. Acta 74, 6731–6740.

Lanson B., Drits V. A., Silvester A., Manceau A. (2000) Structure of H-exchanged hexagonal birnessite and its mechanism of formation from Na-rich monoclinic buserite at low pH. *Am. Mineral*. **85**, 826–838.

Learman D. R., Wankel S. D., Webb S. M., Martinez N., Madden A. S., Hansel C. M. (2011) Coupled biotic–abiotic Mn(II) oxidation pathway mediates the formation and structural evolution of biogenic Mn oxides. *Geochim. Cosmochim. Acta.* **75**, 6048-6063.

Lei G. and Boström K. (1995) Mineralogical control on transition metal distributions in marine manganese nodules. *Mar. Geol*. **123**, 253-261.

Li H.-Y., Schoonmaker J. (2003). Chemical composition and mineralogy of marine sediments. *In:Treatise on Geochemistry. Sediments, Diagenesis, and Sedimentary Rocks*. **7**, pp.1–35.

Ligane J. J and Karplus R. (1946) New method for Determination of Manganese oxidation state. *Ind. Eng. Chem. Anal*. **18**, 191-194.

Little S. H., Sherman D. M., Vance D., Hein J. R. (2014). Molecular controls on Cu and Zn isotopic fractionation in Fe-Mn crusts. *Earth. Planet. Sci. Lett.* **396**, 213-222.

Liu L., Feng Q., Yanagisawa K., Bignall G., Hashida T. (2002) Lithiation reactions of Zn- and Li-birnessites in non-aqueous solutions and their stabilities. *J. Mater. Sci*. **37**, 1315–1320.

Liu Z. H., Kang L., Ooi K., Yoji M. and Feng Q. (2005) Studies on the formation of todorokite-type manganese oxide with different crystalline birnessites by Mg2+-templating reaction. *J. Colloid. Interf. Sci*. **285**, 239–246.

Livi K. J. T., Lafferty B., Zhu M., Zhang S., Gaillot A C., Sparks D. L. (2011) Electron Energy-Loss safe-dose limits for manganese valence measurements in environmentally relevant manganese oxides. *Environ. Sci. Technol.* **46**, 970-976.

Luo J., Zhang Q., Huang A., Giraldo O. and Suib S. L. (1999) Double-aging method for preparation of stabilized Na-buserite and transformations to todorokites incorporated with various metals. *Inorg. Chem*. **38**, 6106–6113.

Malinger K. A., Laubernds K., Son Y. C., Suib S. L. (2004) Effects of Microwave Processing on Chemical, Physical, and Catalytic Properties of Todorokite-Type Manganese Oxides. *Chem. Mater.* **16***,* 4296-4303.

Manceau A. and Combes J. M. (1988) Structure of Mn and Fe oxyhydroxides – a topological approach by EXAFS. *Phys. Chem. Min*. **15**, 283–295.

Manceau, A., and Charlet, L. (1992) X-ray absorption spectroscopic study of the sorption of Cr(III) at the oxide/water interface. 1. Molecular mechanism of Cr(III) oxidation on Mn oxides. *J. Colloid Interface Sci.* **148**,443-458.

Manceau, A., Gorshkov, A. I. and Drits, V. A. (1992) Structural chemistry of Mn,Fe,Co, and Ni in manganese hydrous oxides: Part II. Information from

EXAFS spectroscopy and electron and X-ray diffraction. *Am Mineral*. **77**, 1144-1157.

Manceau A., Marcus M. A. and Tamura N. (2002b) Quantitative speciation of heavy metals in soils and sediments by synchrotron X-ray techniques. *In Rev. Min. Geochem*. **49**, 341–428.

Manceau A., Marcus M. A., Tamura N., Proux O., Geoffroy N., Lanson B. (2004) Natural speciation of Zn at the micrometer scale in a clayey soil using X-ray fluorescence, absorption and diffraction. *Geochim. Cosmochim. Acta.* **68**, 2467-2483.

Manceau A., Lanson M. and Geoffroy N. (2007a) Natural speciation of Ni, Zn, Ba and As in ferromanganese coatings on quartz using X-ray fluorescence, absorption and diffraction. *Geochim. Cosmochim. Acta* **71**, 95–128.

Manceau A., Kersten M., Marcus M. A., Geoffroy N. and Granina L. (2007b) Ba and Ni speciation in a nodule of binary Mn oxide phase composition from Lake Bikal. *Geochim. Cosmochim. Acta* **71**, 1967–1981.

Maréchal C., Nicolas E.,Douchet C., Albarède,F. (2000). Abundance of zinc isotopes as a marine biogeochemical tracer. *Geochem.Geophys.Geosyst*.**1**,1015.

Marcus M. A., Manceau A., Kersten M. (2004) Mn, Fe, Zn and As speciation in a fast-growing ferromanganese marine nodule. *Geochim. Cosmochim. Acta* **68**, 3125–3136.

Margolis S. V. and Burns R. G. (1976) Pacific deep-sea manganese nodules: their distribution, composition, and origin, Annu. Rev. Earth Planet. Sci. **4**, 229- 263.

McKenzie R. M. (1989) Manganese oxides and hydroxides: in minerals in soil environments, J. B. Dixon and S. B.Weed, eds., *Soil Science Society of America.* Madison Wisconsin. 493-502.

McKeown D. A. and Post J. E. (2001) Characterisation of manganese oxide rock mineralogy in rock varnish and dendrites using X-ray absorption spectroscopy. *Am. Mineral.* **86**, 701–713.

Mellin T. A. and Lei G. (1993) Stabilization of 10Å-manganates by interlayer cations and hydrothermal treatment: implications for the mineralogy of marine manganese concretions. *Mar. Geol*. **115**, 67–83.

Meng Y. T., Zehng Y. M., Zhang L. M., He J. Z. (2009) Biogenic Mn oxides for effective adsorption of Cd from aquatic environment. *Environ. Pollut.* **157**, 2577-2583.

Misaelides P., Katranas T., Godelitsas A., Klewe-Nebenius H., Anousis, I. (2002). The chemical behavior of the natural microporous manganese-oxide todorokite in actinides (Th, U, Pa) aqueous solutions. *Separ. Sci. Tecnol*. **37**(5), 1109–1121.

Miyata, N., Maruo, K., Tani, Y., Tsuno, H., Seyama, H., Soma, M., and Iwahori, K. (2006a) Production of biogenic manganese oxides by anamorphic asco-mycete fungi isolated from streambed pebbles. *Geomicrobiol. J*. **23**, 63-73.

Moffett J.W. and Dupont C. (2007) Cu complexation by organic ligands in the sub-arctic NW Pacific and Bering Sea. *Deep-Sea Res*., Part 1, *Oceanogr. Res. Pap*. **54**, 586–595.

Morel F. M. M., Milligan A. J., Saito M. A. (2003). Marine bioinorganic chemistry: the role of trace metals in the oceanic cycles of major nutrients. In: *Treatise on Geochemistry: The Oceans and Marine Geochemistry* (eds. Elderfield H., Holland H. D., Turekian K. K. Elsevier, pp. 113–143.

Morford J. L., Emerson S. R., Breckel E. J., Kim S.H. (2005) Diagenesis of oxyanions (V, U, Re and Mo) in pore waters and sediments from a continental margin. *Geochim. Cosmochim. Acta*. **69**, 5021-5032.

Mullaugh K. M. and Luther G. W. (2011) Growth kinetics and long-term stability of CdS nanoparticles in aqueous solution under ambient conditions. J*. Nanopart. Res.* **13**, 393-404.

Murray K. and Tebo B. (2007) Cr (III) is indirectly oxidised by the Mn(II) oxidising bacterium *Bacillus* sp. strain SG-1. *Environ. Sci. Technol.* **41**, 528-533.

Myneni S. C. B., Traina S. J., Logan T. J. and Waychunas G. A. (1997) Oxyanion behavior in alkaline environments: Sorption and desorption of arsenate in ettringite. *Environ. Sci. Technol.* **31**, 1761-1768.

Nealson K. H. and Ford J. (1980) Surface enhancement of bacterial manganese oxidation: implications for aquatic environments*. Geomicrobiol J.* **2**, 21–37.

Newville M. (2004) Fundamentals of XAFS. *Consortium for advanced radiation sources.* 1-41.

Nielsen S. G., Rehkamper M., Baker J. and Halliday A. N. (2004) The precise and accurate determination of thallium isotope compositions and concentrations for water samples by MCICPMS. *Chem. Geol*. **204**, 109–124.

Nielsen S.G., Wasylenki L.E., Rehkämper M., Peacock C.L. Xue Z., Moon E.M. (2013).Towards an understanding of thallium isotope fractionation during adsorption to manganese oxides. *Geochim.Cosmochim.Acta.* **117**, 252–265.

O'Reilly S. E. and Hochella M. F. (2003) Lead sorption efficiencies of natural and synthetic Mn and Fe-oxides. *Geochim. Cosmochim. Acta.* **23**, 4471-4487.

O'Young C. L. (1993) Manganese oxide octahedral molecular sieves: preparation, characterization and application. *Science.* **260**, 511–515.

Pakarinen J., Koivul R., Laatikainen M., Laatikainena K., Paateroa E., Harjulab R. (2010) Nanoporous manganese oxides as environmental protective materials—Effect of Ca and Mg on metals sorption. *J. Hazard. Mater*. **180**, 234–240.

Pauling L. (1960) The nature of the chemical bond. 3rd. ed. Cornell Univ. Press.

Peacock C. L. and Sherman D. M. (2007a) Sorption of Ni by birnessite: equilibrium controls on Ni in seawater. *Chem. Geol*. **238**, 94–106.

Peacock C. L. and Sherman D. M. (2007b) The crystal chemistry of Ni in marine ferro-manganese crusts and nodules. *Am Mineral*. **92**, 1087-1097.

Peacock C. L. (2009) Physiochemical controls on the crystal chemistry of Ni in birnessite: genetic implications for ferromanganese precipitates. *Geochim. Cosmochim. Acta* **73**, 3568–3578.

Peacock C. L. and Moon E. M. (2012) Oxidative scavenging of thallium by birnessite: Explanation for thallium enrichment and stable isotope fractionation in marine ferromanganese precipitates. *Geochim. Cosmochim. Acta* **84**, 297-313.

Peña J., Kwon K. D., Refson K., Bargar J. R., Sposito G. (2010) Mechanisms of Ni sorption by bacteriogenic birnessite. *Geochim. Cosmochim. Acta* **74,** 3076-3089.

Peña J., Bargar J. R., Sposito G. (2011) Role of Bacterial Biomass in the Sorption of Ni by Biomass-Birnessite Assemblages. *Environ. Sci. Technol.* **45**, 7338-7344.

Penn R. L. and Banfield J. F. (1998a) Imperfect Orientated Attachment: Dislocation Generation in Defect-Free Nanocrystals. *Science*. **281**, 969-971.

Penn R. L. and Banfield J. F. (1998b) Orientated attachment and growth, twinning, polytypism, and formation of metastable phases: Insights from nanocrystalline TiO_2.

Penn R. L., Oskam G., Strathmann T. J., Searson P. C., Stone A. T., Veblen D. R (2001) Epitaxial assembly in aged colloids. *J.Phys.Chem. B*. **105**, 2177-2182.

Penner-Hahn J. E. (1999) X-ray absorption spectroscopy in coordination chemistry. *Coord. Chem. Rev*. **190**, 1101- 1123.

Pokrovsky O.,Viers J., Freydier R. (2005) Zinc stable isotope fractionation during its adsorption on oxides and hydroxides. *J.Colloid. Interface. Sci*. **291,**(1),192–200.

Portehault D., Cassaignon S., Baudrin E. and Jolivet J. P. (2007) Morphology Control of Cryptomelane Type MnO_2 Nanowires by Soft Chemistry. Growth Mechanisms in Aqueous Medium. *Chem Mater*. **19**, 540-5417.

Post J. E. and Bish D. L. (1988) Rietveld refinement of the todorokite structure. *Am. Mineral.* **73**, 861–869.

Post J. E. and Veblen D. R. (1990) Crystal structure determinations of synthetic sodium, magnesium, and potassium birnessite using TEM and the Rietveld method. *Am. Mineral*. **75**, 477-489.

Post J. E. (1999) Manganese oxide minerals: crystal structures and economic and environmental significance. *Proc. Natl. Acad. Sci. U. S. A.* **96**, 3447–3454.

Price N. M. and Morel F. M. M. (1991) Colimitation of phytoplankton growth by nickel and nitrogen. *Liminol. Oceanogr.* **36**, 1071-1077.

Ravel B. and Newville M. (2005) ATHENA, ARTEMIS, HEPHAESTUS: Data analysis for X-ray absorption spectroscopy using IFEFFIT. *J. Synchrotron Radiat.* **12**, 537-541.

Ravel B. (2009) Composing complex EXAFS problems with severe information constraints. *J. Phys.: Conf. Ser.***190**.

Rehkämper M., Frank M., Hein J. R., Porcelli D., Halliday A., Ingri J. and Liebetrau V. (2002) Thallium isotope variations in seawater and hydrogenetic, diagenetic, and hydrothermal ferromanganese deposits*. Earth Planet. Sci. Let*. **197**, 65–81.

Rezaei M., Sanz E., Raeisi E., Ayora C., Vazquez-sune E. and Carrera J. (2005) Reactive transport modeling of calcite dissolution in the fresh-salt water mixing zone. *J. Hydrol*. **311**, 282–298.

Rudge J.F., Reynolds B.C., Bourdon B. (2009) The double spike toolbox. *Chem. Geol*. **265**, 420-431.

Saito M. A., Moffett J. W., Di Tullio G. R. (2004). Cobalt and nickel in the Peru u pwelling region: a major flux of labile cobalt utilized as a micronutrient. Global Biogeochemical Cycles.**18,** 4030–4044.

Santelli C.M., Webb S.M., Dohnalkova A.C., Hansel C.M. (2011). Diversity of Mn oxides produced by Mn(II) oxidising fungi. *Geochim. Cosmochim. Acta*. **75**, 2762- 2776.

Saratovsky I., Wightman P. G., Pasten P. A., Gaillard J. F. and Poeppelmeier K. R. (2006) Manganese oxides: parallels between abiotic and biotic structures. *J. Am. Chem. Soc*. **128**, 11188–11198.

Schauble E. (2004) Applying stable isotope fractionation theory to new systems. *Rev. Mineral. Geochem*. **55**, 65–111.

Sclater F. R., Boyle E. and Edmond J. M. (1976) On the marine geochemistry of nickel. *Earth Planet. Sci. Lett*. **31**, 119–128.

Shen Y. F., Zerger R. P., DeGuzman R. N., Suib S. L., McCurdy L., Potter D. I. and O'Young C-L. (1992) Octahedral Molecular Sieves: Preparation, Characterization and Applications. *J . Chem. Soc. Chem. Commun*. 1213-1214.

Sherman D. M. and Peacock C. L. (2010) Surface complexation of Cu on birnessite (d-MnO2): controls on Cu in the deep ocean. *Geochim. Cosmochim. Acta* **74**, 6721–6730.

Sherman D. M. (2013) Equilibrium isotopic fractionation of copper during oxidation/reduction, aqueous complexation and ore-forming processes: predictions from *ab initio* calculations.*Geochim.Cosmochim.Acta*. **118**,85–97.

Siebert C., Nagler T. F., Kramers J. D. (2001) Determination of molybdenum isotope fractionation by double-spike multicollector inductively coupled plasma mass spectrometry. *Geochem. Geoophys. Geosyst.* **2**, 1525-2027.

Siegel M. D. and Turner S. (1983) Crystalline todorokite associated with biogenic debris in manganese nodules. *Science.* **219**, 172-174.

Silvester E., Manceau A. and Drits V. A. (1997) Structure of synthetic monoclinic Na-rich birnessite and hexagonal birnessite; II, Results from chemical studies and EXAFS spectroscopy. *Am Mineral*. **82**, 962-978.

Somayajulu B. L. K. (2000) Growth rates of oceanic manganese nodules: Implications to their genesis, palaeo-earth environment and resource potential. *Curr. Sci.* **78**, 300-308.

Sparks D.L., Scheidegger A.M., Strawn D.G. and Scheckel K.G. (1999). *Kinetics and Mechanisms of Metal Sorption at the Mineral-Water Interface*. American Chemical Society Symposium Series. **715**,108-135.

Spiro T. G., Barger, J. R., Sposito, G., Tebo, B. M. (2010) Bacteriogenic Manganese oxides. *Acc. Chem. Res*. **43**, 2-9.

Stern E. (1993) Number of relevant independent points in x-ray-absorption fine structure spectra. *Phys. Rev*. **48**, 9825.

Takahashi Y., Manceau A., Geoffroy N., Marcus M. A., Usui A. (2007). Chemical and structural control of the partitioning of Co, Ce, and Pb in marine ferromanganese oxides. *Geochim. et Cosmochim. Acta*. 71, 984–1008.

Tan W. F., Lu S. J., Liu F., Feng X., He J. Z. and Koopal L. K. (2008) Determination of the point-of-zero charge of manganese oxides with different methods including an improved salt titration method. *Soil. Sci*. **137**, 277-286.

Taylor R. M., McKenzie R. M. and Norrish K. (1964) The mineralogy and chemistry of manganese in some Australian soils. *Aust. J. Soil Res*. **2**, 235–248.

Tebo B. M. and He L. M (1999). Microbially mediated oxidative precipitation reactions. In *Mineral-Water Interfacial Reactions Kinetics and Mechanisms*, (ed. D.L. Sparks, T.J. Grundl) pp. 393–414. Washington, DC: *Am. Chem. Soc.*

Tebo B. M., Johnson H. A., McCarthy J. K., Templeton A. S. (2005) Geomicrobiology of manganese (II) oxidation. *Trends Microbiol*. **13,** No.9, 421-428.

Templeton A. S., Staudigel H. and Tebo B. M. (2005) Diverse Mn(II)-oxidizing bacteria isolated from submarine basalts at Loihi Seamount. *Geomicrobiol. J*. **22**, 127–139.

Tenderholt A., Hedman, B. and Hodgson K. O. (2007) PySpline: A modern, cross-platform program for the processing of raw averaged XAS edge and EXAFS data. *AIP Conf. Proc. (XAFS13)* 882, 105-107.

Thauer R. K. (1998) Biochemistry of methanogenesis : a tribute to Marjory Stephenson. *Microbiol.* **144**, 2377-2406.

Tian Z. H., Yin Y. G., Suib S. L. (1997) Effect of Mg2+ Ions on the Formation of Todorokite Type Manganese Oxide Octahedral Molecular Sieves. *Chem. Mater*. **9**, 1126-1133.

Tomic S., Searle B. G., Wander A., Harrison N. M., Dent A. J., Mosselmans J. F. W., Inglesfield J. E. (2005) New Tools for the analysis of EXAFS: The DL EXCURV Package. CCLRC Technical Report DL-TR-2005-001. Council for the Central Laboratory of the Reasearch Councils, Swindon, UK.

Toner B., Manceau A., Webb S. M., Sposito G. (2006) Zinc sorption to biogenic hexagonal-birnessite particles within a hydrated bacterial biofilm. *Geochim. Cosmochim. Acta*. **70**, *27-43.*

Turner D. R., Whitfield M. and Dickson A. G. (1981) The equilibrium speciation of dissolved components in freshwater and sea water at 25^{o}C and 1 atm pressure. *Geochim. Cosmochim. Acta.* **45**, 855–881.

Turner A. and Martino M. (2006) Modelling the equilibrium speciation of nickel in the

Tweed Estuary, UK: voltametric determination and simulations using WHAM. *Mar. Chem*. **102**, 198–207

Turner S., Siegel M. D., Buseck P. R. (1982) Structural features of todorokite intergrowths in manganese nodules. *Nature*. **296**, 841-842.

Usui A., Mellin T. A., Nohara M. and Yuasa M. (1989) Structural stability of marine 10 Á manganates from the Ogasawara (Bonin) Arc: Implication for low-temperature hydrothermal activity. *Mar. Geol.* **86**, 41-56.

Usui A. and Glasby G. P. (1998) Submarine hydrothermal manganese deposits in the Izu-Bonin-Mariana arc: an overview. *Isl Arc*. **7**, 422-431.

Usui A. and Terashima S. (1997) Deposition of Hydrogenetic and Hydrothermal Manganese Minerals in the Ogasawara (Bonin) Arc Area, Northwest Pacific. *Mar. Georesour. Geotech*. **15**, 127-154.

Van Driessche A. E. S., Benning L. G., Rodriguez-Blanco J. D., Ossorio M., Bots P., Garcia-Ruiz J.M. (2012) The role and implications of Bassenite as a stable precursor phase to gypsum precipitation. *Science.* **336**, 69-72.

Vileno E., Ma Y., Zhou H., Suib S. L. (1998). Facile synthesis of synthetic todorokite OMS-1), co-precipitation reactions in the presence of a microwave field. *Micropor. Mesopor. Mat.* **70,** 3-15.

Villalobos M., Toner B., Bargar J. and Sposito G. (2003) Characterization of the manganese oxide produced by Pseudomonas putida strain MnB1. *Geochim. Cosmochim*. Acta **67**, 2649–2662.

Villalobos M., Bargar J. and Sposito G. (2005) Mechanisms of Pb(II) sorption on a biogenic manganese oxide. Environ. Sci.Technol. **39**, 569–576.

Villalobos M., Lanson B., Manceau A., Toner B. and Sposito G. (2006) Structural model for the biogenic Mn oxide produced by Pseudomonas putida. *Am. Mineral*. **91**, 489–502.

Vlaic G. and Olivi L. (2004) EXAFS Spectroscopy: a Brief Introduction. *Croat. Chem. Acta*. **77**, 427-433.

Vraspir J. M. and Butler A. (2009) Chemistry of marine ligands and siderophores. *Annu. Rev. Mar. Sci*. **1**, 43–63.

Wang X. and Muller W. E. G. (2009) Marine biominerals: perspectives and challenges for polymetallic nodules and crusts. *Trends. Biotechnol.* **27**, 375-383.

Wasylenki L. E., Weeks C. L., Bargar J. R., Spiro T. G., Hein J. R. and Anbar A. D. (2011) The molecular mechanism of Mo isotope fractionation during adsorption to birnessite. *Geochim. Cosmochim. Acta* **75**, 5019–5031.

Watt R. K. and Ludden P. W. (1999) Nickel-binding proteins. *Cell. Mol. Life Sci.* **56**, 604-625.

Waychunas G. A., Rea B. A., Fuller C. C. and Davis J. A. (1993) Surface chemistry of ferrihydrite: 1. EXAFS studies of the geometry of coprecipitated and adsorbed arsenate. *Geochim. Cosmochim. Acta.* **57**, 2251-2269.

Waychunas G. A., Kim C. S. and Banfield J. F. (2005) Nanoparticulate iron oxide minerals in soils and sediments: unique properties and contaminant scavenging mechanisms. *J. Nanopart. Res*. **7**, 409-433.

Webb S. M., Tebo B. M. and Bargar J. R. (2005a) Structural characterization of biogenic manganese oxides produced in seawater by the marine Bacillus sp. strain SG-1. *Am. Mineral*. **90**, 1342–1357.

Webb S. M., Dick G. J., Bargar J. R. and Tebo B .M. (2005b) Evidence for the presence of Mn(III) intermediates in the bacterial oxidation of Mn(II). *P. NATL. ACAD. SCI. U. S. A.* **102**, 6. 5558-5563.

Wenk H. R. and Bulakh A. (2004) Minerals: Their constitution and origin.

Westall J. C. and Hohl H. (1980) A comparison of electrostatic models for the oxide/solution interface. *Adv. Colloid Interface Sci*. **12**, 265–294.

Xu H., Chen T., Konishi H. (2010) HRTEM investigation of trilling todorokite and nano-phase Mn-oxides in manganese dendrites. *Am. Mineral*. **95**, 556-562.

Yin H., Wenfeng T., Zehng L., Cui H., Qui G., Liu F., Feng X. (2012) Characterization of Ni-rich hexagonal birnessite and its geochemical effects on aqueous Pb2+/Zn2+ and As(III). *Geochim. Cosmochim. Acta.* **93**, 47-62.

Yoshimura T. (1934) "Todorokite," a new manganese mineral from the Todoroki Mine, Hokkaido, Japan. *Journ. Fac. Sci*. Hokkaido University, Ser. **4**, 289- 297.

Zhang J., Huang F. and Lin Z. (2009) Progress of nanocrystalline growth kinetics based on orientated attachment. *Nanoscale.* **2**, 18-34.

Zhu M., Ginder-Vogel M. and Sparks D. L. (2010) Ni(II) sorption on biogenic Mn-oxides with varying Mn octahedral layer structure. *Environ. Sci. Technol*. **44**, 4472-4478.

Zubavichus Y. V. and Slovokhotov Y. L. (2001). X-Ray synchrotron radiation in physicochemical studies. *Russ. Chem. Rev.* **70**,373-403.